Understanding the Erosion – Corrosion Behaviour of Generic Types of Stainless Steels in a CO_2 – Saturated Oilfield Environment

By

MOHAMMED NABEEL MAJEED

Submitted in accordance with the requirements for the degree of

DOCTOR OF PHILOSOPHY

The University of Leeds

School of Mechanical Engineering

January, 2018

The candidate confirms that the work submitted is his own and that appropriate credit has been given where reference has been made to the work of others.

CONFERENCES

Parts of the current work were presented in a number of local and international conferences held in the United Kingdom and were discussed extensively with a group of academics and industrial experts.

- The 57th Corrosion Science Symposium (CSS), Swansea, 2016.

- The Joint International Electrochem Conference and 58th Corrosion Science Symposium (CSS), Birmingham, 2017.

- The Institution of Engineering and Technology (IET) Poster Competition – *New Challenges in Tribology*, Birmingham, 2018.

- The 15th TriboUK Conference - *The Impact of Tribology in the Modern World*, Sheffield, 2018.

PREFACE

The purpose of the present work is to progress the topic of erosion-corrosion of stainless steels in the oil and gas industry. The problems result from this phenomenon pose a great challenge for the workers in oil and gas installations because of its significant effect on both production and cost. This in turn prompted corrosion researchers, including the author of this work, to conduct many researches related to this important topic to gain better understanding of materials degradation behaviour. This thesis provides improved understanding on the degradation behaviour of generic types of stainless steels used in the oil and gas industry under erosion-corrosion conditions with the aim being to minimize the evolved risks of structural integrity resulting from materials degradation particularly in the Pierce oilfield, North Sea, UK which is operated by Shell.

Mohammed Nabeel Majeed, 2018

DEDICATION

To

Who was my best mentor and had a great impact on my life ... I miss your advices and your beautiful words so much

Haj Abdul-Jabbar Abdul Kareem

Those who have left a void in my heart will not be filled ...Your inexhaustible kindness and deep love cannot be compensated

My Grandmas

All of you will not be absent from my imagination as long as I live ... I ask Allah Almighty to grant your souls the mercy and immortality in the heaven.

I dedicate this humble work

ACKNOWLEDGEMENTS

"Alhamdulillah Rabb al Alalamin"

Praise and thanks to Allah Almighty as it must be for his majesty who guided me to set up this work and awarded me the faith, knowledge, patience and strength to overcome all of the challenges I faced during the doctoral journey in addition to his blessing in my health, livelihood and age to be able to complete this research, hoping to gain his Almighty satisfaction.

I have had the honour of working with a distinguished and knowledgeable supervisor like Professor Anne Neville. I have always enjoyed discussing my work with her and I was so lucky to get such an opportunity particularly I was the first Iraqi working with her. She taught me the true meaning of the word "challenge" and how to overcome it. This in turn has had a great impact on my life both personally and practically. Thank you for your support, encouragement, trust and faith in my abilities.

Also, I would like to express my thankful to my co-supervisor, Dr Richard Barker for his help in the lab in the early stages of my PhD and for accompanying me whenever we went to Aberdeen.

My beloved country, Iraq, I cannot find a suitable word to express my thankful for you for funding my study. All what can I say is that, I will still owe you as long as I live. The funding of this study was through the Higher Committee for Education Development (HCED), which I would like to express my thankful to one of its distinguished staff, Dr. Abdul Hakeem Al-Rawi.

My dear parents, Mr. Nabeel Majeed Neamah and Mrs. Faiza Yaseen Ahmed, I hope that I have achieved what you have dreamed of and compensated a small part of your endless efforts in order to provide a decent life for me. Allah satisfaction then yours

in addition to your continuous praying for me are what give me the power to achieve all that I aspire to in this life. I wholeheartedly appreciate what you have done for me.

My wife, Eng. Eman Sami Ahmed, thank you for the love, patience and support you gave me from the beginning of our marriage until now. You are the air that I breathe without it I cannot live anymore. Although there are no words can really help to express what I feel towards you for everything you did for me since I met you, I just would say: “you are really the best friend for me in this world”.

Also, I would like to thank my daughter, Maryam Mohammed Nabeel. Your beautiful smile was really a balm that heals all of my pains throughout my study. My hope in this life are to see you happy at all times and to be able to provide a dignity life for you and to see you one day, inshallah, an important and positively influential figure in our human society. I live in this world just to give you the happiness and love you deserve.

My appreciation and thanks should also go for my sister Eng. Dina Nabeel Majeed and my brother Dr. Saif Nabeel Majeed for their continued support.

Thank you, I say it with all sincerity and love to my wife's parents, Mr. Sami Ahmed Jasim and Mrs. Faiza Abdulrazzaq Jafar for their continued support, encouragement and trust. Also, I will not forget my relatives, who showed a continual support, especially my dear aunt, Mrs. Thikra Majeed Neamah, who has an affectionate heart. A great thanks and appreciation should be gone to Dr. Sadoun Fahad Dakhil, I value the trust you have put into me. I would also like to thank Dr. Nawal Jasim Hamadi for her kind cooperation. Many thanks to my inspirational teacher, Dr. Kate Taylor for her endless efforts since the language centre days.

A great greeting should be directed to all technicians working in the school of mechanical engineering at Leeds University for their outstanding efforts to implement

and provide all that is necessary to make this work comes to life. Thank you all guys. Hats off to Mr. Jordan Thomas and Mr. Andrew O'Brien for the wonderful help I received from them throughout my work in the lab.

I would like to express my thanks and gratitude to all staff of Leeds Electron Microscopy and Spectroscopy (LEMAS) in particular Mr. John Harrington (FIB), Mr. Stuart Micklethwaite (SEM), Dr. Mike Ward and Dr. Zabeada Islam (TEM) for their diligent help in most of the surface analysis relevant to this work.

I would also like to thank all of my friends either in my country or whom I met here in the UK, especially at the University of Leeds, who supported and advised me and were impressively helpful when needed. A special thanks to my dear mates Dr. Omar Khalooq and Dr. Mustafa Khalifa for their valuable advices and support.

Also, thanks to all previous and the current office mates. You were and will remain a part of my family.

At last but not least ... I would say:

"Life is a beautiful garden, its flowers are good people, who show sincerity and loyalty when helping others ... kindness always wins"

Mohammed Nabeel Majeed, 2018

ABSTRACT

Using of Corrosion Resistant Alloys (CRAs) specifically stainless steels is considered as one of the most effective corrosion control strategies in the oil and gas industry when aggressive environments such as carbon dioxide and chloride ions may be present. This is due to presence of a compact and protective passive film on their surfaces which acts as a barrier between the substrate and the surrounding corrosive environment. However, presence of sand particles in the flowing fluid can reduce the superior corrosion resistance of these alloys because of passive film removal by sand particles impact leaving the substrate exposed directly to corrosive environments. This phenomenon is commonly known as "erosion-corrosion". Sand particles impact may also lead to significant surface and subsurface changes and the latter has a great influence on the erosion and erosion-corrosion resistance of stainless steels knowing that the latter vary in their chemical composition and their mechanical properties. For this reason, it is important to understand how these materials will behave under erosion and erosion-corrosion conditions.

The effect of the static corrosion behaviour on the erosion-corrosion resistance of stainless steels as a function of temperature was investigated. Also, how stainless steels degrade under erosion and erosion-corrosion conditions and specifying the factors contribute to their failure have been addressed. Moreover, the study has investigated how the percentage of contribution of total weight loss components of stainless steels changes with impact angles.

Gravimetric and electrochemical measurements in addition to post-test surface analysis including micro indentation hardness test, surface optical profilometry (Bruker- NPFLEX), Scanning Electron Microscopy (SEM), Focused Ion Beam (FIB),

Transmission Electron Microscopy (TEM) were used to explain the degradation behaviour of the studied materials under erosion-corrosion conditions.

It has been found that there is a good correlation between the static corrosion behaviour and the erosion-corrosion resistance of stainless steels. For example, a good link between the repassivation ability under static conditions (i.e. (E_b-E_r) and i_{max}) and erosion-enhanced corrosion was existed. Also, the same parameters linked well with the repassivation time under erosion-corrosion conditions. Moreover, results revealed that the change in hardness can be used as a prediction parameter to erosion resistance of stainless steels in severe conditions. Furthermore, impact angle has a significant effect on the percentage of total weight loss component contribution. It was found that the percentage of the corrosion-enhanced erosion contribution to be responsible for a distinct erosion-corrosion resistance of stainless streels.

TABLE OF CONTENTS

LIST OF FIGURES

LIST OF TABLES

NOMENCLATURE

BSE: Back Scattered Electron.

CPP: Cyclic Potentiodynamic Polarization.

CPT: Critical Pitting Temperature.

CRAs: Corrosion Resistant Alloys.

dC_E: Erosion-enhanced corrosion.

dE_C: Corrosion-enhanced erosion.

E: Pure erosion.

E_b: Breakdown potential.

EDX: Energy Dispersive X-ray.

E_r: Repassivation potential.

(E_b-E_r): Repassivation ability.

FIB: Focused Ion Beam

HAADF: High Angle Annular Dark Field

***i_{max}*:** Maximum current density

LPR: Linear Polarisation Resistance

mpy: Mils per year.

PP: Potentiostatic Polarisation.

PRE_N: Pitting Resistance Equivalent Number.

RCE: Rotating Cylinder Electrode.

SEM: Scanning Electron Microscopy

SIJ: Submerged Impinging Jet.

TEM: Transmission Electron Microscopy

TWL: Total Weight Loss.

TWLC: Total Weight Loss Components.

Chapter One: Introduction

1.1 Research background

Corrosion is considered as one of the most significant challenges that has an impact at both domestic and industrial levels. One of the main reasons that corrosion causes concern and makes the study and control the problem of corrosion a top priority is safety. There are economic and efficiency factors that are also important. Unexpected explosions in gas pipelines, release of toxic substances and contamination of water due to corrosion are just a few of many examples showing how safety can be affected by corrosion and how much it is important to deal with this issue seriously [1].

In terms of economic, according to the National Institute of Standards and Technology (NIST), the annual costs caused by corrosion in the United States were between $9 - $90 billion. However, this is just an initial estimate as this cost is growing with time. For example, the annual corrosion costs were estimated by the National Association of Corrosion Engineers (NACE) to be about $276 billion as shown in Figure 1-1.

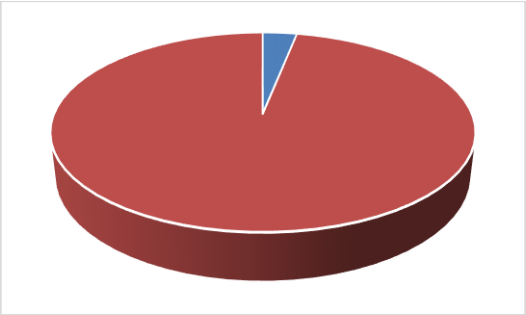

Figure 1-1: Extrapolated corrosion costs: $276 billion, 3.1% of 1998 U.S. gross domestic product ($8.79 trillion) [2]

The cost of corrosion in the oil and gas exploration-production sector alone is about $1.4 billion [2]. The main causes of corrosion in the oil and gas sector can be seen in Figure 1-2.

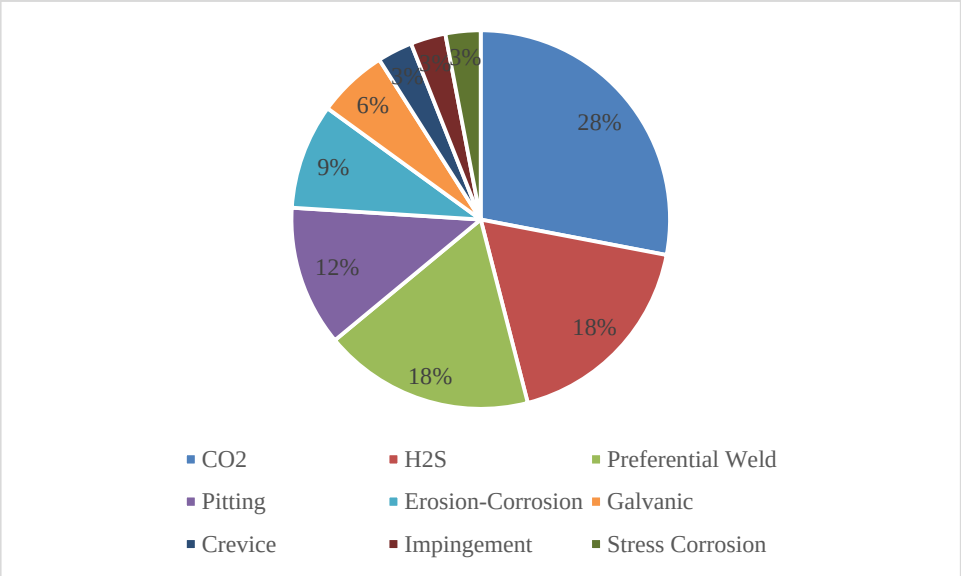

Figure 1-2: Causes of corrosion related to the oil and gas industry [3]

But that's not all, as the latest study showed that the cost of corrosion in 2016 reached $1 trillion, giving a scary impression of the extent of the enormous impact of this phenomenon. Direct and indirect losses are considered as the main classifications of the economics losses. Replacing and/or maintaining of failed (corroded) equipment, components and structures, controlling and monitoring corrosion, use of corrosion resistant alloys or coatings and corrosion inhibitors lie within the direct losses. On the other hand, plant shutdown, product contamination, loss of efficiency and overdesign represent the principal forms of indirect losses. The reservation losses include ores drain, energy consumption will be used in fabrication and manufacturing of the metallic materials and loss of human efforts which will be used to redesign and replace the failed component [4, 5].

A wide range of materials are used in industry. However, important criteria should be taken into account when selecting a material for a specific application. Of these

criteria are the mechanical properties, corrosion resistance in addition to the cost of the selected material [4]. Although carbon steels are widely used in the oil and gas industry due to their preferable cost and mechanical properties, their corrosion resistance is limited. Corrosion inhibitors are used to improve their corrosion resistance. However, usage of corrosion inhibitors in the offshore applications still has a number of limitations. Even though corrosion inhibitors can be used in both offshore and onshore installations, the economic situation of usage is totally different. The life cycle cost of corrosion inhibitor usage onshore is low compared with offshore due to inhibitors cost, transportation, storage in addition to supervision and maintenance of injection components. It should also be noted that one of the main aims of offshore engineering is to reduce the weight of the topside in order to save the structure cost. So, the extra weight due to corrosion inhibitors usage will be superfluous. Moreover, water treatment due to drainage of the inhibited solution to the ocean, which is not acceptable in some locations, will require more cost to remove the inhibitors chemicals. Furthermore, the corrosion resistance of inhibitors is limited and they cannot withstand the harsh environment such as high temperature, high flow velocity, particularly with the presence of sand, which is commonly known in the North Sea oilfields [6].

For the above reasons, many efforts have been made to overcome this challenge and it has been found that the use of CRAs as an alternative method to mitigate corrosion in particular in such environments due to their superior mechanical and corrosion resistance properties is worthwhile. Also, the use of CRAs makes it possible to reduce the diameter of pipes while maintaining its weight, allowing high flow velocities. For example, by replacing carbon steels with UNS S31803, the possible obtained weight reduction was up to 50% with an increase in accelerated flow of 6 -11 m/s and with an eliminated corrosion allowance of 3 mm [6].

There are different types of CRAs. However, stainless steels are considered as the most common type of CRAs in the oil and gas industry. Stainless steels can be used in different sectors within the oil and gas industry. For instance, duplex stainless steels can be used in the subsea pipelines and 13Cr can be found in the casing or wellhead Xmas tree. The superior resistance of stainless steels to corrosion is due to presence of passive film on their surfaces. However, the presence of sand particles in the flowing fluid can disrupt the passive film and expose the substrate directly to the corrosive environment and to be corroded rapidly [7].

Sand may be present within the flowing fluid for many reasons. It is believed that formation failure due to weak mechanical properties of the formation rocks is one of the reasons for occurrence of this phenomenon. Also, it can be due to deformation of weak rocks resulting from the wellbore / perforation stresses in addition to well damage due to drilling and perforating (Figure 1-3). This will result in failure of components due to occurrence of erosion, specifically solid particle erosion. Also, pipelines can block and cause a delay in production [8].

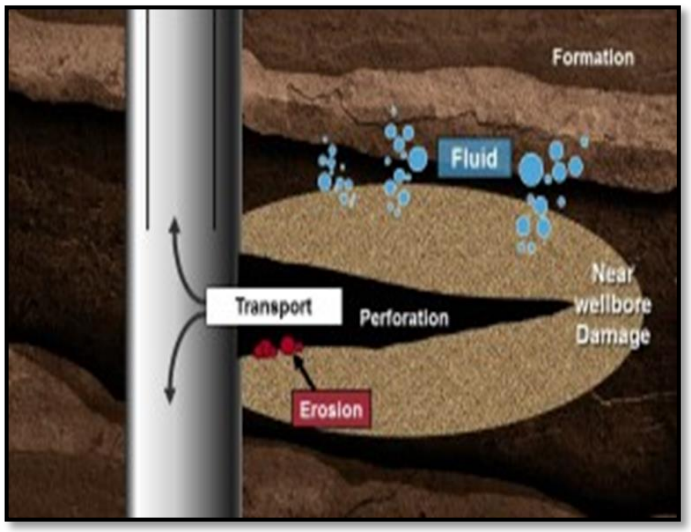

Figure 1-3: Sand production in an oil well [8]

Solid particle erosion will be considered within the scope of this work. The problem can be exaggerated with the presence of a corrosive environment. It is known that corrosion reactions are electrochemical in nature. A combined action of electrochemical and mechanical effects can be encountered. This will result in what is commonly known as “erosion-corrosion”.

It has been mentioned earlier that passive film is what gives stainless steels their unique corrosion resistance property as it acts as a barrier between the substrate and the surrounding corrosive environment. However, if the kinetic energy of the sand particles is higher than the mechanical properties of the passive film, the latter will be disrupted and the surface of the bulk materials will be exposed directly to the corrosive environment. The mechanical properties and corrosion resistance of stainless steels are varied and hence their resistance to erosion-corrosion conditions will not be the same. There are a number of studies in the literature that have dealt with erosion-corrosion of stainless steels in aerated brine solutions. However, few studies have focused on understating the erosion-corrosion behaviour of stainless steels in a CO_2 – saturated oilfield environment. Therefore, this study aims to improve the current understanding of the degradation mechanism of generic types of stainless steels used in the oil and gas industry under CO_2 erosion-corrosion conditions.

1.2 Research objectives

This work aims to improve the current understanding of the degradation behaviour of generic types of stainless steels in a CO_2-saturated oilfield environment under erosion-corrosion circumstances through the following objectives:

1- To evaluate the Critical Pitting Temperature (CPT) of UNS S32760 and UNS S31803 in a 10%NaCl brine CO_2 - saturated solution.

2- To examine the repassivation ability of the studied materials under static corrosion conditions by the Cyclic Potentiodynamic Polarisation (CPP) technique.

3- To examine the repassivation ability of the studied materials under erosion-corrosion conditions by the *In-Situ* Potentiostatic Polarisation technique (PP) and Submerged Impinging Jet (SIJ).

4- To implement the electrochemical measurements of the studied materials under erosion-corrosion conditions by *In-Situ* Linear Polarisation Resistance (LPR) and SIJ.

5- To evaluate the Total Weight Loss (TWL) and its components of UNS S32760 and UNS S31603 as a function of time.

6- To investigate the characteristics of the top surface layer and the deformed sub-layer of the studied materials using a wide range of post – test surface analysis techniques namely: Focused Ion Beam (FIB), Transmission Electron Microscopy (TEM), Scanning Electron Microscopy (SEM), surface optical profilometry (Bruker - NPFLEX) and micro indentation (Vickers) hardness test.

7- To evaluate the TWL and its components of UNS S32760, UNS S31803, UNS S31603 and UNS S42000 as a function of impact angle.

8- To determine surface failures and topography and to understand the degradation mechanism of the studied materials using SEM, TEM and NPFLEX techniques.

1.3 Statement of contribution to literature

This thesis contributes to literature by providing a further understanding of erosion-corrosion degradation behaviour of stainless steels in the oil and gas production. This can be achieved by answering a number of questions such as:

- Does the static corrosion behaviour have an effect on the erosion-corrosion performance of stainless steels at different temperatures including the CPT of material? Particularly it is hypothesised that after each sand particle impact the surface is "activated" and the ability to recover should be important.
- What is the origin of stainless steels failure under erosion-corrosion circumstances and what factors contribute to it?
- How does the variation of impact angle affect the percentage of contribution of TWL components of stainless steels?

Experimentation and surface analysis are combined to give an insight into the degradation behaviour of stainless steels under erosion-corrosion conditions. To date, this study offers a significant contribution to the existing body of knowledge on erosion-corrosion of stainless steels in a CO_2 – saturated oilfield environment. Shell, UK. benefited of the obtained outcomes from the present study.

1.4 Thesis outline

This work is divided into eight chapters:

Chapter one: This chapter outlines the problem that was addressed in this study and points out the rationale which motivated the author to implement this work. Also, it includes the objectives of the present work in addition to the statement of contribution.

Chapter two: This chapter defines the key terms and reviews the basic concepts related to the topic of erosion - corrosion of stainless steel in a CO_2 – saturated

environment which includes solid particle erosion, electrochemical corrosion especially CO_2 corrosion in addition to the influencing factors on both of them. Also, it highlights the generic types of stainless steels used in the oil and gas industry in addition to the relevant main concepts such as the passive film formation and its breakdown.

Chapter three: This chapter provides a step by step description of the experimental techniques used and the procedure followed in the present work. Details on the materials, test solutions, erodent are provided. It also includes a description of the experimental rig used in erosion and erosion-corrosion testing in addition to the post-test surface analysis techniques relevant to this work.

Chapter four: This chapter presents the obtained experimental results aiming to understand how the static corrosion behaviour affects the erosion-corrosion resistance of stainless steels at different temperatures. Both static corrosion and erosion-corrosion experimental results are presented.

Chapter five: This chapter includes a comprehensive gravimetric, electrochemical and post-test surface analysis all of which will help to understand the origin of stainless steels failure used in service.

Chapter six: This chapter investigates the erosion-corrosion behaviour of a range of stainless steels as a function of erodent impact angle.

Chapter seven: This chapter summarises the key findings obtained from the experimental results and discusses the important mechanisms involved in erosion-corrosion of stainless steels. It also provides some new insights on the contribution of these mechanisms to the overall erosion – corrosion of stainless steels.

Chapter eight: Provides overall conclusions and summarises the key findings obtained from this work. Also, future work is proposed in this chapter.

Chapter two: Fundamental theories and literature review of erosion-corrosion of stainless steels

2.1 Introduction

In this chapter, the main literature relevant to the scope of the current work (which is focused on erosion-corrosion of stainless steels in a CO_2 - saturated oilfield environment) will be reviewed to highlight the research progress in this field and serve as a foundation for this work. It is known that erosion-corrosion process is a combination of two significant components; electrochemical corrosion and mechanical solid particle erosion. The combination of these two components will increase the complexity of understanding the topic. For this reason, it was found it will be better to study these components separately including their mechanisms, influencing factors, testing methods etc. to ensure a comprehensive and deep understanding of the whole process.

This chapter will start by providing an overview on solid particle erosion and its mechanisms. Also, the influencing factors affecting it will be highlighted. Then, the nature of electrochemical corrosion and mechanisms in addition to the electrochemical methods used to measure the corrosion rates of materials will be presented. After that, a brief description to the corrosion resistant alloys particularly stainless steels will be introduced. Finally, the erosion-corrosion process and its testing method will be presented.

2.2 Solid particle erosion

2.2.1 Introduction

Wear is defined as the deterioration of a solid surface as a result of mechanical impact of a contact solid, liquid or gas [9]. Wear can be found in different mechanisms and classifications. One of these mechanisms is wear which is resulted from hard particles. Erosive wear is one of the categories of wear by hard particles [10]. When the surface of material is impacted by hard particles, which are carried by a gas or dragged by moving liquid, the wear can be called as erosion. The surface may also be damaged due to the impact of jets or drops of the liquid. For this reason, erosion which is caused by solid particles is either called solid particle erosion or solid impingement erosion and hence it can be easily recognised from the other types of erosion. In the case of a liquid carrying the solid particles, the term slurry erosion is used [10]. Figure 2-1 shows the main types of erosion.

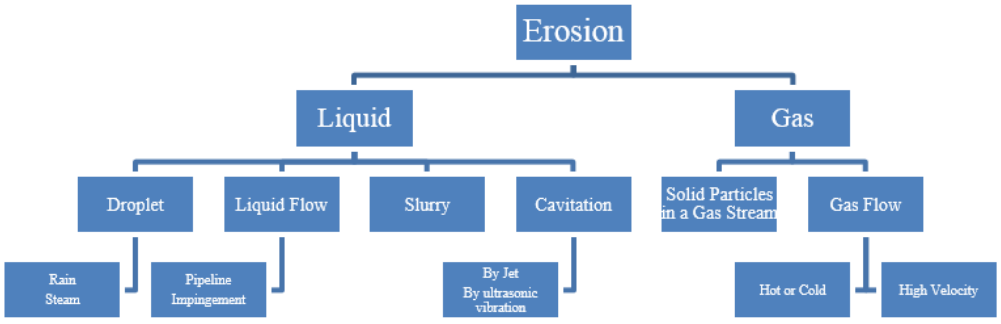

Figure 2-1: Types of erosion [11]

Sand is expected to be produced in the low formation strength (< 2000 psi) oil and gas reservoirs [12]. The impact angle of the particles and their properties are considered as important factors which define the mechanism of material removal.

2.2.2 Mechanisms of solid particle erosion

Mechanisms of solid particle erosion are dependent on some important factors. Different mechanisms can be obtained if these parameters are changed. These factors are the type of targeted material, the properties of the erodent particles and the impact angle. Materials in general can be divided into either ductile or brittle depending on their nature. The mechanism of erosion in the ductile materials is different from the brittle one [10, 13]. In order to understand what solid particle erosion is, it is necessary to know the possible mechanisms of this process as well as the factors that affect its occurrence. For all of this, efforts have begun to achieve this goal. Finnie's work was the first nucleus, which was followed by the relentless efforts to arrive at an integrated understanding of the process. Finnie *et al.* [14, 15] suggested two types of materials removal mechanisms depending on the nature of material. For example, it was suggested that the removal of the ductile material occurred by displacement and cutting. On the other hand, the intersection of propagated cracks is the mechanism responsible for removal of brittle materials.

Impact angle can play an important role as mentioned earlier in the solid particle erosion mechanisms of ductile materials. Although Finnie's model lacked accurate prediction of the material removal at normal impact angle, it succeeded in reaching a rough estimate of the removal of ductile materials at a shallow impact angle. Bitter *et al.* [16, 17] took advantage of this by suggesting the mechanism of ductile material removal at normal impact angle, indicating that two separate types of mechanisms occur at the same time. These mechanisms are deformation (Figure 2-2 – d) and cutting wear. Then the concept of ductile materials removal mechanisms, especially at an acute angle, was developed through the work done by Hutchings *et al.* [18, 19]. They were able to identify three types of mechanisms based on the shape of the

erodent particles. The first type occurs specifically by rounded particles and it was called the ploughing mechanism (Figure 2-2 – a) while the second and third types are limited to the angular particles and have been called type I cutting (Figure 2-2 – b) and type II cutting (Figure 2-2 – c). In these two types, the movement of particles either forward or backward determines which one will occur. Levy [20] concluded that the main mechanism for material loss is due to extrusion and forging of platelets. The bent platelet can be knocked off by any subsequent impacts.

For brittle materials, the mechanism is different because the erodent particles can result in subsurface cracks being formed and the connection of these cracks can cause the materials to be chipped out [21]. This is shown in Figure 2-3.

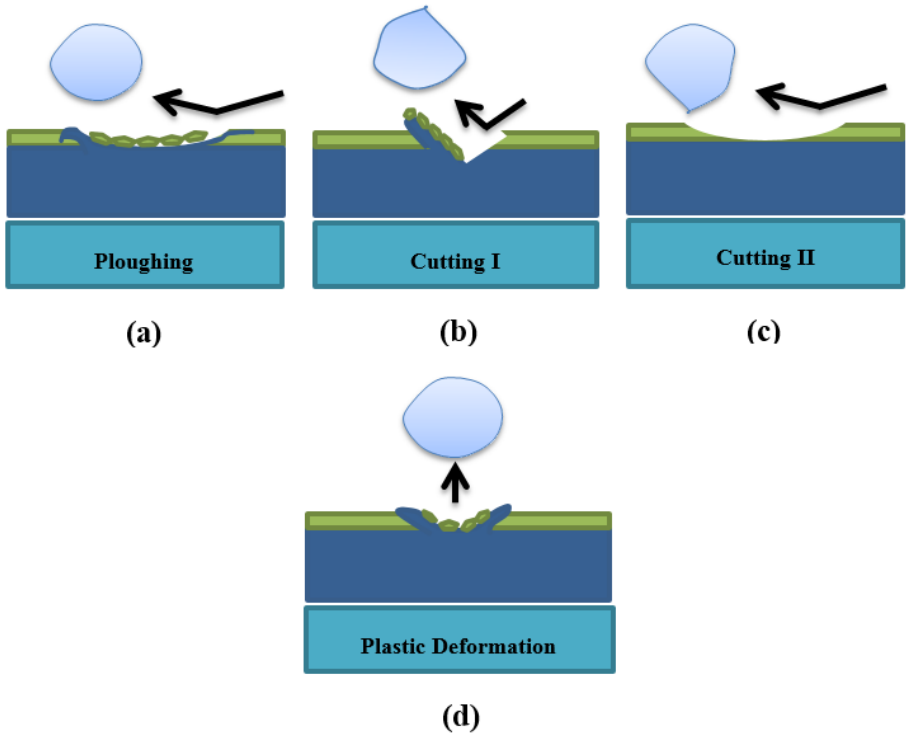

Figure 2-2: Mechanisms of solid particle erosion at oblique impact angle for: **(a)** rounded Particle **(b)**,**(c)** angular particles **(d)** normal impact angle of rounded particle [22]

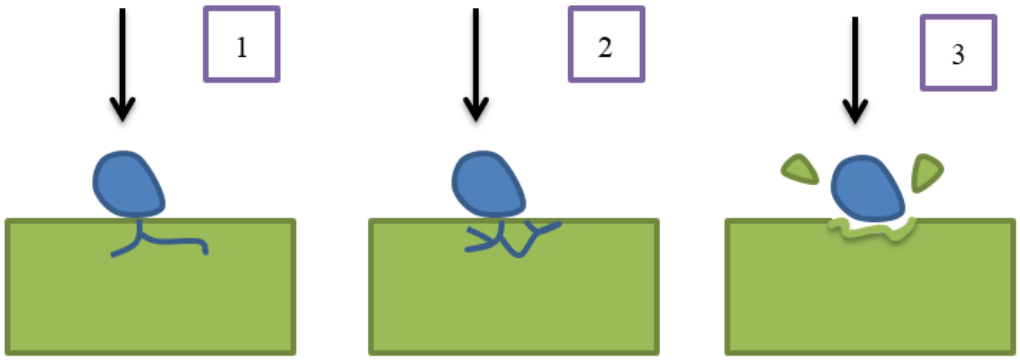

Figure 2-3: Mechanisms of solid particle erosion of brittle materials [21]

2.2.3 Factors affecting solid particle erosion

Solid particle erosion is a complex process. Its complexity is originated from the presence of a number of factors affecting it. The affected material, the impacted erodent which are entrained in the flowing fluid at a certain velocity represent the basic components of erosion process. Therefore, these factors have been classified into several major groups based on the characteristics of the basic components of this system which are mentioned earlier in order to facilitate understanding of their impact on erosion process. The parameters affecting erosion are divided into three groups: impingement factors include particle velocity, impact angle and particle concentration; particles factors including particle shape and size and material factors which include the properties of the material such as hardness [9, 23]. Detailed information regarding the effect of these parameters on erosion will be explained in the following sections.

2.2.3.1 Impact angle

As shown in Figure 2-4, the maximum erosion rate can be obtained at low impact angle (< 30^{o}) for ductile materials while it is about (90^{o}) for brittle materials [21].

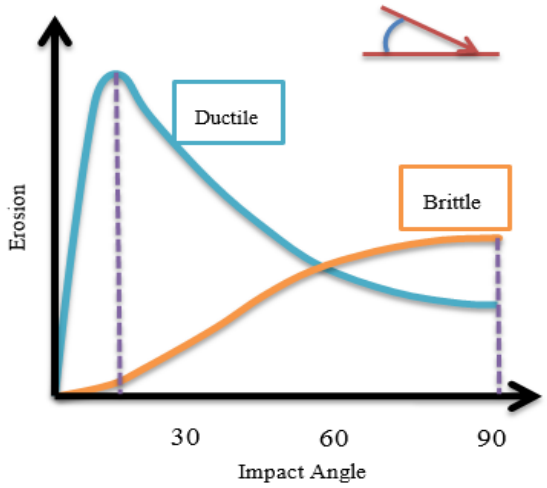

Figure 2-4: Erosion rates versus impact angles [10]

2.2.3.2 Particle Velocity

Erosion rate can be significantly affected by particle velocity according to the following formula [21]:

$$E = kv^n$$

Where:

E: is the rate of erosion.

k: constant.

v: velocity (m/s)

n: exponent which is typically between (2 and 2.5).

Shows the relationship between particle velocity and erosion rates for ductile and brittle materials.

2.2.3.3 Particle shape and size

Solid particles may vary in their shape due to their angularity differentiation and this has a considerable effect on erosion. There are two types of particle shapes: rounded

and angular. The last type has a great impact on the erosion rates compared with the rounded one [10]. This can be clearly seen in Figure 2-5.

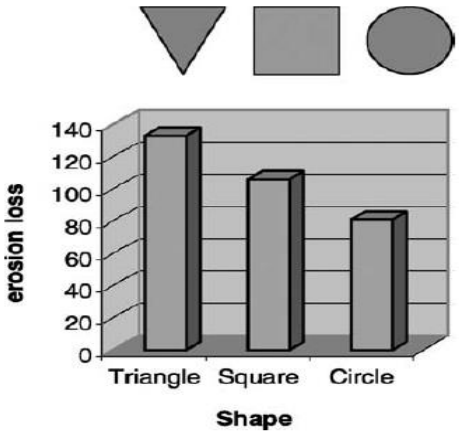

Figure 2-5: Effect of particle shape on the erosion rates of ductile materials [24]

In terms of particle size, although there is an enormous range of particle size, the influential range of particle size on the erosion rates was found to be between 5-500 µm in size. However, the erosion rates will be significantly decreased when particles size less than 100 µm [10]. The hard and quickly moving particles will suddenly and intensively plastically deform the material surface under erosion conditions and hence heat is generated and the latter will lead to an increase in temperature. Consequently, a softening of the material will be expected. In the case of soft materials, this will lead to formation of the extruded lips which can be easily detached from the material surface [25]. Shewmon *et al.* [25] took advantage of this phenomenon, by suggesting a model which assumes that the kinetic energy, which is a function of flow velocity and particle size, of the moving particles will dissipate as heat when it impacts the material surface and this will lead to localised deformation and material loss. However, this is not the case if the particle size is too small or even too large. If the particle size was too small, the generated heat is low and hence less erosion rate. On

the other hand, if the particle size is too large, the generated heat due to particles impact will be dissipated because of longer time between particle impacts [26].

2.2.3.4 Particle concentration

Particle concentration has a critical effect on the erosion rates. Neville *et al.* [27] studied the effect of sand loading on the erosion of UNS S31603 stainless steel and they found that as sand loading increased from 1-10 wt.%, the mass loss of the material was increased. On the contrary, there was a reduction in the erosion rate when more sand was added above 10%, as shown in Figure 2-6. This was attributed to reduction of the impact energy resulting from less impacts and the latter caused by the high interference between the impact and rebounding particles. Dasgupta *et al.* [28] attributed this to prevention of particles mobility at high sand concentration and thus reduce the probability of material surface being impacted by it. However, less sand concentration will allow particles to move more freely and therefore the probability of their impact with the material surface will be increased. They also suggested that when sand concentration will be high enough, sand particles may cover the material surface and prevent the incoming particles to hit it directly causing only a little abrasion.

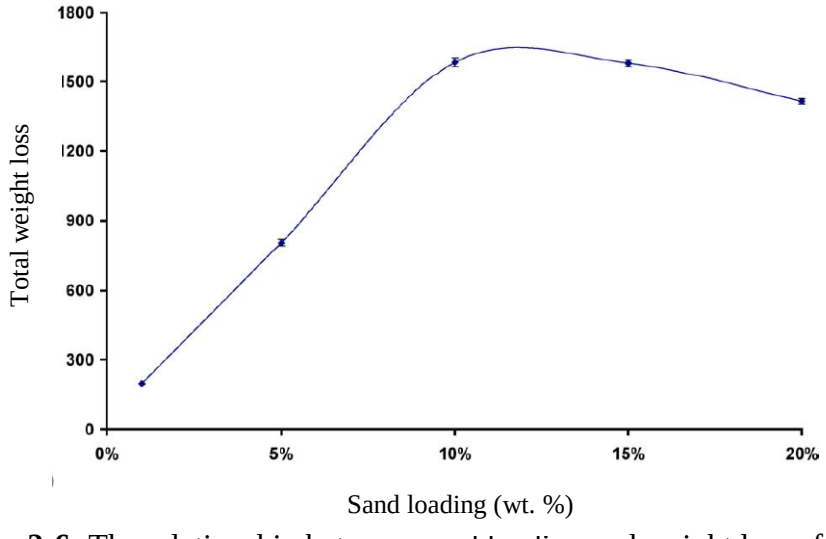

Figure 2-6: The relationship between sand loading and weight loss after [27]

2.2.3.5 Material hardness

The influence of the material hardness on the erosion rates should be taken into account when studying solid particle erosion. It is concluded that the erosion rate may be reduced by increasing surface hardness [29]. Sundararajan [30] who studied the hardness-distance profile of different alloys after erosion found that the hardness increased along the distance of the targeted material that is impacted by solid particles as shown in Figure 2-7.

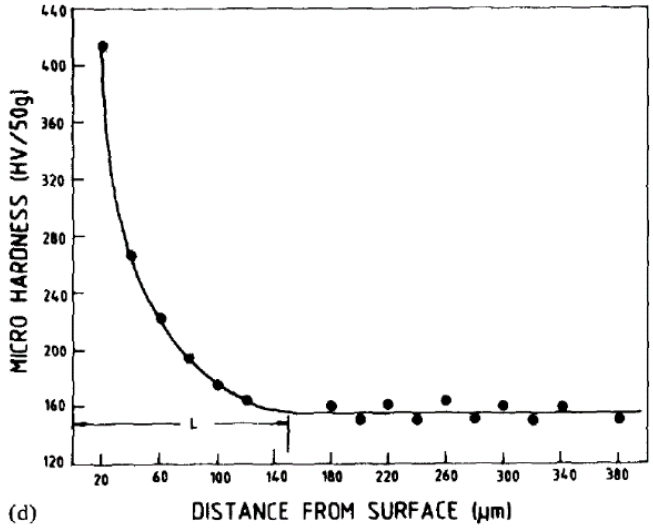

Figure 2-7: The microhardness and distance from surface profile [30]

2.3 Corrosion

Corrosion can be defined as the degradation of materials due to their reaction with the environment. Corrosion processes can be divided into two major classifications as chemical and electrochemical corrosion. Chemical corrosion occurs due to the reaction of materials with non - electrolyte while electrochemical corrosion involve dissolving the materials in an electrolyte [31].

2.3.1 Basic mechanisms of corrosion

In order to overcome the problems resulting from corrosion, it is necessary to focus on understanding the mechanism of corrosion. Corrosion cannot occur without any of its main elements which all together form what is known as a corrosion cell. These elements are anode , cathode, electrolyte and salt bridge [1, 31]. This is shown in Figure 2-8. Anode is an electrode where the anodic reaction occurs which involve the transformation of metal into metal ions in the solution and electrons which move towards the other electrode in the corrosion cell (the cathode) where electron consumption occurs due to reduction reactions. These electrodes are connected together and immersed in a conductive electrolyte to complete the corrosion cell.

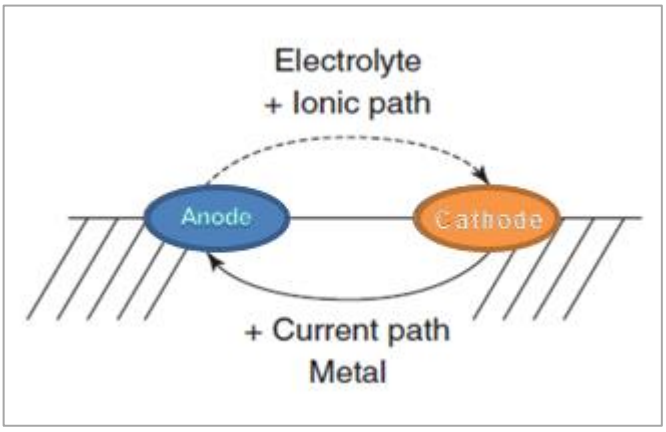

Figure 2-8: The main components of corrosion cell [31]

Below are formulas which represent both anodic and cathodic reactions:

(Anodic Reaction)

$Fe \rightarrow Fe^{+2} + 2e^{-}$

(Cathodic Reactions)

$2H^{+} + 2e^{-} \rightarrow H_2$ (De-aerated- acid solutions)

$O_2 + 4H^{+} + 4e^{-} \rightarrow 2H_2O$ (Aerated- acid solution)

$2H_2O + O_2 + 4e^- \rightarrow 4OH^-$ (Neutral solutions)

2.3.2 Types of corrosion

2.3.2.1 Pitting corrosion

This type of corrosion is considered as the one of the most commonly known types of localised corrosion that occurs for film-forming materials especially stainless steels when a sufficient amount of chloride ions is available [1]. Chloride ions have an adverse effect on the passive film stability and this can be attributed to the adsorption of these ions on the material's surface and their incorporation into the passive film that is weakens the film and thus leads to pit formation [32]. To illustrate this, the anodic reaction is as follows [1]:

$M \rightarrow M^{+n} + ne^-$

The cathodic reaction is [1]:

$O_2 + 2H_2O + 4e^- \rightarrow 4OH^-$

A high amount of metal ions will accumulate as a result of anodic reaction continuity. To achieve a charge balance, chloride ions will leave the electrolyte towards the anodic site as follows [1]:

$M^+Cl^- + 2H_2O \rightarrow MOH + H^+ + Cl^-$

The perforation of the metal is considered a final stage for this reaction to be stopped [1]. This can be clearly seen in Figure 2-9.

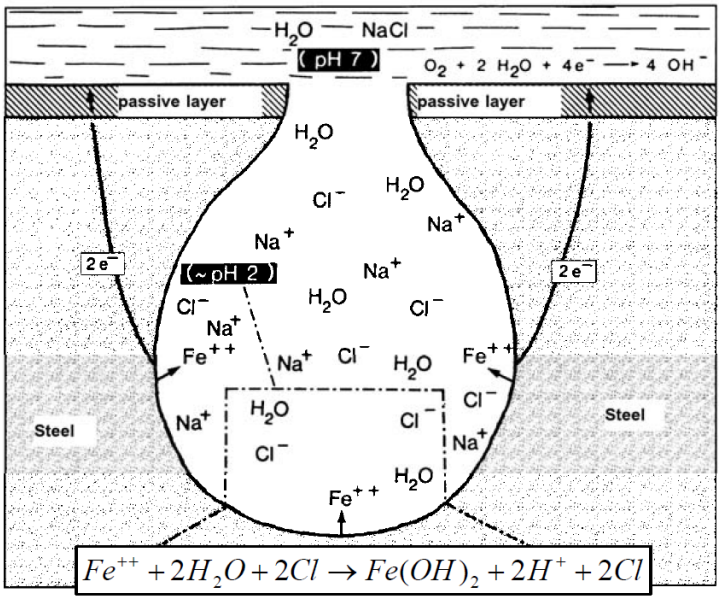

Figure 2-9: Mechanism of pitting in stainless steels [33]

Alloying elements have a significant influence on stainless steel resistance to pitting corrosion. The resistance of stainless steels to pitting corrosion due to alloying elements can be expressed in terms of Pitting Resistance Equivalent Number (PRE_N). The PREN formula is as follows [34]:

$$PRE_N = \%Cr+3.3(\%Mo) +16(\%N)$$

Where:

Cr: Chrome, Mo: Molybdenum and N: Nitrogen.

The pitting resistance of stainless steel is enhanced effectively by Molybdenum. This may be attributed to the enrichment of hexavalent Mo on material surface which adsorb on material surface and form a complex with iron ions and hence block the active sites [32]. Similarly, Nitrogen plays a significant role in the pitting corrosion resistance. This is because of two reasons. Firstly, it may be due to the reaction of chloride ions with either ammonia or ammonium ions and hence reduce the effect of pitting corrosion which is enhanced by chloride ions. The other reason is through reduction of alloying elements dissolution rate by forming a nitride between the

substrate and the film [32]. Addition of alloying elements in addition to the use of corrosion inhibitors can reduce or prevent pitting corrosion [1].

2.3.2.1.1 Electrochemical methods to evaluate pitting corrosion

It was explained earlier that the passive film disruption is the main causes for pitting corrosion of stainless steels. Anodic polarisation hysteresis is one of the electrochemical measurements used to indicate the pitting corrosion occurrence. This can be obtained through evaluation the breakdown potential. Three different parameters can be obtained from what is known as cyclic polarisation curve shown in Figure 2-10. These parameters are open circuit, breakdown and protection potentials. This curve can be obtained by scanning at slow rate towards the noble direction from the open circuit potential. Then, this scan will be reversed at a specific point towards the active potential to close the loop. It can be noticed from Figure 2-10 presence of three regions as follows: the immunity region where no pits can propagate at any potential lower than the protection potential, followed by the propagation region, where the already formed pits will propagate. Finally, pitting will commence at region 3 when the critical pitting potential is reached and exceeded [1].

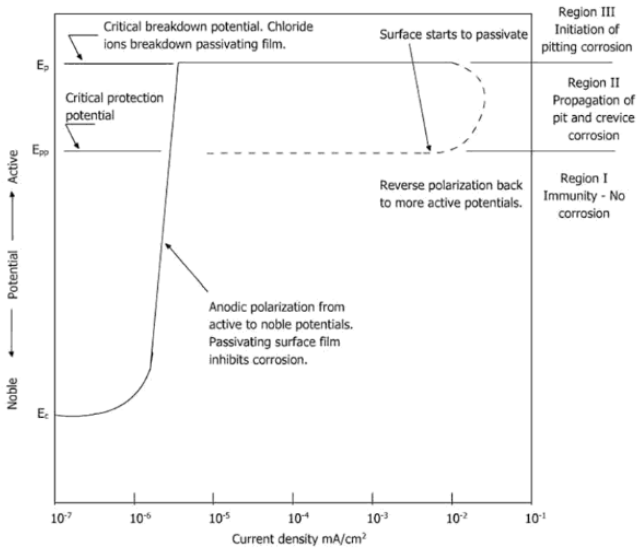

Figure 2-10: Cyclic polarisation curve [1]

It is known that temperature is one of the factors which has a significant influence on the pitting corrosion. The temperature at which a stable pit is formed is called the Critical Pitting Temperature (CPT). The CPT is affected by different factors [35-42] and can be evaluated by different techniques [43-47]. In order to identify the temperature at which pitting will take place, the potentiostatic polarisation technique is used as suggested by ASTM-G03.02 [48].

2.3.2.1.2 Mechanical disruption

Abrading electrode [49], scratching electrode technique [50, 51], cavitation technique [52], micro and Nano indentations [53-57], single impact by sand and glass beads [22, 58] are some of the methodologies used to disrupt the passive film of materials mechanically to evaluate its repassivation ability.

2.3.2.1.3 Repassivation ability of the damaged passive film

Because of the ability of CRAs to restore their oxide film after its damaging either electrochemically or mechanically, it has been found that it is necessary to examine the repassivation mechanism of such alloys depending on the measurement of repassivation time as an important factor to identify the susceptibility of these materials to recover the passive film and study the effect of influential factors on the re-passivation time. Environmental factors such as flow velocity, sand concentration, pH and temperature in addition to the material characteristics which include the alloying elements can be considered as the main parameters to be taken into consideration.

McMahon *et al.* [59] studied the effect of mechanical damage on corrosion resistant alloys resulting from abrasion due to wireline operations under sweet and sour conditions to mimic the oilfield circumstances by using a technique called a scratch

test. A number of findings have been obtained through this work. 13Cr showed a fast repassivation (about 45 minutes) at 50^{o}C in mildly sour conditions by scratch test whereas it took about 1 hour (both 13Cr and 22Cr) in sweet environment at a range of temperatures from (50-150^{o}C) by acid cleaning. Also, by raising pH, the repassivation rate was quicker as the scaling tendency was raised. However, the repassivation rate was slower by raising the temperature. They suggested that scratch test technique can be used to examine the erosion-enhanced corrosion component of materials. Rincon *et al.* [60] took advantage of this technique to study erosion-corrosion of CRAs and the repassivation rates of 13Cr in CO_2 environment and compared the results obtained with those obtained from multiphase flow loop by using scratch test. They found that the output current follows a second degree equation and after conducting several mathematical calculations, correlations have been developed to calculate the relationship or variable that represents the tendencies of such alloy to recover the passive film. The impact of pH and temperature on the repassivation time has been investigated. They found that the tendencies of the alloy to repassivate increases with increasing pH while it was decreased with increasing temperature as shown in Figure 2-11. This confirmed the results that have been obtained by McMahon *et al.* [59].

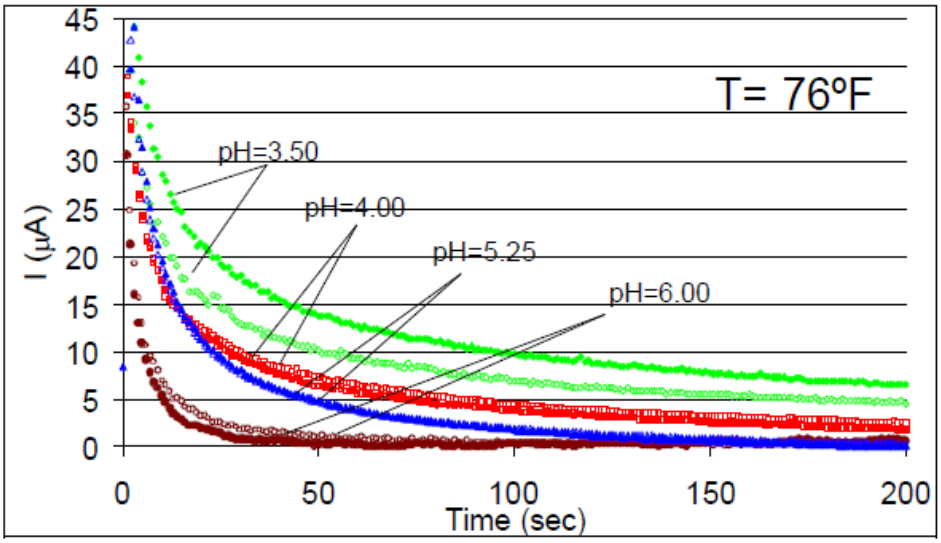

(a)

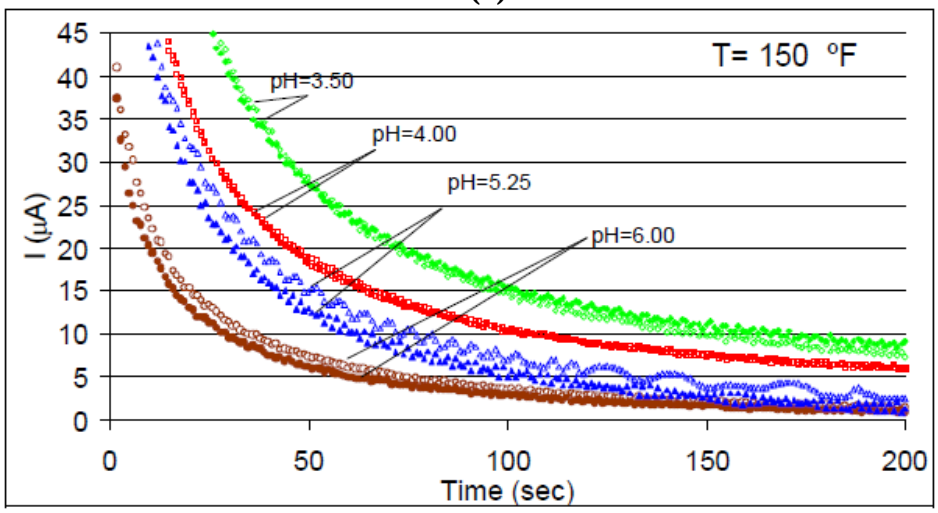

(b)

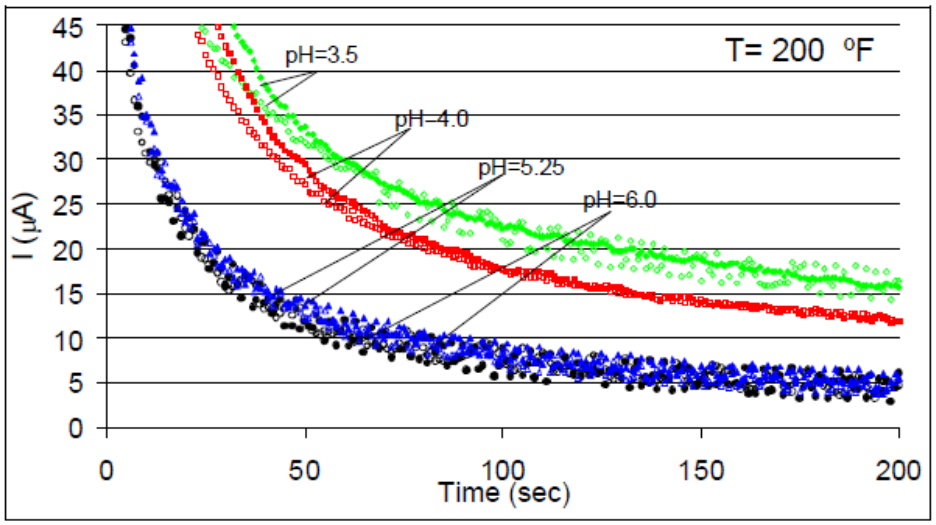

(c)

Figure 2-11: Effect of pH on the repassivation process of 13Cr at **(a)** 76ºF (24.4ºC), **(b)** 150ºF (65.6ºC) and **(c)** 200ºF (93.3ºC) [60]

In terms of materials effect on the repassivation ability, Rincon *et al.* [61] studied the repassivation ability of different types of materials by using scratch test. These materials are 13Cr, S13Cr and 22Cr. They found that 22Cr showed a good ability to repassivate in comparison with the other materials as shown in Figure 2-12.

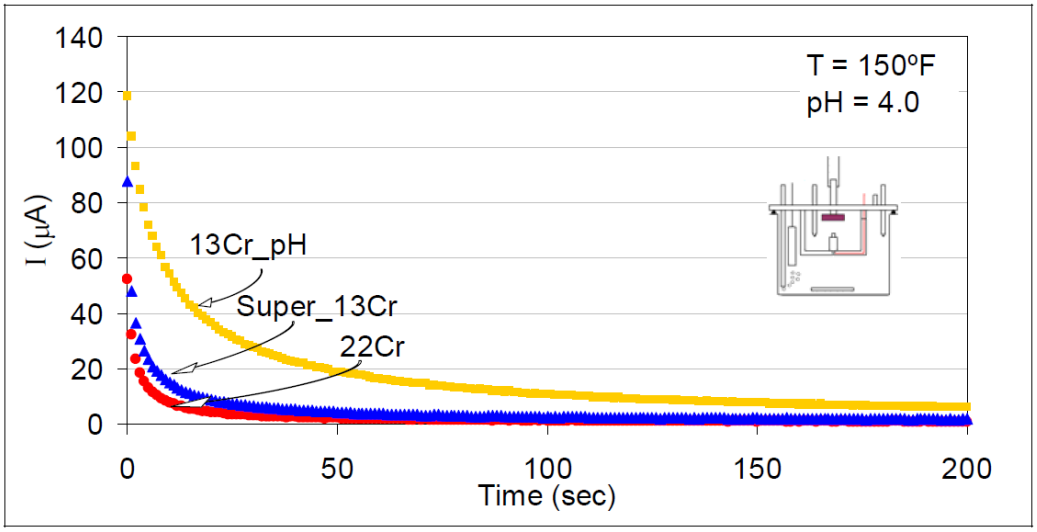

Figure 2-12: The repassivation ability (current decay) of different materials at a specific temperature and pH [61]

The ability of a material to repassivate in a time (t) can also be represented by the following equation [52]:

$$i(t) = A.t^{-n}$$

Where:

i: Current density (A/cm^2)

A: constant.

t: time (second).

n: repassivation index.

By rearranging the equation by adding log to both of its sides, the following equation can be obtained [52]:

$$\log i(t) = logA - nlog(t)$$

By plotting $\log i$ versus $\log(t)$ (Figure 2-13), the value of (n), which represents the passive film formation rate, can be obtained and it is proportional to rate of the passive film formation [52]. This model has been adopted by others [62].

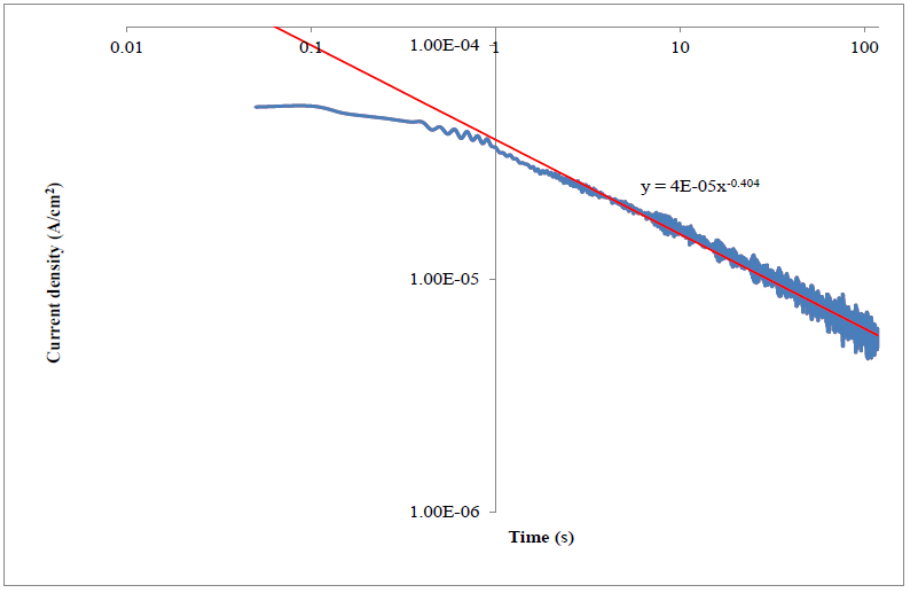

Figure 2-13: Current decay after impingement by sand particles [62]

2.3.2.2 Crevice corrosion

It is one of the localised corrosion which occurs due to presence of voids between the metal to metal or metal to non-metals components. Different factors can affect crevice corrosion. Material type and the bulk environment composition in addition to passive film characteristics are considered as the main affecting factors [1].

2.3.2.3 Galvanic corrosion

Galvanic corrosion can be defined as the electrical contact between two different metals; the noble metal will behave as cathode while the less noble will act as anode, causing preferential corrosion on the anode. This is evident in an electrolyte for materials such as stainless steel and carbon steel. This is not the only case as stainless

steel can be in contact with more noble metals. There are two scenarios in this situation. Slight or no corrosion can occur in the case of stainless steel in the passive state. However, high corrosion can be obtained if stainless steel is in its active state [63].

2.3.3 Corrosion in the oil and gas industry

Corrosion problems in the oil and gas industry vary in their forms and in the ways used to reduce their significant effect. So, it is necessary to increase the awareness of field operators, pipeline engineers and designers with regard to the problems resulting from this phenomenon to ensure smooth and easy flow of oil and gas products to the consumer. CO_2, H_2S and O_2 corrosion are considered as the main causes of corrosion in the oil and gas industry [64-66]. However, CO_2 corrosion will only be reviewed due to its relevancy with the scope of this work.

2.3.3.1 CO_2 corrosion

2.3.3.1.1 Overview of CO_2 corrosion of steels

Although the following mechanism of CO_2 corrosion is relevant to carbon steel, it is thought it can give an idea about the influence of carbon dioxide when it is present in an environment.

Anodic Reaction:

$$Fe \longrightarrow Fe^{2+} + 2e^-$$

Cathodic Reactions:

CO_2 will dissolve in water as follows [67]:

$$CO_{2\,(g)} \longrightarrow CO_{2\,(aq.)}$$

Carbonic acid will be formed as a result of CO_2 dissolving in water [67]:

$CO_2 + H_2O_{(l)} \longrightarrow H_2CO_{3\,(aq.)}$

As it is not fully dissociated, bicarbonate and carbonate will form as follows [67]:

$H_2CO_3 \longrightarrow H^+ + HCO_3^-$

$HCO_3^- \longrightarrow H^+ + CO_3^-$

Then, hydrogen evolution will be followed [67]:

$2H^+ + 2e^- \longrightarrow H_2$

The cathodic reduction of hydrogen in a carbon dioxide environment with pH less than 4 will be dominant. While both of hydrogen and H_2CO_3 reduction reactions will occur with an industrial range of ($4 < pH < 6$) as follows [67]:

$2H_2CO_3 + 2e^- \longrightarrow H_2 + 2HCO^-_3$

At ($P_{CO2} << 1$ and $pH > 6$), the reduction of bicarbonate can be occurred as following [67]:

$2HCO^-_3 + 2e^- \longrightarrow H_2 + 2CO_3^{-2}$

When the $[Fe^{2+}]$ and $[CO_3^{-2}]$ >> Solubility limit, iron carbonate ($FeCO_3$) according to the following equations can form [68]:

$Fe^{2+} + CO_3^{-2} \longrightarrow FeCO_3$

$Fe^{2+} + 2HCO_3^- \longrightarrow Fe\,(HCO_3)_2$

$Fe\,(HCO_3)_2 \longrightarrow FeCO_3 + CO_2 + H_2O$

$FeCO_3$ is one of the corrosion films that is formed on carbon steel surfaces in CO_2 environments and for this film to be formed and to be protective, a high super saturation is required [69]. Supersaturation in addition to high temperature can result in a dense and protective $FeCO_3$ [68]. The favoured range of high temperature for the formation of protective iron carbonate is 60-100^oC [69]. However, a porous and non-

protective film will form under low supersaturation and temperature [68]. CO_2 corrosion is influenced by different parameters. For example, CO_2 corrosion rates can be affected by temperature as the last has a great influence on the surface film. Different types of corrosion films can be formed on the metal surface. The rate of surface film formation in addition to its nature, characteristics and morphology are affected significantly by the operating temperature. This can be clearly seen in Table 2-1. At high temperature (T>80^{o}C), the iron carbonate will be less soluble in the solution and it can be precipitated as a result of high supersaturation. And thus, the adherence and protectiveness of a $FeCO_3$ film will be increased and a low corrosion rate can be obtained. However, at low temperature (T<70^{o}C), the solubility of the iron carbonate will be increased which will result in high corrosion rates [69, 70].

Table 2-1: Types of corrosion films after [69]

Corrosion Film	Temperature of Formation	Characteristics	Composition
Transparent	Room temperature and below	1 µm thick	Fe and O
Iron carbide	No range	<100 µm thick	Fe and C
Iron carbonate	Min. (50-70)^{o}C	Adherent and protective	Fe, C and O
Iron carbonate + iron carbide	Max. 150^{o}C	depends	Fe3C + FeCO3

Both the electrochemical mechanisms of carbon dioxide corrosion of carbon steel and $FeCO_3$ film formation can be influenced by pH. In terms of the electrochemical mechanism, the anodic corrosion rate of iron will reduce as a result of slowing down of the cathodic reduction of hydrogen ions when pH increases. In the same way, the solubility of $FeCO_3$ is reduced and hence a protective iron carbonate can be obtained [69, 70]. The corrosion rate of metal in addition to film formation can be affected by flow in different ways depending on the critical flow intensity. Below the critical flow

intensity, a low corrosion rate can be found while above the critical flow intensity, high dissolution rates may result, since high flow velocity can disrupt the surface film and hinder its reformation. Also, both of iron ions and cathodic species can be affected by high flow and hence low supersaturation and slow precipitation rate may be obtained [70].

2.3.3.1.2 Corrosion of stainless steels in a CO_2-saturated oilfield environment

CO_2 corrosion of stainless steels has not received much attention unlike carbon steels except in recent years. For example, Hosni [71] compared the corrosion behaviour of AISI316L in aerated and CO_2-saturated chloride solutions (0.1-2 M) NaCl at 25, 50 and 80^oC. It has been found that CO_2 has no significant influence on the pitting potential regardless of the chloride concentration. However, its detrimental influence was evident at 50 and 80^oC as the breakdown potential reduced to more negative values at high temperatures and chloride concentrations. CO_2 was thought to accelerate the cathodic reactions due to excessive amount of hydrogen ions which can contribute to the formation of unstable passive film.

Presence of CO_2 enhance defects and heterogeneity of the passive film. The combined action of CO_2 and temperature was found to be harmful to the protective properties of the passive film [72].

The effect of temperature (90, 120 and 150) ^oC on the corrosion behaviour of 13Cr in a CO_2-satuurated brine solution was examined by Zhang *et al.* [73]. They concluded that the microstructural and chemical characteristics of the oxide film are highly affected by temperature and they change in parallel to the changes that have affected the corrosion reactions.

The corrosion behaviour of modified 13Cr, 15Cr and 22Cr in a high temperature (160^{o}C) and high pressure (50MPa) CO_2 environment was studied by Kimura *et al.* [74]. Both types of martensitic stainless steels showed a good corrosion resistance of about 5mpy. This is because of formation of a compact corrosion film as can be seen in Figure 2-14. martensitic stainless steels also showed a good corrosion resistance compared with 22Cr in acidizing environment. Their corrosion resistance was improved by adding the corrosion inhibitor. The galvanic corrosion between the ferrite and austenite was responsible for the high corrosion rate of 22Cr.

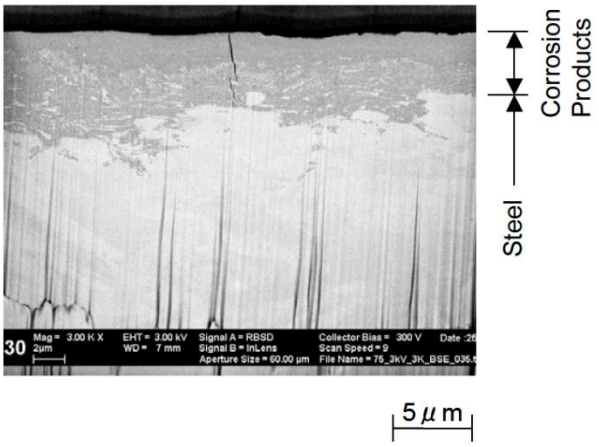

Figure 2-14: Presence of corrosion product after corrosion test of 15Cr in a 20%NaCl at 200^{o}C and 30MPa CO_2 [74]

The breakdown potentials of lean duplex, standard duplex and austenitic stainless steels were evaluated and compared in both 3.5% NaCl aerated and CO_2-saturated brine solutions at two different temperatures (20 and 50)^{o}C by Aribo *et al.* [75]. They found that the pitting corrosion initiation tendency for all of the studied materials was higher in CO_2 –saturated than the aerated one as shown in Figure 2-15. Also, they noticed that there was no significant difference in the breakdown potentials of lean duplex and austenitic stainless steels and they concluded that there is not a comprehensive relationship between the breakdown potentials and PRE_N for lean duplex and austenitic stainless steels.

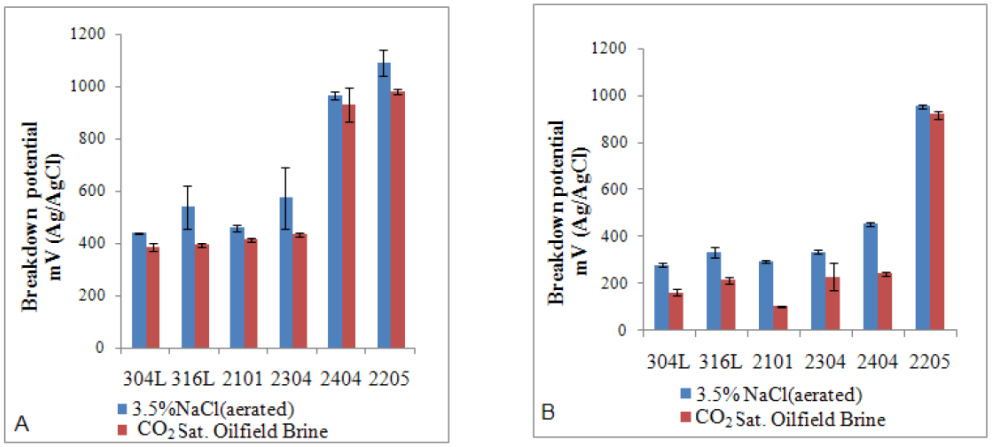

Figure 2-15: A comparison in the breakdown potential of the studied materials between aerated and CO_2-saturated in (a) 20°C and (b) 50°C [75]

2.3.4 Corrosion measurements

2.3.4.1 Electrochemical techniques for corrosion measurements

2.3.4.1.1 Tafel extrapolation

Tafel extrapolation is one of the electrochemical methods used to evaluate the corrosion rate of materials. In this technique, the specimen is polarized to +/- 300 mV from E_{corr}, which is known as the corrosion potential or the open circuit potential that can be defined as the potential difference in an electrolyte between the corroding surface and the reference electrode at $i_{net} = 0$ [1]. The corrosion current density which can be translated to a corrosion rate via Faraday's law can be obtained by extrapolating the curves as shown in Figure 2-16. The values of β_a and β_c, which are called as anodic and cathodic Tafel slopes respectively, can be used to calculate the value of B [1]. The latter will be used to calculate the corrosion current in the linear polarisation resistance method which will be explained in the next section.

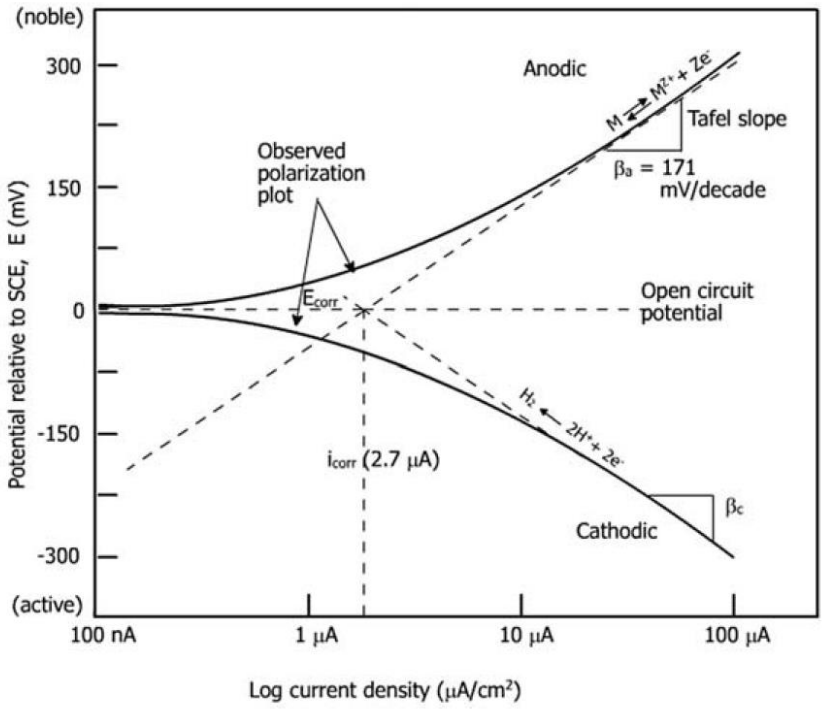

Figure 2-16: Representation of Tafel extrapolation [1]

2.3.4.1.2 Linear polarization resistance

Corrosion rates can be determined by using an electrochemical technique which is known as polarization resistance or Linear Polarization Resistance (LPR). A current vs. potential plot is obtained by scanning in a range of +/- 15 mV from $E_{corr.}$ The slope of the plot represents the resistance (R_p) which is equal to dE/di and relates to the corrosion current as shown in the following equation [1, 76]:

$$\frac{dE}{di} = R_p = \left[\frac{\beta_a \beta_c}{2.3\ (\beta_a + \beta_c)(i_{corr})}\right]$$

$$\left[\frac{\beta_a \beta_c}{2.3\ (\beta_a + \beta_c)}\right] = B$$

$\beta_a\ and\ \beta_c$: Anodic and cathodic Tafel constants respectively (V/decade).

i_{corr}: corrosion current density (A/cm^2).

R_p: is the polarisation resistance (ohm.cm^2)

By arrangement:

$$i_{corr} = \frac{B}{R_p}$$

So,

$$Corrosion\ Rate\ (mpy) = [\frac{0.13 i_{corr}(E.W)}{d}]$$

mpy: mils per year.

E.W.: equivalent weight of the corroding species.

d= density of the corroding species (g/cm^3).

This can be clearly seen in Figure 2-17.

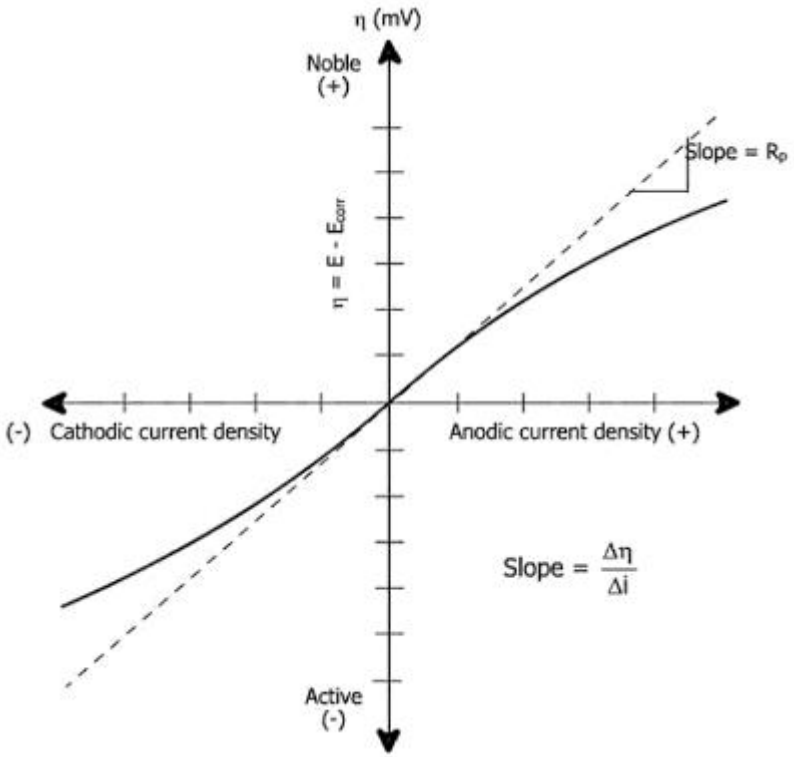

Figure 2-17: Hypothetical LPR [1]

2.3.4.1.3 Potentiodynamic and potentiostatic polarization techniques

The potentiodynamic polarisation technique is used to evaluate the breakdown potentials of the passive materials. Regarding the potentiodynamic technique, an initial value of potential about (-0.3V) to (+1.25V) that is considered as a final value with 0.1667 mV/s scan rate is used according to ASTM standard. A reverse scan is set at 500 $\mu A/cm^2$.

Potentiostatic techniques were used in this work as they can be considered as a reliable method in tribo-corrosion studies and it can help to identify the behaviour of metals under depassivation/repassivation circumstances [77]. In this technique, a specific and constant potential is applied and the current density is monitored with time.

2.4 Erosion-corrosion

2.4.1 Overview

Pumps, agitators, valves and pipelines and any other slurry handling components in chemical, mining, hydraulic and metallurgical industries are most frequent places for erosion-corrosion to occur [78-80]. A 9% of the total failures related to erosion-corrosion, put it among the five most important causes of failure in the oil and gas components. This made the understanding of this issue is urgently needed. As the name suggested, it is a combination of mechanical component and electrochemical component. The most commonly known erodent in the oil and gas industry is sand or any other particles come along with the production fluid. In terms of electrochemical effect, CO_2 dissolving in the produced water is considered as the main affected factor to the transportation and production pipelines. The combined effect of these two components is responsible for the deterioration of pipes and any other equipment

involved in the production operation sector. Equations (a) and (b) simply describe the erosion-corrosion components and their interaction as follows [81]:

Erosion-corrosion rate = erosion rate + corrosion rate + effect of erosion on the corrosion rate + effect of corrosion on the erosion rate … (a)

$$EC = E + C + dC_E + dE_C \ldots (b)$$

2.4.2 Mechanism of erosion-corrosion

Solid particle impingement which disrupt the protective film and/or the substrate in addition to the electrochemical corrosion are considered as the main mechanisms leading to erosion-corrosion in aqueous systems [77, 82]. In the absence of any particles within the corrosive flowing fluid, the development of brittle scales resulting from a rapid corrosion of material will act as a barrier between the surface of material and the flowing fluid and hence the penetration rate will be reduced. This is also true in the case of low-level erosion. However, both erosion and corrosion are interacted at intermediate erosion level and this in turn will lead to formation of pitted surface due to the formation of scale and its removal periodically by erosive particles while the scale will be totally removed from the material surface and erosion will be dominant at high erosion level. [83].

2.4.3 Factors affecting erosion-corrosion

In general, erosion-corrosion can be affected by both environmental and materials parameters. Passive film resistance to erosion-corrosion is dependent on the mechanical removal rate and their self-healing rates and these are directly dependent on the sand concentration, flow velocity and the other environmental parameters [84]. The resistance of a passive alloy to erosion-corrosion can be improved by adding a third or even fourth element to it. For example, 316 SS that is resulting from addition

of Molybdenum to 304 SS will produce a protective film that can withstand erosion-corrosion [85]. Another important factor influencing erosion-corrosion is the galvanic coupling of different materials under erosion-corrosion circumstances [85].

2.4.4 Erosion-corrosion testing methods

2.4.4.1 Submerged impinging jet

SIJ is one of the most important techniques to study erosion-corrosion. This is due to its ability to provide a varied and high flow velocity and shear stresses across the affected sample [86]. The SIJ simulates many flow scenarios in the oil and gas industry where sand impacts surfaces. This is different to other techniques such as Rotating Cylinder Electrode (RCE) where the sand transport and mobility is less well defined [86].

2.4.4.1.1 Flow profile of SIJ

Three regions can be obtained which represent the hydrodynamic profile of the SIJ. These regions as shown in Figure 2-18 are: zone A (stagnation), zone B (transition) and zone C (wall jet region). Zone A lies directly under the nozzle of the impinging jet. The transition region starts from a radial distance of about 2 mm away from the centreline while the wall jet region starts from 4 mm away from the centre [87].

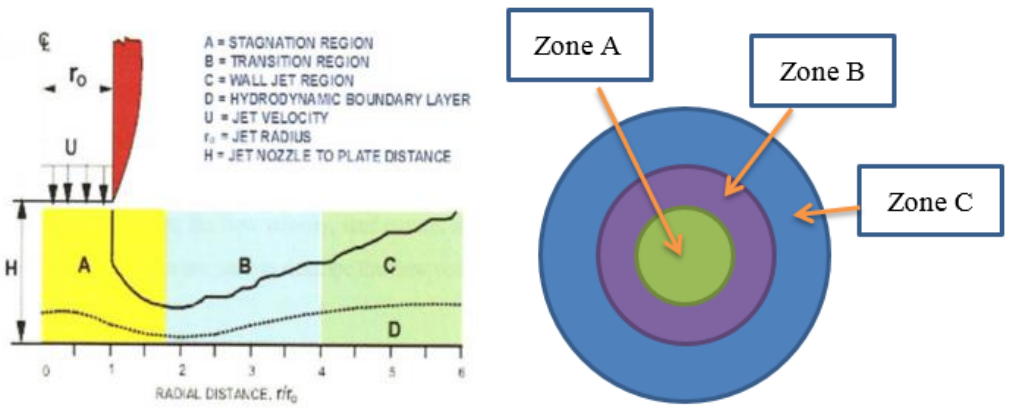

Figure 2-18: The hydrodynamic profile of SIJ [87]

Wall shear stress, which is considered one of the main hydrodynamic parameters that influence erosion-corrosion [88] can be calculated depending on the radial distance according to the following equation [87]:

$$\tau w = 0.179\ \rho V^2 Re^{-0.182}(\frac{r}{r_o})^{-2}$$

$$Re = \frac{2r_o V}{v}$$

Where:

ρ: fluid density (g/cm^3)

V: jet velocity (m/s)

Re: Reynolds number.

r: distance from the centre of the jet (mm)

r_o: is the orifice radius (mm)

v: kinematic viscosity (Pa.s).

2.4.5 Material loss in erosion-corrosion

As mentioned earlier in section 2.4.1, TWL can be written as [89]:

$$TWL=E + C + dC_E + dE_C$$

Gravimetric measurements are used to evaluate both TWL and E. However, ($C + dC_E$) represent the corrosion part and can be measured by using *In-Situ* electrochemical methods as corrosion current density (i_{corr}) can be obtained using such methods. In this work, the term C will be neglected due to its negligible value for passive materials. So, the equation will be as follows [90]:

$$TWL=E + dC_E + dE_C$$

As all the terms in the total wear loss equation should be expressed in terms of weight loss (mg), there is a need to convert the value of the obtained corrosion current in terms of weight loss. For this reason, Faraday's law should be applied to get the value of corrosion part in grams as following [1]:

$$Mass\ Loss\ (g) = \left[\frac{i_{corr}.M.A.t}{nF}\right]$$

Where:

i_{corr}: Corrosion current density (A/cm^2)

M: is the molar mass (g/mol)

A: is the surface area of the specimen (cm^2)

t: is the time (s)

n: No. of electrons

F: Faradays constant = 96500 C/mol.

It should be noted that the wear rates resulting from the individual effects of erosion and corrosion are less than the sum of these two processes together which is known as Synergy [91]. This will be dealt with in more details in the following section.

2.4.6 Erosion-corrosion synergy

This term is used to describe the interaction between corrosion and erosion which results in a higher loss in materials compared to the sum of the individual effects of each component [77]. Wood *et al.* [92] suggested that in order to evaluate the synergy, corrosion tests in addition to erosion tests needed to be done to determine the corrosive and erosive wear rates respectively. Also, these two tests to be combined to evaluate the total wear loss and hence synergy can be found by using the following equation [92]:

$S = T - (E + C)$

Where:

S: is the synergy; T: the total weight loss; E: erosive wear rate and C: is the corrosive wear rate. After that, Stack *et al*. [93] presented another equation for evaluating the total weight loss in erosion-corrosion circumstances as follows:

$K_{EC} = K_{EO} + K_{CO} + dK_{EC}$

Where:

K_{EC}: the total weight loss

K_{EO}: the sum of erosion rates

K_{CO}: the sum of corrosion rates and

dK_{EC}: the interaction of two processes.

This is similar to the one which is suggested by Wood *et al.* [92]. However, they suggested that the term (dK_{EC}) can be divided into (dK_E) and (dK_C) which refer to enhancement of erosion by corrosion and erosion enhancement of corrosion by erosion, respectively. So, the equation will be in this form [93]:

$K_{EC} = K_{EO} + K_{CO} + dK_E + dK_C$

In terms of corrosion component, (K_C) can be used to combine the effect of corrosion components as follows [93]:

$K_C = K_{CO} + dK_C$

In the same way, erosion components (K_E) can be written as [93]:

$K_E = K_{EO} + dK_E$

Neville *et al.* [89] used another formula depending on the same equation:

$TWL = E + C + S$

Where:

TWL: total weight loss

E: pure mechanical effect

C: pure electrochemical effect and

S: synergy

Similar to above equation, the synergy is divided into dC_E and dE_C which refer to change in corrosion due to erosion and change in erosion due to corrosion, respectively. According to them, ($C + dC_E$) is equal to C in the above equation and (dE_C) to (S) [94].

Erosion can enhance corrosion and corrosion can enhance erosion in different ways. For example, corrosion can be enhanced by erosion by surface film removal, acidified pit locally, surface roughening and reduce fatigue limit. However, one of the ways which is corrosion enhanced erosion by softening the work-hardened surface and hence erosion rates will increase [92]. Synergy can be dependent on the environmental factors such as velocity, temperature and sand concentration [80, 95, 96]. Also, the dominance of either erosion enhanced corrosion or corrosion enhanced erosion is affected by test conditions [97]. This will be explained in detail in the subsequent sections.

2.4.6.1 Erosion-enhanced corrosion

Erosion can enhance corrosion in different ways. Of these ways is by removing the formed films on material surfaces. Different types of films can be formed on materials surfaces depending on the type of the materials and the affecting environments. For example, iron carbonate can form on the carbon steel surface under specific conditions. Formation of iron carbonate on material surface will participate in reducing their corrosion rates. Also, adding corrosion inhibitor in high enough concentrations to the pipe to be protected will lead to formation of an inhibitor film which will act as a barrier between the substrate and the corrosive environment and

thus reducing the corrosion rates. Moreover, corrosion resistant alloys are known, as will be explained later, in their superior corrosion resistance due to the presence of the passive film on their surfaces. All of these films can be partially or completely removed by sand particles impact and hence the bare material surface will be directly exposed to the corrosive environment [81, 91, 98-101]. Also, erosion can enhance corrosion by increasing the local turbulence/mass transfer (Figure 2-19) [102-104].

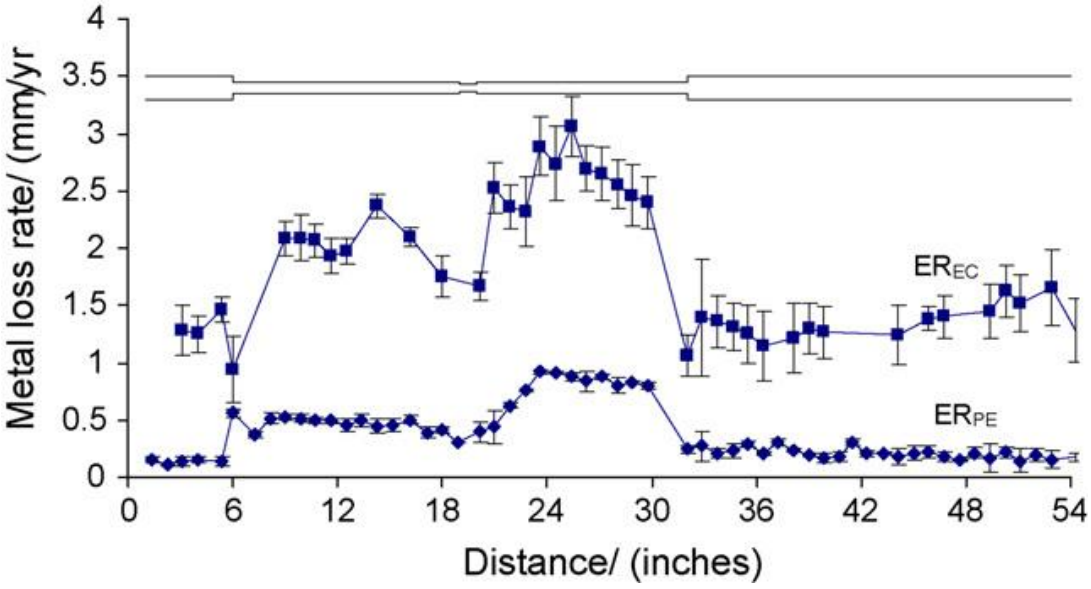

Figure 2-19: Comparison of pure erosion (ER_{PE}) and combined erosion–corrosion (ER_{EC}) attack (2 wt. % sand slurry, pH 4, PCO_2 1.2 bar, 4 h) [102]

Moreover, pitting corrosion can be stimulated by nucleation of numerous metastable pits because of the erosive impact by solid particles [105]. Furthermore, the galvanic corrosion can be enhanced by erosion. For instance, the galvanic coupling of Stellite 6 and UNS S32760 was studied by Neville *et al.* [106]. Three sets of conditions were used in this work to determine the evolved galvanic currents. Both materials were put in static conditions, erosion-corrosion and the last one when Stellite 6 was exposed to erosion-corrosion while the SS remained in static condition. In static conditions, a negligible galvanic coupling was obtained. However, under erosion-corrosion conditions, there was a quick increase in the resultant current similar to the case when

Stellite 6 exposed individually to erosion corrosion circumstances as shown in Figure 2-20.

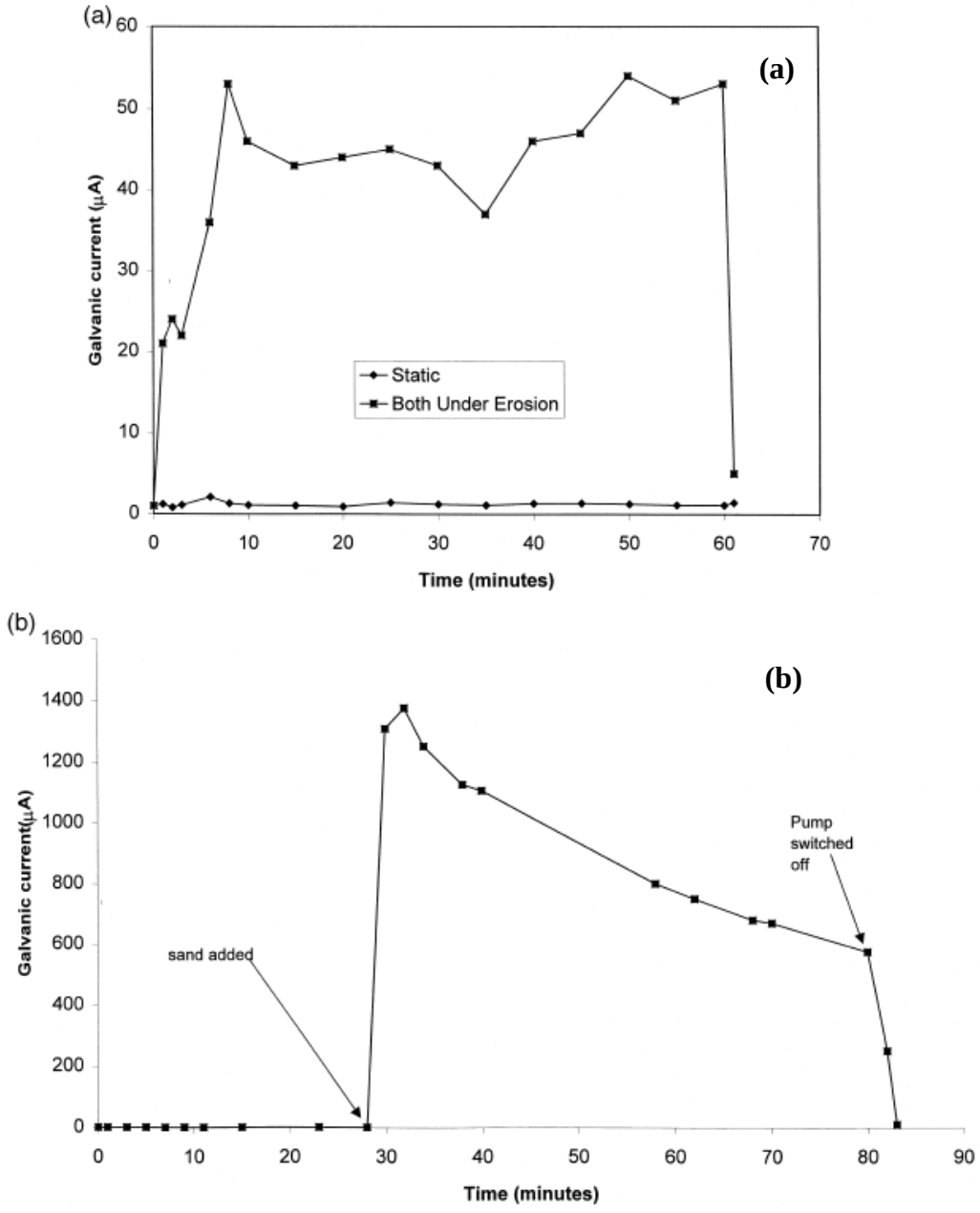

Figure 2-20: Galvanic currents between Stellite 6 and UNS S32760 at 50°C (a) both are subject to liquid–solid erosion (b) only the Stellite 6 is subject to liquid–solid erosion [106]

Erosion accelerated galvanic coupling of carbon steel/ stainless steel in chloride solutions was evaluated by Dong *et al.* [107] who took into consideration the influence of flow velocity and anode/cathode area as main parameters. They found that with

increasing both of flow velocity and anode to cathode area, the galvanic current will increase. Also, while they were doing erosion-corrosion tests, it was found that the corrosion part of the total mass loss was increased with increasing anode to cathode areas.

2.4.6.2 Corrosion-enhanced erosion

Corrosion can enhance erosion in different ways. For example, the work-hardened surfaces will be removed due to corrosive environment and hence the less hard bulk material will be directly affected by erosion process [108, 109]. Also, the grain boundaries will be preferentially attacked. This in turn will lead to grain loss or depletion of chromium, molybdenum and silicon causing a high dissolution of matrix and hence enhanced erosion rates [97, 103, 110]. The rate of crack growth will be enhanced by corrosion on the evolved flake resulting from sand impact will be detached and erosion rate will increase [111]. It should also be noted that erosion is highly affected by the slurry chemistry as confirmed by [112, 113].

2.5 Corrosion resistant alloys

It is known that carbon and low-alloy steels are widely used in the oil and gas production. One of the reasons attracted this sector to use this type of materials is its demand to use large quantities of metals in addition to the decline in the value of oil and gas products. Also, no significant corrosion problems was noticed. This reality has changed recently as the price of oil and gas products has increased and facing harsh conditions when digging deeper wells has made an urgent need to use of CRAs in the oil and gas industry. What increased the importance of this type of materials is the development of high-strength form of them which allowed use of less quantities of these materials in this sector through reducing the thickness of pipes and vessels

walls [114]. Also, the superior CO_2 corrosion resistance of the majority of these materials in particular flow induced-CO_2 corrosion [81].

As the name suggested, CRAs can be defined as materials which can resist general and/or localised corrosion. This is because of their ability to form a protective passive film on their surfaces [115]. Stainless steels are considered as the main types of CRAs as shown in Figure 2-21. Stainless steels are commonly used in the oil and gas industry due to their preferable mechanical and corrosion resistance properties [116].

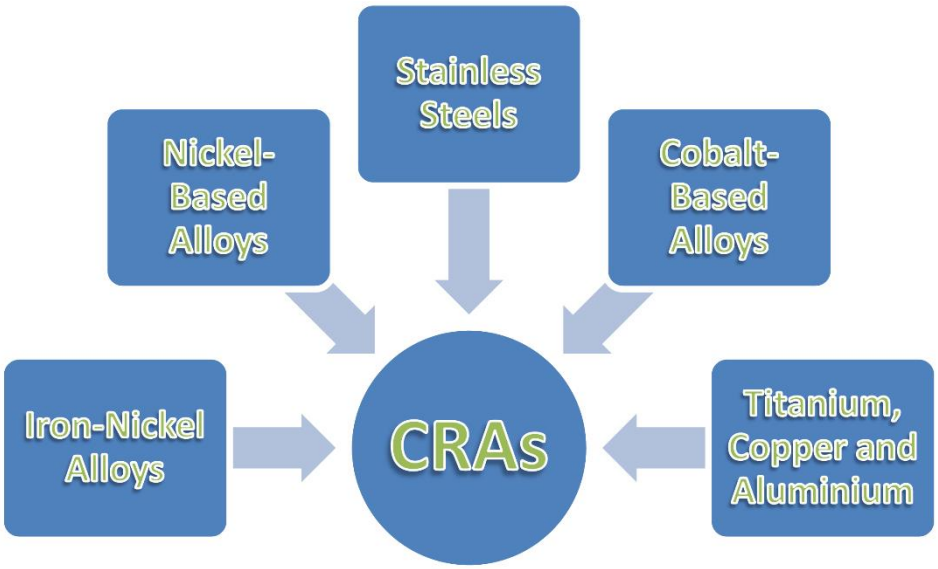

Figure 2-21: Classification of corrosion resistant alloys [116]

2.5.1 Stainless steels

When the percentage of chromium reach to more than 10% in iron-based alloys, it can be called as stainless steel and a protective passive film can be formed because of chromium as can be seen in Figure 2-22. Depending on its microstructure and alloying elements, different types of stainless steels can be found as shown in Figure 2-23. These types can be varied in their corrosion resistance as their alloying elements are varied [117]. Austenitic, Martensitic and Duplex will be reviewed in the next section due to their relevancy with the scope of this work.

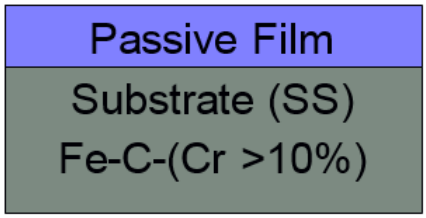

Figure 2-22: The general structure of stainless steels

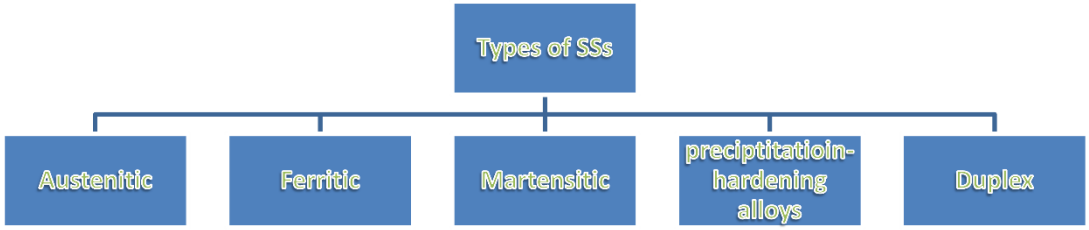

Figure 2-23: The main types of stainless steels [116]

Austenitic stainless steels has a Face–Centred Cubic (FCC) crystal structure and the latter can be stabilised by adding nickel to iron-chromium alloys. Addition of nickel with (18-28 Cr %) will improve their corrosion resistance. Hardness and strength can be increased by cold working.

A hard and brittle Martensitic stainless steel with a chromium and carbon content of about 11-20% and 0.15% respectively and with a Body-Centred Tetragonal (BCT) crystal lattice can be obtained by rapidly cooling of the fully austenite at high temperature. Tempering allow reducing its hardness and improve toughness to the required level.

Duplex stainless steel has a dual phase structure composed from austenite and ferrite. A (18-28 Cr %) and (4.5-8 Ni %) are the main alloying elements in this type of stainless steels in addition to other alloying elements such as molybdenum, copper, tungsten, nitrogen, manganese and silicon which are added to obtain a high corrosion resistance. This type of stainless steels is known for its superior resistance to pitting, crevice and stress corrosion cracking [118-122].

2.5.1.1 Anodic polarisation of passive materials

In the active region, the anodic curve is polarised towards the noble direction from open circuit potential E_{corr} until a point which represents the extreme value of current density which is commonly known as a *critical current density (i_{crit})* and the potential is called the *primary passive potential (E_{pp})*. At this point, the behaviour of materials will turn from *active* to *passive*. After this point, the current density decreases as the oxide film will form on the materials surface. This behaviour continues till the *flade potential (E_f).* At this point, the current density will stay constant while the potential increases. Also, the full passivity will start. This will correspond to the passive current density (i_p). This region will continue until the transpassive potential where the passive film at this potential is brought down and the current density will increase again [1, 123]. All of these stages are shown clearly in Figure 2-24.

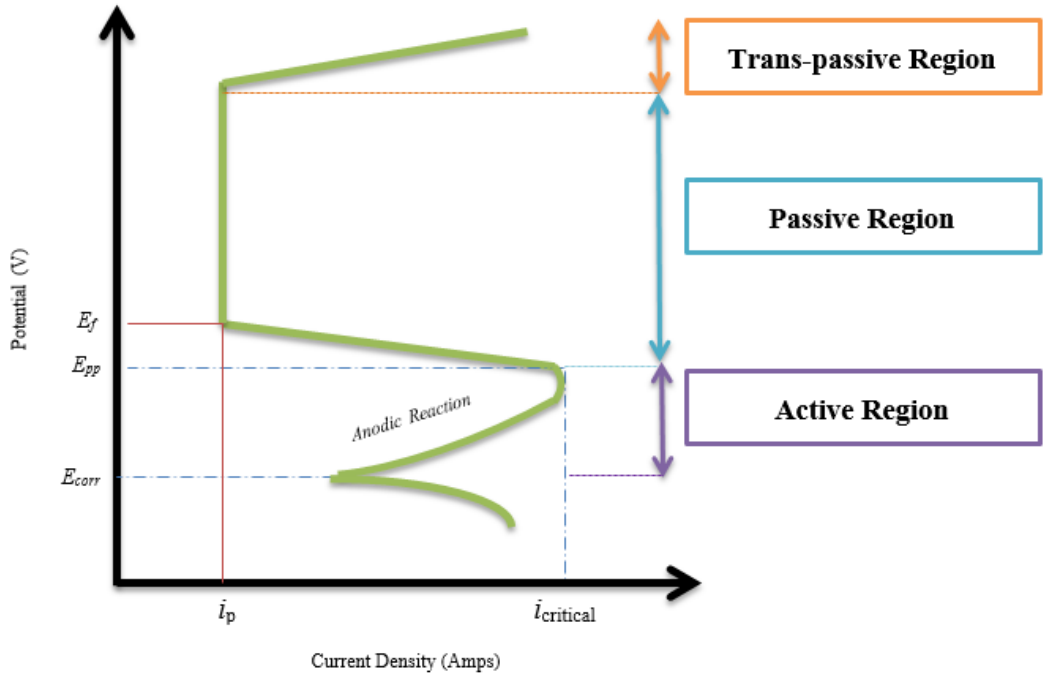

Figure 2-24: Polarization curve of active-passive metals [1]

2.5.1.2 Passive film

Passivity is defined as the formation of a stable, solid hydroxide or oxide film on a metallic surface to retard corrosion as it works as an impediment between the corrosive environment and the bulk material [1, 123]. This film is mainly comprised from metal oxides or its alloying elements oxides [13]. It can be formed either chemically or electrochemically depending on the presence of the metal ions in solution. If there are no metal ions, adsorbed oxygen might incorporate with the metal to form metal oxide as shown in the following equation [1]:

$2Fe_{(s)} + 3/2\ O_{2\ (ads)} = Fe_2O_{3(s)}$

a film can also be precipitated from metal ions-containing solution according to the following equations [1]:

$Fe^{3+}{}_{(aq.)} + 3OH^-{}_{(aq.)} = Fe\ (OH)_{3(s)}$

$2Fe\ (OH)_3 = Fe_2O_{3(s)} + 3H_2O$

Two conditions should be provided so that the oxide film can provide adequate protection for the material: low solubility in most environments and act as a good barrier that prevents the transportation of ions to and from the surface of the material.

It is observed that (Fe-Cr) alloys include two oxide layers: an inner and outer layer. The inner is mainly comprised of Cr while the outer one is Fe rich layer. The acidity of the solution can affect the Cr/Fe ratio depending on the solubility of Fe and Cr oxide films in both of acid or alkaline environment. Fe oxide is soluble in acidic solution. However, Cr oxide shows a markedly less solubility. For the above reasons, the Cr oxide enrichment can reach to more 80% in the Fe-Cr alloy and show superior passivity [13].

On the other hand, the passive film can be deteriorating as a result of chloride ions [1]. Adsorption of these anions on the metal surface or incorporation of them in the passive film can be prejudicial to the stability of the passive film and thus lead to initiation of pitting on the metal surface [32]. The effect of chloride on pitting is explained depending on three different models as follows: The film is locally dissolved due to chloride adsorption, the weakness of oxide bond which is resulted from the permeation of anion through the film and then the breakdown of the film [32].

2.6 Erosion-corrosion of stainless steels

2.6.1 Effect of temperature on erosion-corrosion of stainless steels

Flow velocity, sand loading, impact angle and temperature are considered as environmental factors which should be taken into consideration in order to understand the erosion-corrosion behaviour of materials. The effect of flow velocity, sand concentration on erosion-corrosion of stainless steels has been studied extensively. Neville *et al.* [124] assessed the erosion-corrosion behavior of UNS S31245, UNS S32654 and UNS S32750 at 17 m/s flow velocity, 18ºC and different sand concentration. It was found that TWL for all of the studied materials was highly affected by sand loading. However, TWL of UNS S31245 was the highest compared with the other materials. They interpreted this due to its high corrosion activity of UNS S31245 compared with the other materials under severe erosion-corrosion conditions particularly at high sand loading. They confirmed their findings by electrochemical measurements as can be seen in (Figure 2-25) and by surface analysis (Figure 2-26) of the damaged surfaces both under pure erosion and erosion-corrosion.

UNS S31245 was found to be more prone to corrosion than other materials as it showed the highest corrosion rates compared to UNS S32750 and UNS S32654.

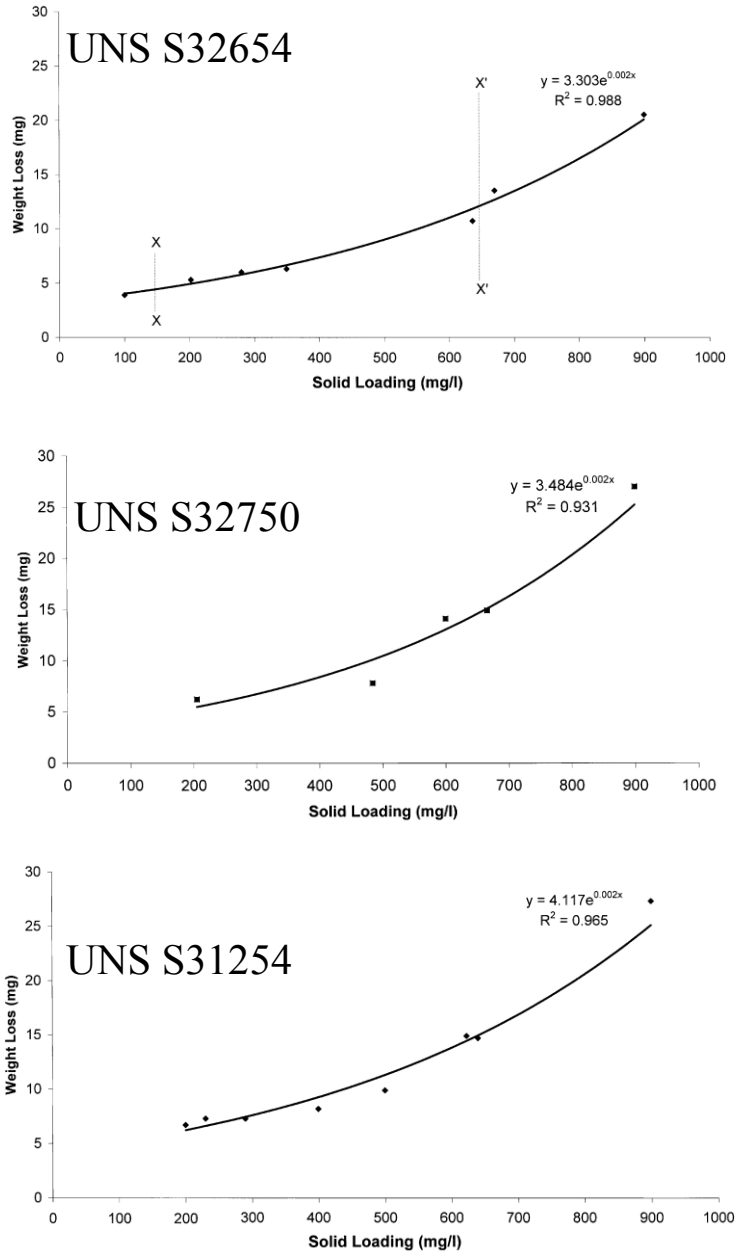

Corrosion current density values for three materials under different liquid–solid erosion conditions

	150–200 mg/l ($\mu A/cm^2$)	600–640 mg/l ($\mu A/cm^2$)
UNS S31254	6.5	37.7
UNS S32654	3.6	23.2
UNS S32750	4.8	25.9

Figure 2-25: Showing how total weight loss and corrosion current density of the studied materials affected by sand loading [124]

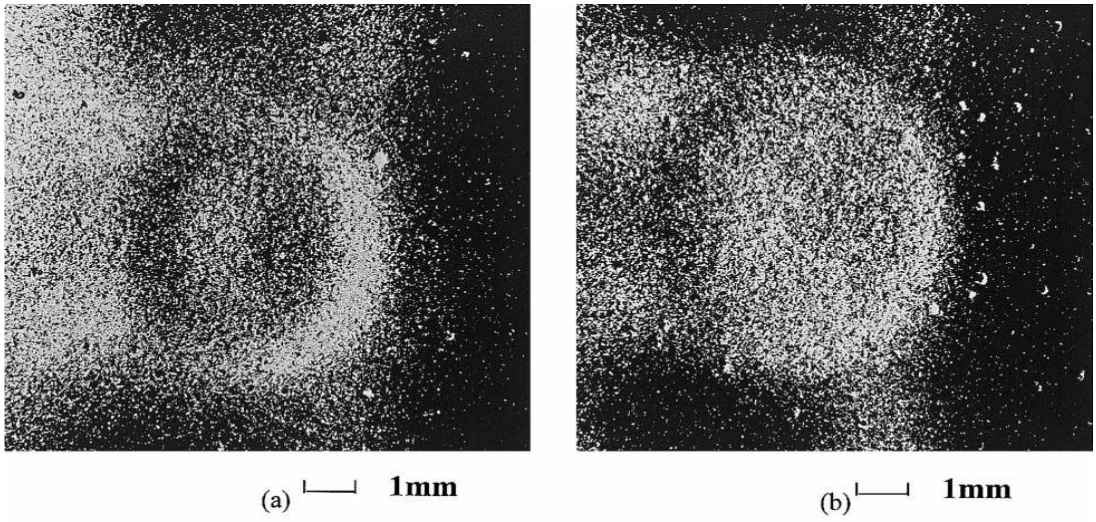

Figure 2-26: Stereo microscope images of the wear scar on UNS S32654 with 600-640 mg/l solids (a) no Cathodic Protection (CP) applied (b) with applied CP [124].

The corrosion products debris on UNS S31254 was much more than the one of UNS S32654 (Figure 2-27). Furthermore, it was found that the corrosion activity increases by increasing sand loading and there was a good correlation between the erosion-corrosion resistance of the studied materials and their corrosion resistance demonstrating the significant effect of corrosion on erosion-corrosion resistance of materials under solid –liquid impingement.

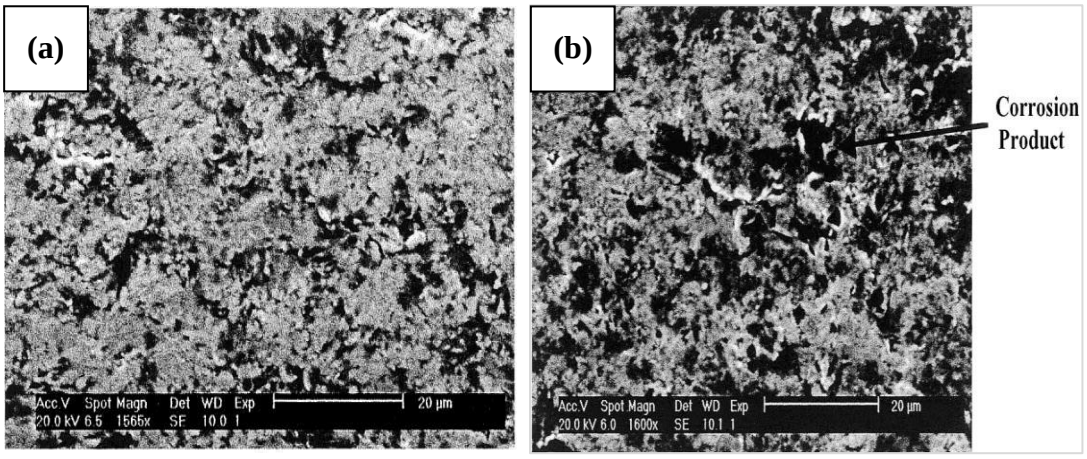

Figure 2-27: SEM images showing the density of corrosion product debris on **(a)** UNS S32654 compared to **(b)** UNS S31254 [124]

Similarly, Hu *et al.* [89], assessed the electrochemical characteristics of UNS S32654 and UNS S31603 using corrosion potential measurements, anodic polarization, linear

polarisation and potentiostatic polarisation techniques under erosion-corrosion conditions. They found that TWL of both materials increased by increasing sand loading. However, UNS S32654 showed better resistance to erosion-corrosion than UNS S31603. Also, it has been found that although sand loading has a significant effect on the current density of the studied materials, the current density of UNS S31603 was systematically higher than UNS S32654. They concluded that addition of alloying elements to UNS S32654 improves its corrosion resistant and repassivation ability, which in turn makes it highly resistant to erosion-corrosion compared with UNS S31603 suggesting that corrosion resistance play a vital role in determining the susceptibility of materials to erosion-corrosion resistance [125].

Hu *et al.* [77, 126], who examined the corrosion resistance under erosion-corrosion circumstances of UNS S32654 and UNS S31603 in a 3.5%NaCl solution at two different temperatures and at sand loading ranging from10-6000 mg/l and the overall erosion-corrosion resistance of both materials, found that TWL of both materials was highly affected by sand loading and temperature as can be shown in Figure 2-28.

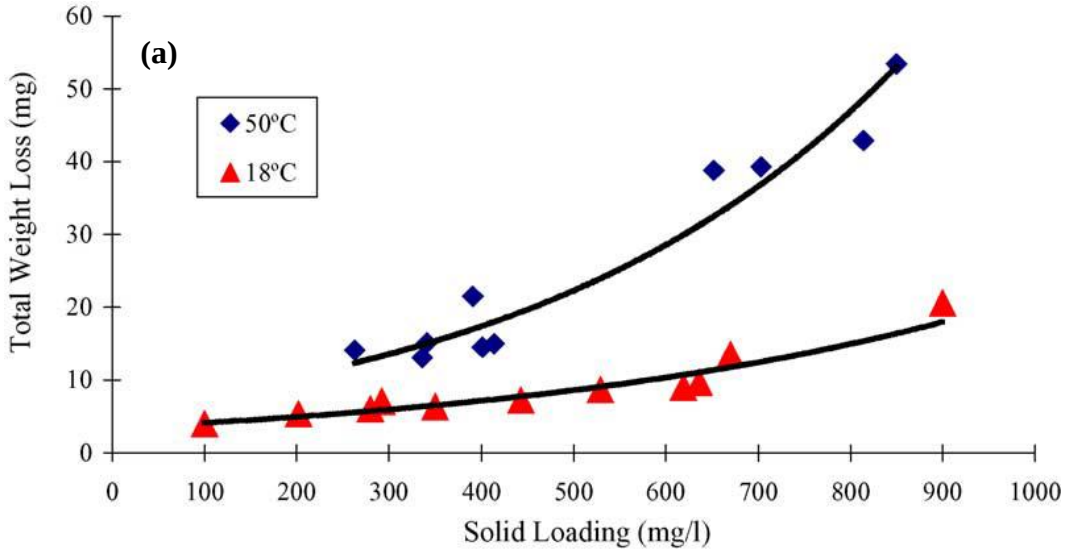

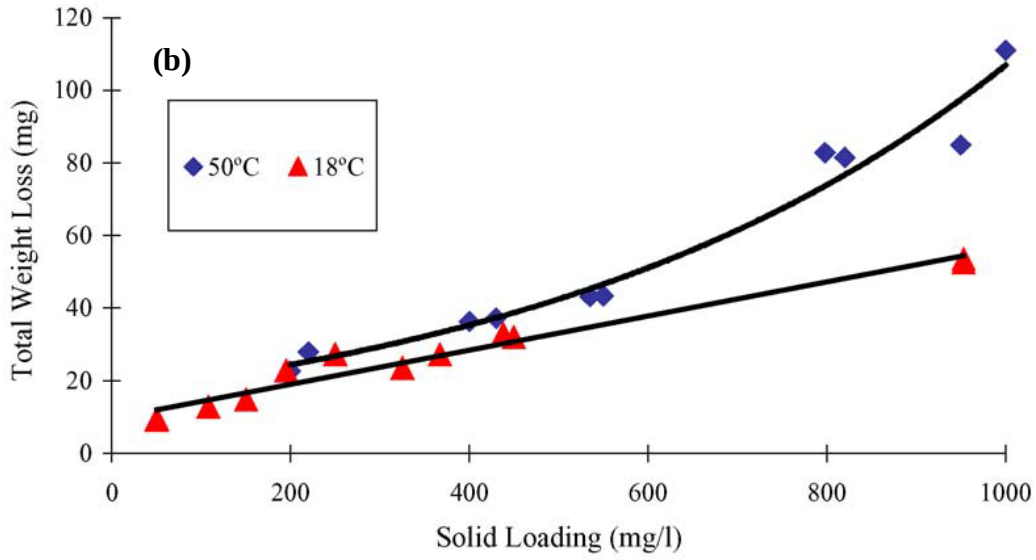

Figure 2-28: Showing the relationship between the TWL of **(a)** UNS S32654 and **(b)** UNS S31603 and sand loading at different temperatures [77]

Also, they found that sand loading has a significant effect on the corrosion current density of both materials. The corrosion current density of UNS S31603 was higher than the one of UNS S32654. The corrosion current density increases with increasing sand concentration. This increase worsens at high temperatures as can be shown in Figure 2-29. They also found that both pitting and crevice corrosion initiated at 18^{o}C on all surfaces of the studied materials in particular UNS S31254 under static conditions. Pitting was more pronounced on UNS S32654 surface at 70^{o}C. They concluded that incomplete healing of the severely damage passive film at lower impact angles regions can trigger pits formation which will affect the corrosion resistance and hence erosion-corrosion resistance of materials [126].

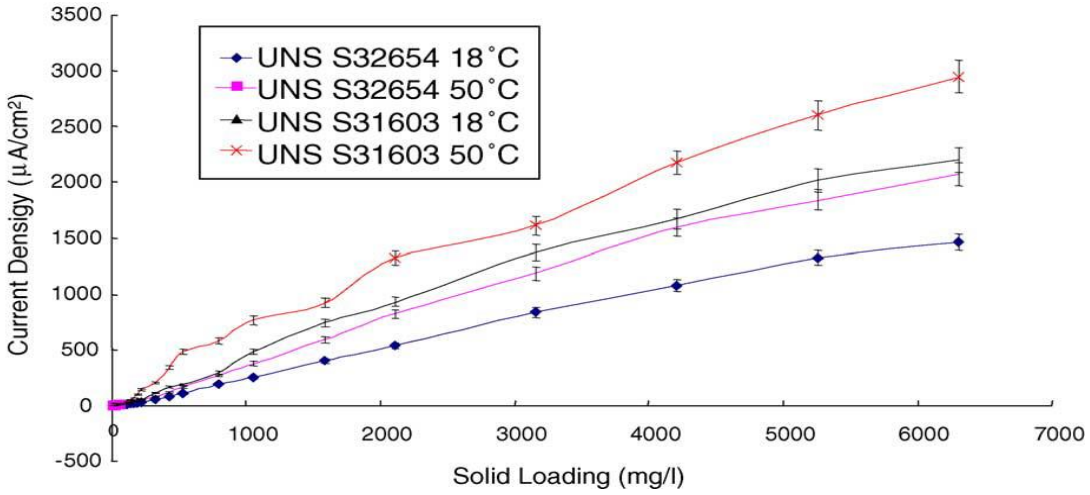

Figure 2-29: Showing the relationship between the current density of UNS S32654 and UNS S31603 and sand loading at different temperatures [77]

They suggested that high sand loading will increase the probability of sand particles impacting the material surface, passive film removal and hence high dissolution rates. Also, the repassivation ability probably will be hindered due to multiple and continuous impacts. They also found that the current density increases as the flow velocity increases (Figure 2-30) suggesting that both the high kinetic energy and number of impacts of particles at high fluid velocity are the main causes of severe degradation as they will lead to several deformation and cutting mechanism. They concluded that there is a strong link between corrosion and the total mass loss of materials.

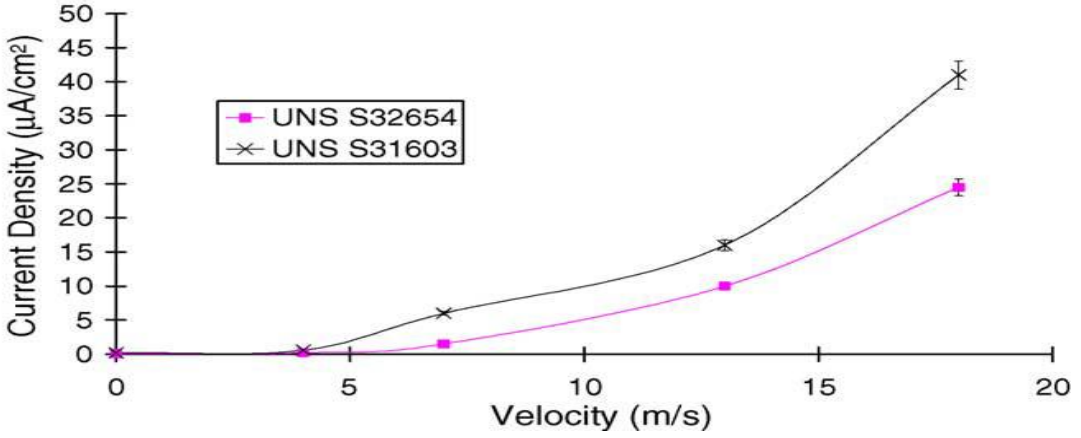

Figure 2-30: Showing the relationship between the current density of UNS S32654 and UNS S31603 and flow velocity [77]

Erosion-corrosion of UNS S31254 super austenitic stainless steels in a CO_2-satuarted Forties brine solution at different flow velocities and sand loading was studied by Bargmann *et al.* [7]. They concluded that there is a strong link between the corrosion resistance and erosion-corrosion degradation rates of the studied materials.

Hu *et al.* [127], who examined the corrosion behavior of UNS S31254, UNS S32654 and UNS S32750 under solid-liquid impingement in 3.5%NaCl at 17 m/s flow velocity, (100, 360 and 600) mg/l sand loadings and at 18^{o}C found that the material showed highest corrosion resistance in the static medium also showed lowest corrosion current density under severe erosion-corrosion circumstances. Although the small percentage of corrosion contribution to the total wear loss, the interaction between the active electrochemical corrosion and the mechanical erosion is a principal factor in enhancing material removal [106].

It should be noted that most of the previous works highlighted the importance of corrosion in the wear resistance of materials, especially under erosion conditions and has taken the concentration of sand as a key factor. It is known that erosion-corrosion is affected by several factors such as flow velocity, sand loading and temperature. Temperature greatly affects the corrosion resistance of materials. It was mentioned earlier that corrosion activity greatly affects erosion. However, a little number of studies investigated the effect of temperature on TWL and its components (i.e. pure erosion, pure corrosion, erosion-enhanced corrosion and corrosion-enhanced erosion).

For example, Chen *et al.* [128] investigated the effect of different temperature (70,150 and 200)^{o}F on pure erosion (N_2 purge) and erosion-corrosion (3%NaCl) saturated in a CO_2 (pH=4) of 13Cr and they found that both pure erosion and erosion-corrosion of 13Cr are highly affected by temperature. As temperature was increased, the pure erosion and erosion-corrosion rates increased. There was a linear relationship between

erosion-corrosion of 13Cr and the affected temperature. Also, they found that erosion-corrosion was higher than pure erosion at all of the studied temperatures. The erosion-corrosion of the studied material at 70^{o}F was around 2-3 times of pure erosion while it was 4-6 times at 150^{o}F and 200^{o}F. Although there was no clear interpretation why the erosion-corrosion rates are highly affected by temperature, it is suggested that the increase in pure erosion was due to reduction of the flowing fluid viscosity.

The effect of flow velocity, sand loading, fluid temperature and their interaction on the total weight loss and its components of both UNS S32760 and UNS S31603 in 3.5%NaCl has been studied by Meng *et al.* [80] who concluded that the environmental factors have a considerable effect on the corrosion part which is divided into static (C_o) and dynamic corrosion (dC_E). It has been suggested that the dynamic corrosion is strongly affected by the environmental factors, which will increase erosion and thus corrosion, while the static corrosion, which is affected by temperature, will not be changed. This is true, but one aspect that has been overlooked is that the static corrosion is an inestimable part of the dynamic corrosion. When sand particle impacts the material surface and the surrounding passive film, two important things should be taken into consideration. First, it should be taken into account the period of time between the repeated impacts (i.e. the time between impact of one particle and another) bearing in mind that the static corrosion will play an important role during this period of time. The second is the extent to which the passive film can be recovered especially at high temperature as both of these processes are highly affected by temperature. The same authors suggested that temperature had no considerable effect on materials loss compared with the other influencing factors. It should be noted that the range of temperature used in this work was between 18-50^{o}C. It is known that the corrosion resistance of stainless steels is highly affected by temperature in saline solution especially at their Critical Pitting Temperature (CPT). The range of

temperature which was used in this work was lower than the CPTs of some of stainless steels. So, any change in the corrosion resistance of materials will affect the erosion-enhanced corrosion and the latter can be responsible for a distinct difference in the erosion-corrosion resistance of material [129]. Once erosion-enhanced corrosion is highly affected by temperature and a high dissolution and low repassivation ability is expected at high temperature, it is expected that this effect will exacerbate at the CPT of materials due to their limited corrosion resistance at such temperature. So, it is important to assess the effect of static corrosion on erosion-corrosion of stainless steels to understand how the latter will be affected.

2.6.2 Effect of surface and sub-surface microstructural evolution on degradation behaviour of stainless steels

In spite of significant changes that may occur within the sub surface microstructure of stainless steels under erosion - corrosion conditions due to particles impact, there are only few studies that have been interested in this subject. These studies were also limited to only specific types of stainless steels. Moreover, the contribution of sub-surface microstructure on synergy of stainless steels was not studied well.

Buscher *et al.* [130] observed increase in hardness of the worn surface of a forged low carbon CoCrMo-alloy from 450 HV at 30µm to 660 HV at 3µm. They concluded that the change in hardness was resulted from the change in the subsurface microstructure. Rajahram *et al.* [131] studied the surface and sub-surface wear evolution of UNS S31603 under erosion-corrosion in 3.5%NaCl as a function of time ranging from 0.5minute - 2hr using slurry pot erosion tester. Between 0.5 and 20 minutes, they noticed that the number of craters and lips increase with time progresses which might increase the likelihood of lips removal per impacts. Also, they found with the aid of FIB that presence of three notable layers varied according to the distribution of their

grain size. The first layer is a thin nanocrystalline layer smaller than 100 nm in size on the top surface. The thickness of this layer increased from 300 to 700 nanometres for the period between 0.5 to 10 minutes while it experienced a remarkable stability in its depth between 10 to 20 minutes. The second layer is the micro-grains layer followed by the bulk grain, which falls directly below the micro-grain layer. This can be clearly seen in Figure 2-31.

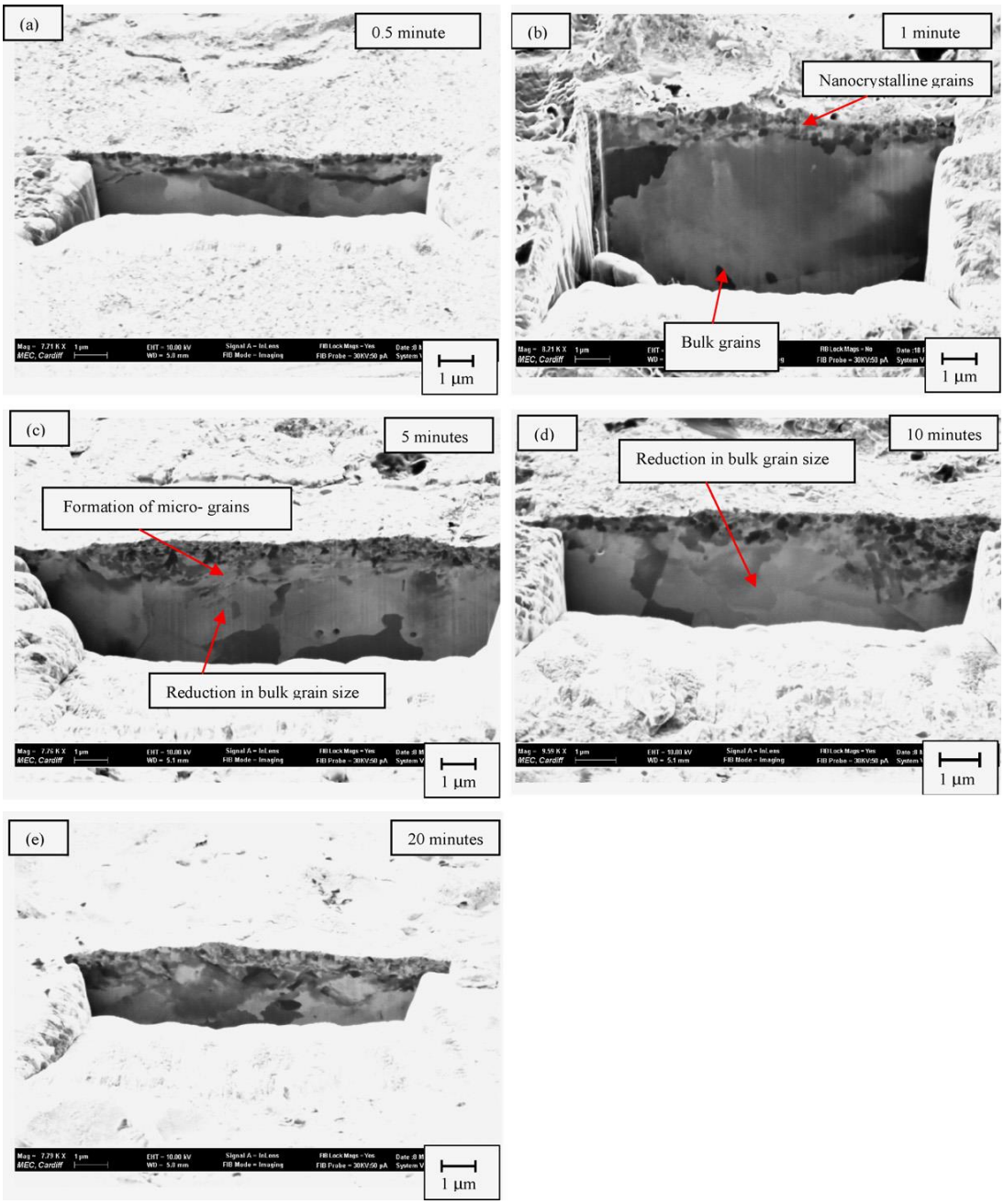

Figure 2-31: Showing the main features related to sub-surface evolution with time under erosion-corrosion conditions [131]

The erosion-corrosion mechanism of UNS S31603 in 3.5%NaCl for 1h was investigated with the aid of FIB and TEM [132]. It has been found that there was a grain size reduction in addition to presence of a nanocrystalline layer. The thickness of the nanocrystalline layer before erosion was 200 nm while it was about 2 µm after being eroded. Also, Network of cracks and sand particles were presented on the brittle top surface (Figure 2-32). The grain size reduction was intense in the region above the crack than the one underneath it. Moreover, the studied material experienced a stress-induced phase transformation from austenite to martensite (Figure 2-33a). Embedded sand particles were also noticed in (Figure 2-33b).

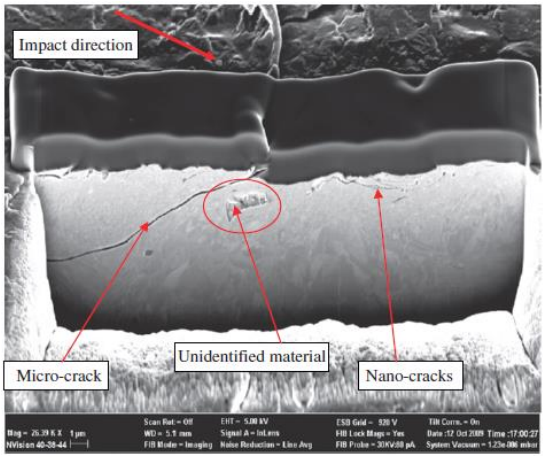

Figure 2-32: Confirms the presence of micro and Nano cracks in the surface sub-layer of UNS S31603 after erosion-corrosion [132]

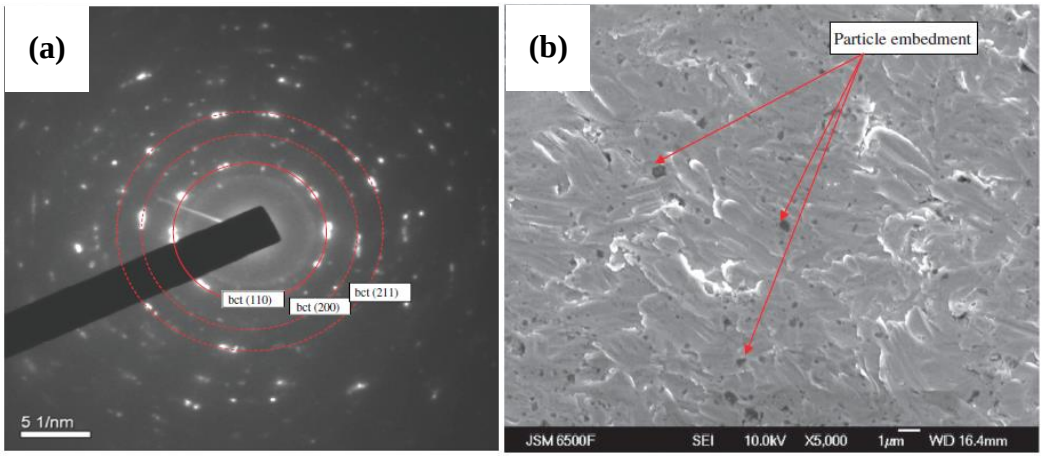

Figure 2-33: (a) Selected area diffraction pattern showing the phase transformation and **(b)** sand embedment on the material surface of UNS S31603 after erosion-corrosion [132]

Wood *et al.* [133] made a comparison between the UNS S31603 samples under erosion (water) and erosion-corrosion (3.5%NaCl) at 7 m/s flow velocity and 1% silica for 1h to understand the effect of microstructure on their degradation mechanism. They found that longer lips were formed in the case of erosion-corrosion compared to their counterparts in the case of erosion. They explained this by the reduction of the work hardened layer thickness, observed as a reduction in the martensitic volume fraction. The latter occurred because of martensite dissolution in the presence of the corrosive solution. Aribo *et al.*[134], who studied erosion and erosion-corrosion of lean duplex stainless steels UNS S32304, UNS S32101, UNS S30403 and UNS S32205 in an aerated 3.5%NaCl environment at 15 m/s and 500 mg/l sand, found that inferior mechanical properties, phase transformation and sand embedment were responsible for the high erosion-corrosion rates of UNS S30403 compared with other studied materials.

2.6.3 Effect of impact angle on erosion-corrosion of stainless steels

Erosion-corrosion of different types of materials as a function of impact angle received special attention in the current decade [58, 135-140]. Stainless steels have a wide range of classification depending on their microstructure, mechanical properties and chemical compositions. However, the effect of this important factor on the most types of stainless steels was not studied. Also, most of these studies were conducted at relatively low flow velocity and in aerated brine solutions.

For example, Burstein *et al.* [22], who studied the erosion-corrosion behavior of 304L stainless steels in 0.6M NaCl and at 3.4 m/s as a function of impact angle found that the maximum erosion and erosion-corrosion rates was between 40^{o} and 50^{o}.

The effect of flow velocity on AISI 304 (UNS S30400) and AISI 420 (UNS S42000) at 4.5 m/s and 8.5 m/s in a 0.5M H_2SO_4 + 3.5%NaCl and 30 wt.% quartz particles was

examined by Lopez *et al.* [141] at normal and oblique impact angles under erosion and erosion-corrosion conditions. Despite the great variation in the mechanical properties of both materials, they showed a ductile behaviour. Also, the surface roughness of AISI 420 was higher than that of AISI 304 indicating the importance of corrosion effect on AISI 420 under erosion-corrosion conditions. It was also found that the current density was not affected adversely by increasing flow velocity but on the contrary it had a positive effect on the passive current density. It was thought that the surface passivation ability was increased due to enhanced active species transportation at high flow velocities. They concluded that high impact velocities and oblique impact angles are the main causes of the high erosion-corrosion rates in the case of AISI 304 while AISI 420 showed high degradation rates at low and medium velocities at normal and oblique impact angles due to its limited corrosion resistance.

A number of interesting observations related to AISI 420 was also noticed in the work of Ranjbar *et al.* [142], who studied the erosion-corrosion behaviour of AISI 420 (UNS S42000) in a 3.5%NaCl solution, 6.5 m/s flow velocity and at different impact angles varying from 20-90^{o}. They found that the highest pure erosion and erosion-corrosion rates were obtained at 35^{o} and 50^{o} respectively while the minimum ones was obtained at 90^{o}. There was a distinct difference in the maximum degradation rates of the studied material under pure erosion and erosion-corrosion conditions in about 15^{o}. This was interpreted to the presence of oxide passive film, which was confirmed by SEM/EDX on the material surface under erosion-corrosion conditions. The highest synergism, which was positive at all impact angles, was obtained at 50^{o}. The pits density was more pronounced on the material surface after erosion-corrosion at 50^{o}. However, pits were not observed neither on the surface of erosion-corrosion at 90^{o} nor on the pure erosion surface at all impact angles as shown in Figure 2-34.

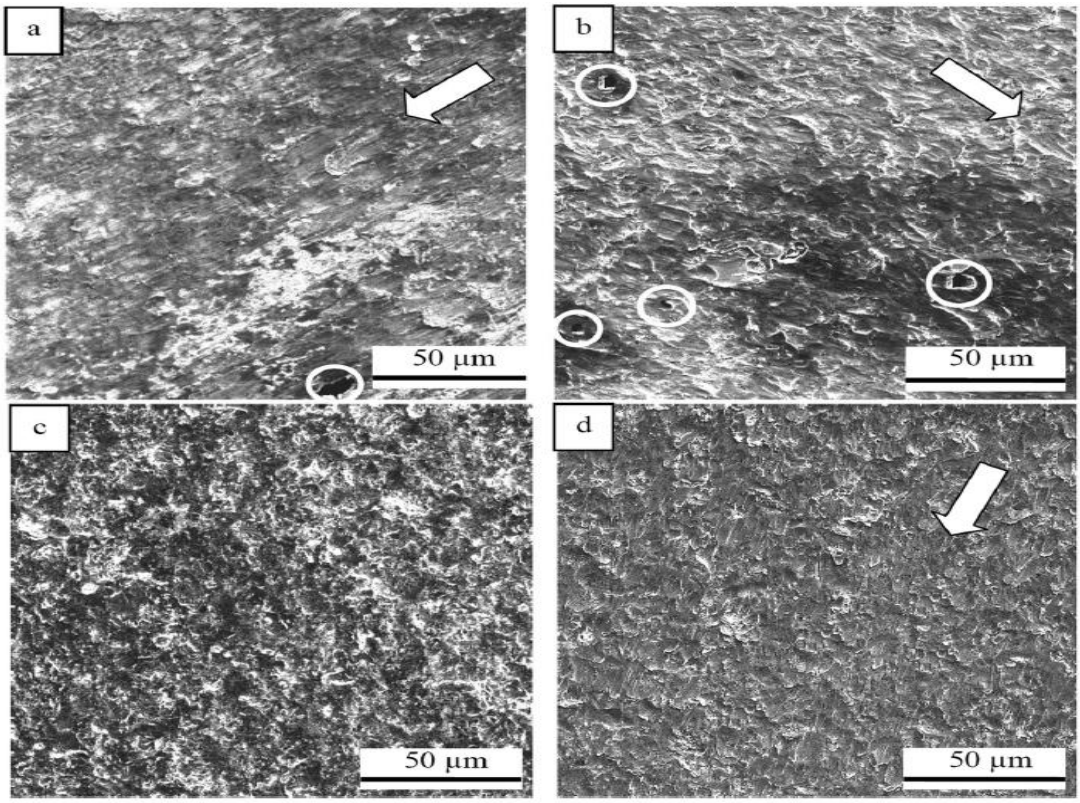

Figure 2-34: Showing the material surface after erosion-corrosion at different impact angles (a) 30°, (b) 50° and (c) 90° and after pure erosion at (d) 50° [142]

Ghasemi *et al.* [143], who studied erosion-corrosion of 316 stainless steel using jet slurry apparatus in a 3.5%NaCl solution containing 10wt. % SiO_2 at 6 m/s flow velocity and at 25°, 55° and 90° impact angles, found that the erosion and erosion-corrosion rates showed a similar trend as both of them peaked at 25° and decreased as impact angle was increased. The cutting mechanism was dominant at low impact angles while high work hardening, which is resulted from particles impacts, could be responsible for the obtained lower erosion rates at high impact angles. Positive synergy was noticed at all impact angles. The highest synergy was noticed at 25° of about 57% followed by about 37% at 55° and then about 57% at 90°. They suggested that losing of metallic bonds due to pitting corrosion which is resulted from stagnant corrosive solution underneath the cutting edges knowing that the latter was formed due to predominant cutting mechanism at this impact angle is responsible for high

synergism at 20°. At 55°, however, less cutting is presented and hence there will be a reduction in the effective area for corrosion while the disruption of the passive film at normal impact angle was responsible for the high synergy at this impact angle.

Zhao *et al.* [144], studied erosion-corrosion of AISI 316L under high speed impingement of about 20.5 m/s and 0.5 wt.% sand concentration and at 45°C. The effect of test time and chloride ions on the erosion-corrosion of the studied material was also investigated using silica and sea sand. It was found that the weight loss of the studied material effectively increased as impact angle was decreased from 75-20°. It also increased as the test time progresses because of the continued cutting mechanism. Moreover, weight loss by sea sand impact was higher than the one caused by silica sand due to the higher content of chloride ions in sea sand compared with silica sand (Figure 2-35).

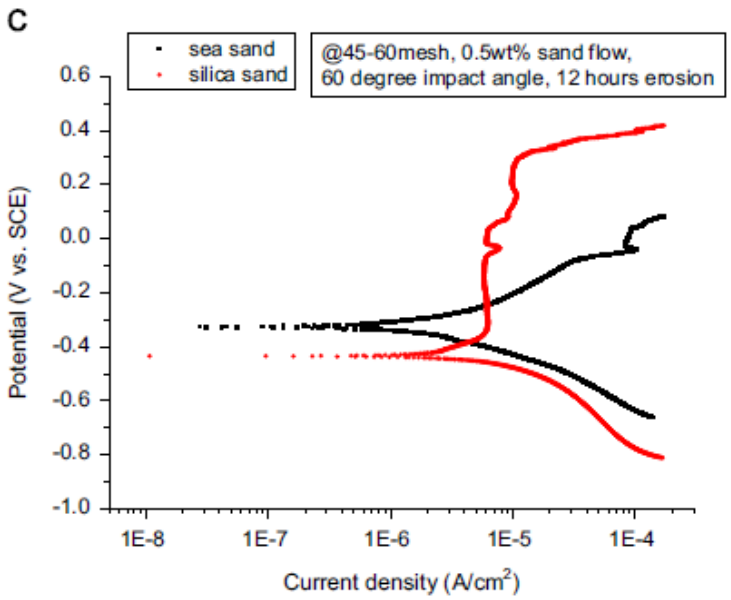

Figure 2-35: Potentiodynamic polarisation of AISI 316 using silica and sea sand [144]

In terms of surface analysis, it was observed from SEM images that grooves and prows were the main features noticed at low impact angles while craters and indentation-like marks was more pronounced at high impact angles. Also, with the aid of XPS, it was

found that the content of chromium was lost after erosion for 26h. Concerning the electrochemical measurements, they found from the potentiodynamic results that, although there was no significant difference in the cathodic branch of the studied material at different impact angles, the anodic branch was different at all impact angles due to a variation in the active dissolution, passivity and increase in the current density. The best corrosion resistance was found to be at 60^{o} while high corrosion current density was found at 20^{o} and 75^{o} impact angles as shown in Figure 2-36. It was interpreted to the incomplete passivity because of high dissolution of material at small pits and cracks resulted from erosion.

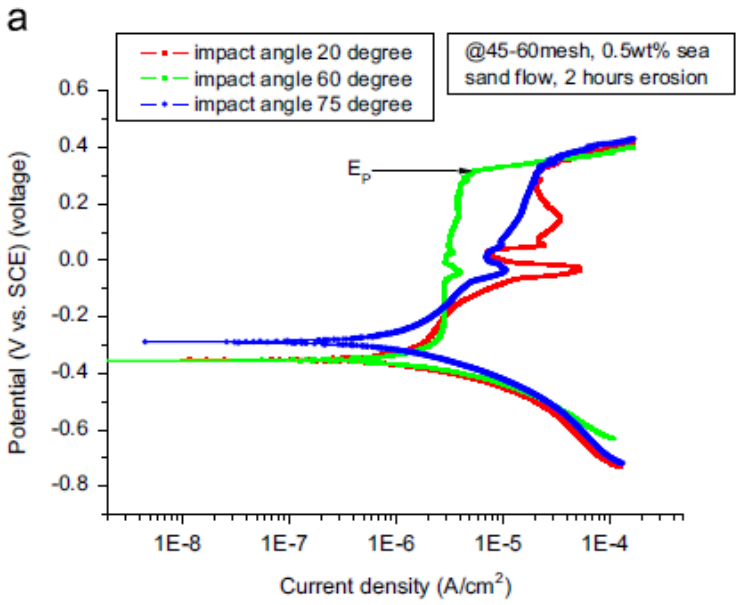

Figure 2-36: Potentiodynamic polarisation of AISI 316 at different impact angles [144]

Andrews *et al.* [145] found that SS316 showed ductile behaviour at low impact angles particularly at 45^{o} when it eroded in 3.5%NaCl solution containing 1.177 g/l sand particles at 19 m/s for 1h as shown in Figure 2-37.

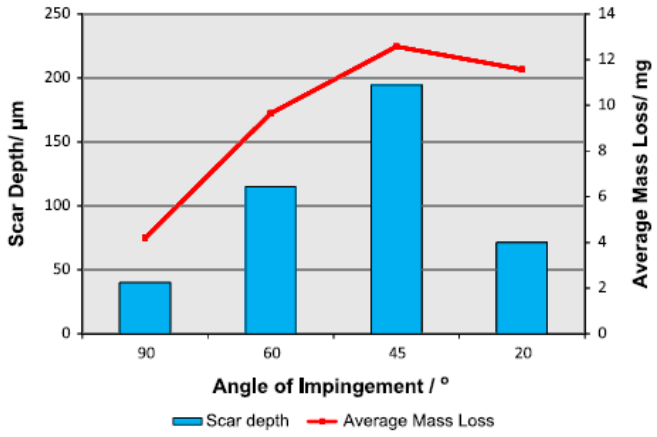

Figure 2-37: The scar depth and average mass loss of SS316 as a function of impact angle [145]

2.7 Summary

In this chapter, a literature on the topics of solid particle erosion, electrochemical corrosion, erosion-corrosion and stainless steels was reviewed to survey the research progress in these fields. From the literature review, it was found that limited research has been carried out in the following:

- The relationship between the static corrosion behavior and erosion-corrosion of stainless steels at different temperatures is not well understood. The electrochemical effect that occurs during erosion-corrosion has to be further investigated.
- The evolution of wear and the subsurface microstructure of material in response to erosion and erosion-corrosion have not been thoroughly investigated. More research is needed on the role and contribution of the subsurface microstructure to synergy.
- Understanding the erosion-corrosion behavior of stainless steels as a function of impact angle has not been fully developed particularly at high flow velocity and in CO_2-saturated environment. The effect of impact

angle on the percentage of contribution of the total weight loss components needs to be investigated.

This project aims to bridge some of the gaps between existing research and the research areas listed above which are vital in the understanding the erosion-corrosion degradation behavior of stainless steels.

Chapter three: Experimental methods

3.1 Introduction

The general aim of this study is to improve the current understanding of stainless steel degradation behaviour in a 10%NaCl (CO_2 – saturated) environment under erosion-corrosion conditions. In order to achieve this goal, a number of objectives have been specified as shown in section 1.2. To address these objectives, gravimetric and electrochemical measurements in addition to different post-test surface analysis techniques were used as can be seen in Figure 3-1.

UNS S32760, UNS S31803, UNS S31603 and UNS S42000 were chosen as candidate materials. These materials represent the generic types of stainless steels used in the oil and gas industry. A 20 m/s flow velocity and 1500 mg/l sand concentration were used as a basis of the environmental conditions in most of the tests carried out in this work to simulate the operation conditions belonging to the Pierce oilfield which lies in the North Sea, UK. and operated by Shell.

The chapter will start by presenting the chemical composition and the mechanical properties of the studied materials. After that, the procedure followed to prepare samples to any of the required tests will be described. Then, a brief description of the Submerged Impinging Jet (SIJ) apparatus used to implement erosion and erosion-corrosion tests and its calibrations will be highlighted. Moreover, detailed information about the gravimetric, the electrochemical measurements and post-test surface analysis techniques used in the current study will be presented.

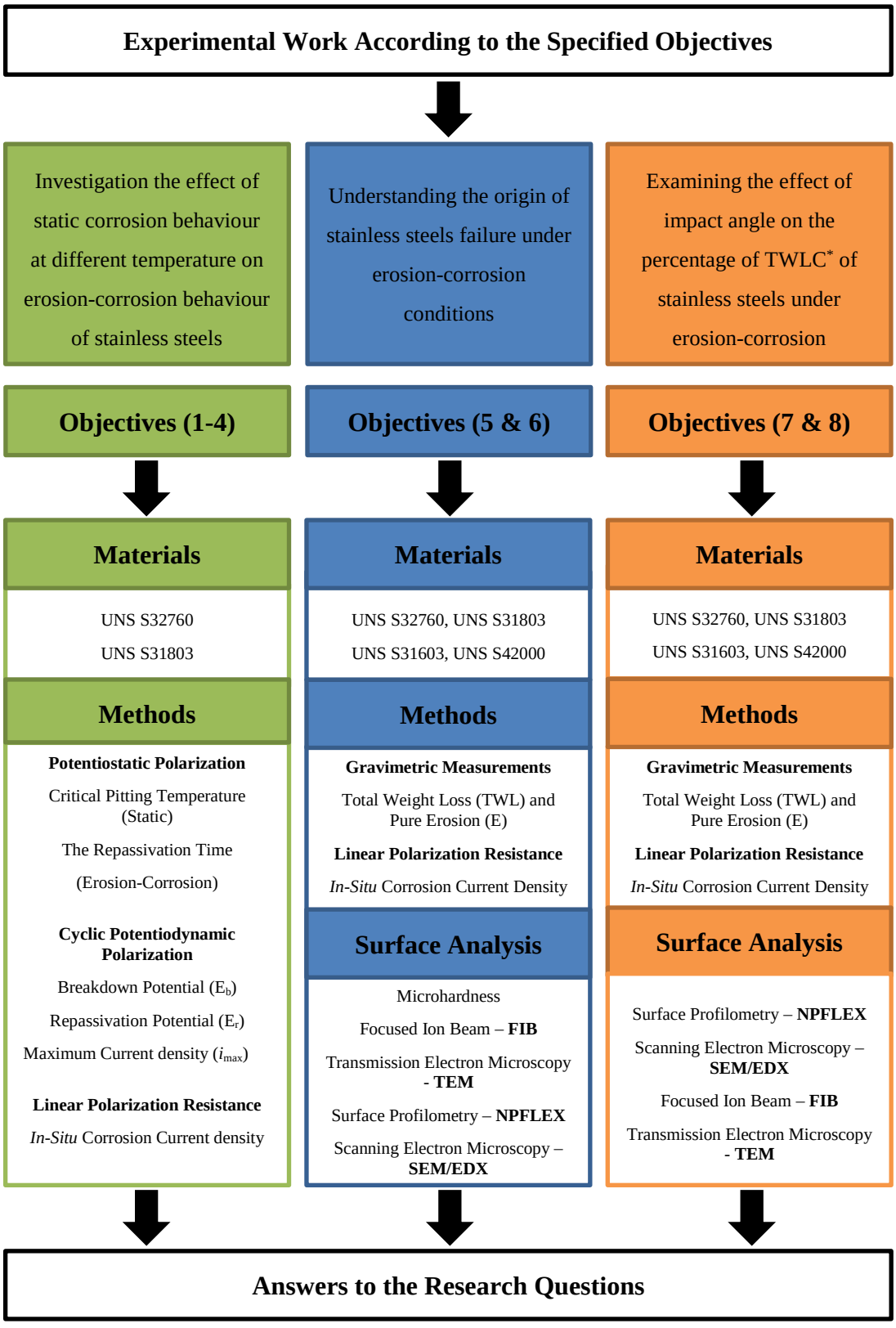

Figure 3-1: Showing the details of the experimental methods of the current work

*TWLC: Total Weight Loss Components.

3.2 Materials

The materials used in this study were super duplex UNS S32760, duplex UNS S31803, austenitic UNS S31603 and martensitic UNS S42000. Their chemical composition in addition to their mechanical properties are shown in Table 3-1 and Table 3-2, respectively.

Table 3-1: The chemical composition of the studied materials

Material	Cr	Ni	Mo	C	W	Cu	N	Mn	Si	P	S
UNS S32760	24-26	6-8	3-4	0.03	0.5-1	0.5-1	0.2-0.3	1	1	0.03	0.01
UNS S31803	21-23	4.5-6.5	2.5-3.5	0.03	-	-	0.08-0.2	2	1	0.03	0.02
UNS S31603	18	14	3	0.03	-	-	0.1	2	0.75	0.04	0.03
UNS S42000	12-14	-	-	0.15	-	-	-	1	1	0.04	0.03

Table 3-2: The mechanical properties of the studied materials

Material	Ultimate Tensile Strength (MPa)	Yield Strength (0.2% Offset) (MPa)	Elongation (%)	Hardness (HV)
UNS S32760	750	550	25	330
UNS S31803	620	448	25	303
UNS S31603	485	170	40	218
UNS S42000	690	414	15	247

3.3 Sample preparation

Circular 25 mm disc samples with 5 mm thickness were used in this study. The samples were wet-ground using different grades of metallographic silicon carbide abrasive papers (Met Prep) as follows: P 320, 600, 800 and 1200, rinsed with distilled water and acetone and then dried by compressed air. This procedure was used to prepare samples which were used for gravimetric measurements of erosion-corrosion tests. In terms of the electrochemical measurements, the same procedure as above was followed, with one exception being that an electrical copper wire was attached to one of the sample sides. Then, the sample was mounted in an epoxy resin (Varidur-10 Buehler) and the sample left until it dried.

One of the tests carried out in this work aims to evaluate the corrosion current density of the deformed region of the studied materials. A 6mm disc (4 mm represents the stagnant /deformed region + 2 mm left to apply an acrylic varnish) with 5 mm thickness was used for this purpose as shown in Figure 3-2. Also, samples used to implement the galvanic coupling effect between the deformed and non-deformed regions of the studied materials can be seen in Figure 3-2.

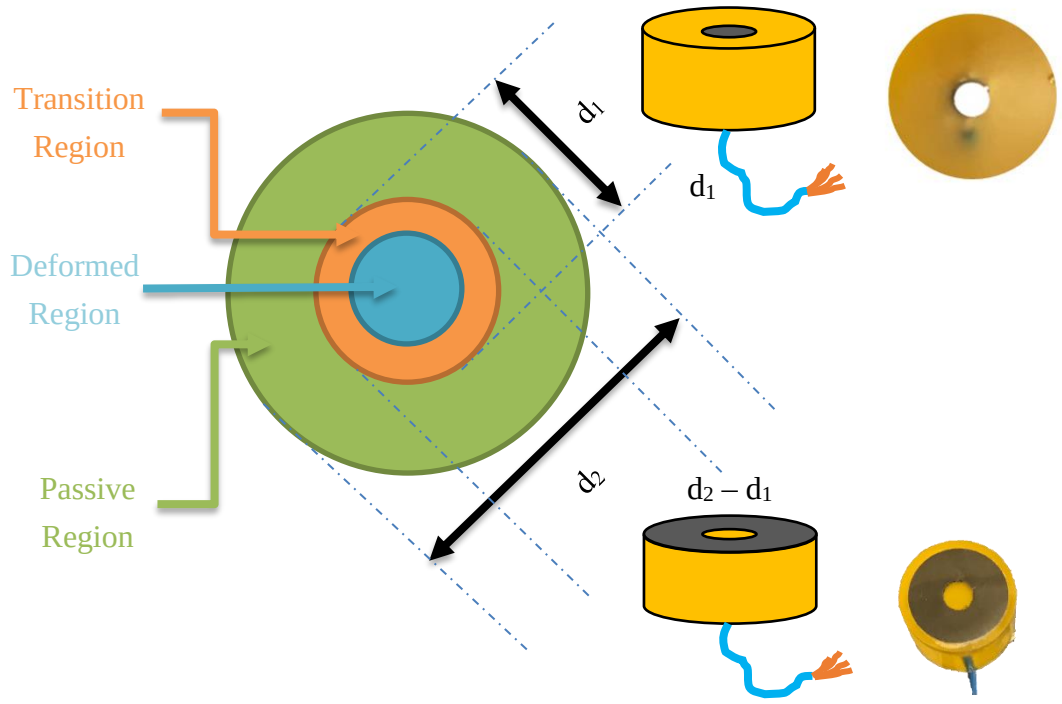

Figure 3-2: The samples used to evaluate the corrosion current density of the deformed region in addition to the one used to evaluate the galvanic coupling between the deformed and non-deformed regions of the studied materials

Moreover, 2.25 cm^2 square samples were used to implement the cyclic potentiodynamic polarization and the potentiostatic technique tests. An acrylic varnish was applied on the sample edge between the sample and the resin to prevent occurrence of crevice corrosion.

3.4 Test solutions and erodent

A 10%NaCl brine solution saturated in CO_2 for at least 16 hours to maintain a pH of about 4 and to ensure that there is no dissolved oxygen in the containing reservoir was used to implement erosion-corrosion tests. To simulate the erosion behaviour, de-aerated tap water (N_2 purged, pH=7) was used to quantify the mechanical effect of the impacting particles. HST60 silica sand (Figure 3-3 – A) 250 µm in size (Figure 3-3 - B) was utilised as an erodent in both pure erosion and erosion-corrosion tests.

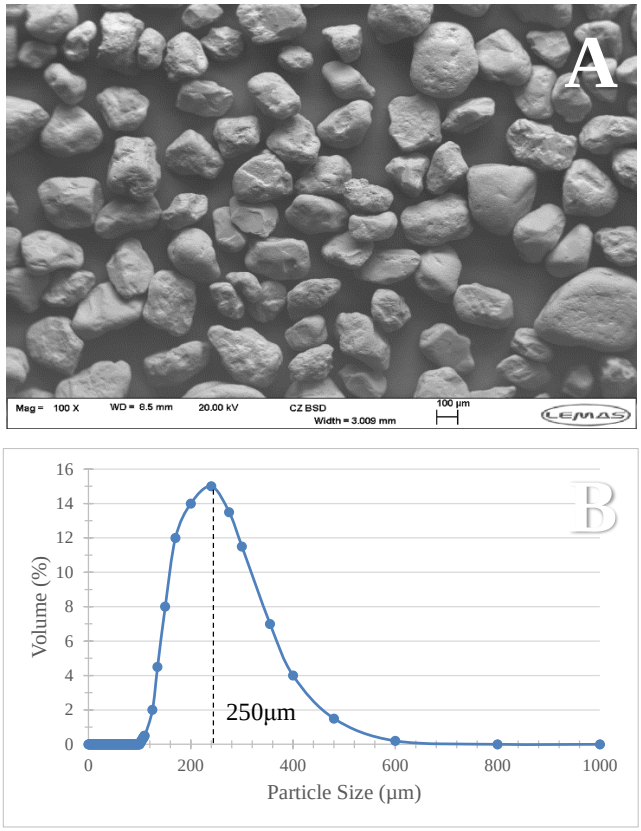

Figure 3-3: (A) Sand particle distribution and **(B)** scanning electron microscopy image of sand particles

3.5 Experimental rig apparatus

3.5.1 Description

Erosion-corrosion tests were conducted using a Submerged Impinging Jet (SIJ) apparatus shown in Figure 3-4. SIJ was used in this work due to its ability to provide

a high flow velocity, varying impact angles. Also, its ability to produce a wide range of local impact conditions similar to those obtained in oil and gas pipeline systems gave this powerful technique the advantage of using it to evaluate the materials performance under erosion-corrosion conditions. The SIJ rig comprised a 50-litre tank connected to a centrifugal pump (*INVENT HYDROVAR - Max. Frequency = 50Hz*). The pump used to recycle the flowing fluid to the tank through a dual nozzle (each 4 mm diameter) placed 5 mm away from sample holders in order to establish a well-defined hydrodynamic on the materials surface. Several sample holders with different impact angles (30, 45, 60, 75 and 90)^{o} were used to implement erosion and erosion-corrosion tests. Each test was repeated three times to ensure its reproducibility.

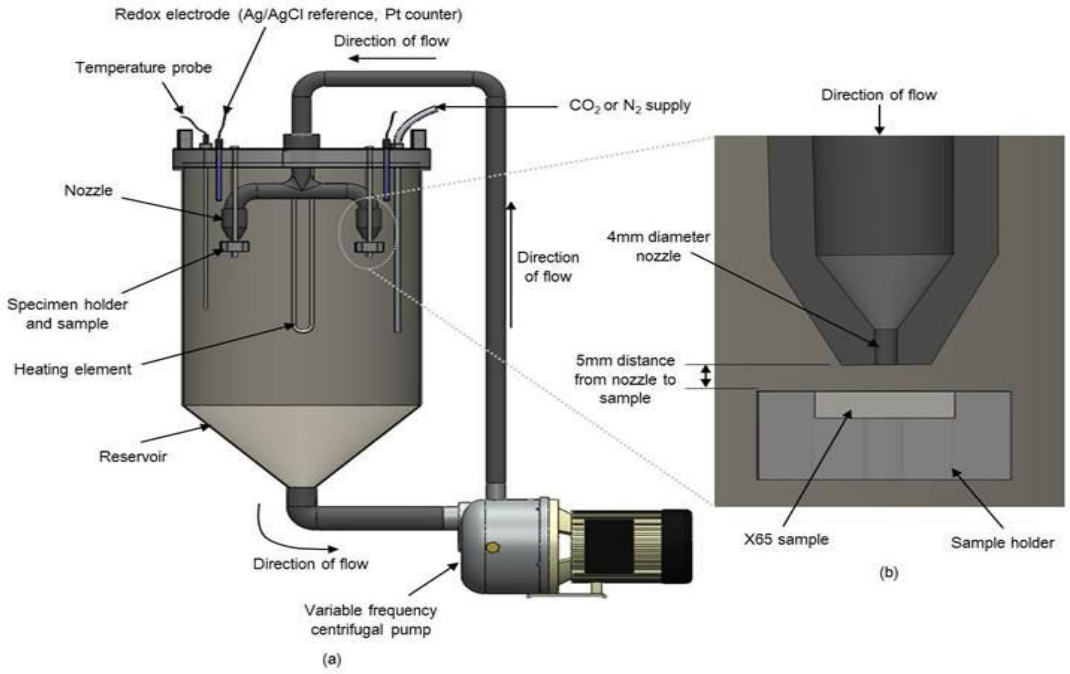

Figure 3-4: The SIJ Setup

3.5.2 Calibration

3.5.2.1 Velocity calibration

In order to get a specific value of flow velocity which comes out through the SIJ rig nozzles in (m/s), the following procedure was followed. Firstly, the tank was filled

with 50 L in water. Then, the nozzles, which are used for calibration purposes, were fixed. The pump was operated at its maximum velocity (50Hz). Then, a 1litre beaker was filled with a specific amount of water that comes out from the nozzle to calculate the volume of the water obtained in litre and then converted to (m^3). Also, a stop watch was used to calculate the required time for the beaker to be filled with a specific amount of water in seconds and hence the volumetric flow rate in (m^3/s) can be calculated. Since the diameter of the nozzle is known (4 mm), the velocity at each volumetric flow rate was obtained. This can be clearly shown in Table 3-3.

Table 3-3: The flow velocity calibration of SIJ

SIJ Flow Velocity Calibration							
Frequency (Hz)	**Volume (L)**	**Volume (m^3)**	**Time (s)**	**Volumetric Flow Rate (m^3/s)**	**Area (m^2)**	**Velocity (m/s)**	**Average Velocity (m/s)**
50	0.83	0.00083	2.65	0.000313208	1.26E-05	24.93690662	24.25
	0.85	0.00085	2.81	0.000302491	1.26E-05	24.08368656	
	0.85	0.00085	2.85	0.000298246	1.26E-05	23.74566991	
40	0.84	0.00084	3.38	0.000248521	1.26E-05	19.78668074	19.63
	0.87	0.00087	3.53	0.000246459	1.26E-05	19.62252576	
	0.85	0.00085	3.47	0.000244957	1.26E-05	19.50292773	
30	0.9	0.0009	4.85	0.000185567	1.26E-05	14.7744435	14.73
	0.9	0.0009	4.87	0.000184805	1.26E-05	14.71376816	
	0.89	0.00089	4.81	0.000185031	1.26E-05	14.73178225	
20	0.89	0.00089	7.44	0.000119624	1.26E-05	9.524176426	9.52
	0.9	0.0009	7.53	0.000119522	1.26E-05	9.516075824	
	0.89	0.00089	7.44	0.000119624	1.26E-05	9.524176426	
10	0.5	0.0005	22.78	2.19491E-05	1.26E-05	1.747538068	1.61
	0.5	0.0005	22.62	2.21043E-05	1.26E-05	1.75989908	
	0.5	0.0005	30.06	1.66334E-05	1.26E-05	1.324315276	

The calibration was repeated three times at each pump frequency to avoid errors and to get reliable flow velocity. Figure 3-5 shows clearly the relationship between the pump frequency and the correspondence flow velocity.

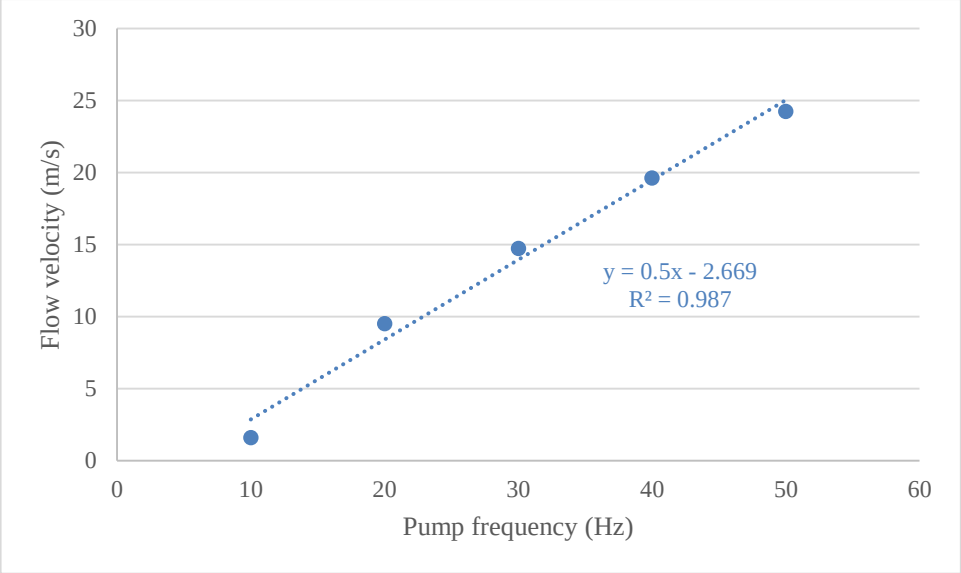

Figure 3-5: Data to be used to get the equivalent value of pump frequency (Hz) corresponding to the required flow velocity (m/s)

3.5.2.2 Sand concentration calibration

The sand calibration procedure is a bit more complex than the flow velocity calibration. This calibration allows the required sand concentration at a specific flow velocity to be determined.

Firstly, the pump was operated at a specific frequency that gives the required flow velocity as explained in the previous section. Then, a specific amount of sand was added (20 g) to the tank. A 1 litre beaker was filled with water that comes out from the SIJ nozzles and the beaker left for about 3 minutes to allow sand settlement. The obtained water volume was measured. After that, the water was poured in a cylinder through a filtration paper that was fixed on its topside that is already prepared to trap the sand in the filtration paper. The filtration paper was taken out of the cylinder and kept in a box for 2-3 days until it fully dried. Subsequently, the dried sand was weighed and the sand concentration was obtained by dividing the weight of dry sand per the water volume as clearly seen in Table 3-4.

Table 3-4: The sand concentration calibration of SIJ

	Add 20,000			Add 20,000		
	1	2	3	4	5	6
Sand Loading (mg)	20000	19563.94	19203	38615.59	37651.14	36657
Volume (l)	0.85	0.88	0.9	0.85	0.89	0.84
Dried Weight (mg)	436.06	360.8	587.55	964.45	994.29	936.6
C (ppm)=dried weight/Volume	513	410	652	1134	1117	1115
	Add 20,000			Add 20,000		
	7	8	9	10	11	12
	55720.25	54378.89	53127	71917.2	70308.89	68610
	0.89	0.82	0.85	0.81	0.84	0.86
	1341.36	1251.43	1210.3	1608.31	1699.31	1634
	1507	1526	1423	1985	2022	1899

The relationship between the added sand and the corresponding sand concentration is shown in Figure 3-6.

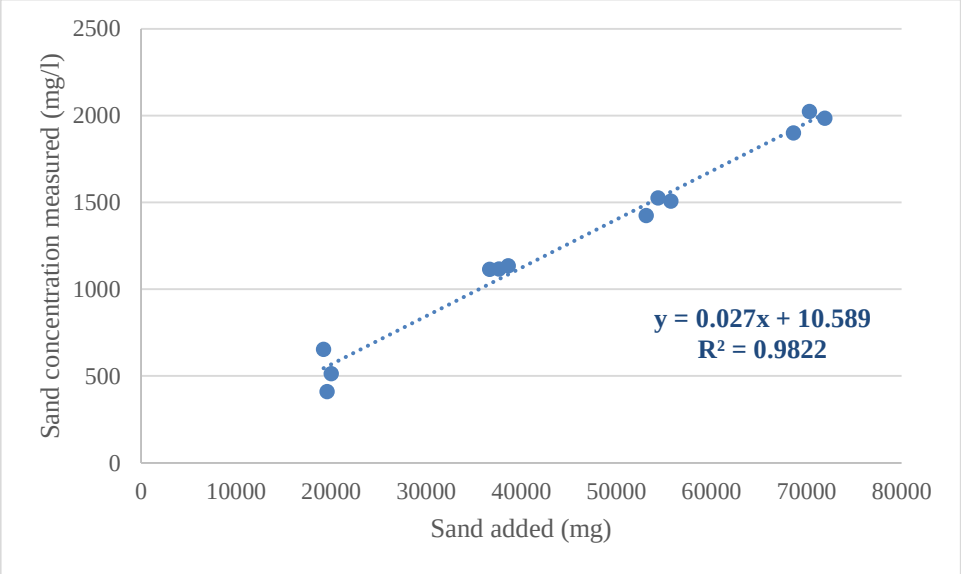

Figure 3-6: Data to be used to get the equivalent value of sand concentration at 20 m/s flow velocity in correspondence to the added sand

3.6 Gravimetric measurements

Before conducting any weight loss test, the sample was weighed to record the initial weight and after a period of time (depending on the required test), the sample was taken out of the rig, rinsed with distilled water and then by acetone and dried by compressed air. Then, the sample was weighed and the final weight was recorded.

The difference in the sample weight before and after the test was measured using a very sensitive scale (5 decimal places). This difference represents the mass loss due to either pure erosion or erosion-corrosion.

3.7 Electrochemical measurements techniques

Various commonly known electrochemical measurements were used in this work as will be explained in the next sections. A three electrodes cell was used with a silver-silver chloride reference electrode (*inLab*) combined with a platinum auxiliary electrode. The corrosion current density of the sample of interest was measured using an *ACM-Gill* potentiostat. The electrochemical measurements were performed three times to ensure the test reproducibility.

3.7.1 Linear polarisation resistance

The LPR technique was employed to evaluate the corrosion current density of the studied materials under erosion-corrosion conditions. A sweep started at -0.015 negative to the OCP and ended at +0.015V positive to the OCP was done at a scan rate of 0.25 mV/s. The OCP was allowed to stabilise for 10 minutes. The test duration was 4 hours.

3.7.2 Tafel extrapolation

In this technique, the cathodic and anodic measurements were separated starting with the cathodic branch to avoid electrode destruction. Before starting the measurement, the OCP was left until it was stabilised and then the measurement of a cathodic branch was implemented by polarising the electrode from -300 mV with respect to OCP. Then, the anodic branch was started by polarising the electrode to +300 mV. A scan rate of 0.5 mV/s was used in this technique.

3.7.2.1 Corrosion rate evaluation of the deformed region

The sample was eroded at 20 m/s flow velocity and 1500 mg/l sand concentration in a 10%NaCl (CO_2-saturated) brine solution. Then, it was taken out of the rig, rinsed with distilled water and acetone, dried by air and then acrylic varnish was applied to the edge of the samples to prevent crevice corrosion. After that, either the corrosion rate of the deformed region in a static 10%NaCl (CO_2-saturated) brine solution was evaluated by the Tafel extrapolation technique or it was used to carry out the galvanic coupling measurements as it will be explained in the subsequent section.

3.7.3 Galvanic coupling measurement

Two working electrodes were connected together to measure the galvanic current. These electrodes are working electrode 1 representing the deformed region (anodic) and working electrode 2 which is the non-deformed region. Both of them are immersed in a 10%NaCl (CO_2-saturated) brine solution for 1 hour and the evolved galvanic current was monitored.

3.7.4 Cyclic potentiodynamic polarisation

The CPP techniques were used to evaluate the breakdown potential (E_b), the repassivation potential (E_r) and the maximum current density (i_{max}) for the studied materials. A 0 mV vs. open circuit potential was utilised as an initial potential, 2000 mV as a final potential and 500 µA/cm^2 was used as a criterion for test reversal. A value of potential at current density of 10^{-5} A/cm^2 represents (E_b) while (E_r) can be specified once the reverse scan intersect with the forward scan. The scan rate is 0.1667 mV/s. The maximum current density (i_{max}), as the name suggested, represents the maximum value of current density recorded once the scan is reversed. It indicates the extent of which the corrosion is propagating.

3.7.5 Potentiostatic polarisation

3.7.5.1 The Critical Pitting Temperature (CPT) evaluation

The CPT of the studied materials was evaluated by the potentiostatic polarisation technique. The procedure used to evaluate this factor was according to the ASTM standard G-150-99 [48]. The sample were polarised at 800 $mV_{Ag/AgCl}$ and 100 $\mu A/cm^2$ was chosen as a criterion to determine the CPT of the studied materials. The temperature was increased by a rate of 1^oC/min. During the test, the current density was recorded at the same time with temperature increasing. Once the current density increased to 100 $\mu A/cm^2$ and kept continuing for 2-3 mins, the experiment was stopped. The temperature at which the current density reached to 100 $\mu A/cm^2$ was considered as the CPT. The test was repeated at least three times in order to assure its repeatability.

3.7.5.2 The repassivation time evaluation

In order to evaluate the repassivation time of the studied materials after sand particles impact, the potentiostatic polarisation technique was used for this purpose. Before starting the test, a potential of -850 mV was applied for ½ hour to remove the native oxide passive film. Then, a potential of 50 mV away from OCP was applied for a test lasts 3 hours and divided into 3 stages. Each stage lasted around 1 hour. The first stage is the passive film formation followed by its depassivation. The pump was switched on in the depassivation stage. This allowed the flowing fluid, which contains sand particles, to hit the material surface and hence induce passive film removal. Finally, the pump was switched off until the end of the test to allow healing/reformation of the passive film.

3.8 Surface analysis techniques

3.8.1 Microhardness

A Mitutoyo HM – 122 microhardness tester shown in Figure 3-7 was used to evaluate microhardness of the studied materials after erosion process. A pyramid indenter with a 0.5 kg load was used with a loading time of 10 seconds. The measurement was taken along the distance on the sample surface as shown in Figure 3-8.

Figure 3-7: The microhardness tester

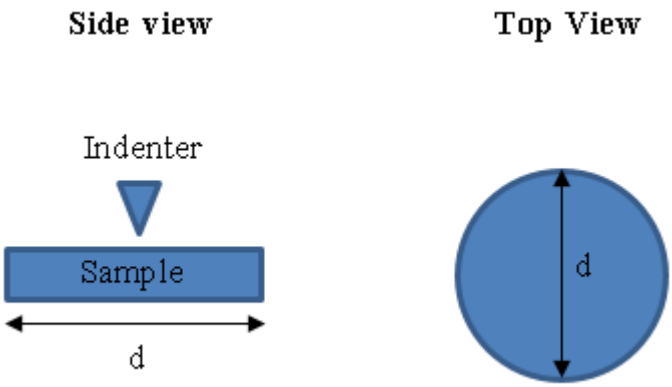

Figure 3-8: Explains the procedure of hardness measurement

3.8.2 Focused ion beam

A FEI Nova 200 Nano lab dual beam FIB-SEM at the University of Leeds with a 30Kv Ga ion source was used to prepare the samples for Transmission Electron Microscopy (TEM) as can be shown in Figure 3-9. A protective Platinum layer was deposited on area of interest by electron beam with a current 1.6 nA. A needle was used to lift out the prepared sample and attach it to a Cu TEM grid. A 50pA was implemented for fine polishing purposes. A final thickness of the prepared TEM lamella was around 100 nm.

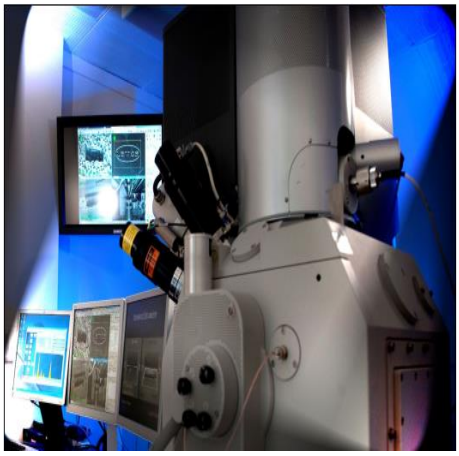

Figure 3-9: Focused ion beam

3.8.3 Transmission electron microscopy

TEM is considered the most important microscopic tool available to date. The morphology, composition and crystallography of the studied material are the main information in addition to a high-resolution, detailed image resolution of less than 1 nanometre in size can be obtained by this technique. TEM analysis was carried out using FEI Tecnai F20 FEGTEM (Figure 3-10) operating at an accelerating voltage of 200 kV fitted with a High Angle Annular Dark Field (HAADF) detector and a Gatan Orius SC600 CCD camera. In a TEM mode, Selective Area Electron Diffraction (SAED) was used to confirm phase transformation of the eroded samples.

In STEM mode, EDX maps were obtained using the Oxford instruments Aztec EDX system with a 50mm X-mas SDD detector. Electron beam is produced in a vacuum chamber and the emitted electron will be accelerated through an electromagnetic field pass through electromagnetic lenses which focus the beam. Then, the focused beam will penetrate the thin (100 nm) sample of the studied material. After that, electrons will hit phosphor screen, CCD camera and an image will be produced.

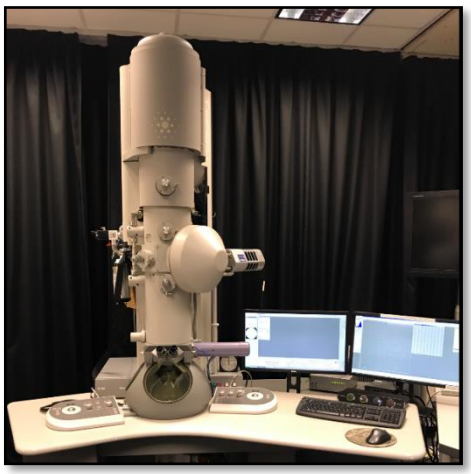

Figure 3-10: Transmission electron microscopy

3.8.4 Surface profilometry

A Bruker NPFLEX 3D Surface Metrology System (Figure 3-11) was used to quantify the scar wear depth, surface roughness and wear diameter of the eroded samples. A 15 mm diameter spiral scan starting from the centre of the eroded sample was utilised. The objective used was 2.5X with an about 3.5 mm working distance. After implementing the test, the raw data was analysed to obtain the requested results using vision 64 software.

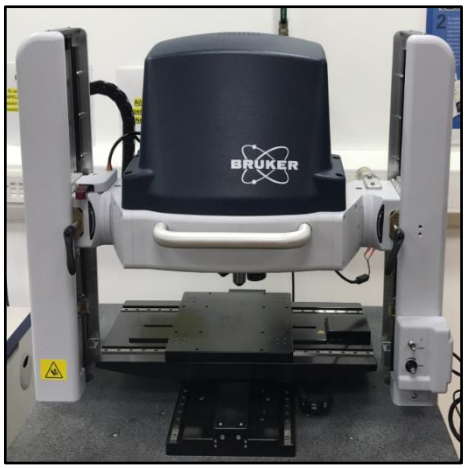

Figure 3-11: The white light interferometry (NPFLEX)

3.8.5 Scanning electron microscopy and energy dispersive x-ray

A Carl Zeiss EVO MA15 SEM (Figure 3-12) was used to examine the erosion and erosion-corrosion mechanism of the studied materials. A 20 kV accelerating voltage and a working distance of about 8 mm were used to collect Secondary Electron (SE) and Back Scattered Electron (BSE) images. EDX analysis -Oxford instruments X-mas with a 80mm^2 detector was used in this study to confirm presence of sand particles on the materials surfaces.

Figure 3-12: Scanning electron microscopy

Chapter four: Effect of the static corrosion behaviour on erosion-corrosion of stainless steels

4.1 Introduction

The aim of this chapter is to investigate the effect of the static corrosion behaviour on erosion-corrosion of stainless steels as a function of temperature. The tests carried out in this work were divided into two types: static and dynamic (erosion-corrosion) tests. In the first set of the tests, the CPT of UNS S32760 and UNS S31803 in a static 10%NaCl (CO_2-saturated) solution was determined using the potentiostatic polarisation technique. Then, the anodic polarization parameters (i.e. E_b, E_r and i_{max}) were evaluated at different temperatures using the cyclic potentiodynamic polarisation technique.

In the dynamic tests, both erosion-enhanced corrosion (dC_E) and the repassivation time were determined for both materials at different temperatures and at 20 m/s flow velocity and 1500 mg/l sand concentration in a 10%NaCl (CO_2-saturated) by linear polarisation resistance and by potentiostatic polarisation techniques respectively using SIJ apparatus. Figure 4-1 depicts clearly the structure of the present chapter.

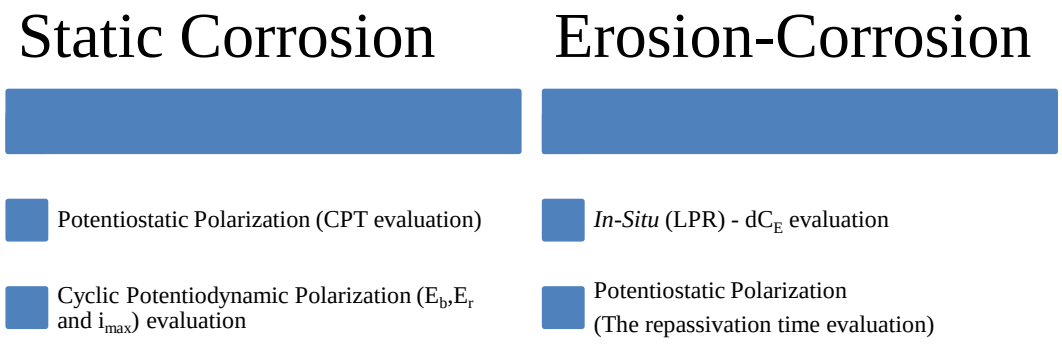

Figure 4-1: The general structure of the current chapter

4.2 Static corrosion results

4.2.1 The critical pitting temperature evaluation

The CPT of UNS S32760 and UNS S31803 was evaluated in a static 10%NaCl (CO_2 - saturated) solution as shown in Figure 4-2. As can be seen from the figure, the current density in the case of UNS S32760 raised gradually while a sharp increase in the current density was noticed in the case of UNS S31803. This is due to the higher amount of molybdenum and less amount of manganese in UNS S32760 compared with UNS S31803 [40, 146]. As expected, the CPT of UNS S32760 was higher than that of UNS S31803. The CPT values were recorded at about 61°C and 48°C for UNS S32760 and UNS S31803 respectively as shown in Figure 4-3.

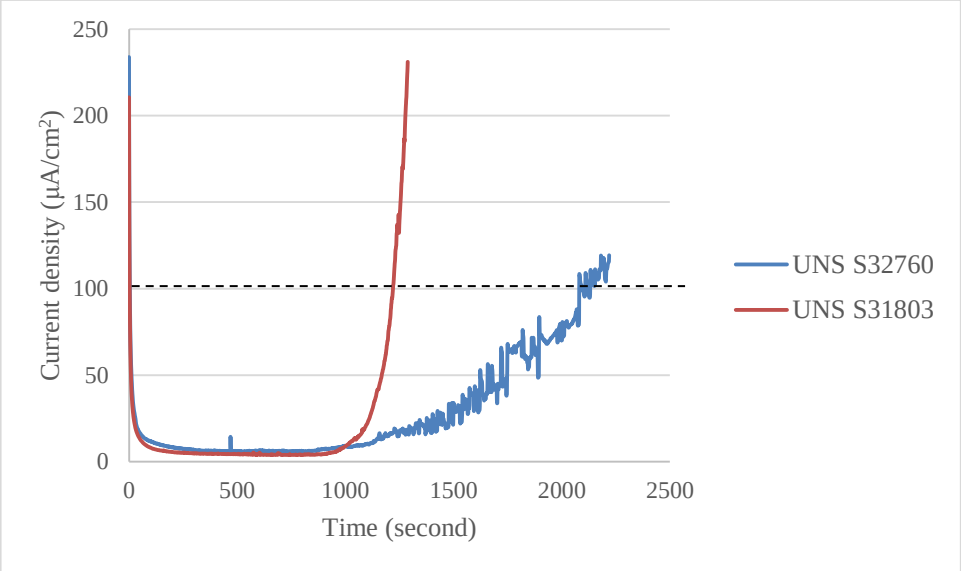

Figure 4-2: The potentiostatic polarization method used to obtain the CPT of the studied materials in a static 10% NaCl (CO_2-Saturated) solution. An applied potential of 800m$V_{Ag/AgCl}$ was used.

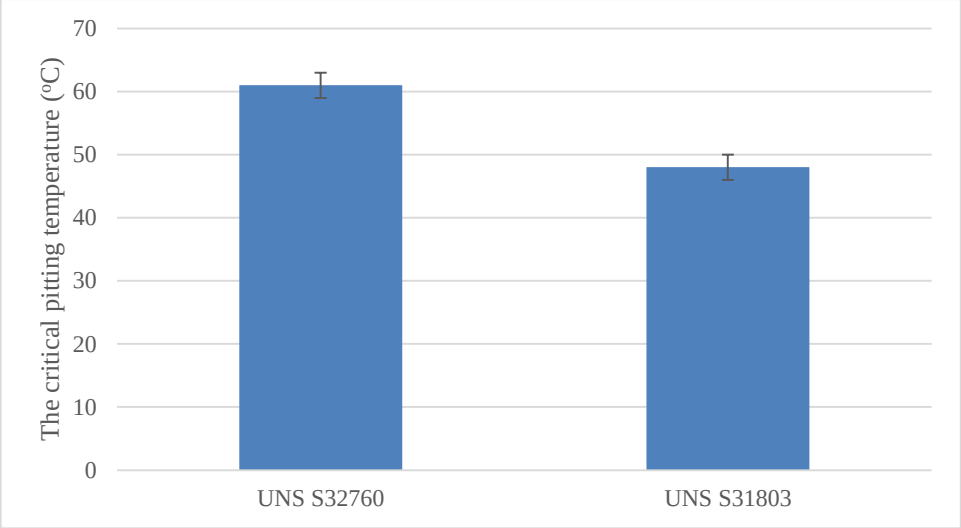

Figure 4-3: The obtained CPT values of the studied materials in a static 10%NaCl (CO_2-Saturated) solution (error bars are spread of 3 data points)

4.2.2 Anodic polarization parameters as a function of temperature

The Cyclic Potentiodynamic Polarisation (CPP) technique was utilised to evaluate the anodic polarization parameters namely E_b, E_r and i_{max} for UNS S32760 and UNS S31803 in a static 10%NaCl (CO_2 – saturated) solution at 25°C, 48°C and 61°C as can be shown in Figure 4-4, Figure 4-5 and Figure 4-6, respectively.

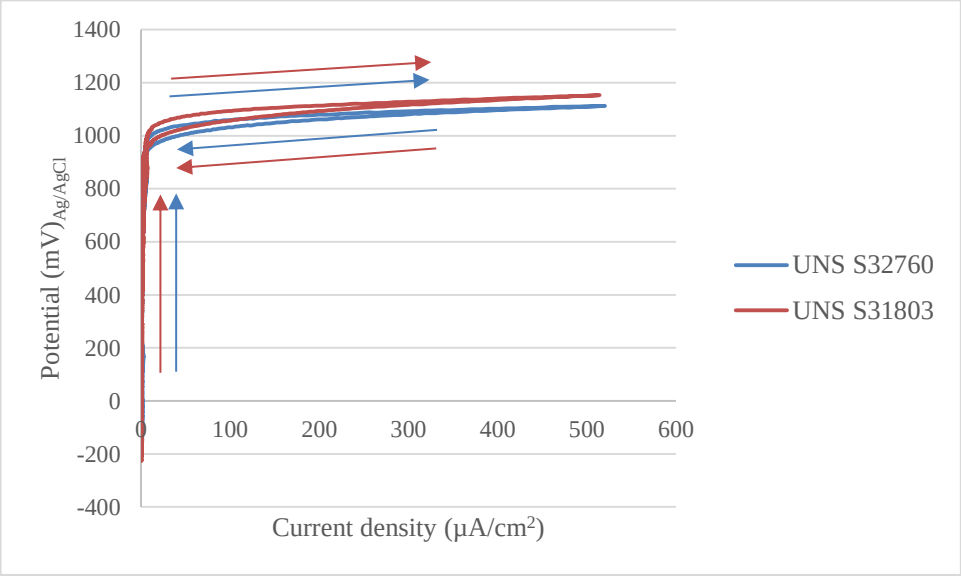

Figure 4-4: CPP of the studied materials in a static 10%NaCl (CO_2 – saturated) solution at 25°C

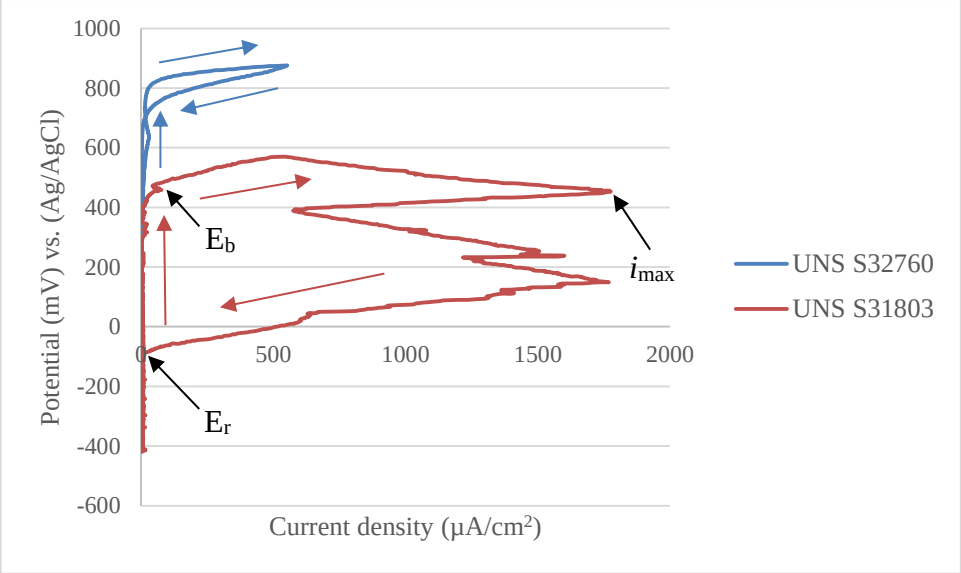

Figure 4-5: CPP of the studied materials in a static 10%NaCl (CO_2 – saturated) solution at 48°C

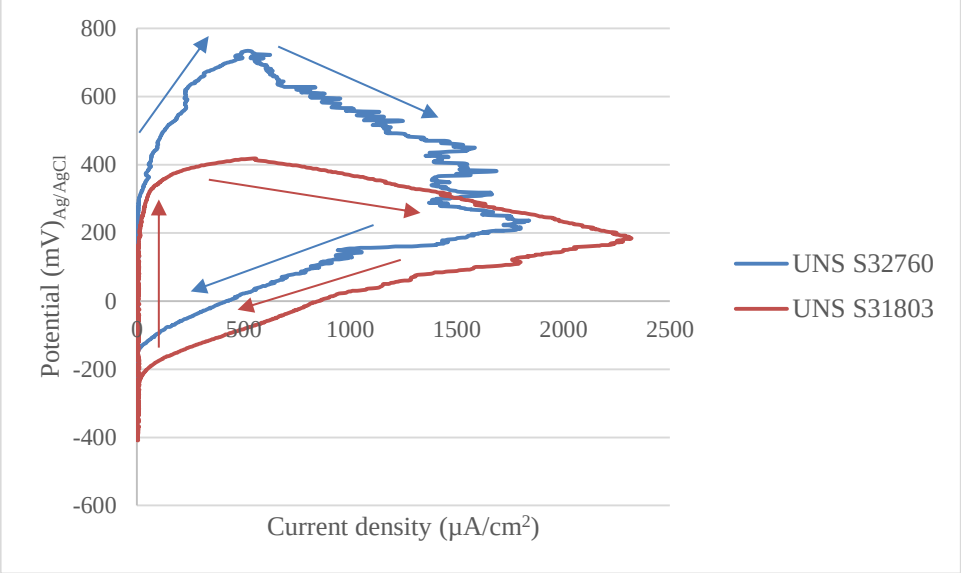

Figure 4-6: CPP of the studied materials in a static 10%NaCl (CO_2 – saturated) solution at 61°C

The breakdown potential (E_b) of the studied materials as a function of temperature can be seen in Figure 4-7. Clearly, there was a significant reduction in the (E_b) of materials as temperature increases. For instance, the breakdown potential of both materials was almost the same at 25°C in about 1000 mV. When the temperature rose to 48°C, however, UNS S31803 showed a higher decline in E_b compared with UNS S32760. The breakdown potential of UNS S31803 at 48°C was about 400 mV while it was

about 800 mV in the case of UNS S32760. At 61°C, E_b of both materials were highly affected by temperature. For instance, a 300 mV and 190 mV was recorded for UNS S32760 and UNS S31803 respectively.

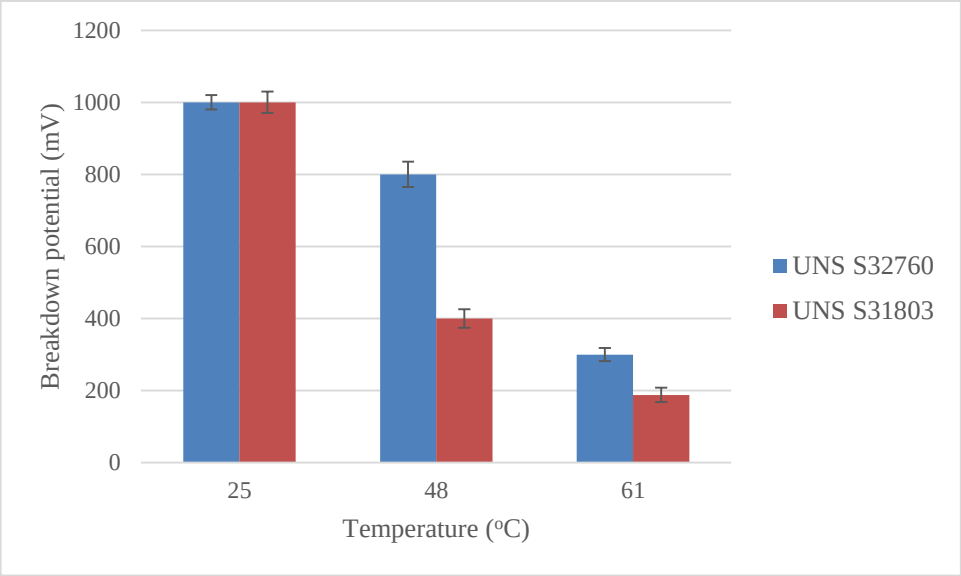

Figure 4-7: The breakdown potential of the studied materials in a static 10%NaCl (CO_2-saturated) solution versus temperature (error bars are spread of 3 data points)

A similar trend to that obtained in the breakdown potential was followed by the repassivation ability of materials in a static 10%NaCl (CO_2-saturated) solution, which is represented by (E_b-E_r) and i_{max} as can be shown in Figure 4-8 and Figure 4-9.

(E_b-E_r) of UNS S32760 and UNS S31803 at 25°C was almost the same for both materials at about 30 mV. UNS S31803 showed higher (E_b-E_r) value at 48°C at about 500 mV whereas UNS S32760 did not show a significant increase until 61°C as its (E_b-E_r) value increased from 94 mV at 48°C to 440 mV at 61°C.

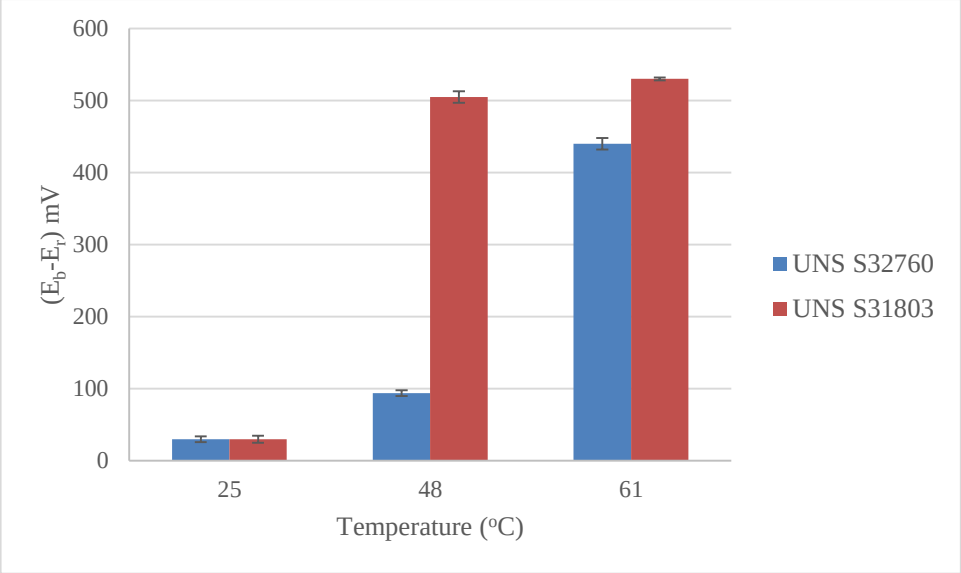

Figure 4-8: The repassivation ability (E_b-E_r) of the studied materials as a function of temperature in a static 10%NaCl (CO_2-saturated) solution (error bars are spread of 3 data points)

Similarly, the maximum current density (i_{max}) increased from around 500 µA/cm^2 for both materials at 25°C to 553 µA/cm^2 and 1776 µA/cm^2 for UNS S32760 and UNS S31803 at 48°C respectively. The maximum current density of both materials continued in increase at 61°C to reach about 1870 µA/cm^2 in the case of UNS S32760 while it was about 2320 µA/cm^2 for UNS S31803.

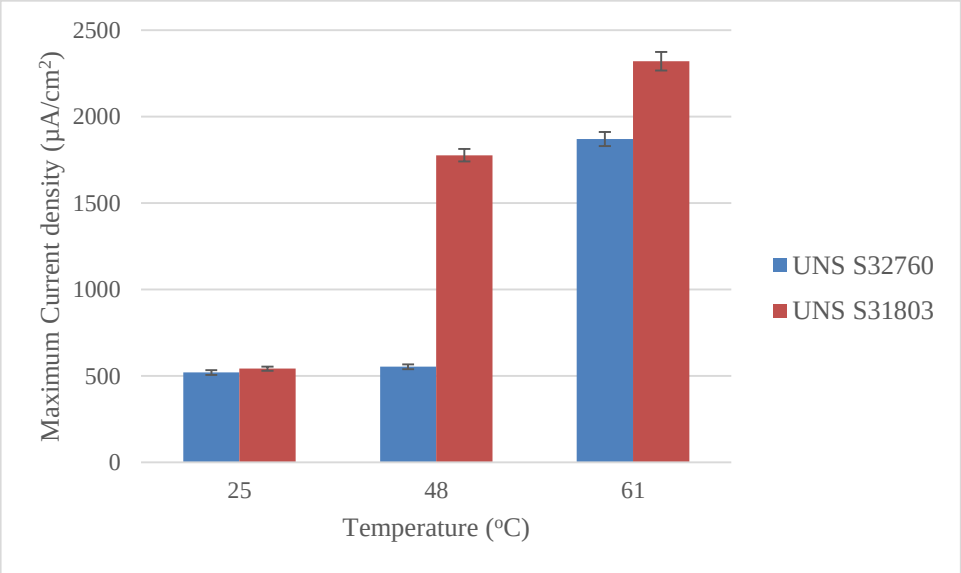

Figure 4-9: The maximum current density (i_{max}) of the studied materials as a function of temperature in a static 10%NaCl (CO_2-saturated) solution (error bars are spread of 3 data points)

4.3 Erosion-corrosion results

4.3.1 Erosion-enhanced corrosion as a function of temperature

The corrosion current density under erosion-corrosion conditions in a 10%NaCl (CO_2-saturated) brine solution at 20 m/s flow velocity, 1500 mg/l sand concentration and at different temperatures was conducted using LPR as shown in Figure 4-10 and Figure 4-11 for UNS S32760 and UNS S31803 respectively. Erosion-enhanced corrosion of the studied materials was calculated by substituting the obtained current density values of each material at each temperature in the Faraday's law calculations as can be seen in Figure 4-12. Clearly, both materials showed a slight difference in erosion-enhanced corrosion of about 0.083 and 0.089 mg of UNS S32760 and UNS S31803 respectively at 25°C. At 48°C, however, UNS S31803 showed a higher erosion-enhanced corrosion of about 0.16 mg compared with UNS S32760 of about 0.1 mg. Moreover, at 61°C, UNS S31803 continued to increase until 0.19 mg with a sudden rise in erosion-enhanced corrosion of UNS 32760 of about 0.145 mg.

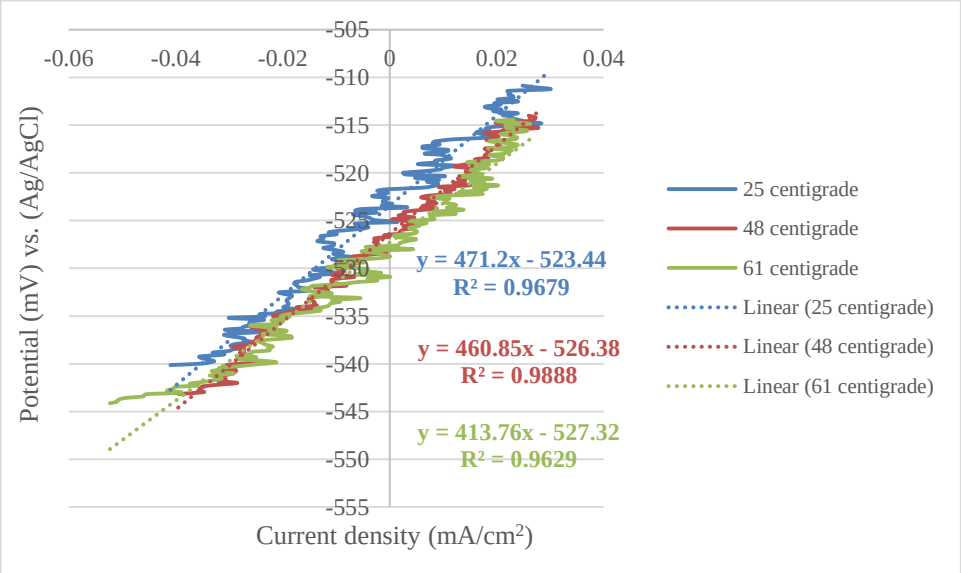

Figure 4-10: LPR of UNS S32760 in a 10%NaCl (CO_2-saturated) solution at 20 m/s flow velocity, 1500 mg/l sand concentration as a function of temperature

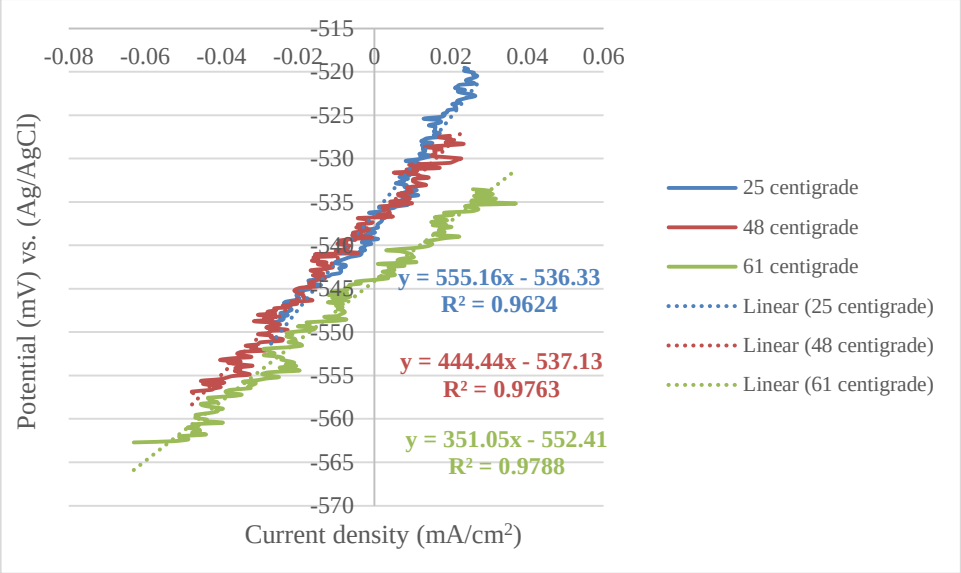

Figure 4-11: LPR of UNS S31803 in a 10%NaCl (CO_2-saturated) solution at 20 m/s flow velocity, 1500 mg/l sand concentration as a function of temperature

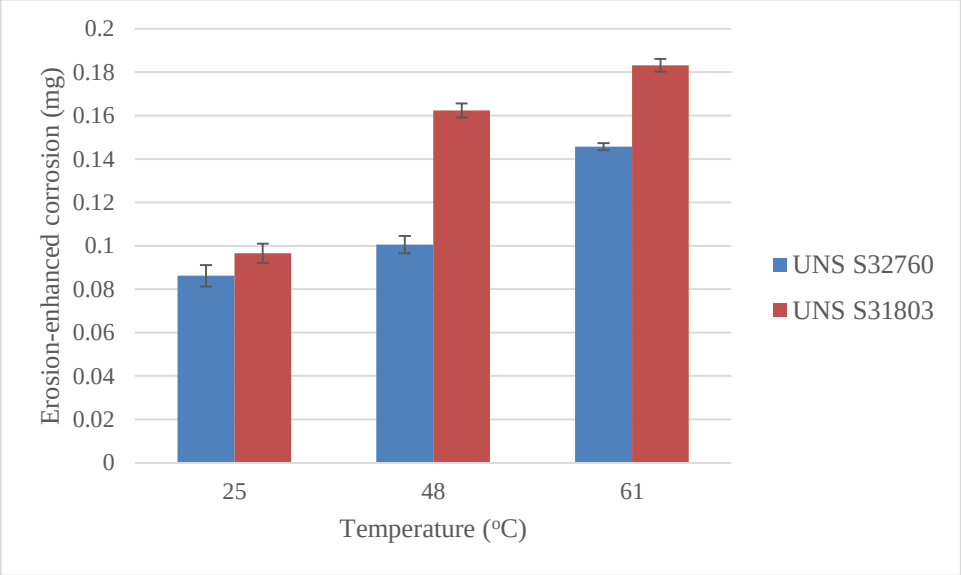

Figure 4-12: Erosion-enhanced corrosion of the studied materials in a 10%NaCl (CO_2-saturated) solution at 20 m/s flow velocity and 1500 mg/l sand concentration as a function of temperatures (error bars are spread of 3 data points)

4.3.2 The repassivation time as a function of temperature

The evaluation of the repassivation ability of the studied material includes three consecutive stages. These stages are as follows: the passive film removal / formation (the native oxide film was first removed by applying -850 mV for 30 minutes then the

passive film formation in the test solution was allowed), the passive film depassivation (by sand impacts) and lastly the passive film repassivation stage. These stages can be shown in Figure 4-13. This figure will be used as a model to give an idea about how these stages were carried out. The repassivation part will only be presented as can be shown in Figure 4-14, Figure 4-15 and Figure 4-16.

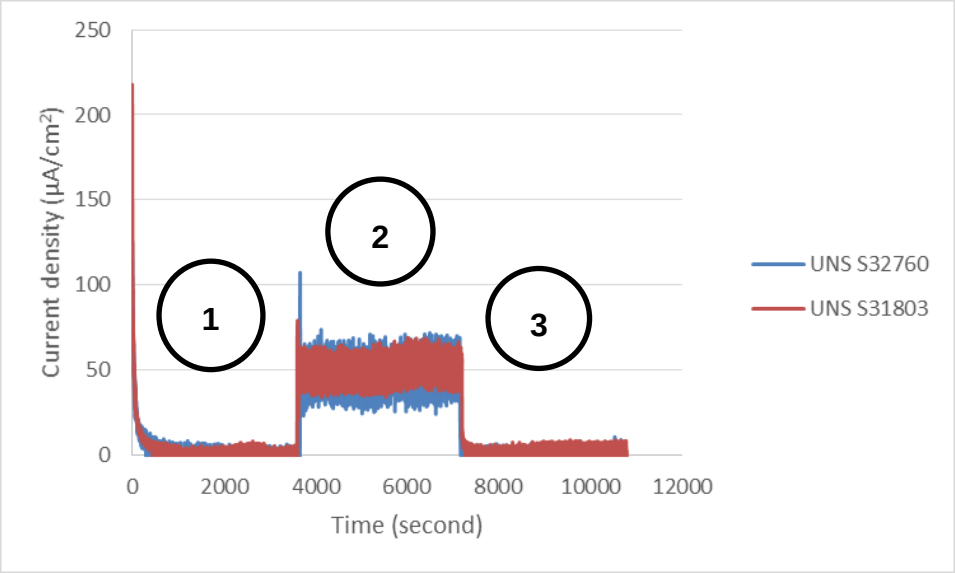

Figure 4-13: Showing **(1)** passive film removal/ formation **(1 hour) (2)** the passive film de-passivation process, 20 m/s flow velocity, 1500 mg/l sand concentration and 25°C **(1 hour) (3)** the passive film re-passivation process **(1 hour)** of UNS S32760 and UNS S31803 in a 10%NaCl (CO_2-saturated) solution

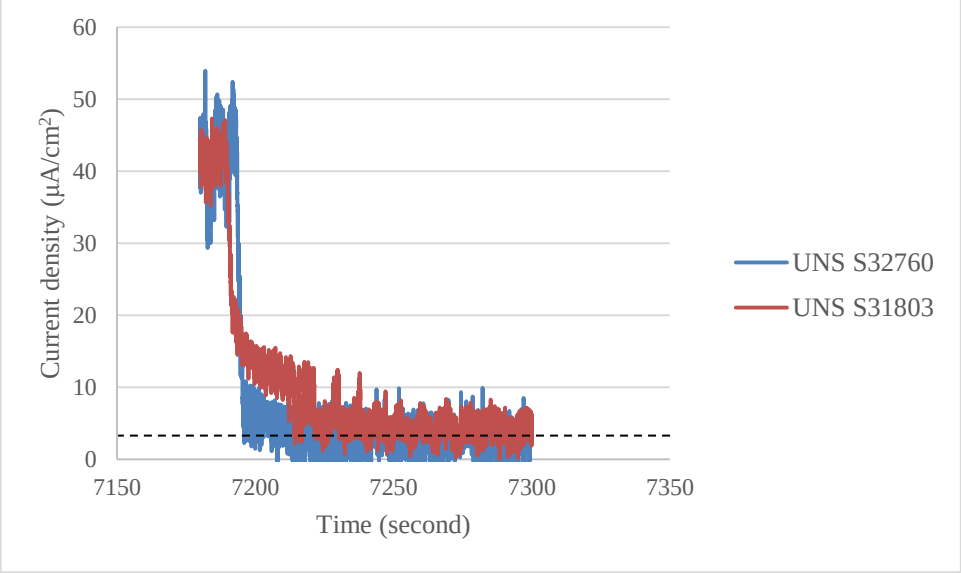

Figure 4-14: Comparison of the repassivation ability of the studied materials after de-passivation at 20 m/s flow velocity, 1500 mg/l sand concentration and 25°C in a 10%NaCl (CO_2-saturated) solution ($E_{applied}$ = -175 mV)

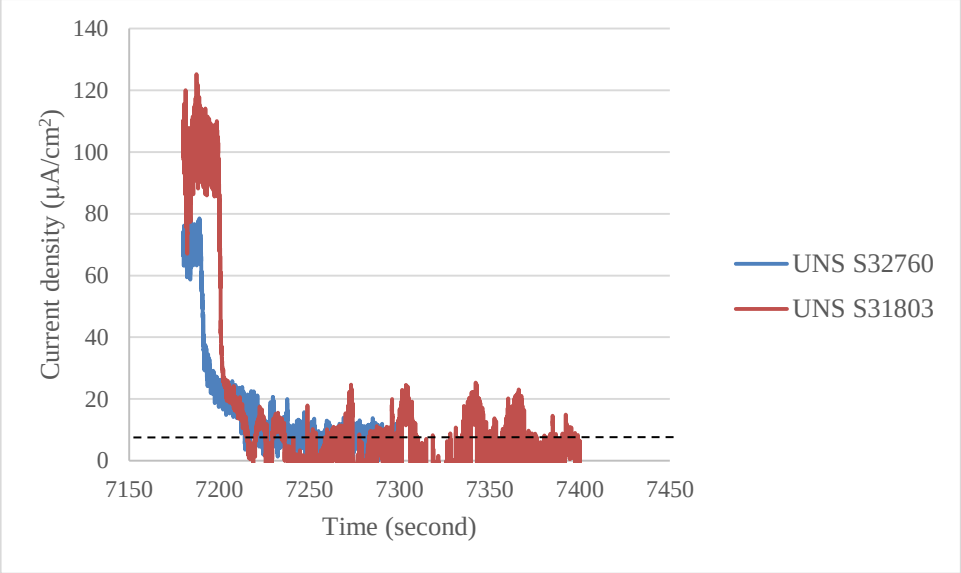

Figure 4-15: Comparison of the repassivation ability of the studied materials after depassivation at 20 m/s flow velocity, 1500 mg/l sand concentration and 48°C in a 10%NaCl (CO_2-saturated) solution ($E_{applied}$ = -350 mV)

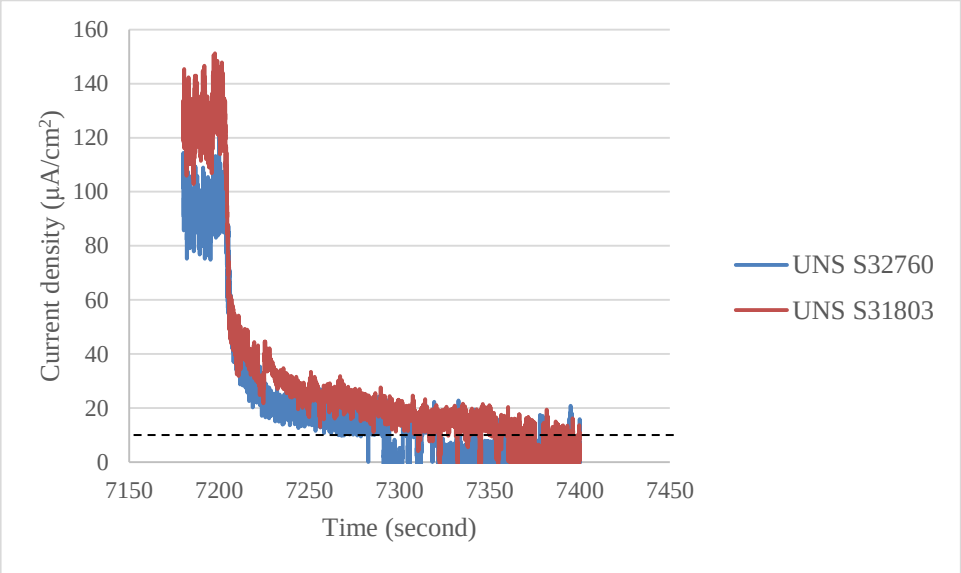

Figure 4-16: Comparison of the repassivation ability of the studied materials after de-passivation at 20 m/s flow velocity, 1500 mg/l sand concentration and 61°C in a 10%NaCl (CO_2-saturated) solution ($E_{applied}$ = -350 mV)

To quantify the repassivation time of the studied materials after the depassivation process at different temperatures, an approach which was firstly suggested by McMahon *et al.* [147] and then by Rincon *et al.* [148] was used in the present work. This model suggests that the anodic current decay following the 2nd order equation as follows:

$$\frac{dI}{dt} = -I^2 m \quad (1)$$

Where:

I: is the measured current (Amp)

t: is the time (second)

m: material and environmental conditions dependent constant.

By integration, equation (1) will be as follows:

$$\frac{1}{I} = \frac{1}{I_o} + mt \quad (2)$$

Where:

I_o: is the initial current (i.e. before depassivation).

By plotting $\frac{1}{I}$ against *t* for each material at different temperatures, the following results can be obtained:

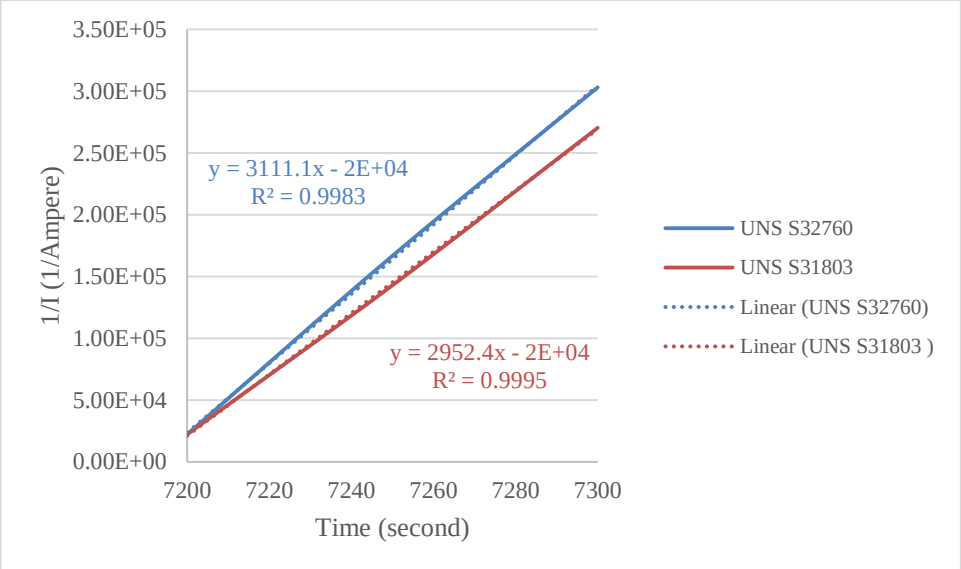

(A)

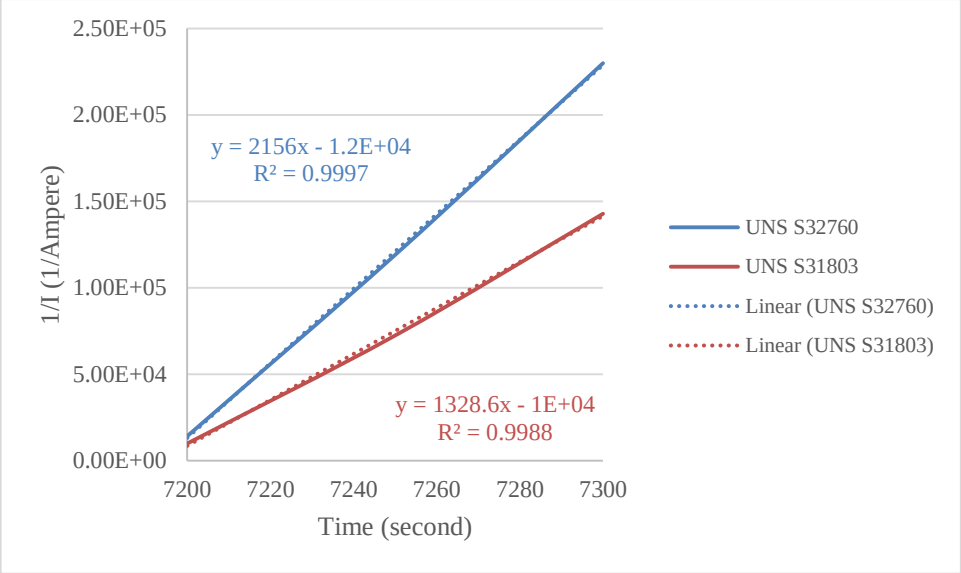

(B)

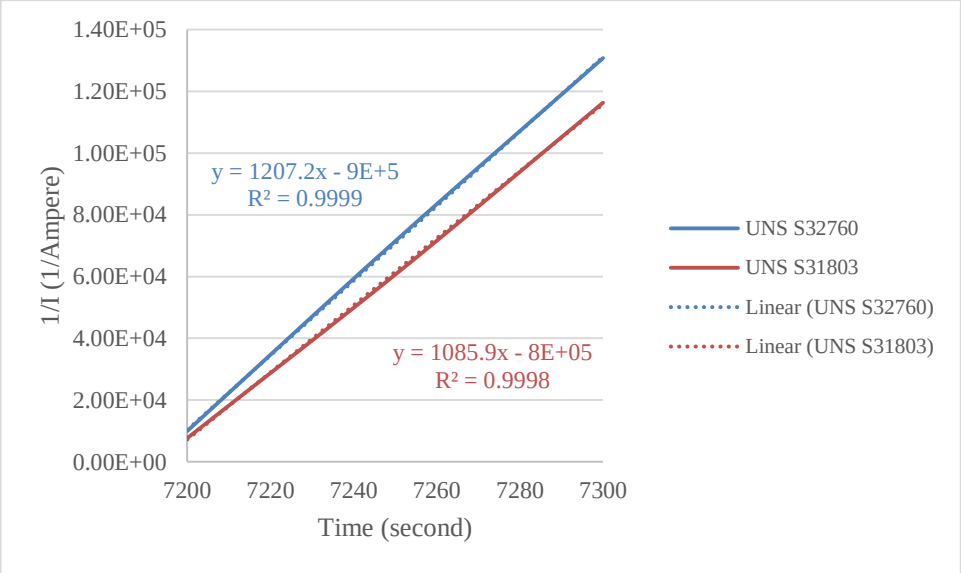

(C)

Figure 4-17: The current inverse against time for each material at **(A)** 25ºC, **(B)** 48ºC and **(C)** 61ºC

T(ºC)	m							
	Test 1		Test 2		Test 3		Average	
	A	B	A	B	A	B	A	B
25	3111.10	2952.40	3100.25	3004.85	3092.85	3020.85	3101	2992
48	2156.81	1328.60	2126.19	1460.50	2146.9	1397.70	2143	1395
61	1207.20	1085.90	1203.15	1181.80	1223.55	1161.00	1211	1142

A and B in the above table are denoted to UNS S32760 and UNS S31803 respectively.

Clearly, m values decreased as temperature increases.

In order to calculate the repassivation time (t^*), the following equation should be used [148]:

$$t^* = \frac{1}{m.I^*} - \frac{1}{m.I_o}$$

By knowing the initial current density before depassivation (I_o), the current density of interest (I^*) and m of each material at each temperature, the repassivation time (t^*) can be quantified as shown below:

Table 4-1: Showing the calculated repassivation time (t^*) as a function of temperature

T(ºC)	t* (second)							
	Test 1		Test 2		Test 3		Average	
	A	B	A	B	A	B	A	B
25	80.4	84.7	80.6	83.2	80.8	82.8	80	83
48	119.8	383.9	129.4	298.9	122.9	337.4	124	338
61	355.0	394.7	356.2	362.6	350.3	369.1	353	374

4.4 Summary

One of the interesting findings obtained from the current chapter is that the repassivation ability under static condition (i.e. (E_b-E_r) in addition to the maximum current density (i_{max})) of the studied materials are highly affected by temperature particularly at their critical pitting temperature. Also, temperature affected the repassivation ability of the studied materials under erosion-corrosion conditions significantly. Moreover, it was found that temperature has a considerable effect on erosion-enhanced corrosion of UNS S32760 and UNS S31803. The nature of temperature effect on the static corrosion behavior and its impact on erosion - erosion will be discussed extensively in the discussion chapter.

Chapter five: Understanding the erosion-corrosion degradation evolution of stainless steels

5.1 Introduction

The principal aim of the present chapter is to understand how erosion-corrosion degradation of stainless steels occurs and what factors contribute to the difference in their erosion-corrosion resistance. For these reasons, the chapter will firstly start by presenting the Total Weight Loss (TWL) in addition to its components (i.e. pure erosion (E), erosion-enhanced corrosion (dC_E) and corrosion-enhanced erosion (dE_C)) of UNS S32760, UNS S31803, UNS S31603 and UNS S42000. These are considered as the most common types of materials used in the oil and gas industry. The materials of interests which are planned to be studied in detail will be the ones that will show the best and the worst performance under this study condition.

The total weight loss and pure erosion of the studied materials will be evaluated as a function of time. Also, pure erosion as a function of flow velocity and sand size will be determined. Then, the electrochemical measurements are presented. It should be noted that these measurements include a wide range of tests. For example, the corrosion current density as a function of time will be evaluated by LPR, the corrosion current density of the deformed region by Tafel Plot in addition to the galvanic current measurement between the deformed and non-deformed regions are the main tests included in this section.

Concerning the surface analysis, microhardness of the damaged surfaces of the studied materials is determined as a function of time, flow velocity and sand size. Moreover, both scanning electron microscopy images and surface profilometry of the eroded surfaces will be obtained at different times. Furthermore, the characteristics of

the sub-surface deformed layer of the studied materials were investigated in terms of microstructural changes. Transmission Electron Microscopy (TEM) was used on sections prepared by Focused Ion Beam (FIB). The characteristics of the deformed layer of both materials were studied after 10, 60 and 240 minutes of exposure to an impinging jet of fluid containing solids. A roadmap for this chapter is presented in Figure 5-1.

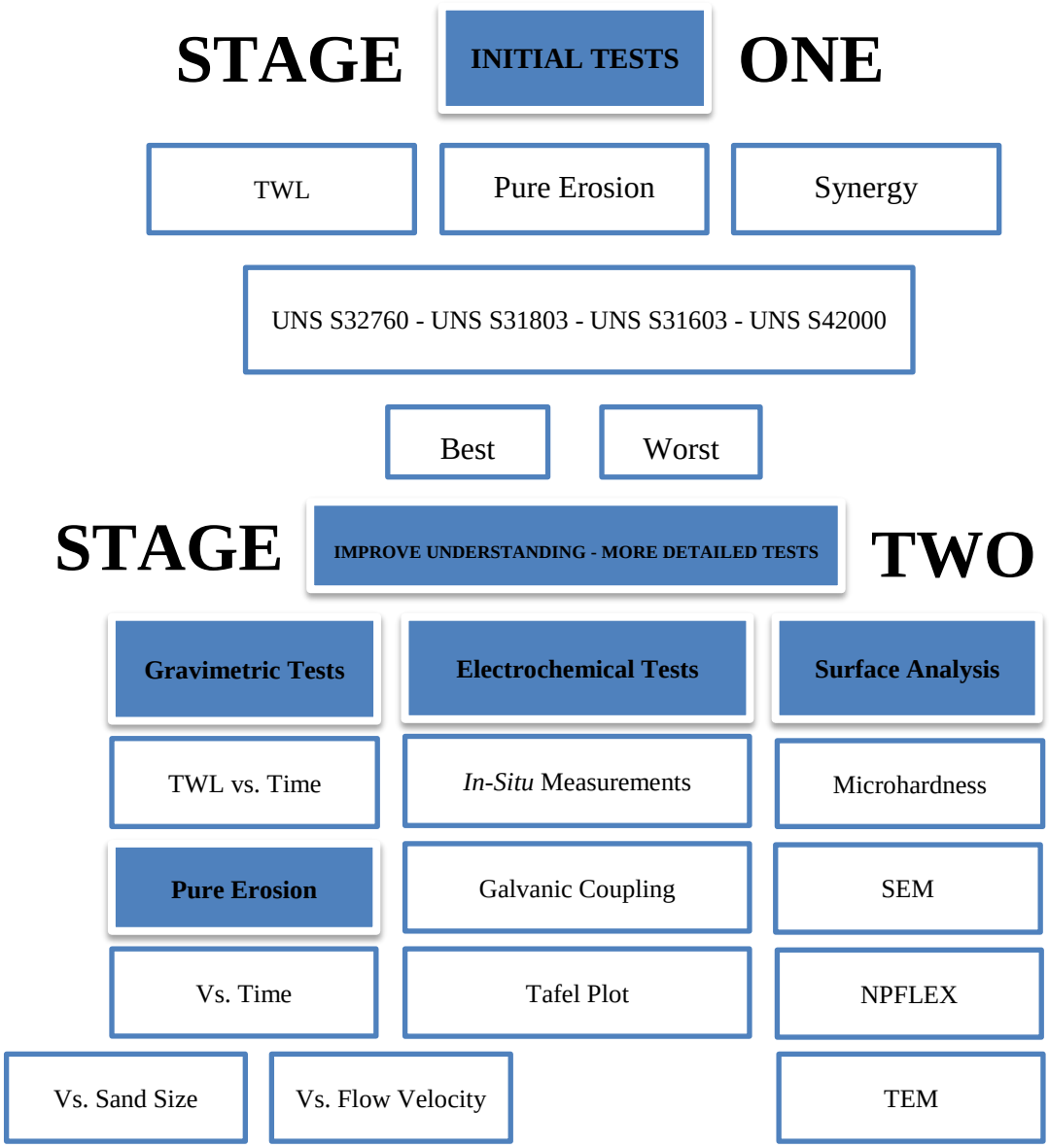

Figure 5-1: The general structure of the current chapter

5.2 Initial experimental tests

As stated earlier, the aim of the present tests is to choose materials that will show the best and the worst performance under the current erosion-corrosion condition.

As can be seen in Figure 5-2, the total weight loss and pure erosion of the studied materials were evaluated. Clearly, UNS S32760 showed a superior performance as expected due to its superior mechanical and corrosion resistance properties compared with the other materials and in particular UNS S31603 which showed the worst performance under both pure erosion and erosion-corrosion conditions.

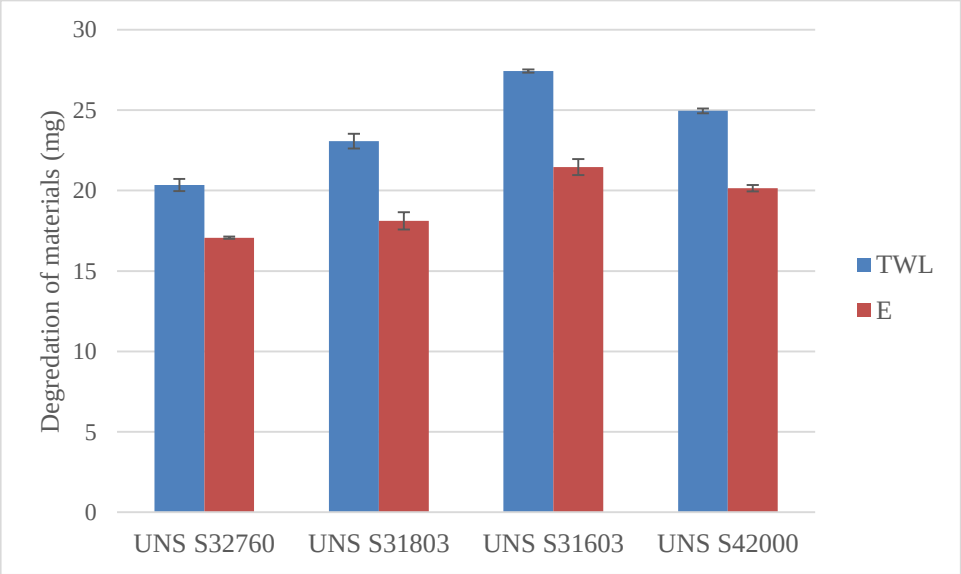

Figure 5-2: Total weight loss (CO_2-saturated) and pure erosion (N_2- Purged) of the studied materials at 20 m/s flow velocity, 1500 mg/l sand concentration and 50°C for 4 hours (error bars are spread of 3 data points)

The synergy of the studied materials was also evaluated and presented as can be shown in Figure 5-3. Although all of the studied materials showed slight differences in their erosion-enhanced corrosion except UNS S42000 which its dC_E was a bit higher than the others, the corrosion-enhanced erosion of the studied materials was dissimilar. Again, UNS S32760 showed a best corrosion-enhanced erosion resistance while UNS S31603 showed a limited one.

From the previously obtained results, UNS S32760 and UNS S31603 are chosen as candidate materials to be studied in detail as they represent the most and the least erosion-corrosion resistant materials.

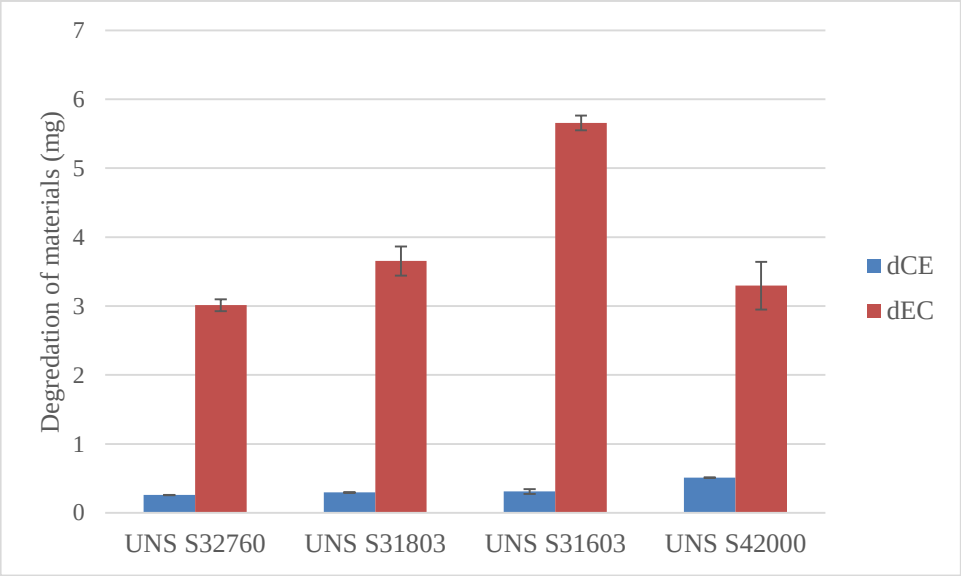

Figure 5-3: Erosion-enhanced corrosion (dC_E) and corrosion-enhanced erosion (dE_C) of the studied materials in a 10%NaCl (CO_2–Saturated) solution at 20 m/s flow velocity, 1500 mg/l sand concentration and 50°C for 4 hours (error bars are spread of 3 data points)

5.3 Gravimetric measurements

5.3.1 Total weight loss of UNS S32760 and UNS S31603 vs. time

Figure 5-4 and Figure 5-5 show the total weight loss of UNS S32760 and UNS S31603 as a function of time. The total weight loss of UNS S31603 was higher at all times compared with UNS S32760 which showed lower degradation rates. Generally, there was a slight difference in their total weight loss for the period of time between 5-30 minutes. At 60 minutes and afterwards, however, there was a distinct difference in their erosion-corrosion rates. For example, at 60 minutes the TWL values of UNS S32760 and UNS S31603 were about 4.2 mg and 5.4 mg respectively. At 240 minutes, the total weight loss raised dramatically to reach about 20 mg and 28 mg for UNS S32760 and UNS S31603, respectively.

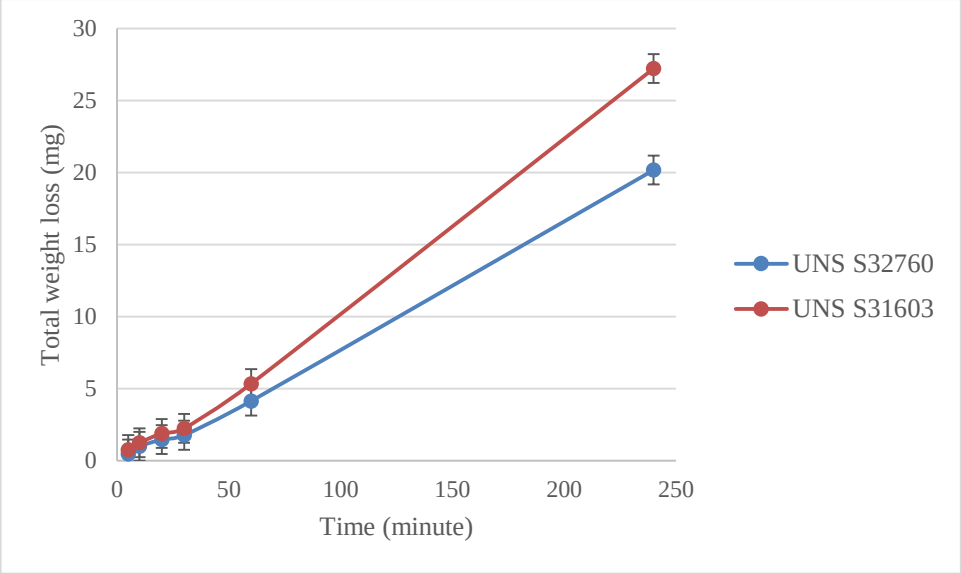

Figure 5-4: Total weight loss of UNS S32760 and UNS S31603 in a 10%NaCl (CO_2–saturated) solution as a function of time at 20 m/s flow velocity, 1500 mg/l sand concentration and at 50°C (error bars are spread of 3 data points)

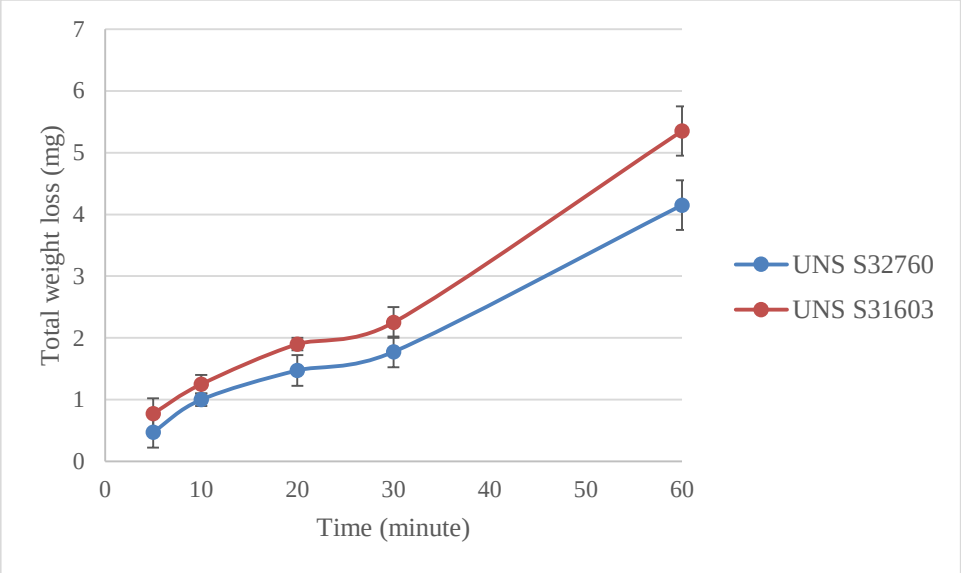

Figure 5-5: A higher magnification of Figure 5-4 for the period of time between (5-60) minute (error bars are spread of 3 data points)

5.3.2 Pure erosion of UNS S32760 and UNS S31603

5.3.2.1 Erosion rate as a function of time

The degradation rates due to pure erosion of both materials as a function of time can be shown in Figure 5-6. There was a very slight difference in the materials resistance for the period of time between 5-30 minutes. However, the difference was evident

from 60 minutes and continued to increase until 240 minutes where the erosion rates were at its highest value at about 17 mg and 23 mg for UNS S32760 and UNS S31603, respectively.

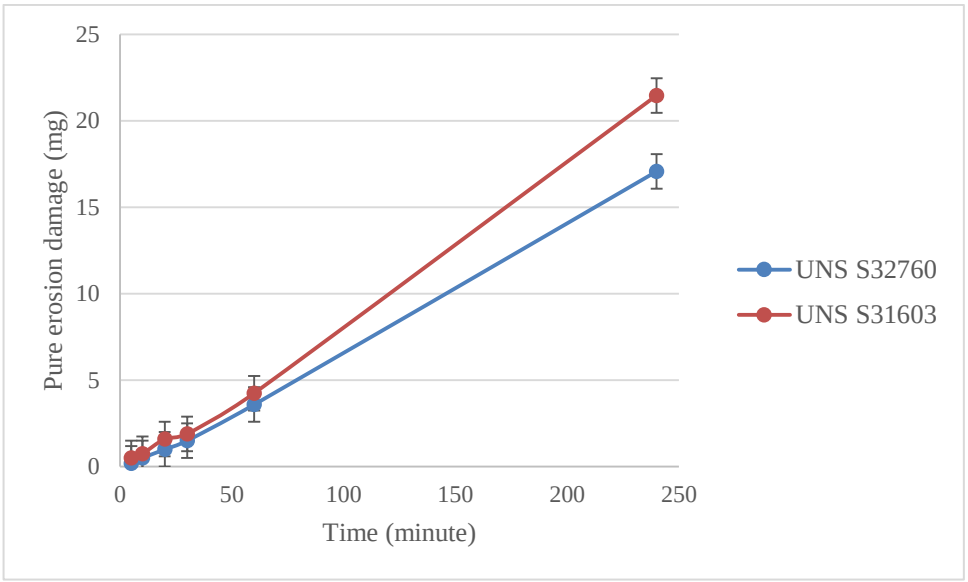

Figure 5-6: Pure erosion damage (N_2 Purged) of UNS S32760 and UNS S31603 at 20 m/s flow velocity, 1500 mg/l sand concentration and 50°C for 4 hours vs. time (error bars are spread of 3 data points)

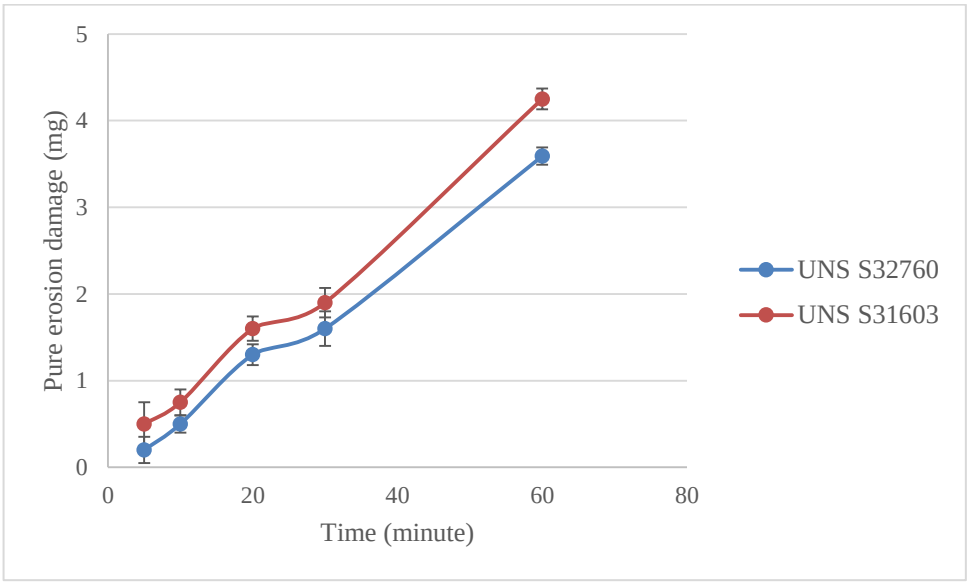

Figure 5-7: A higher magnification of Figure 5-6 for the period of time between (5-60) minute (error bars are spread of 3 data points)

5.3.2.2 Erosion rate as a function of flow velocity

The influence of flow velocity on the pure erosion of the studied materials was determined as can be shown in Figure 5-8. Clearly, as the flow velocity was increased,

pure erosion of both materials as expected increased. Pure erosion of both materials at 15 m/s was almost the same of about 1.85 mg. However, with increasing the flow velocity, the deterioration rates began to vary especially at 24 m/s as a distinct difference in pure erosion of both materials was noticed. Pure erosion of UNS S32760 at 20 m/s and 24 m/s was about 4.5 mg and 6.8 mg while it was around 6.2 mg and 9.9 mg for UNS S31603 respectively. This is believed to increasing the kinetic energy of the hitting particles with flow velocity increases as shown in Figure 5-9.

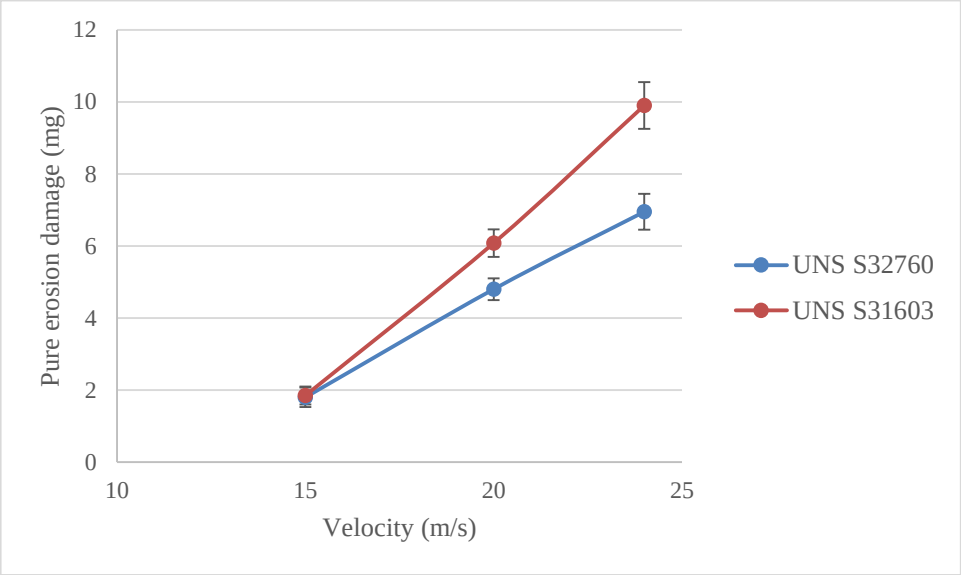

Figure 5-8: Pure erosion (N_2-Purged) of the studied materials as a function of the flow velocity at 500 mg/l sand concentration and 50°C for 4 hours (error bars are spread of 3 data points)

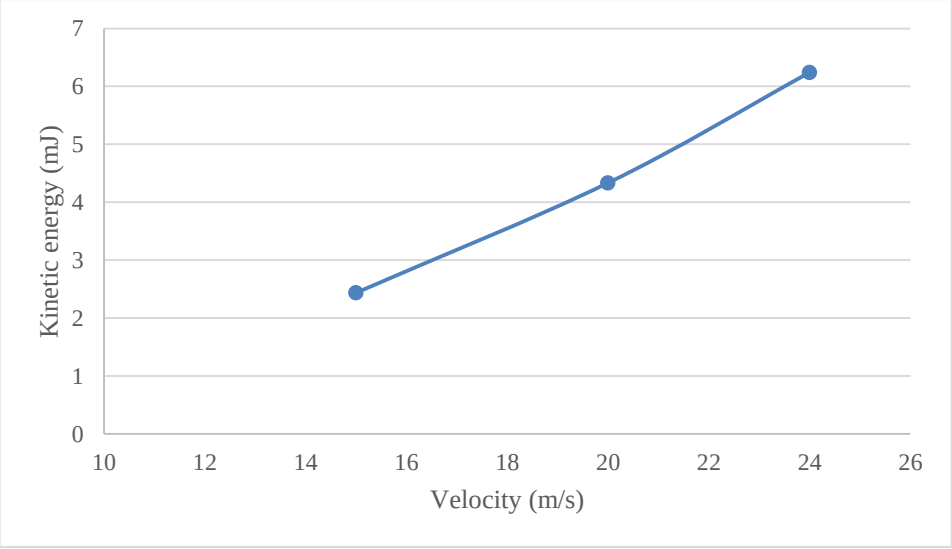

Figure 5-9: Kinetic energy vs. flow velocity

5.3.2.3 Erosion rate as a function of particle size

Figure 5-10 depicts pure erosion of the studied materials as a function of sand particle size. Pure erosion of both materials increased as sand size was increased. At all particle sizes, pure erosion of UNS S32760 was lower than the one of UNS S31603. For example, pure erosion of UNS S32760 at 100 µm and 250 µm was roughly 7.5 mg and 17.4 mg respectively whereas it was about 9.9 mg and 21 mg in the case of UNS S31603.

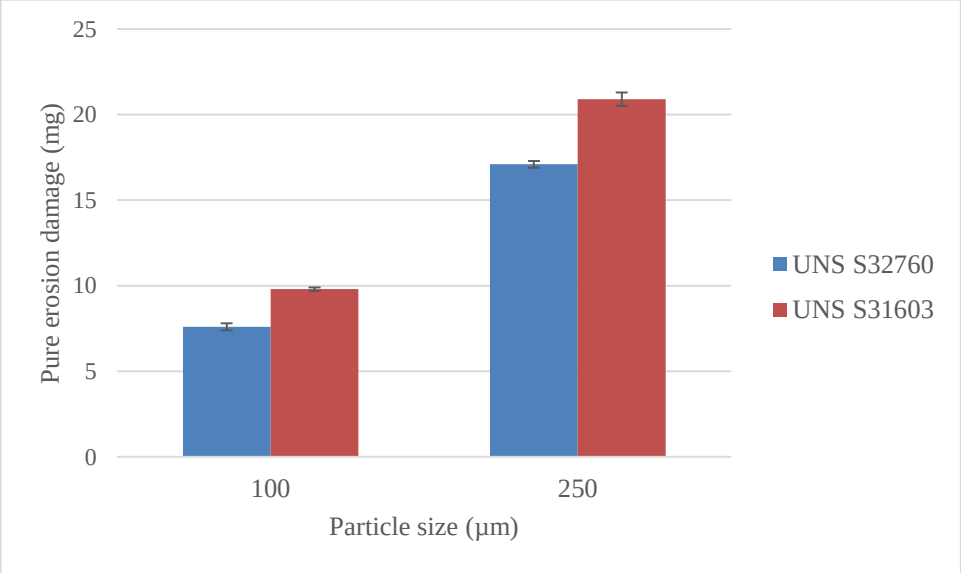

Figure 5-10: Pure erosion (N_2-Purged) of the studied materials as a function of particle size at 20 m/s flow velocity, 1500 mg/l sand concentration and 50°C for 4 hours (error bars are spread of 3 data points)

5.4 The electrochemical measurements

5.4.1 The corrosion current density of UNS S32760 and UNS S31603 as a function of time

The corrosion current density of UNS S32760 and UNS S31603 with time is shown in Figure 5-11. From the figure, it is evident that the corrosion current density of UNS S31603 was slightly higher than that of UNS S32760 for the period of time between 5-60 minutes. Also, both materials showed a gradual increase in the early stages

followed by a considerable decrease until the corrosion current density of both materials was equal at 240 minutes. Figure 5-12 shows the obtained polarisation resistance of the studied materials along the test duration and confirms their corrosion resistance improvement with time progression.

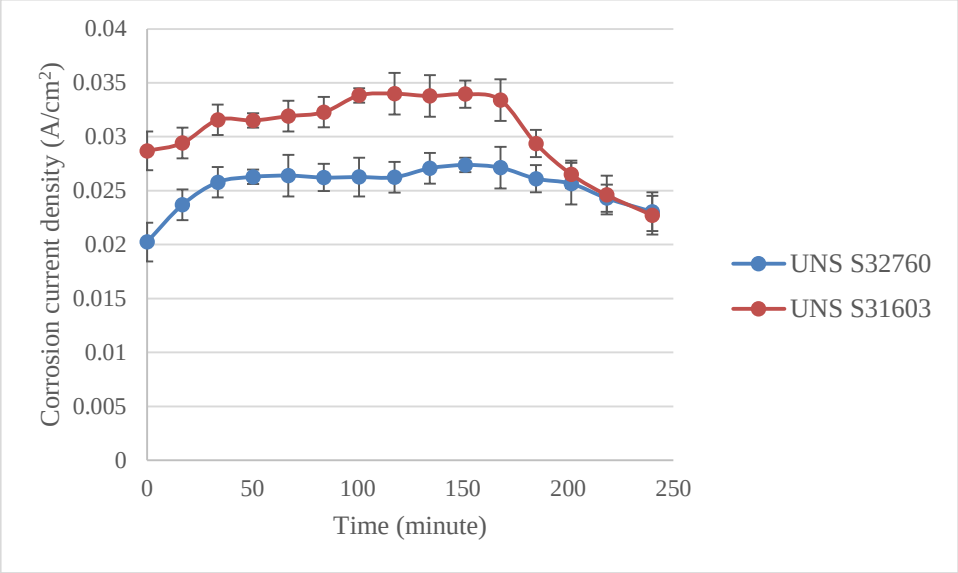

Figure 5-11: The corrosion current density of UNS S32760 and UNS S31603 in a (CO_2 – saturated) solution at 20 m/s flow velocity, 1500 mg/l sand concentration and at 50ºC as a function of time (error bars are spread of 3 data points)

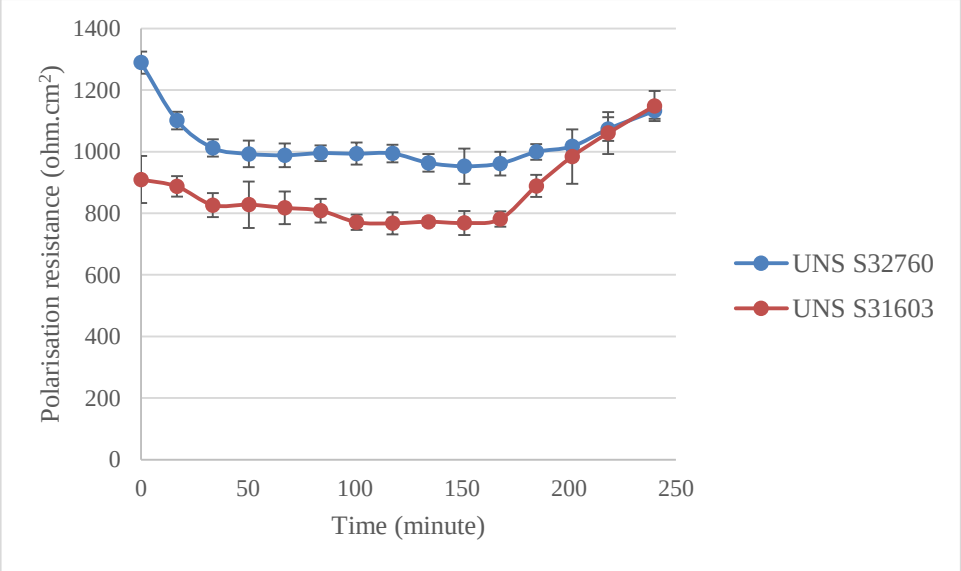

Figure 5-12: The polarisation resistance of UNS S32760 and UNS S31603 in a (CO_2 – saturated) solution at 20 m/s flow velocity, 1500 mg/l sand concentration and at 50ºC as a function of time (error bars are spread of 3 data points)

5.4.2 Electrochemical measurements of the deformed region

5.4.2.1 The corrosion current density evaluation

The corrosion current density of the non-deformed and deformed regions of both materials was evaluated by Tafel plot technique as can be shown in Figure 5-13 to Figure 5-18. A summary of the obtained corrosion rates of the deformed (at different times) and non-deformed regions can be seen in Figure 5-19. From Figure 5-19, it can be seen that there was a significant difference in the corrosion resistance between the non-deformed and deformed regions. Also, the corrosion current density of the deformed regions for both materials increased as the test duration time was increased. Furthermore, the corrosion resistance of UNS S32760 was higher than for UNS S31603 at all times.

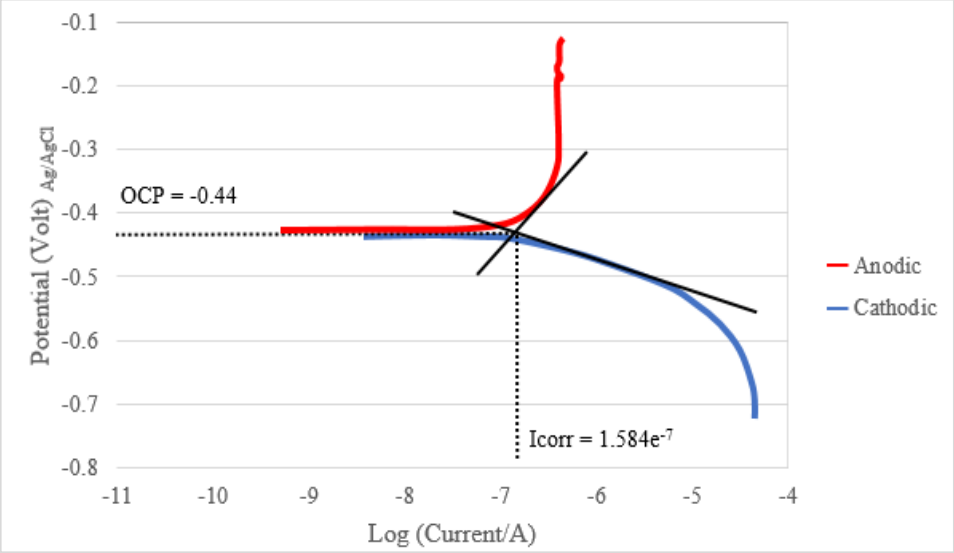

Figure 5-13: Tafel plot of UNS S32760 in a static 10%NaCl (CO_2 – saturated) solution

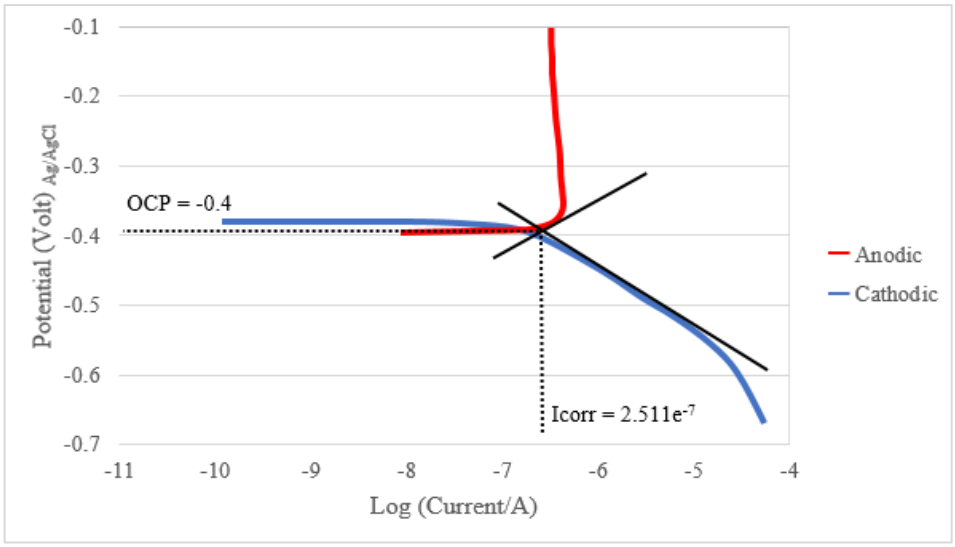

Figure 5-14: Tafel plot of UNS S31603 in a static 10%NaCl (CO_2 – saturated) solution

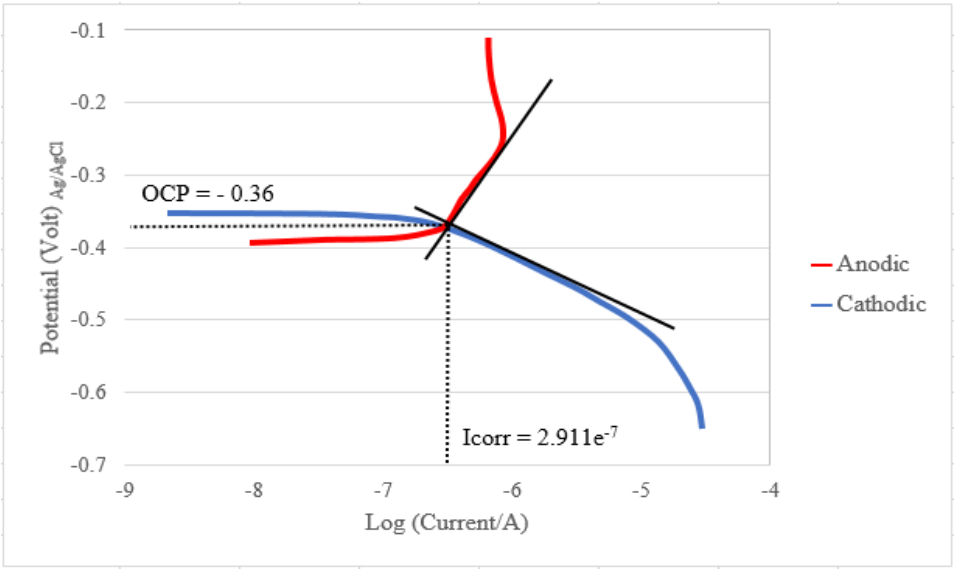

Figure 5-15: Tafel plot of the deformed region of UNS S32760 in a static 10%NaCl (CO_2 – saturated) solution after erosion-corrosion at 20 m/s flow velocity and 1500 mg/l sand concentration for 60 minutes

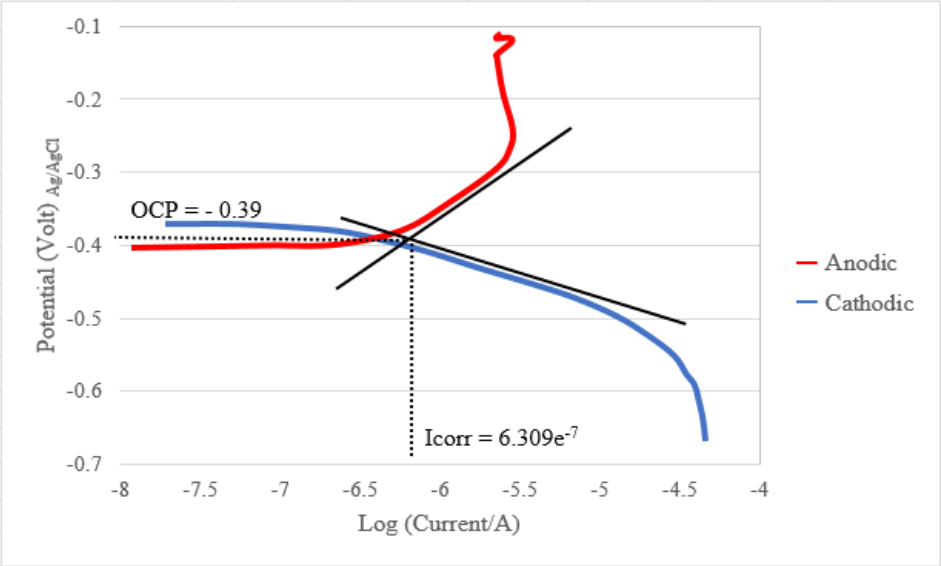

Figure 5-16: Tafel plot of the deformed region of UNS S31603 in a static 10%NaCl (CO_2 – saturated) solution after erosion-corrosion at 20 m/s flow velocity and 1500 mg/l sand concentration for 60 minutes

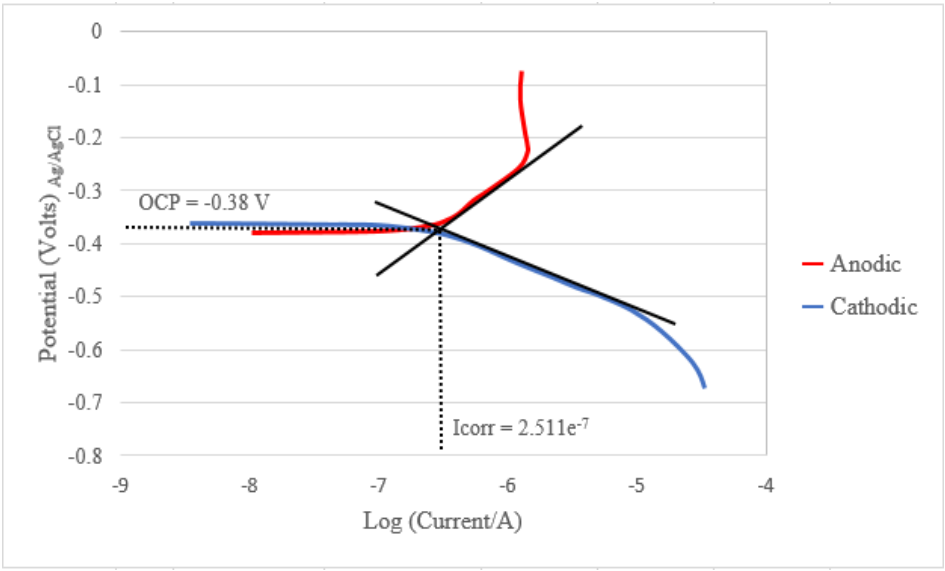

Figure 5-17: Tafel plot of the deformed region of UNS S32760 in a static 10%NaCl (CO_2 – saturated) solution after erosion-corrosion at 20 m/s flow velocity and 1500 mg/l sand concentration for 240 minutes

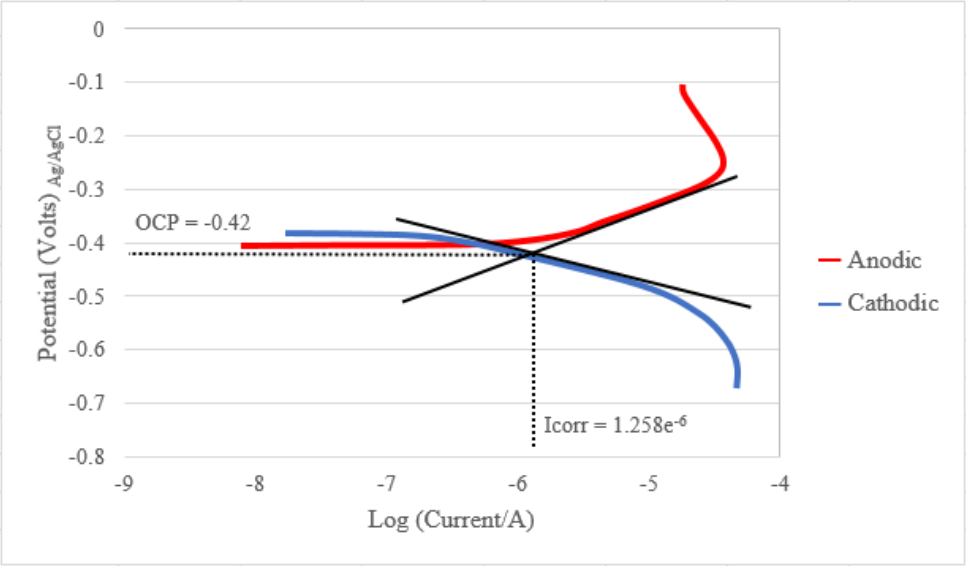

Figure 5-18: Tafel plot of the deformed region of UNS S31603 in a static 10%NaCl (CO_2 – saturated) solution after erosion-corrosion at 20 m/s flow velocity and 1500 mg/l sand concentration for 240 minutes

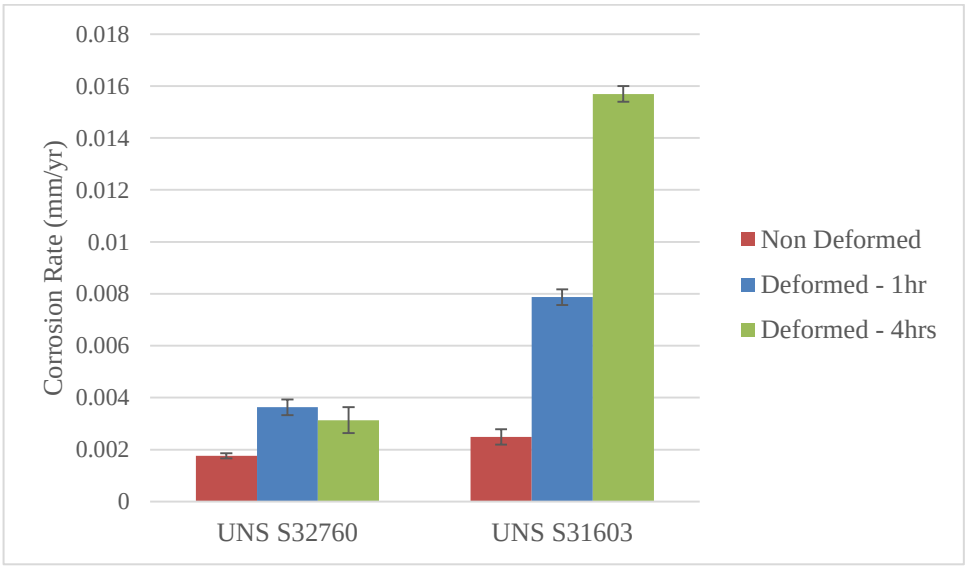

Figure 5-19: The obtained corrosion rates of the non-deformed and the deformed regions of both materials in a static 10%NaCl (CO_2 – saturated) solution (error bars are spread of 3 data points)

5.4.2.2 Galvanic coupling

Figure 5-20 shows the galvanic currents between the deformed and non-deformed regions for both UNS S32760 and UNS S31603 in a static 10%NaCl (CO_2-saturated) solution.

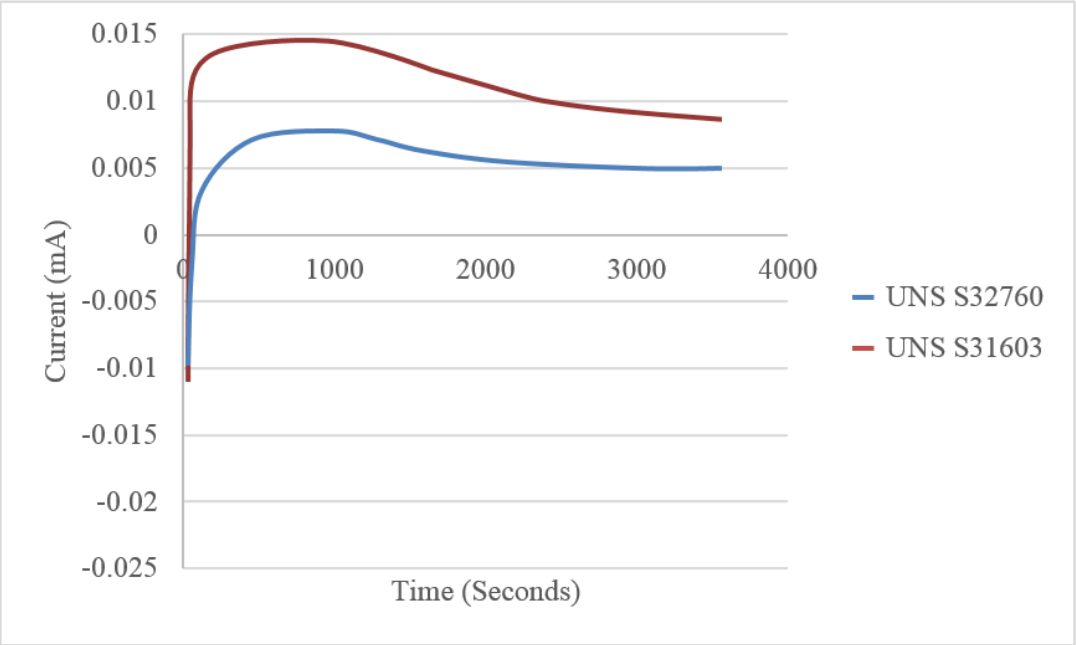

Figure 5-20: The evolved galvanic current between the deformed and non-deformed regions of both materials in a static 10%NaCl (CO_2-saturated) solution

It is evident from the figure that the galvanic current for UNS S31603 was higher than the one for UNS S32760. The current in the case of UNS S31603 reached around 0.015 mA while it was just around 0.005 mA in the case of UNS S32760. Also, the galvanic current of UNS S31603 reduced to about 0.008 mA after 1 hour to be close to the one of UNS S32760.

5.5 Erosion and corrosion synergy as a function of time

Erosion-enhanced corrosion of UNS S32760 and UNS S31603 in a 10%NaCl (CO_2 – saturated) solution can be seen in Figure 5-21. Erosion-enhanced corrosion of UNS S31603 and UNS S32760 was almost the same at all times except after 60 minutes as the one for UNS S31603 showed an increase in its value to be about 0.38 mg compared with 0.22 mg for UNS S32760. At 240 minutes, however, erosion-enhanced corrosion of UNS S31603 reduced to be equal to that for UNS S32760.

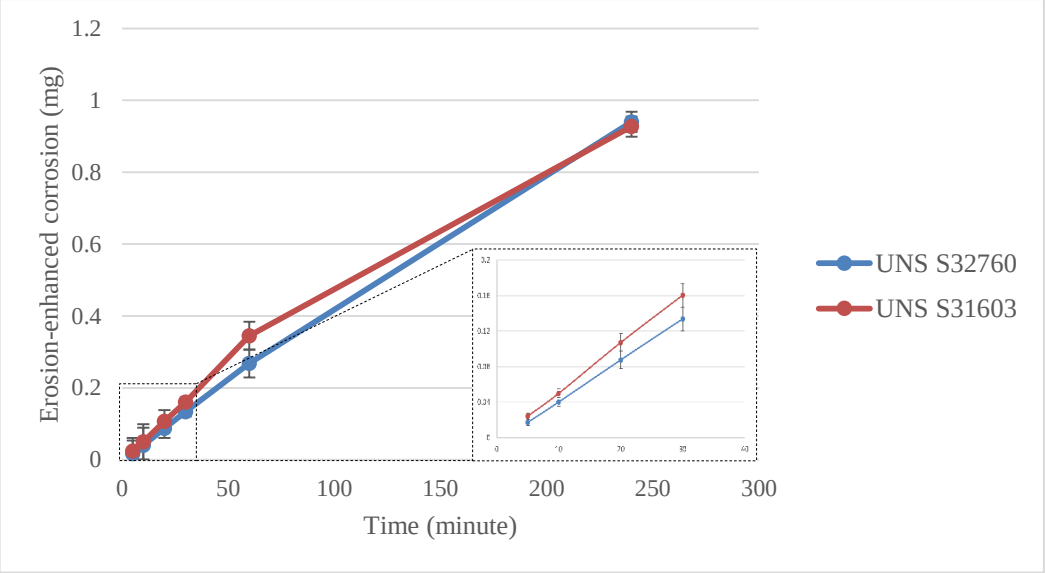

Figure 5-21: Erosion-enhanced corrosion of UNS S32760 and UNS S31603 in a 10%NaCl (CO_2 – saturated) solution at 20 m/s flow velocity, 1500 mg/l sand concentration and at 50°C as a function of time (error bars are spread of 3 data points)

On the other hand, corrosion-enhanced erosion of both materials showed different trends in their behaviour. As can be seen from Figure 5-22, there was no difference in corrosion-enhanced erosion of UNS S31603 and UNS S32760 for period of time between 5-30 minutes. However, a significant difference in the corrosion-enhanced erosion of both materials was noticed at 60 minutes and afterwards. UNS S31603 showed a higher corrosion-enhanced erosion degradation at 60 minutes of about 0.8 mg compared with the one of UNS S32760 which was about 0.3 mg. The difference between corrosion-enhanced erosion of both materials began to increase sharply with time in particular at 240 minutes as corrosion-enhanced erosion of UNS S31603 was about 5.8 mg whereas it was around 3 mg in the case of UNS S32760.

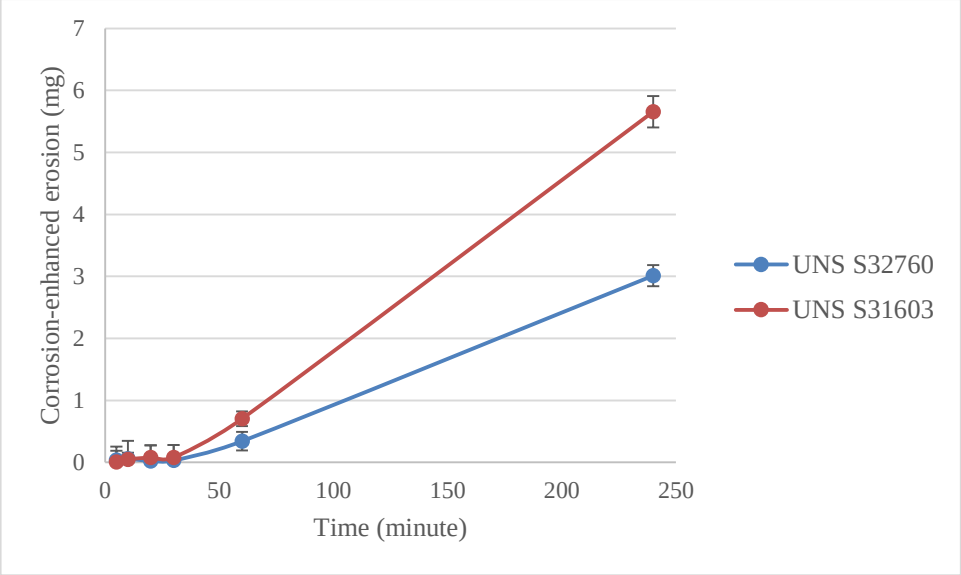

Figure 5-22: Corrosion-enhanced erosion of the studied materials as a function of time (error bars are spread of 3 data points)

5.6 Characterization of the damaged surfaces of UNS S32760 and UNS S31603

5.6.1 Microhardness

5.6.1.1 Hardness as a function of erosion time

Microhardness of the damaged surface of the studied materials as a function of erosion time was evaluated as shown in Figure 5-23 and Figure 5-24. It can be seen from the figures that as the time was increased, the hardness of the deformed region of both materials increased. Also, although the hardness of UNS S32760 was higher than that of UNS S31603 for the period of time between 5-30 minutes, the final hardness in both materials was almost the same at 60 and 240 minutes with an average value of about 450 and 465 HV respectively.

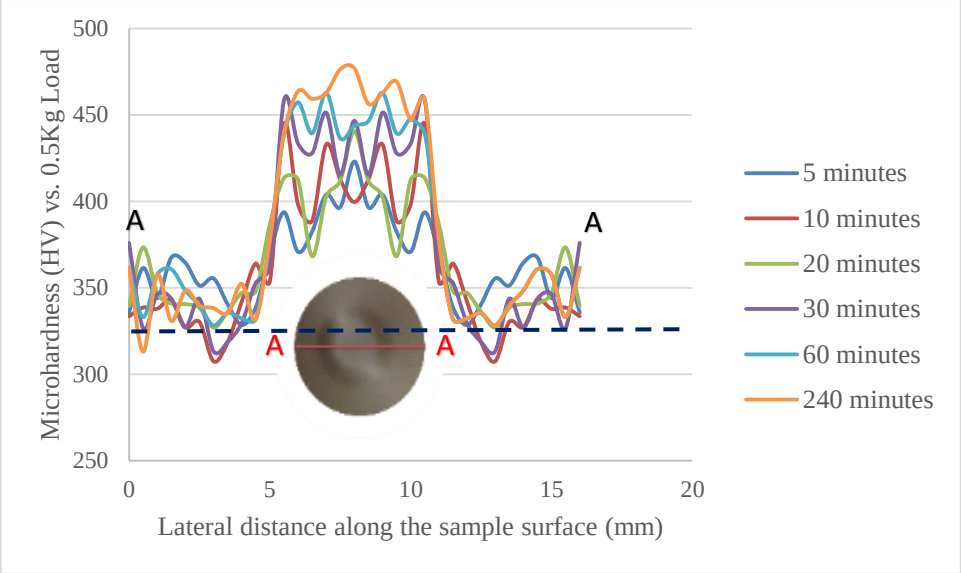

Figure 5-23: Microhardness along the eroded surface (A-A) of UNS S32760 at 20 m/s flow velocity, 1500 mg/l sand concentration and 50°C for 4 hours versus time (dotted line represents the pre-erosion hardness)

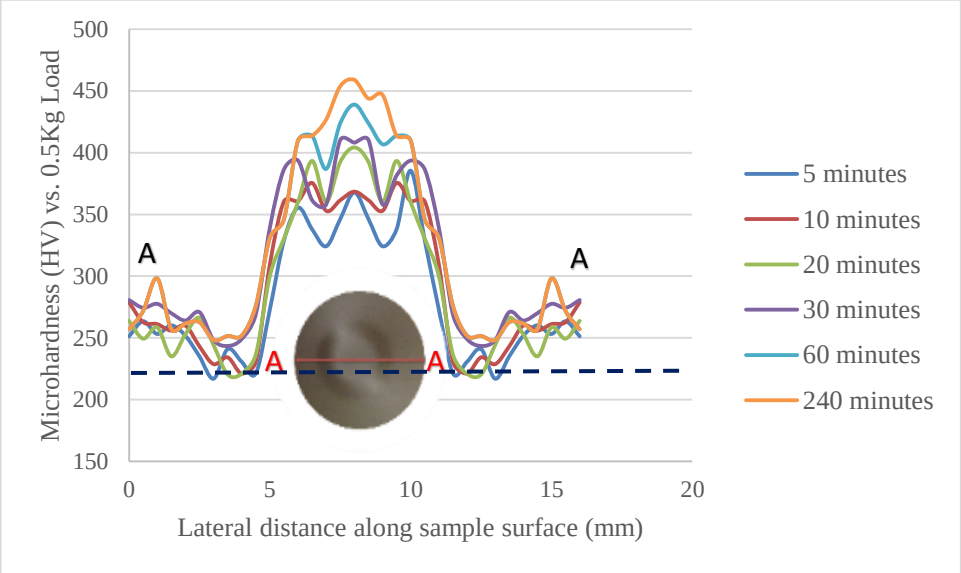

Figure 5-24: Microhardness along the eroded surface (A-A) of UNS S31603 at 20 m/s flow velocity, 1500 mg/l sand concentration and 50°C for 4 hours versus time (dotted line represents the pre-erosion hardness)

5.6.1.2 Hardness as a function of flow velocity

Figure 5-25 describes the obtained microhardness of UNS S32760 as a function of flow velocity. It is illustrated by the figure that the hardness of the material increased as the flow velocity was increased, as expected. For example, at 15 m/s, the hardness

was about 390 HV and increased to reach about 420 HV and 450 HV when the flow velocity was increased from 20 m/s to 24 m/s, respectively.

Similarly, UNS S31603 showed an increase in the hardness as the flow velocity was increased. For example, the hardness of the studied material at 15 m/s was around 360 HV while it was about 410 and 460 HV at 20 and 24 m/s respectively. This can be seen in Figure 5-26.

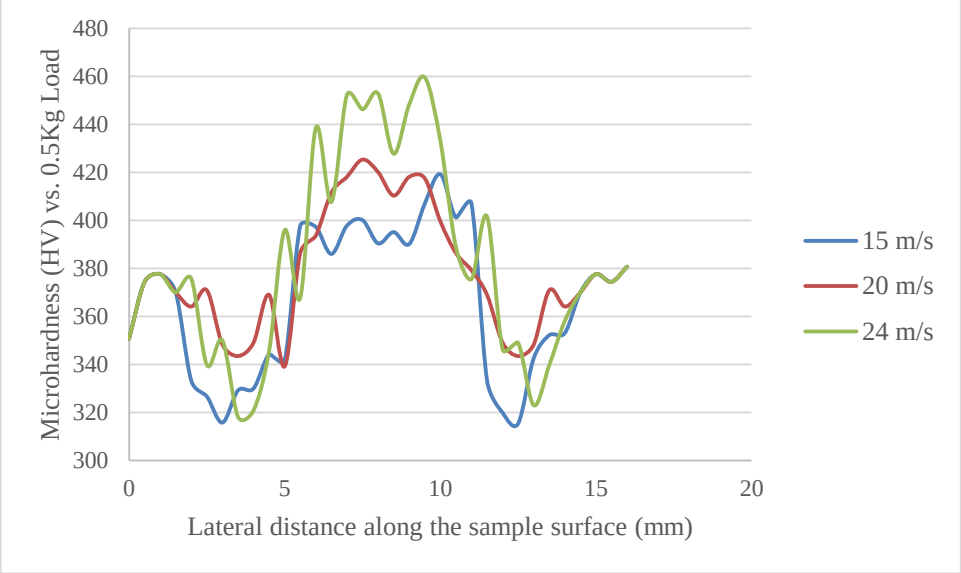

Figure 5-25: Microhardness of the eroded surface of UNS S32760 at 500 mg/l sand concentration and 50ºC for 4 hours versus flow velocity

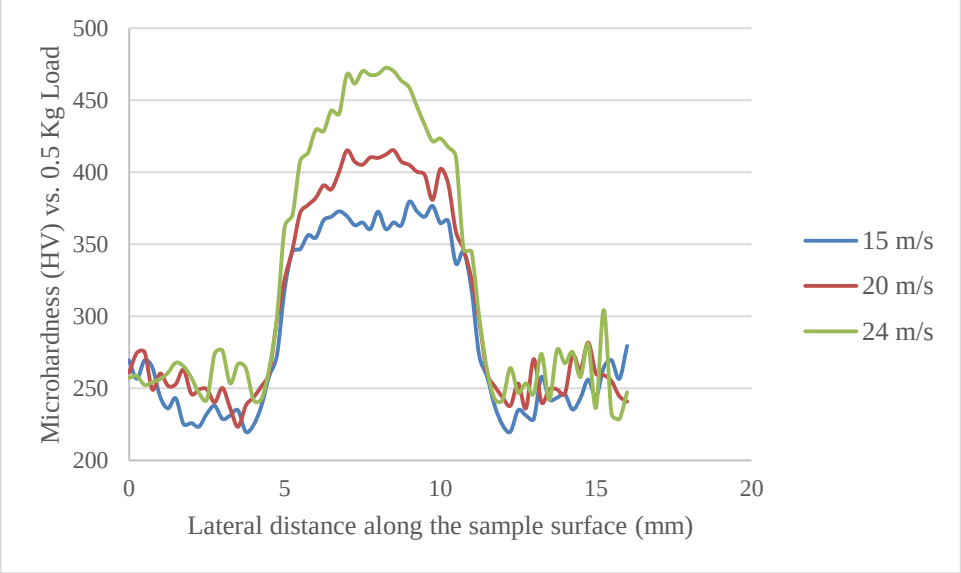

Figure 5-26: Microhardness of the eroded surface of UNS S31603 at 500 mg/l sand concentration and 50ºC for 4 hours versus flow velocity

5.6.1.3 Hardness as a function of particle size

It was found that sand size has a significant influence on the hardness of the studied materials as shown in Figure 5-27 and Figure 5-28. As can be seen from Figure 5-27, the hardness of the damaged surface of UNS S32760 increased from around 435 HV at 100 µm sand size to about 465 HV at 250 µm. Similarly, the hardness of the UNS S31603 damaged surface increased from around 350 HV to 470 HV when the sand size was increased from 100 µm to 250 µm respectively as shown in Figure 5-28.

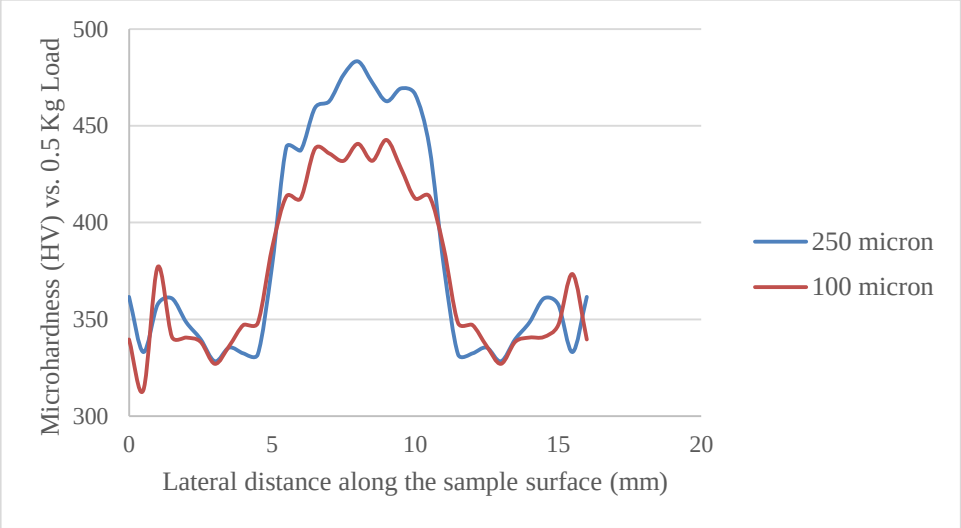

Figure 5-27: Microhardness of the eroded surface of UNS S32760 at 20 m/s flow velocity, 1500 mg/l sand concentration and 50°C for 4 hours versus sand size

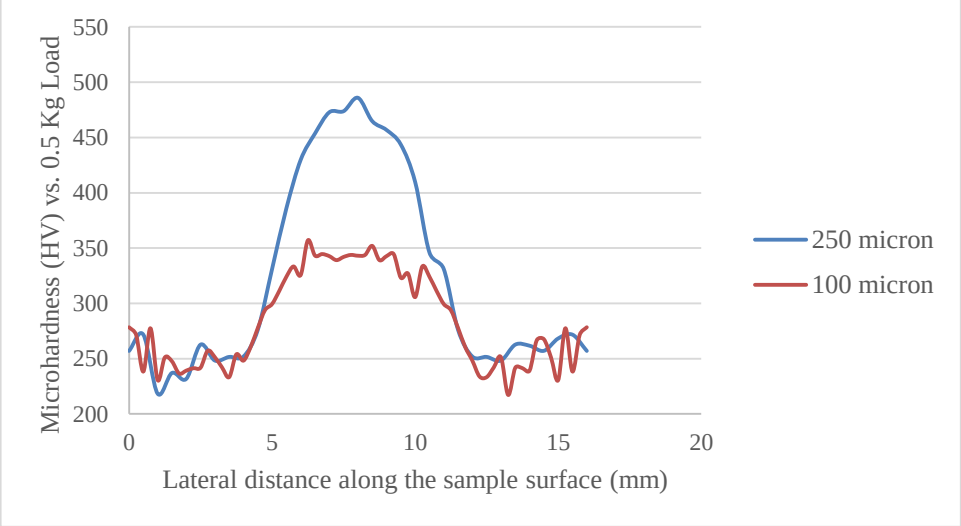

Figure 5-28: Microhardness of the eroded surface of UNS S31603 at 20 m/s flow velocity, 1500 mg/l sand concentration and 50°C for 4 hours versus sand size

5.6.2 Scanning electron microscopy as a function of time

The SEM images of the damaged surfaces of UNS S32760 and UNS S31603 as a function of erosion time are shown in Figure 5-29 and Figure 5-30, respectively. Clearly, as the time progressed, there was no significant change on the material surface of UNS S32760. In terms of UNS S31603, however, sand embedment was the main noticed feature as shown in Figure 5-31.

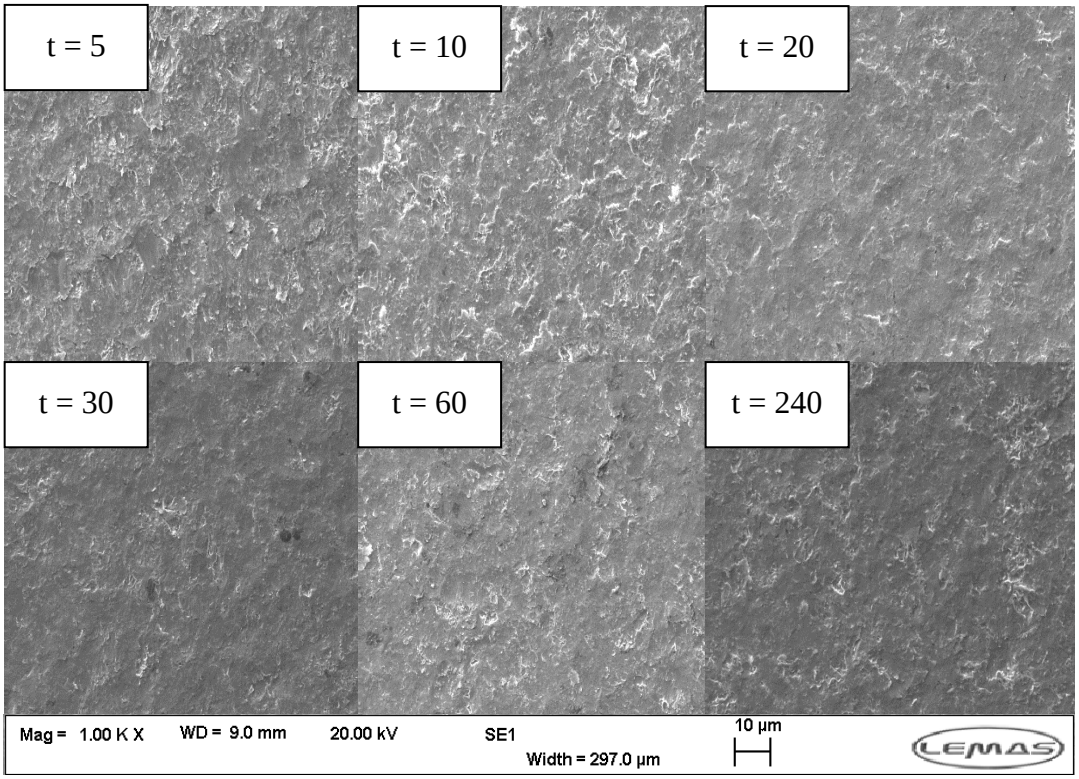

Figure 5-29: SEM images of UNS S32760 after erosion as a function of time (minutes)

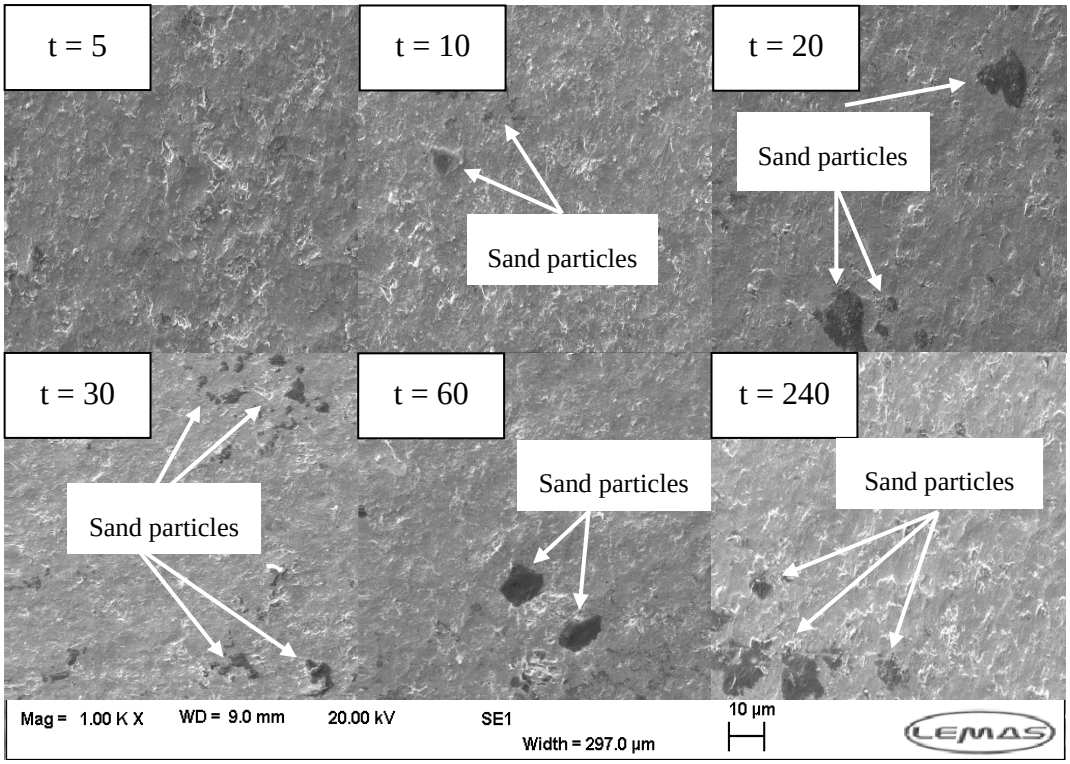

Figure 5-30: SEM images of UNS S31603 after erosion as a function of time (minutes)

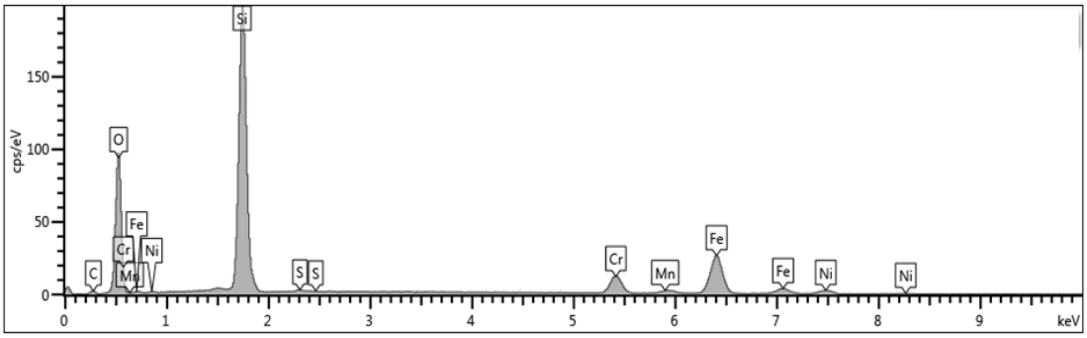

Figure 5-31: EDX of the embedded sand on UNS S31603 surface

5.6.3 Surface profilometry as a function of time

The penetration depth of the materials surfaces after different times of erosion was evaluated as can be seen in Figure 5-32 and Figure 5-33. Figure 5-34 summarizes the obtained penetration depth of the studied materials. As can be seen from this figure, the penetration depth of both materials was almost the same for period of time between 5-30 minutes. However, at 60 minutes, UNS S31603 showed a higher penetration depth of about 25.9 µm than the one of UNS S32760 which was about

16.47 µm. This depth aggravates at 240 minutes to reach about 64.42 µm in the case of UNS S31603 whereas it was around 53.09 µm in the case of UNS S32760.

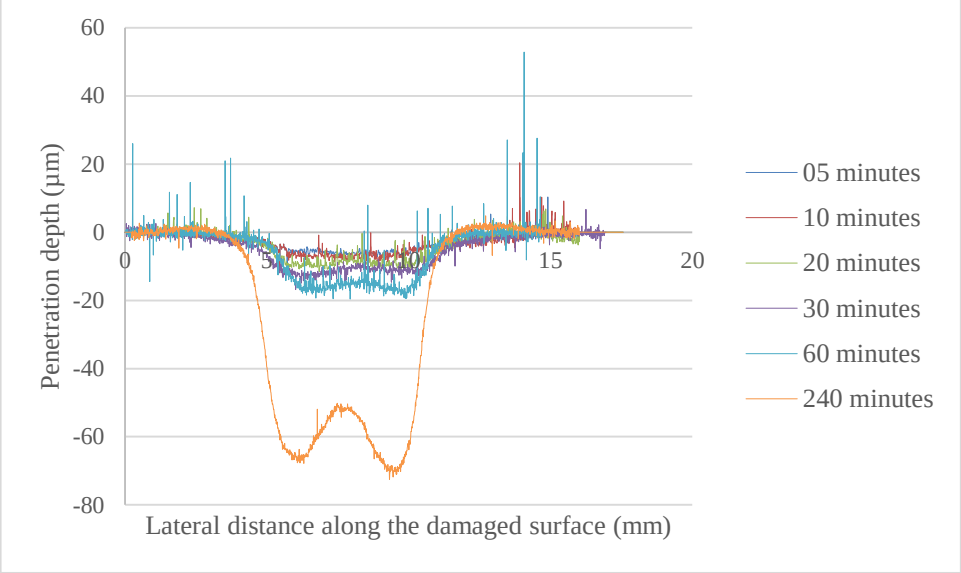

Figure 5-32: The penetration depth of the damaged surface of UNS S32760 after pure erosion (N_2 Purged) for 4 hours at 20 m/s flow velocity and 1500 mg/l sand concentration

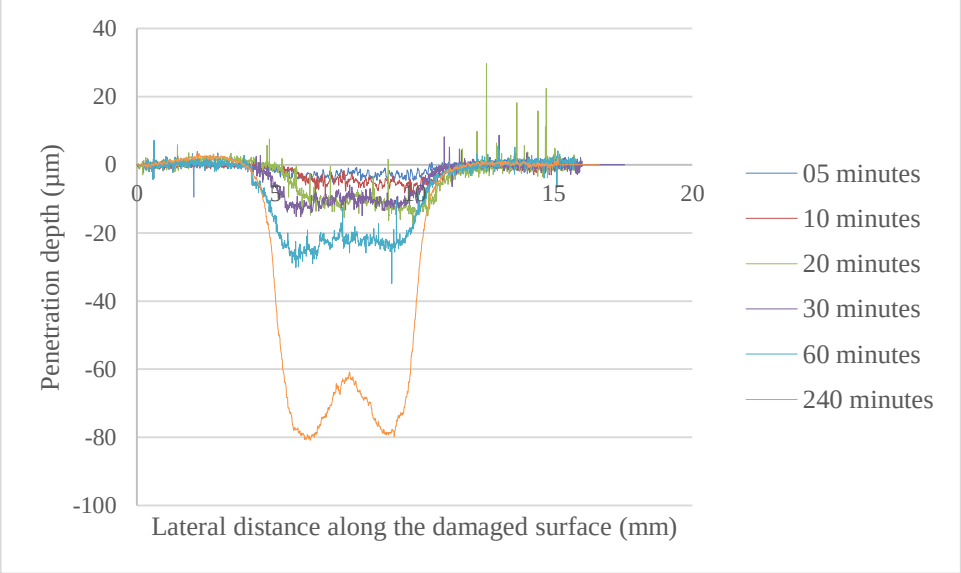

Figure 5-33: The penetration depth of the damaged surface of UNS S31603 after pure erosion (N_2-Purged) for 4 hours at 20 m/s flow velocity and 1500 mg/l sand concentration

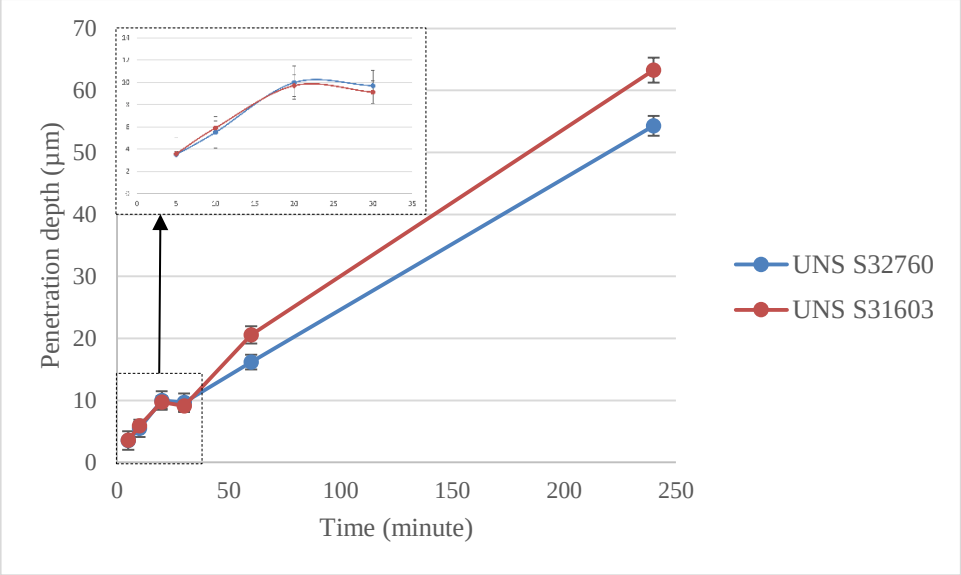

Figure 5-34: Comparison of the penetration depth of the studied materials as a function of time after erosion at 20 m/s flow velocity, 1500 mg/l sand concentration and 50°C (error bars are spread of 3 data points)

5.6.4 TEM as a function of time

5.6.4.1 As received (test time = 0 minute)

TEM images of the as-received samples (before implementing the erosion tests) of UNS S32760 and UNS S31803 was characterized as can be seen in Figure 5-35 and Figure 5-36 respectively. It can be noticed from the obtained images presence of a very thin deformed layer in the sub surface of both materials. It is thought this is because of the polishing process which preceded each test.

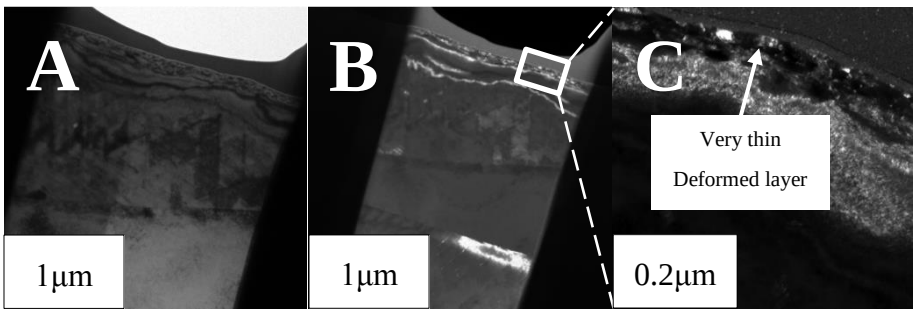

Figure 5-35: Bright field **(A)** and dark field **(B)** and **(C)** TEM images of as-received UNS S32760

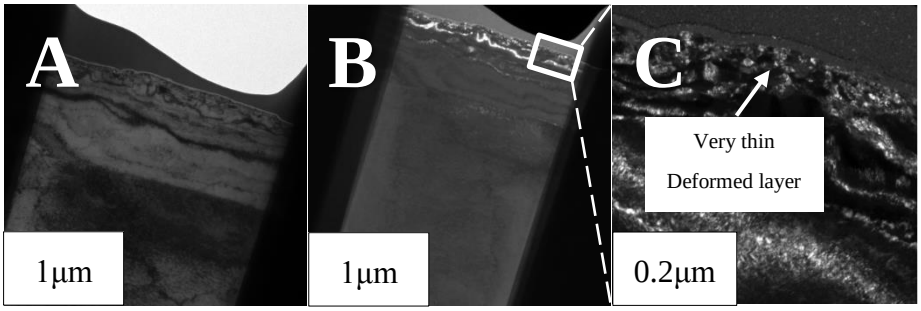

Figure 5-36: Bright field **(A)** and dark field **(B)** and **(C)** TEM images of as-received UNS S31603

5.6.4.2 After Erosion (Test time = 10, 60 and 240 minutes)

The subsurface layer of the studied materials after erosion was characterized by Transmission Electron Microscopy (TEM) as can be seen in Figure 5-37 to Figure 5-42. Clearly, the deformed sub-layer thickness of both materials increased as time progresses. Also, there was a significant reduction in the grain size of both materials under erosion condition especially near the top surface as the grain size can reach to (15-20) nm (i.e. nanocrystalline layer). This was confirmed qualitatively in Figure 5-43 and Figure 5-44 for UNS S32760 and UNS S31603, respectively and quantitatively in Figure 5-45. It can be seen from Figure 5-45 that there is no significant difference in the reduction of grain size for both UNS S3260 and UNS S31603. The average grain size for both materials was obtained using Gatan Digital Micrograph Software (Version.3.01). Moreover, the deformed sub-layer of UNS S31603 witnessed presence of cracks either within the sub deformed layer itself (Figure 5-46 and Figure 5-47) or around the sand particles themselves (Figure 5-48). Sand particle was also present at 60 minutes and afterwards (confirmed by EDX as shown in Figure 5-49). However, there were no cracks presented within the deformed sub-layer and even around the embedded sand particle on UNS S32760 as can be shown in Figure 5-50 and Figure 5-51. Presence of sand particle was confirmed in Figure 5-52.

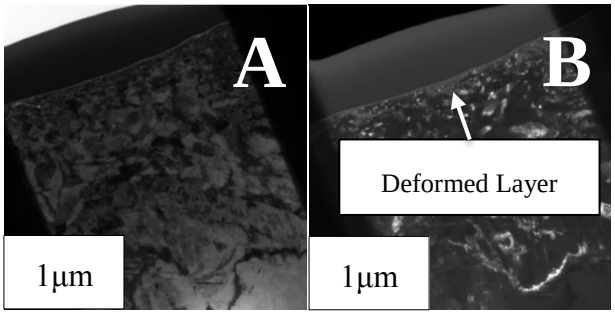

Figure 5-37: Bright field **(A)** and dark field **(B)** TEM images of UNS S32760 after erosion for 10 minutes

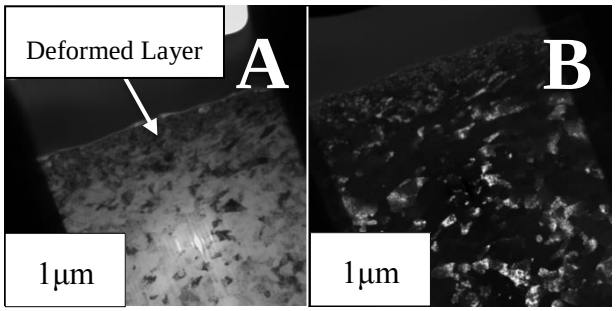

Figure 5-38: Bright field **(A)** and dark field **(B)** TEM images of UNS S31603 after erosion for 10 minutes

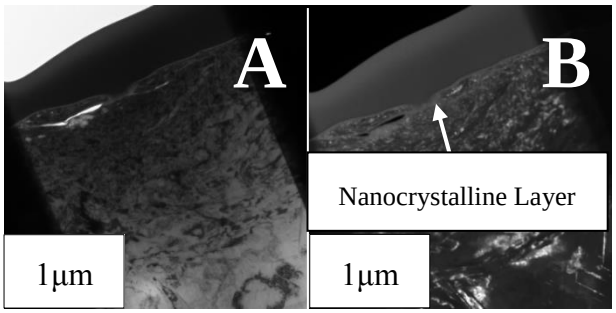

Figure 5-39: Bright field **(A)** and dark field **(B)** TEM images of UNS S32760 after erosion for 60 minutes

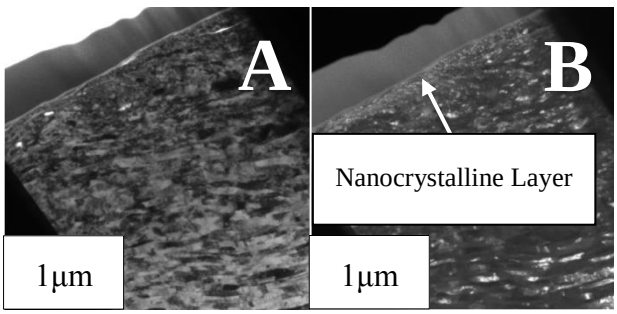

Figure 5-40: Bright field **(A)** and dark field **(B)** TEM images of UNS S31603 after erosion for 60 minutes

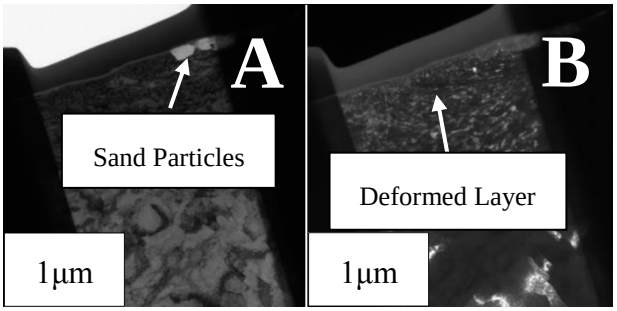

Figure 5-41: Bright field **(A)** and dark field **(B)** TEM images of UNS S32760 after erosion for 240 minutes

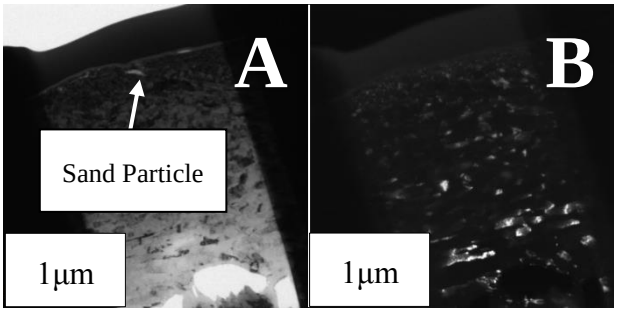

Figure 5-42: Bright field **(A)** and dark field **(B)** TEM images of UNS S31603 after erosion for 240 minutes

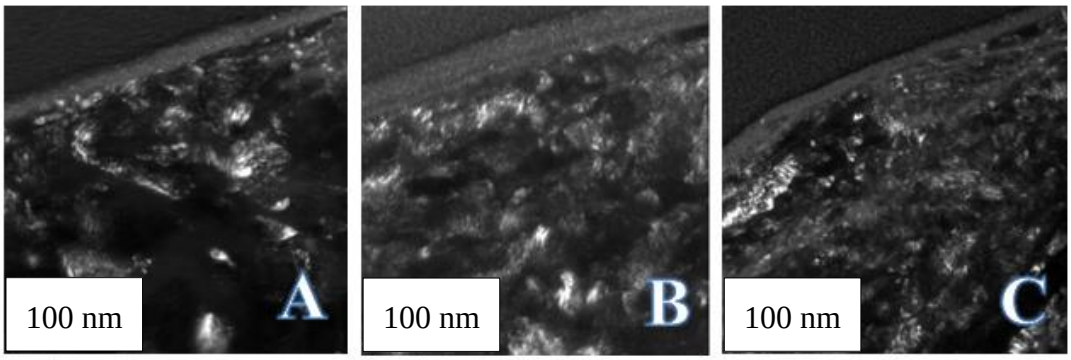

Figure 5-43: TEM images of UNS S32760 after erosion for **(A)** 10 minutes **(B)** 60 minutes and **(C)** 240 minutes showing the reduction in the grain size

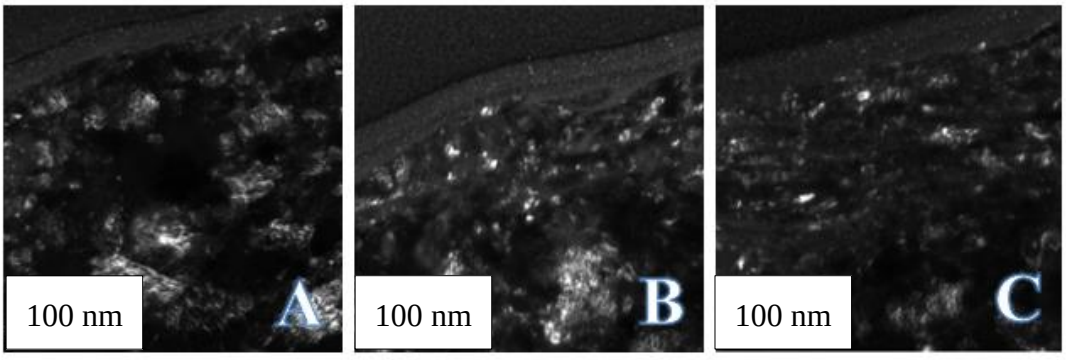

Figure 5-44: TEM images of UNS S31603 after erosion for **(A)** 10 minutes (**B)** 60 minutes and **(C)** 240 minutes showing the reduction in the grain size

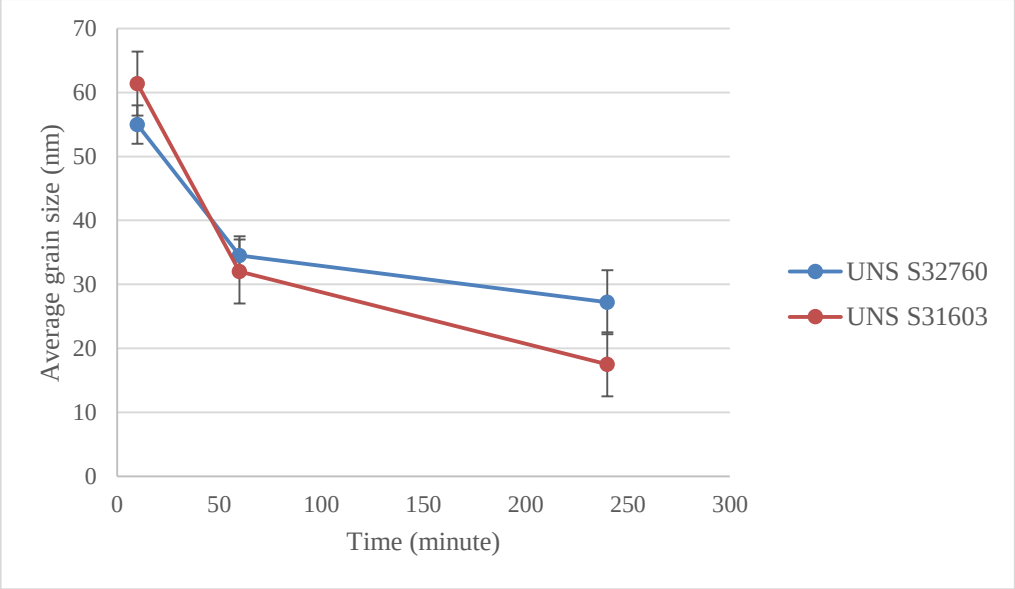

Figure 5-45: Average grain size of the deformed sub-layer of UNS S32760 and UNS S31603 as a function of erosion time (error bars are spread of 3 data points)

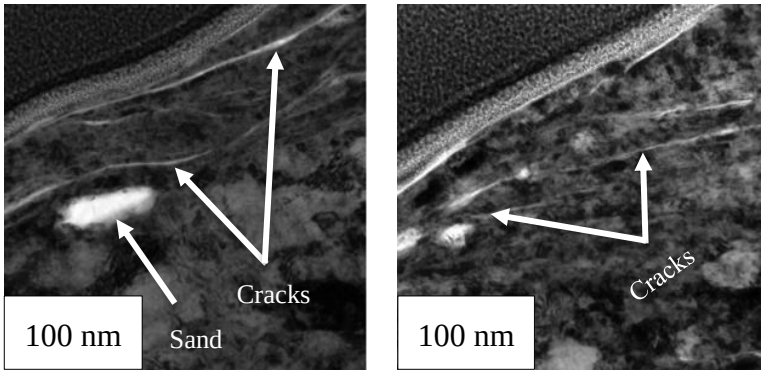

Figure 5-46: A network of cracks within the deformed sub-layer of UNS S31603 after erosion for 60 minutes

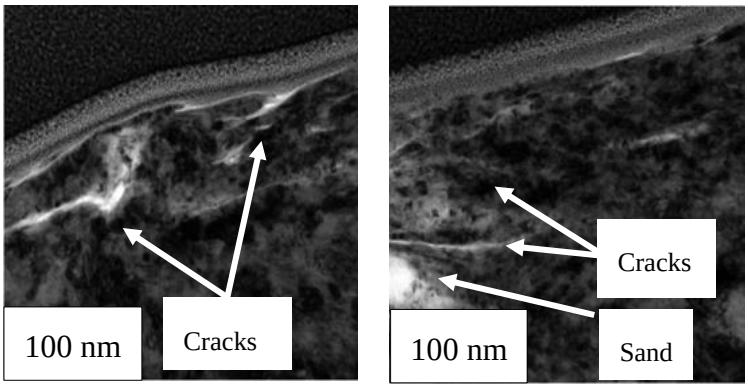

Figure 5-47: Showing the presence of sand and cracks within the deformed sub-layer of UNS S31603 after erosion for 240 minutes

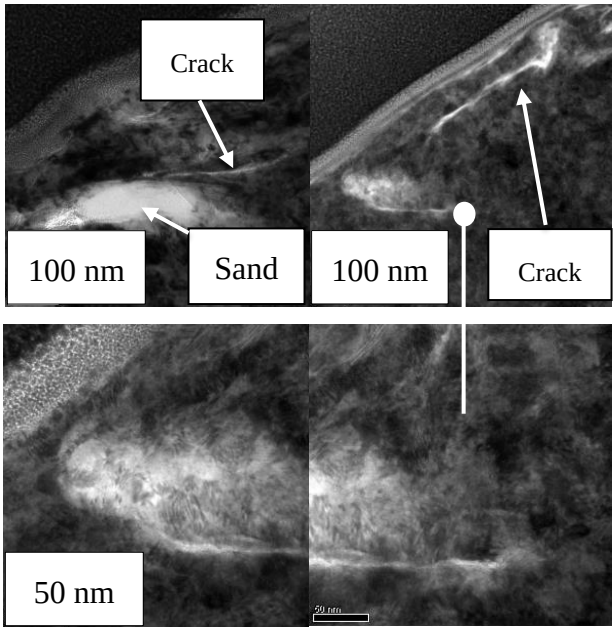

Figure 5-48: Magnified images of the deformed sub-layer of UNS S31603 showing presence of cracks around the embedded sand particle after erosion for 240 minutes

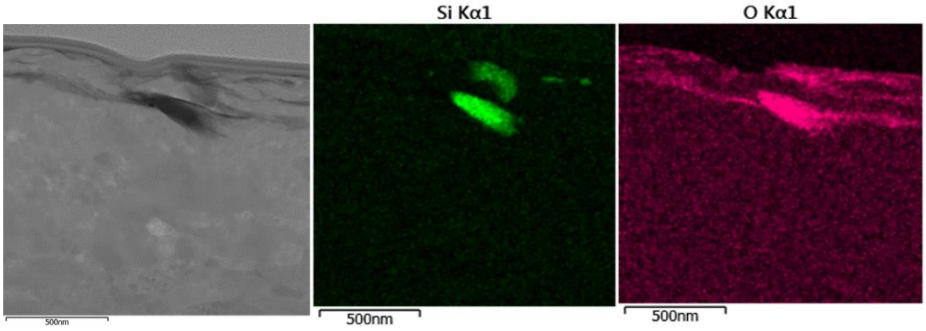

Figure 5-49: EDX confirms presence of sand particles within the deformed sub-layer of UNS S31603 after erosion for 240 minutes

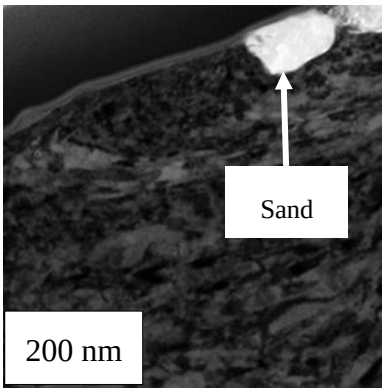

Figure 5-50: Showing presence of sand with no cracks within the deformed sub-layer of UNS S32760 after erosion for 240 minutes

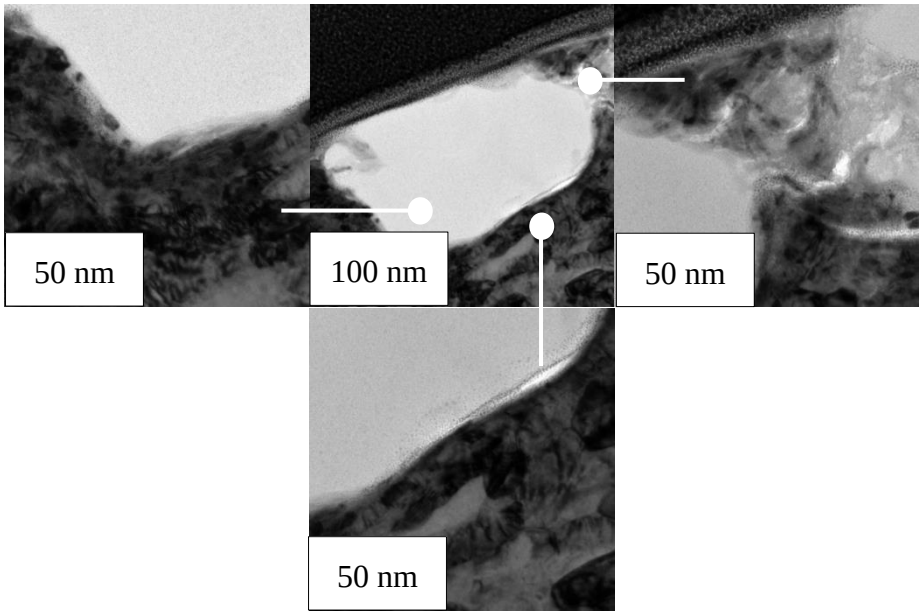

Figure 5-51: Magnified images of the deformed sub-layer of UNS S32760 showing absence of cracks around the embedded sand particle after erosion for 240 minutes

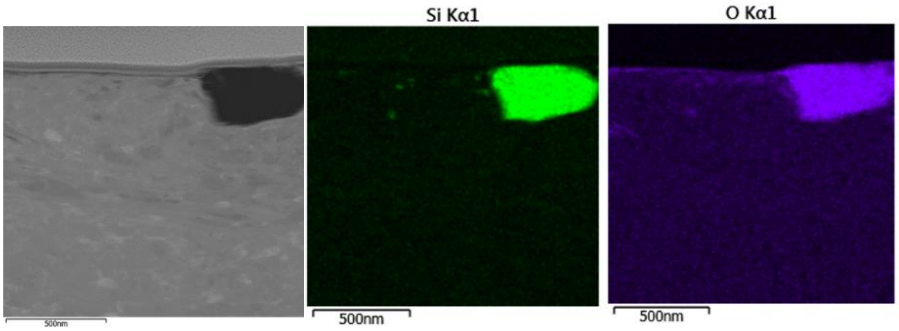

Figure 5-52: EDX confirms presence of sand particles within the deformed sub-layer of UNS S32760 after erosion for 240 minutes

5.6.5 Selected area diffraction pattern after erosion-corrosion

The selected area diffraction patterns images of the deformed region of both materials after erosion-corrosion are shown in Figure 5-53 and Figure 5-54 for UNS S32760 and UNS S31603, respectively. It is clear from the figures that there was a phase transformation within the sub surface deformed area of both materials from (FCC) austenite to (BCT) martensite.

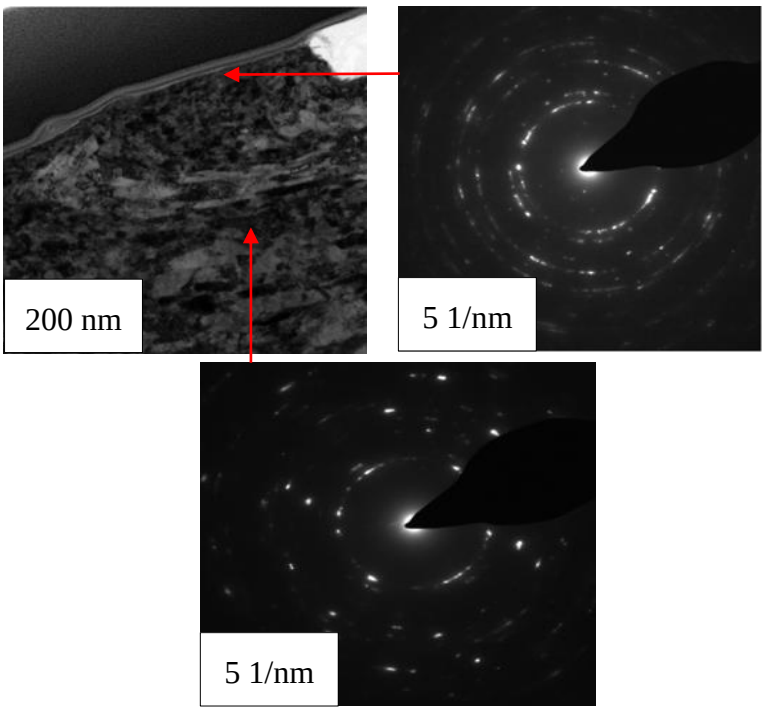

Figure 5-53: Selected area diffraction pattern of UNS S32760 after erosion-corrosion in a 10%NaCl (CO_2-saturated) solution for 4 hours at 20 m/s flow velocity and 1500 mg/l sand concentration

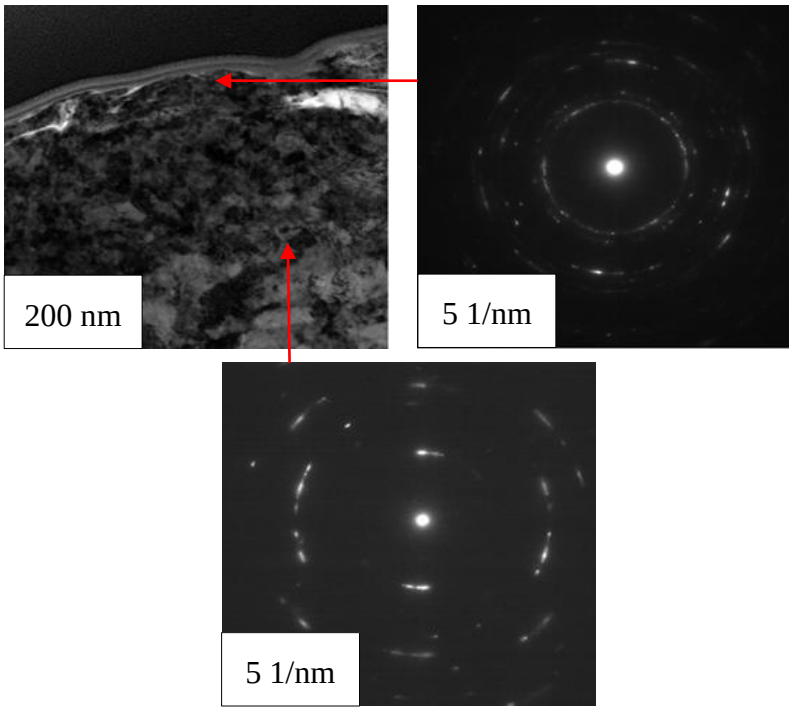

Figure 5-54: Selected area diffraction pattern of UNS S31603 after erosion-corrosion in a 10%NaCl (CO_2-saturated) solution for 4 hours at 20 m/s flow velocity and 1500 mg/l sand concentration

5.7 Summary

- The erosion and erosion-corrosion resistance of UNS S32760 and UNS S31603 was not significantly different for the period of time between 5-30 minutes. However, the situation suddenly changed at 60 minutes and afterwards as a distinct difference in the erosion resistance between the studied materials was existed.
- The hardness of both materials was almost the same at 60 minutes and afterwards. SEM images showed presence of sand particles on UNS S31603 at most of the test times in particular at 60 minutes and afterwards.
- Cracks were present either within the deformed sub-layer or even around the embedded sand particles in the case of UNS S31603 while there were no cracks in the case of UNS S32760.
- The penetration depth difference between the studied materials was significant at 60 minutes and afterwards.
- The erosion-enhanced corrosion of the studied materials was slightly different for the period of time between (5-30) minutes and it was equal at 240 minutes. The corrosion-enhanced erosion of both materials was almost the same between 5 to 30 minutes. However, at 60 minutes and afterwards, UNS S31603 showed a sudden increase.

Chapter six: Influence of impact angle on erosion-corrosion of stainless steels

6.1 Introduction

The principal aim of the present chapter is to investigate the effect of impact angle on erosion-corrosion of stainless steels in a 10%NaCl (CO_2-saturated) brine solution at a high flow velocity and to understand the effect of the mechanical properties and/or the corrosion resistance on the general behaviour of the studied materials.

The erosion-corrosion of UNS S32760, UNS S31803, UNS S31603 and UNS S42000 at a flow velocity of 20 m/s and 1500 mg/l sand loading at 50^{o}C for 4 hours at different impact angles (30, 45, 60 and 75) ^{o} will be evaluated.

In the first section of this chapter, the total weight loss of the studied materials and its components will be presented. Then, Scanning Electron Microscopy (SEM) images of the damaged surfaces of the studied materials will be shown followed by a SEM-EDX. Finally, the surface profilometry parameters (i.e. surface roughness, scar wear depth and diameter) will be presented. This can be clearly seen in Figure 6-1

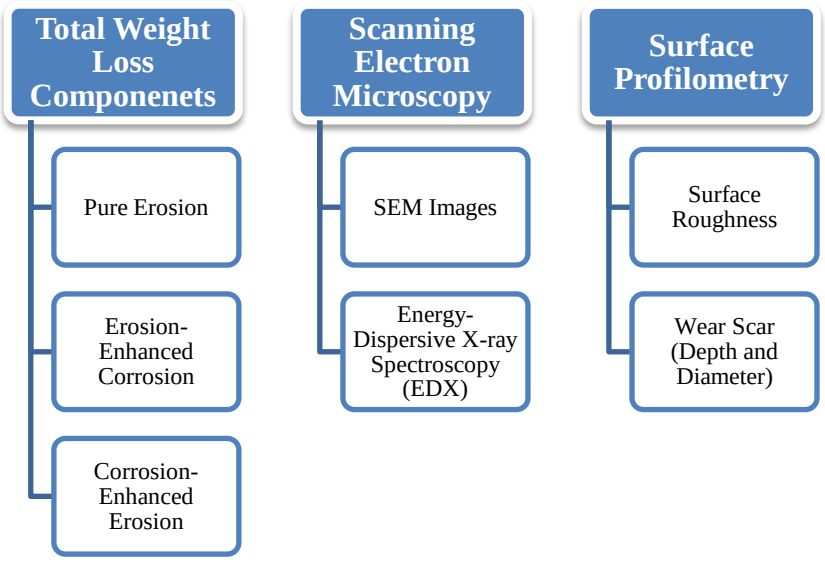

Figure 6-1: The general structure of the current chapter

6.2 Total weight loss of the studied materials and its components as a function of impact angle

Figure 6-2 shows the general behavior of the studied materials under erosion – corrosion conditions at 20 m/s flow velocity, 1500 mg/l sand concentration, 50ºC for 4 hours in a 10%NaCl (CO_2-saturated) brine solution and at different impact angles of (30, 45, 60 and 75)º. There is no doubt that there is a variation in the erosion-corrosion resistance of the studied materials, although the general trend of the TWL of the studied materials versus impact angle was almost the same. For example, all of the studied materials showed high TWL at 30º and 45º followed by a gradual decrease at 60º and a sharp reduction at 75º. However, there was a distinct difference in their TWL particularly as mentioned earlier especially at 30º and 45º.

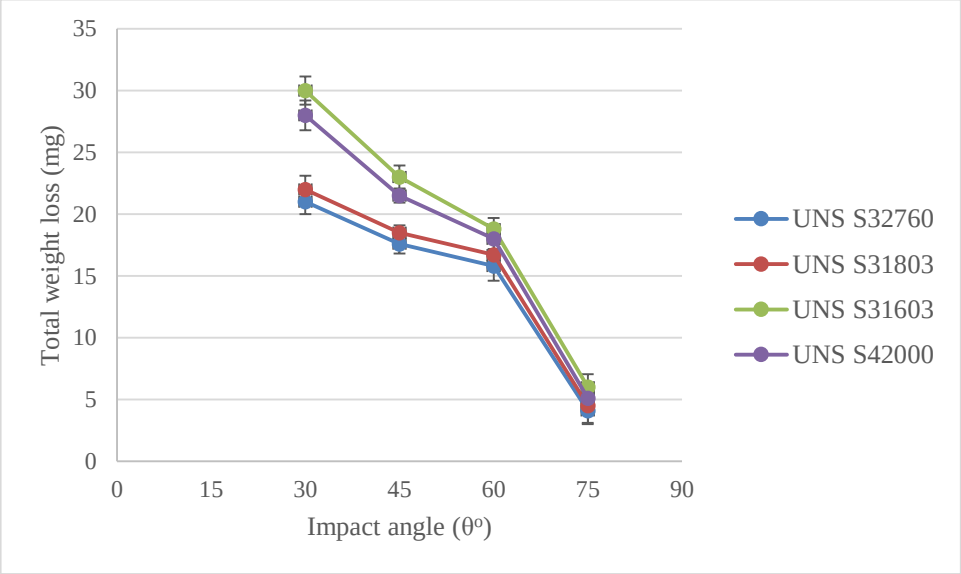

Figure 6-2: Total weight loss of the studied materials in a CO_2-saturated brine solution at 20 m/s flow velocity, 1500 mg/l sand concentration and at 50ºC for 4 hours as a function of impact angle (error bars are spread of 3 data points)

The general trend for the pure erosion damage of the studied materials as a function of the impact angle mirrored the TWL trends. However, the pure erosion damage of all of the studied materials was lower than the TWL as expected. Also, all of the

studied materials showed similar or slightly different values of pure erosion damage at all impact angles except UNS S31603 which showed higher values of pure erosion at 30 and 45° impact angle as shown in Figure 6-3.

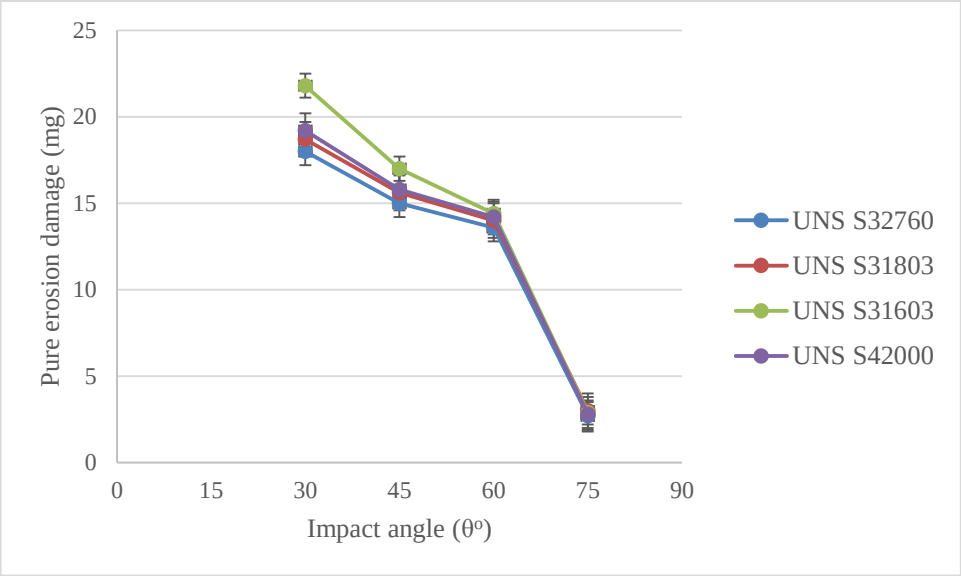

Figure 6-3: Pure erosion (N_2-Purged) of the studied materials at 20 m/s flow velocity, 1500 mg/l sand concentration and at 50°C for 4 hours as a function of impact angle (error bars are spread of 3 data point)

UNS S32760, UNS S31803 and UNS S31603 showed a comparable erosion-enhanced corrosion values but dC_E of UNS S42000 was the highest at all impact angles. All materials showed highest erosion-enhanced corrosion at 30° while the lowest value was at 75°. This can be seen in Figure 6-4.

Figure 6-5 depicts corrosion-enhanced erosion of all materials at different impact angles. The highest values of corrosion-enhanced erosion was at 30° while the lowest value was at 75° for all of the studied materials. UNS S32760 and UNS S31803 showed lower values of dE_C compared with UNS S31603 and UNS S42000 which showed the highest values at all impact angles.

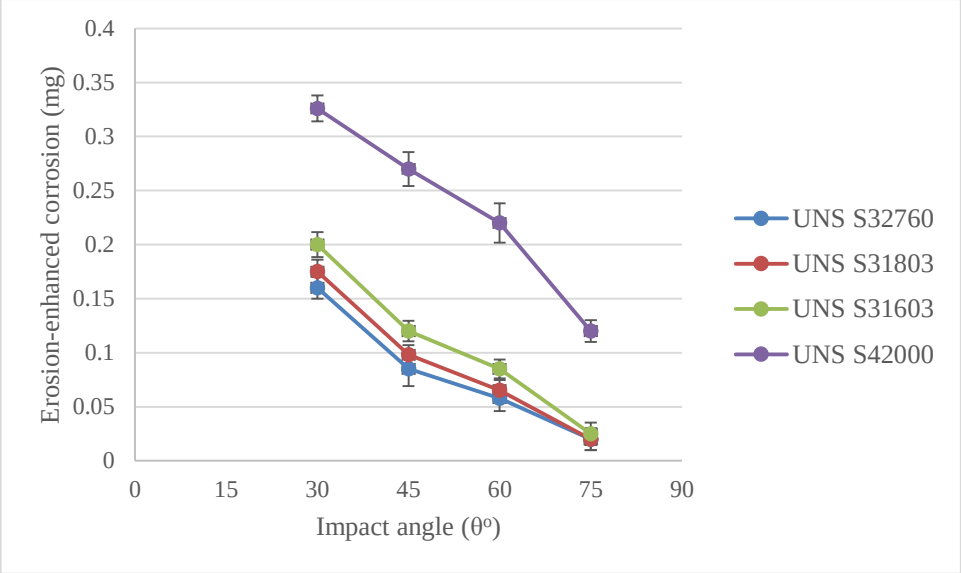

Figure 6-4: Erosion-enhanced corrosion of the studied materials in a CO_2-saturated brine solution at 20 m/s flow velocity, 1500 mg/l sand concentration and at 50ºC for 4 hours as a function of impact angle (error bars are spread of 3 data points)

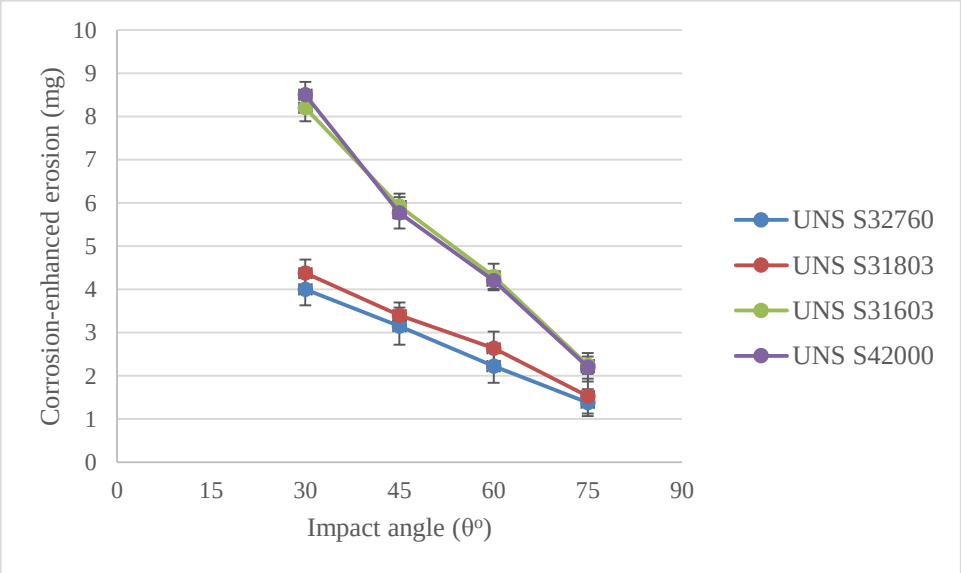

Figure 6-5: Corrosion-enhanced erosion of the studied materials in a CO_2-saturated brine solution at 20 m/s flow velocity, 1500 mg/l sand concentration and at 50ºC for 4 hours as a function of impact angle (error bars are spread of 3 data points)

6.3 Surface analysis of the damaged surfaces of the studied materials as a function of impact angle

Post to erosion and erosion-corrosion tests, surface analysis was done to investigate and examine the characteristics of the damaged surfaces of the studied materials at different impact angles.

6.3.1 Scanning electron microscopy

6.3.1.1 Pure erosion

SEM images of the damaged surfaces after pure erosion of UNS S42000 at 30^o and 45^o were obtained as can be seen in Figure 6-6. Clearly, cutting and lips formation were the dominant features. Also, sand particles were not present on the material surfaces at both impact angles.

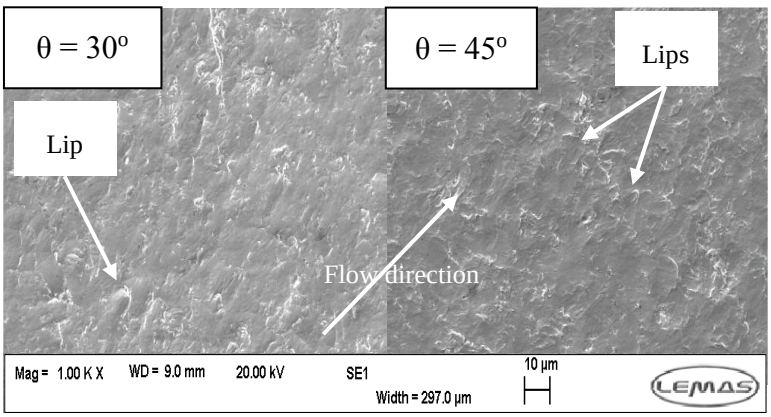

Figure 6-6: SEM images of the damaged surface of UNS S42000 at 30^o and 45^o after pure erosion (N_2-Purged) at 20 m/s flow velocity and 1500 mg/l sand concentration and 50^{o}C for 4 hours

6.3.1.2 Erosion-Corrosion

There was a distinct difference in the surface characteristics of the damaged surfaces of the studied materials after erosion-corrosion at different impact angles. These differences can be seen in Figure 6-7, Figure 6-8, Figure 6-9 and Figure 6-10 for UNS

S32760, UNS S31803, UNS S31603 and UNS S42000 respectively. For example, sand particles were present on both UNS S31603 and UNS S42000 surfaces at all impact angles. This was confirmed by EDX as shown in Figure 6-11 and Figure 6-12. However, there were no or little sand particles on the surfaces of UNS S32760 and UNS S31803.

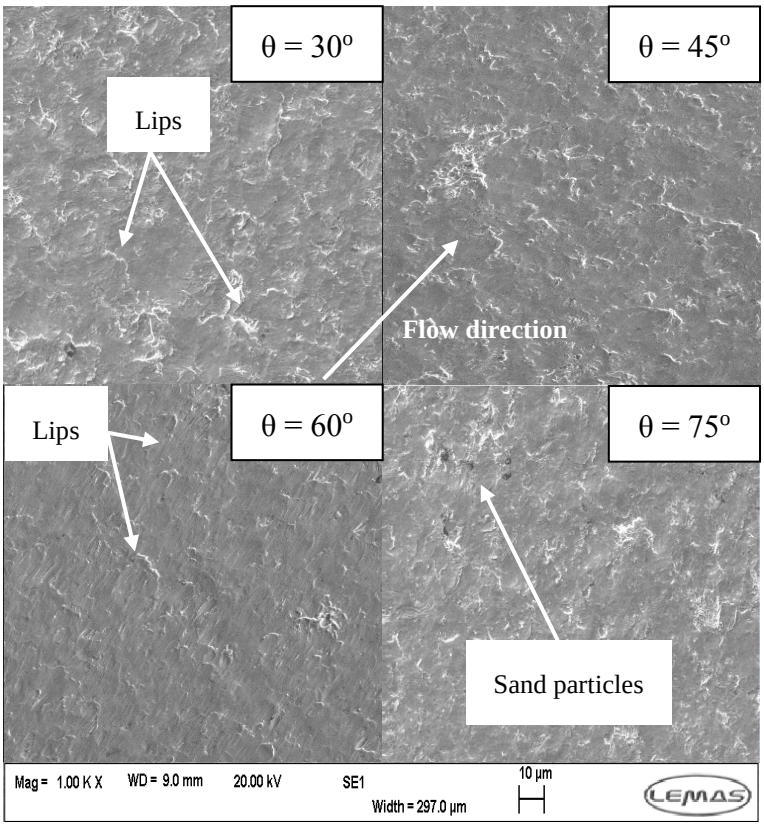

Figure 6-7: SEM images of the damaged surface of UNS S32760 at different impact angles after erosion-corrosion in a CO_2 – saturated brine solution at 20 m/s flow velocity and 1500 mg/l sand concentration and 50°C for 4 hours

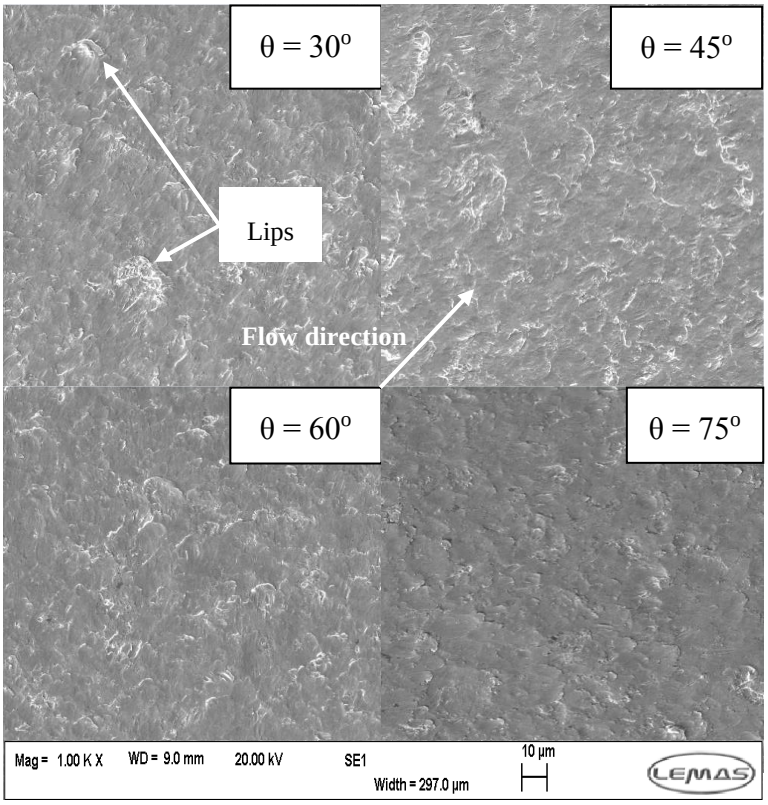

Figure 6-8: SEM images of the damaged surface of UNS S31803 at different impact angles after erosion-corrosion in a CO_2 – saturated brine solution at 20 m/s flow velocity and 1500 mg/l sand loading and 50°C for 4 hours

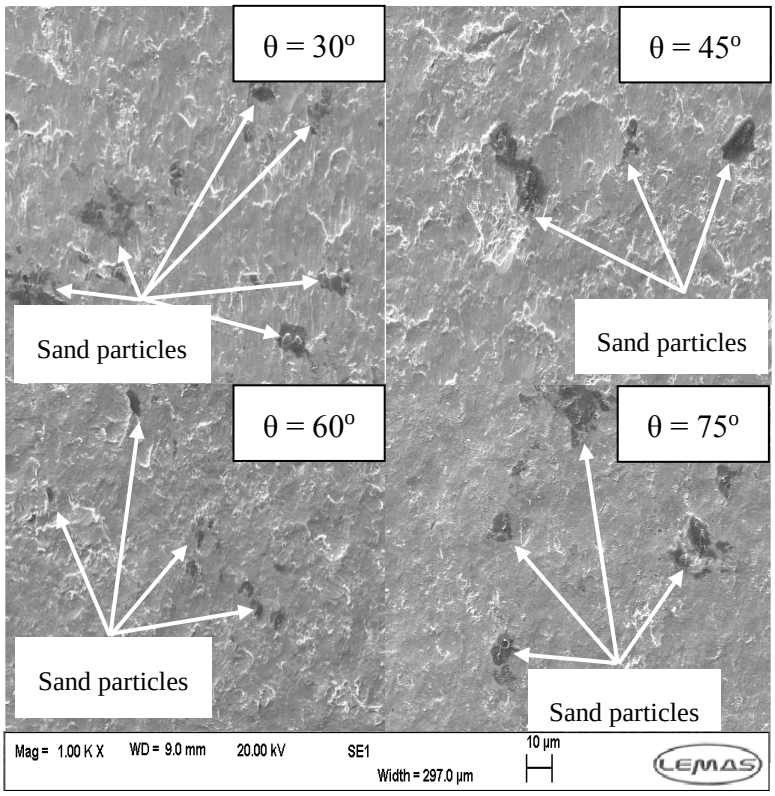

Figure 6-9: SEM images of the damaged surface of UNS S31603 at different impact angles after erosion-corrosion in a CO_2 – saturated brine solution at 20 m/s flow velocity and 1500 mg/l sand loading and 50°C for 4 hours

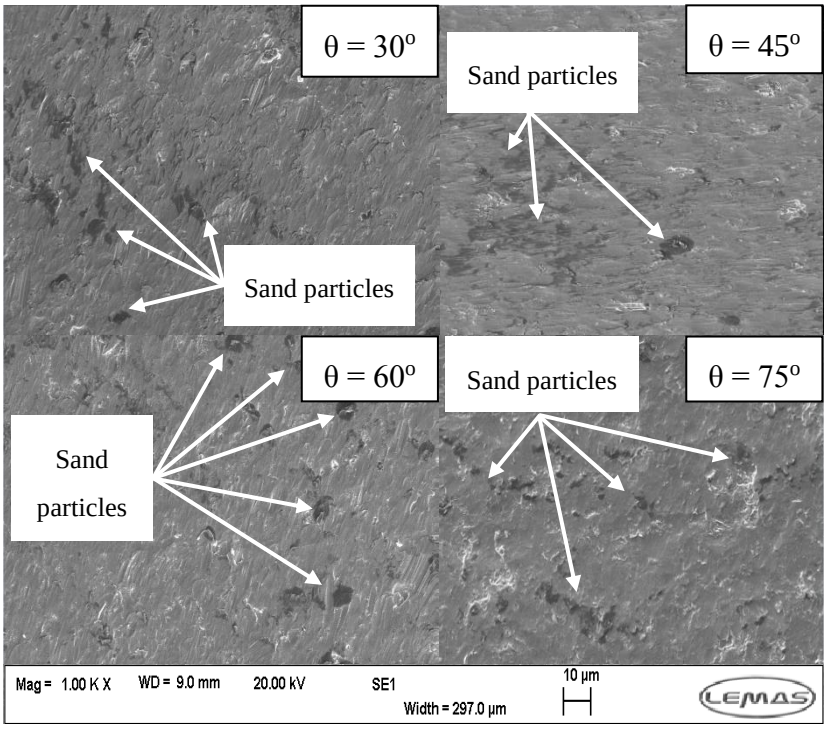

Figure 6-10: SEM images of the damaged surface of UNS S42000 at different impact angles after erosion-corrosion in a CO_2 – saturated brine solution at 20 m/s flow velocity and 1500 mg/l sand loading and 50°C for 4 hours

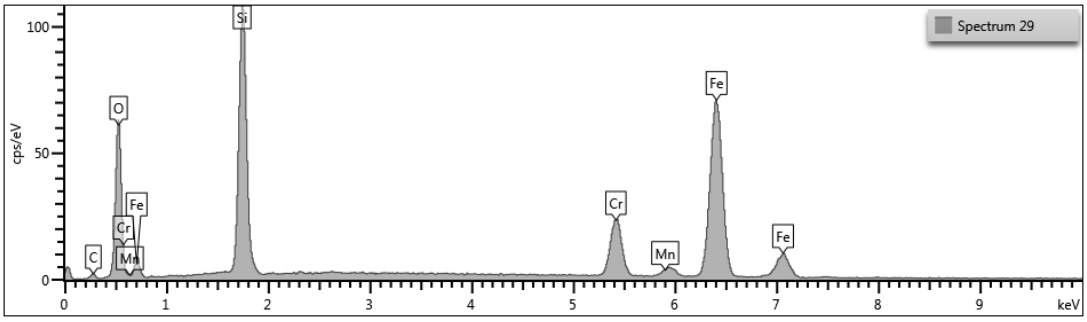

Figure 6-11: EDX confirms presence of sand particles on UNS S42000 surface

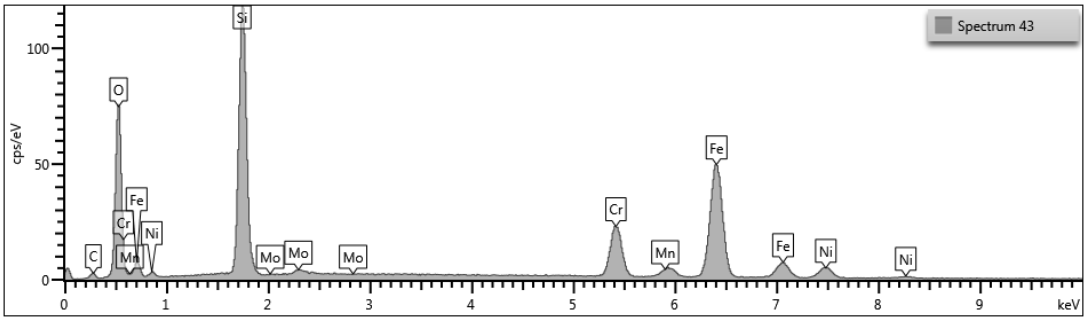

Figure 6-12: EDX confirms presence of sand particles on UNS S31603 surface

6.3.2 Surface Profilometry

6.3.2.1 Penetration depth, surface roughness (R_a) and wear diameter (D) as a function of impact angle

3D profilometry images and photos obtained after erosion-corrosion of the studied materials in a 10%NaCl (CO_2-saturated) brine solution at 20 m/s flow velocity and 1500 mg/l sand concentration and 50^{o}C for 4 hours as a function of impact angle can be seen in Figure 6-13 and Figure 6-14, respectively. Figure 6-15 shows the penetration depth of the studied materials after erosion-corrosion as a function of impact angle. It is evident from the figure that the penetration depth of the studied material are highly affected by the impact angle and the type of the affected material. Although the highest penetration depth for all materials was at 30^o, UNS S32760 showed the lowest penetration depth of about 66.53 µm while UNS S42000 showed the highest amongst other materials of about 105.05 µm. On the other hand, at impact angles of 60^o and 75^o, all materials showed a slight difference in their penetration depth. Again, UNS S32760 showed lowest penetration depth of around 31.41 µm. Conversely, UNS S31603 showed the highest value of the penetration depth of around 43.94 µm.

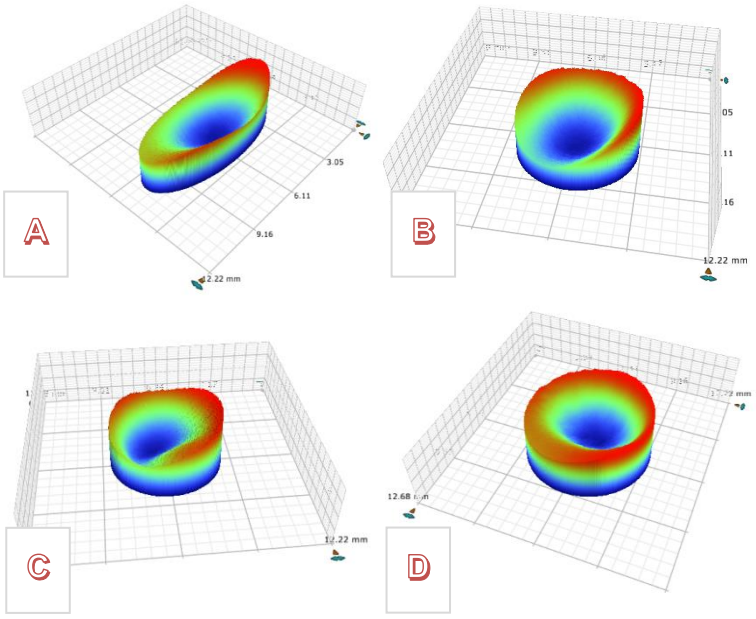

Figure 6-13: Representative 3D profilometry images obtained after erosion-corrosion on UNS S32760 samples positioned at (A) 30º, (B) 45º, (C) 60º and (D) 75º relative to SIJ nozzle

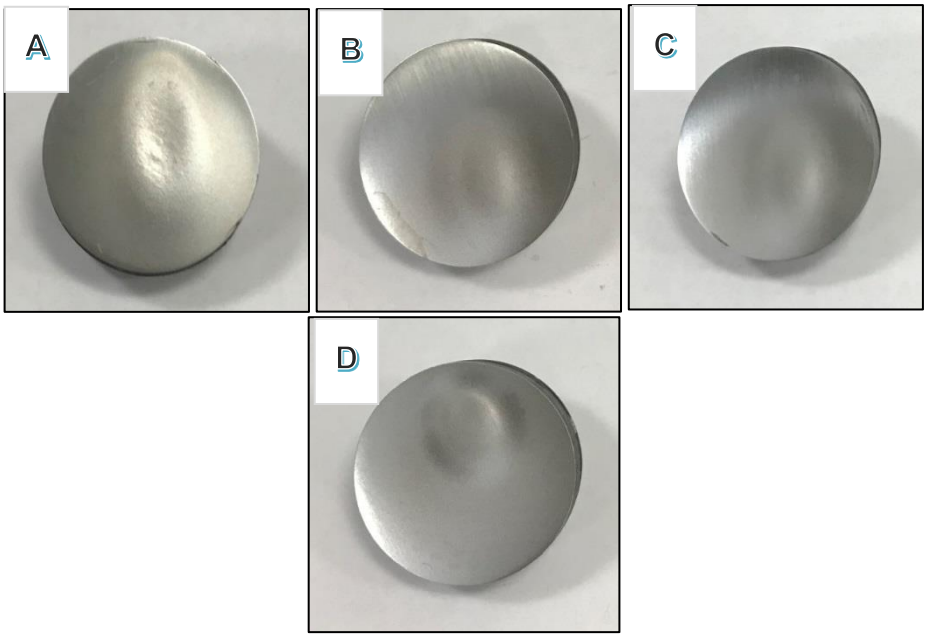

Figure 6-14: Representative photos obtained after erosion- corrosion on UNS S32760 samples positioned at (A) 30º, (B) 45º, (C) 60º and (D) 75º relative to SIJ nozzle

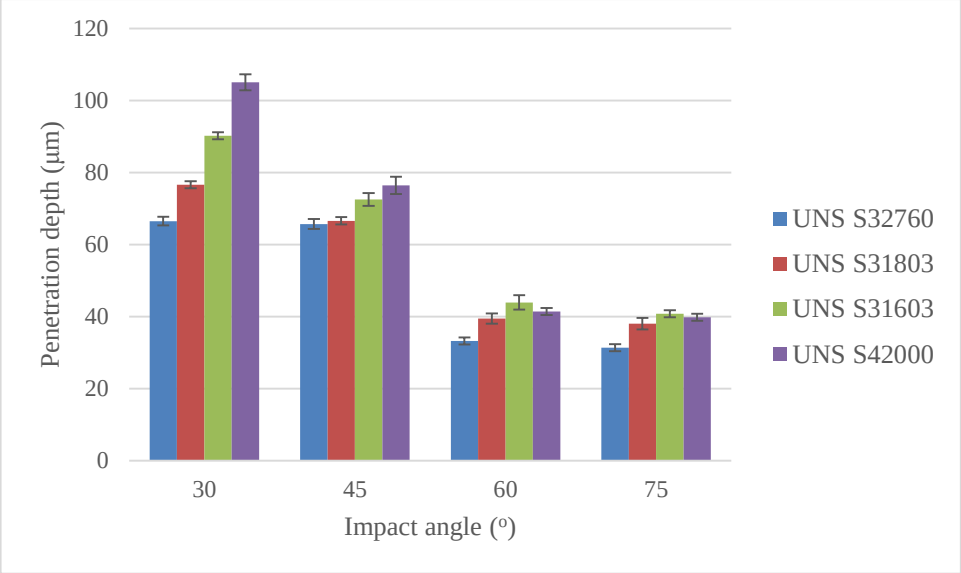

Figure 6-15: The penetration depth of the studied materials after erosion-corrosion in a 10%NaCl (CO_2-Saturated) solution at 20 m/s flow velocity,1500 mg/l sand concentration and 50°C for 4 hours as a function of impact angle (error bars are spread of 3 data points)

As can be seen from Figure 6-16 and Figure 6-17, impact angle has a significant influence on both the surface roughness of the studied materials and their wear diameter. The surface roughness of all of the studied materials increased with impact angle reduction. However, both UNS S32760 and UNS S31803 had less surface roughness than UNS S31603 and UNS S42000.

In the same way, the wear diameter increased as the impact angle was decreased. The wear diameter of UNS S32760 and UNS S31803 were lower than the one of UNS S31603 and UNS S42000.

It should be noted that the studied materials showed comparable surface roughness and wear diameter at 60° and 75° impact angles.

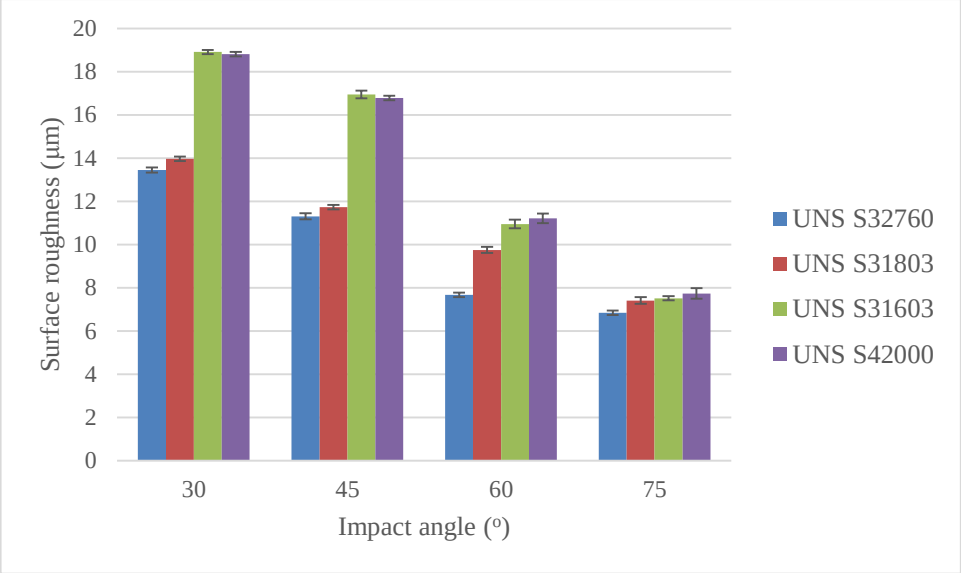

Figure 6-16: The surface roughness of the studied materials after erosion-corrosion in a 10%NaCl (CO_2-saturated) solution at 20 m/s flow velocity,1500 mg/l sand concentration and 50°C for 4 hours as a function of impact angles (error bars are spread of 3 data points)

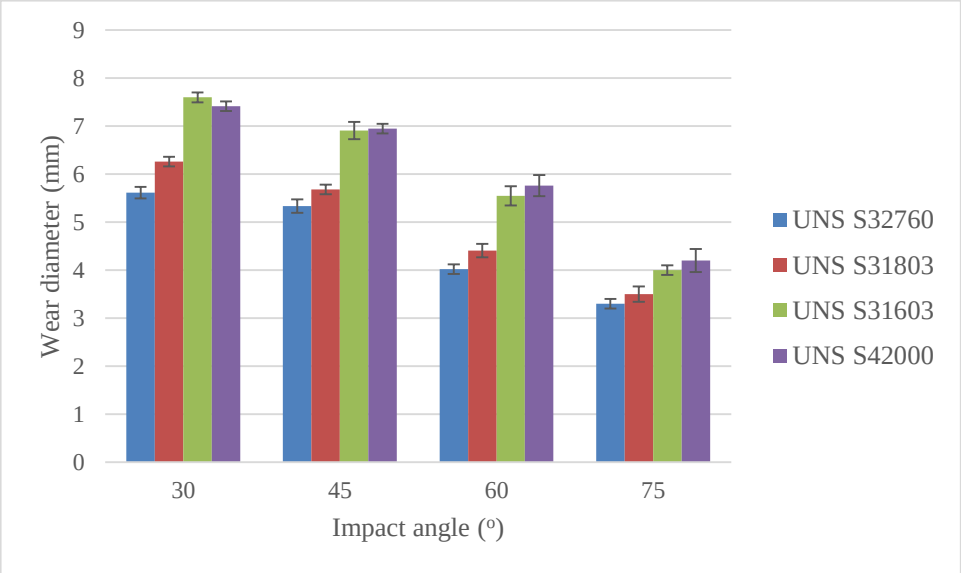

Figure 6-17: The wear diameter of the studied materials after erosion-corrosion in a 10%NaCl (CO_2-saturated) solution at 20 m/s flow velocity,1500 mg/l sand concentration and 50°C for 4 hours as a function of impact angles (error bars are spread of 3 data points)

6.3.3 TEM and SADP Images at 75°

TEM images of UNS S31603 and UNS S42000 at 75° impact angle were obtained as can be seen in Figure 6-18. These images prove that cracks were present within the deformed sub-layer of both materials at high impact angle.

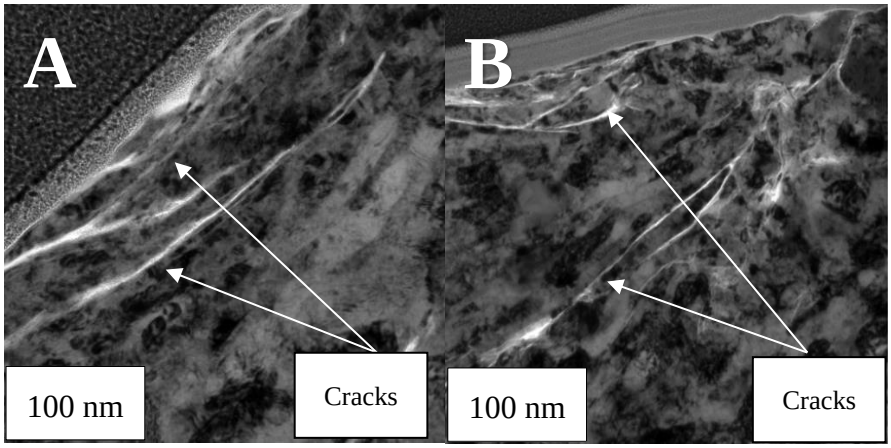

Figure 6-18: Dark field images of **(A)** UNS S31603 and **(B)** UNS S42000 after erosion-corrosion in a 10%NaCl (CO_2-saturated) solution at 20 m/s flow velocity, 1500 mg/l sand concentration and 50ºC for 4 hours at 75º impact angle

Also, SADP images confirm stress-induced martensitic phase transformation in all of the austenite-containing studied materials at high impact angle, as shown in Figure 6-19.

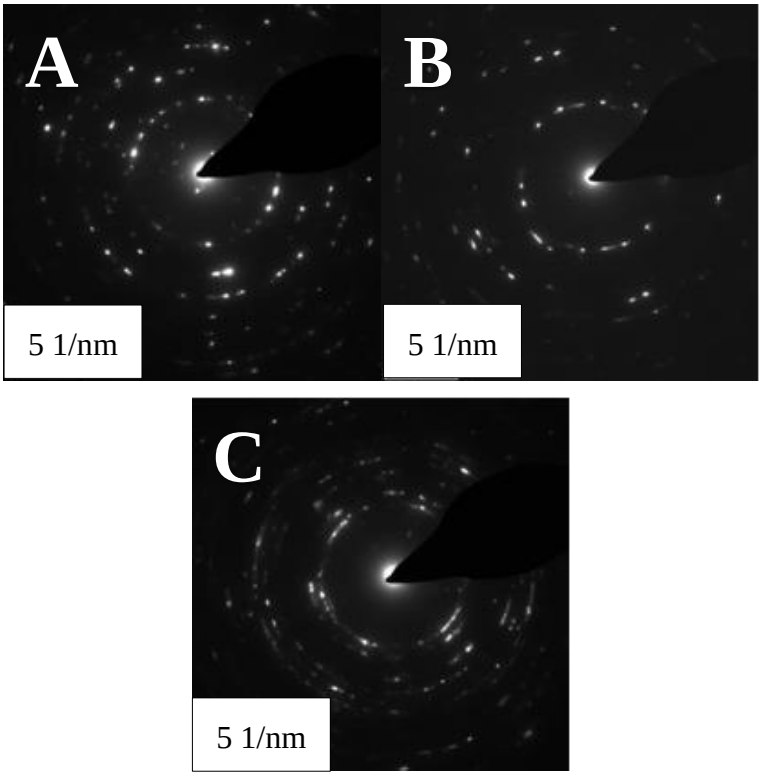

Figure 6-19: Selected area diffraction pattern confirming phase transformation of **(A)** UNS S32760 **(B)** UNS S31803 and **(C)** UNS S31603 after erosion-corrosion in a 10%NaCl (CO_2-saturated) solution at 20 m/s flow velocity, 1500 mg/l sand concentration and 50ºC for 4 hours at 75º impact angle

6.4 Summary

- A number of interesting findings were obtained from the present chapter. One of these findings is that the TWL of UNS S42000 and UNS S31603 was the same under erosion-corrosion conditions in a 10%NaCl (CO_2-saturated) at 20 m/s, 1500 mg/l and at 30^o and 45^o impact angles, despite the large difference in their mechanical properties and underlying crystallographic structure.
- Also, there was little or no difference in the erosion-corrosion resistance of UNS S32760 and UNS S31803. Their erosion-corrosion resistance was higher than that of UNS S42000 and UNS S31603 at 30^o and 45^o impact angles.
- Although the mechanical properties of UNS S42000 are very similar to those of UNS S32760 and UNS S31803, their erosion-corrosion resistance is significantly different. Also, the pure erosion resistance of the studied materials (with the exception of UNS S31603) was almost the same at all impact angles investigated.
- Erosion-enhanced corrosion of the studied materials was almost the same with the exception of UNS S42000. Corrosion-enhanced erosion of UNS S42000 and UNS S31603 was higher than the other materials at 30^o and 45^o impact angles which seems to be the reason behind their high erosion-corrosion rates compared with the other materials.
- In terms of surface analysis results, SEM images confirmed the presence of embedded sand particles on the material surface of UNS S42000 and UNS S31603 at all impact angles under erosion-corrosion conditions while there were little or no embedded sand particles on the surfaces of UNS S32760 and UNS S31803. Also, embedded sand particles were not present on the UNS S42000 surface after pure erosion at 30^o and 45^o impact angles.

- The highest penetration depth, surface roughness and wear diameter for all of the studied materials were at 30^{o} and 45^{o} impact angles. These parameters are inversely proportional to impact angle. However, the penetration depth, surface roughness and wear diameter of UNS S32760 and UNS S31803 was lower compared to the other materials. Also, there was no significant difference in the already mentioned parameters for all of the studied materials at 60^{o} and 75^{o} impact angles. This will be discussed extensively in the subsequent chapter.

Chapter Seven: Discussion

7.1 Introduction

In this chapter, the main findings obtained throughout this comprehensive study will be highlighted. Then, the interpretation of the key findings will be given.

This chapter is split into discussion of the following key points.

- Influence of the static corrosion behaviour on the erosion-corrosion resistance of stainless steels.
- Linking the static corrosion behaviour to erosion-corrosion of stainless steels.
- Change in hardness as an erosion resistance prediction parameter of stainless steels.
- Effect of surface deformation on synergy of stainless steels.
- Effect of Pitting Resistance Equivalent Number (PRE_N) on corrosion-enhanced erosion of stainless steels at different impact angles.
- The role of sand embedment in corrosion-enhanced erosion of stainless steels.
- Effect of work-hardening on corrosion-enhanced erosion of stainless steels at high impact angle.

7.2 Influence of the static corrosion behaviour on the erosion-corrosion resistance of stainless steels

The most remarkable result that emerged from static experiments is that (E_b-E_r) was highly affected by temperature. It is known that assess of the repassivation ability of the passivating material after passive film damage can be made by finding the value of (E_b-E_r). As this value increases, the repassivation ability of material will decrease and vice versa (see Figure 2-10). This is in line with Neville *et al.* [149] who studied

the effect of temperature on the static corrosion of a wide range of materials categorized as stainless steels, Ni-base alloys and Co-base alloys. They found that the (E_b-E_r) increased as the temperature was increased as shown in Figure 7-1.

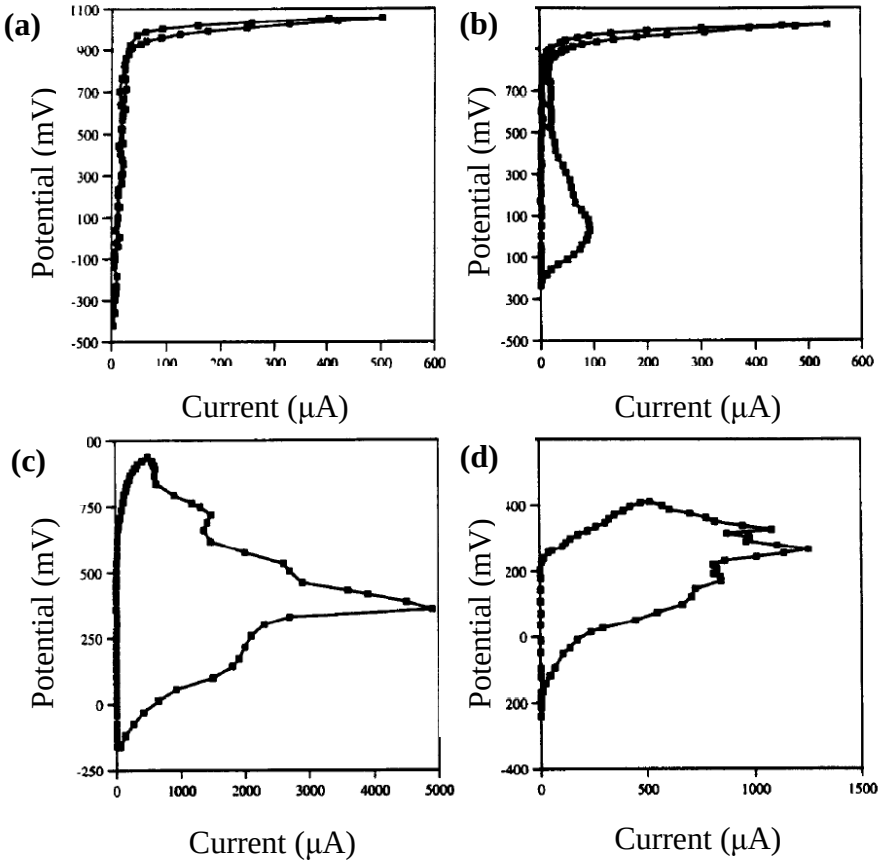

Figure 7-1: Showing the anodic polarization of the super duplex alloy in static sea water at **(a)** 30°C, **(b)** 40°C, **(c)** 50°C and **(d)** 60°C [149]

It also should be noted that (E_b-E_r) of the materials increased suddenly once each material reached its critical pitting temperature as can be seen in Figure 4-8. Moreover, it is interesting to note that the maximum current density is also affected by temperature as shown in Figure 4-9. These findings can be attributed to the high ability of chloride ions to chemisorb on the passive surface and hence causing passive film damage [150] in particular in CO_2-saturated brine solutions as confirmed by Anselmo *et al.* [151] who studied the corrosion behaviour of super martensitic stainless steel in an aerated and CO_2-saturated sea water at different chloride

concentrations (20000, 30000, 40000, 60000 and 80000) ppm and different temperatures (5, 25 and 60)^{o}C and found that the synergistic effect of CO_2 and chloride concentration has an effective influence on the breakdown potential of the studied material as can be seen in Table 7-1.

Table 7-1: The breakdown potential of super martensitic in both aerated and CO_2-saturated brine solutions as a function of temperatures and chloride concentrations after [151]

[Cl-] (ppm)	E_p (mV) x SCE					
	5ºC		25ºC		60ºC	
	Aerated	CO_2	Aerated	CO_2	Aerated	CO_2
20000	134	218	102	149	-39	-12
30000	130	135	70	67	-70	-26
40000	121	94	50	25	-71	-102
60000	87	75	34	16	-72	-120
80000	78	35	6	-68	-96	-136

On the other hand, Park *et al.* [152] proposed that enhancing the metal dissolution and retarding the repassivation ability at high temperature encourages formation of stable pits and hence declines the breakdown potential.

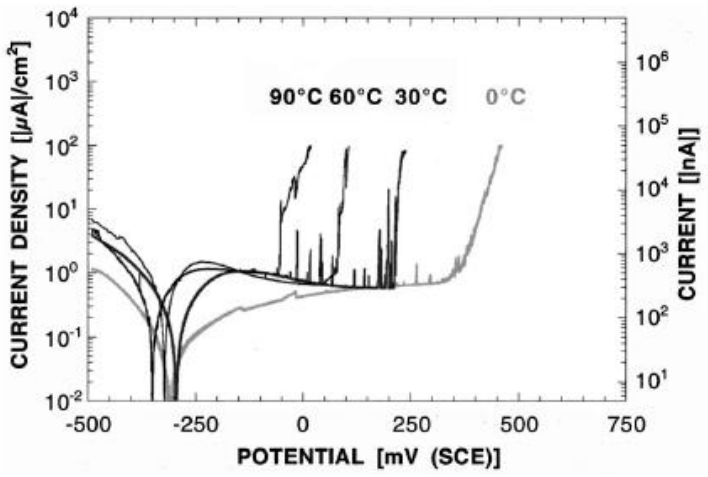

Figure 7-2: Showing how temperature affect the static corrosion behaviour of AISI 304 in (0.1M) NaCl [152]

Another possibility that can give an indication about the effect of temperature on the corrosion resistance properties of stainless steel in saline solutions is that its effect on the protective properties of the passive film at high temperatures as explained by Wang *et al.* [153], who attributed this into two reasons. One of these reasons is that the porosity of the passive film increases as the temperature increases and it was suggested that presence of chloride ions within the passive film at high temperature compared with the one at 25°C can confirm this hypothesis. Also, the precipitated chloride salts can be dissolved at high temperature and transported by convection leading to high porosity [150]. Another reason is thought to be due to a change in the chemical composition/ physical structure of the passive film at high temperatures. Presence of voids, porous and change in the film density can be considered as common examples [153].

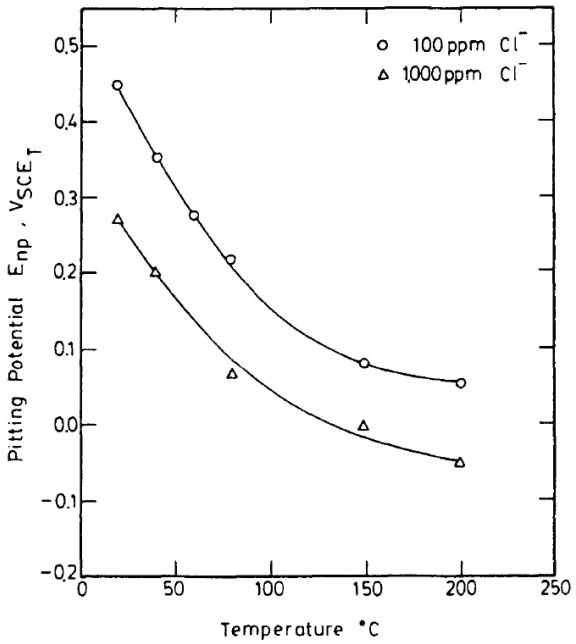

Figure 7-3: Showing how breakdown potential is affected by temperature at different chloride concentrations [153]

Since the total amount of degradation of materials due to erosion-corrosion, which is known as the total weight loss, is composed of several components according to the

following relationship: $TWL = E + C + dC_E + dE_C$, its value varies depending on the extent of impact of the affecting factors on any of its components. Although the effect of temperature on pure erosion and TWL has been studied as previously mentioned in section 2.6.1, its effect on both static corrosion and erosion-enhanced corrosion has not been studied extensively. It is known that the corrosion rates of stainless steels are very low and can be neglected under static conditions. However, it is not possible to neglect the effect of corrosion activity when materials are being depassivated by sand particles impacts. The three main features of the static corrosion results indicate that the erosion-corrosion resistance of the studied materials will probably be affected by temperature increasing as the latter will be responsible for decreasing both the breakdown potential (E_b) and the repassivation ability (E_b-E_r) in addition to increasing the maximum current density(i_{max}) of the studied materials.

In order to prove what has been mentioned earlier, each of these parameters was linked to erosion-enhanced corrosion of the studied materials as can be seen in Figure 7-4 and Figure 7-5. Obviously, there is a good correlation between erosion-enhanced corrosion of the studied materials and both (E_b-E_r) and (i_{max}). So, it can be deduced that the static corrosion behavior has a significant effect in terms of how materials react to their depassivation by sand impacts under dynamic conditions and this is an important factor in erosion-corrosion.

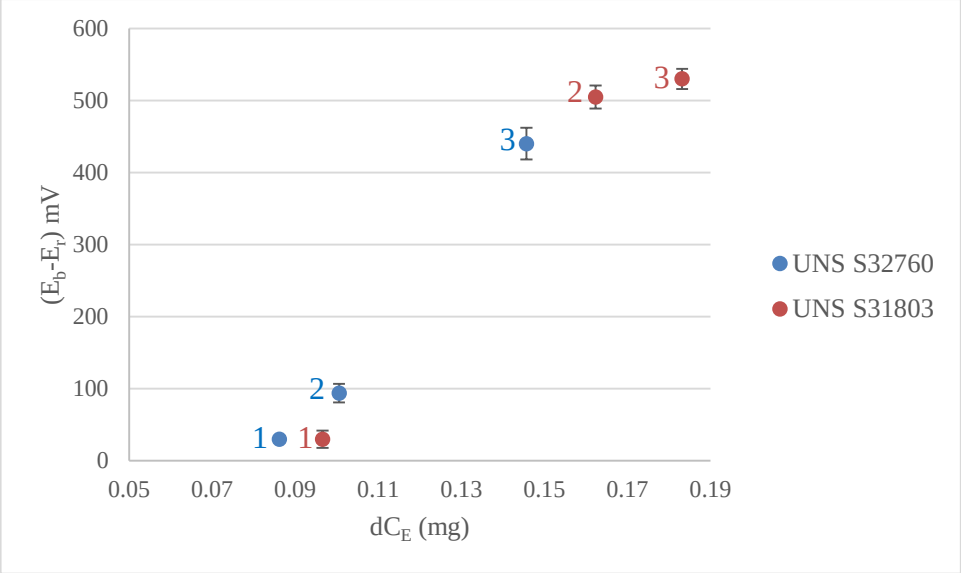

Figure 7-4: The relationship between the repassivation ability in static condition (E_b-E_r) and erosion-enhanced corrosion (dC_E) for UNS S32760 and UNS S31803 at different temperatures (1) 25°C, (2) 48°C and (3) 61°C

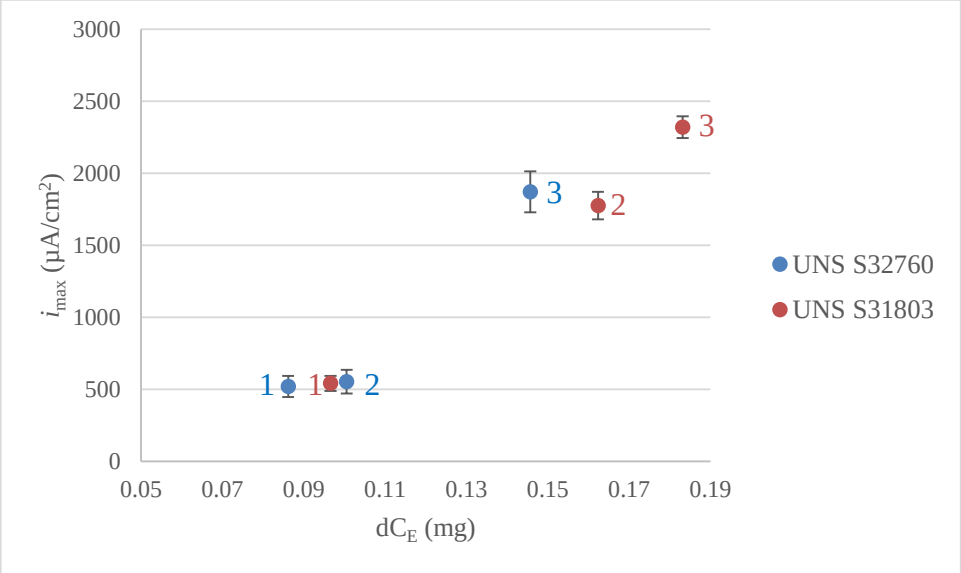

Figure 7-5: The relationship between the maximum current density (i_{max}) and erosion-enhanced corrosion (dC_E) for UNS S32760 and UNS S31803 at different temperatures (1) 25°C, (2) 48°C and (3) 61°C

The repassivation ability of materials is linked to its erosion-enhanced corrosion resistance. This can give an indication that the repassivation ability under dynamic

conditions might follow a similar trend to the one of static corrosion as will be discussed in the subsequent section.

Results obtained from the figures in section 4.3.2 revealed that there is a considerable effect of temperature on the repassivation ability of the studied materials after erosion-corrosion. As illustrated in Table 4-1, the required time to return back to the original current value of both materials was increased by increasing temperature. This is in agreement with Rincon *et al.* [154] who studied the repassivation ability of S13Cr and 22Cr in a CO_2-saturated oilfield environment after erosion-corrosion. They found that the initial current of materials needs more time to return back to its original state (i.e. before depassivation) at high temperatures. Although there was no clear interpretation for occurrence of this phenomenon in their work, it is probably thought that cold deformation resulting from sand impacts on the materials surface, play a vital role in its occurrences.

For instance, cold deformation encourages metastable pits formation in duplex stainless steels. It is known that duplexes have a superior resistance to corrosion particularly the pitting corrosion. However, it has been found that cold deformation has a detrimental effect on its corrosion resistance as it is found that the deformation increases the metastable pitting events. One of the reasons is the slightly changes in the elements distribution in both phases in the duplex stainless steels (i.e. ferrite and austenite) due to dislocation movement resulting from cold deformation and thus the PRE_N of austenite which is less than the one for ferrite before cold deformation will be higher after deformation and hence occurrence of pits corrosion in the ferrite knowing that the surface energy of ferrite phase unlike the austenite phase will increase after deformation because the latter will experience a phase transformation [155].

Another possibility for pit formation may be attributed to the presence of Cr enriched areas, which are resulted from deformation and distributed in a uniform way in the ferrite phase, which in turn may form micro galvanic cells with the Cr depleted zones and thus enhance pitting corrosion [155].

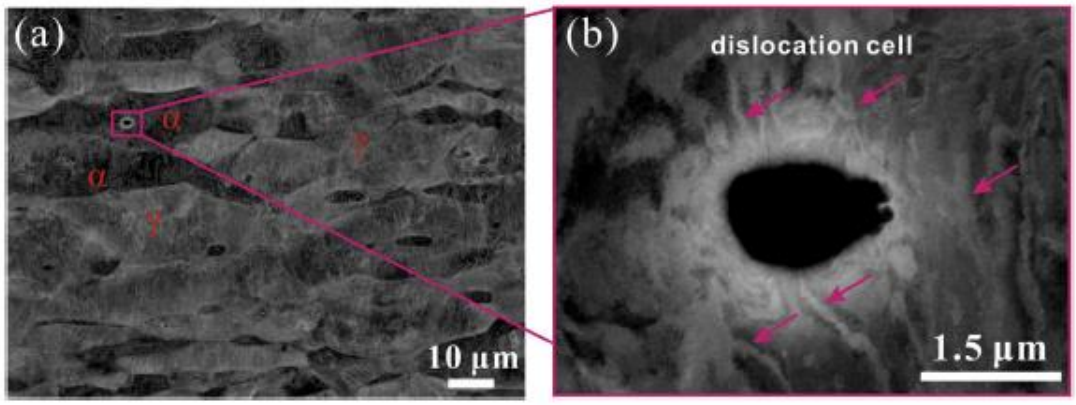

Figure 7-6: SEM-BSE morphologies of the metastable pitting for UNS S31803 duplex stainless steel with 90% cold deformation in 3.5 wt.% NaCl at room temperature. (α: ferrite phase, γ: austenite phase) [155]

Cold deformation enhance chloride ions adsorption onto the passive film. Moreover, cold deformation affects the passive film stability and its protection property specially the repassivation ability. It was found that both the corrosion resistance and the repassivation capacity of the passive film decrease by cold deformation as the latter is responsible for the reduction in the Cr/Fe ratio which is necessary for achieving repassivity of stainless steels [155, 156]. Also, the bound water in the passive film will decrease due to heavy deformation. This in turn will lead to two deleterious effect on the passive film protectiveness and hence the corrosion resistance of stainless steels. First, it will reduce the repassivation ability of the passive film. Also, the ability to pick up the active metal ions to form a new passive film will be lost with the absence of the bound water [155].

Another possibility for this to be happened may be due to what is known as a “slip dissolution”. It can be defined as the perforation of the passive film due to the

dislocation movement by the mechanical deformation. So, the bare metal will be exposed to the corrosive environment (Figure 7-7) [157].

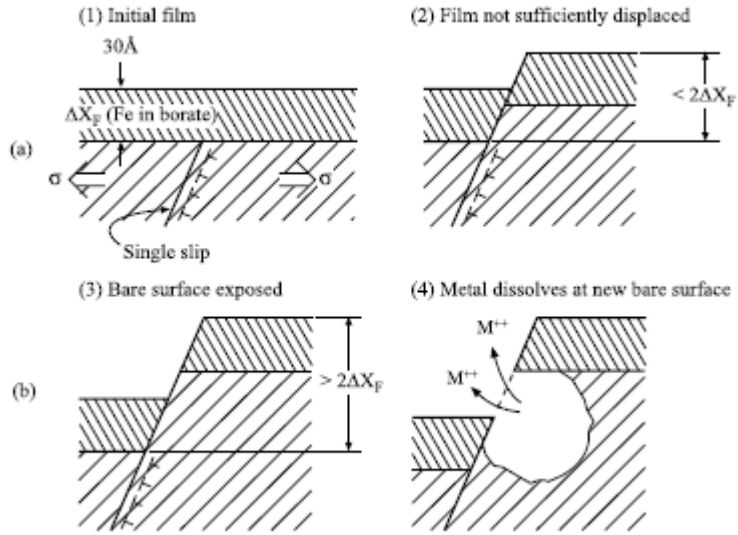

Figure 7-7: Showing the slip dissolution [157]

Moreover, Wang *et al.* [158] is thought the interfacial bonding between the passive film after deformation with the substrate will be weak due to the presence of defects such as high dislocation density. Figure 7-8 summarizes the proposed mechanism of static corrosion influence on erosion-corrosion of stainless steels.

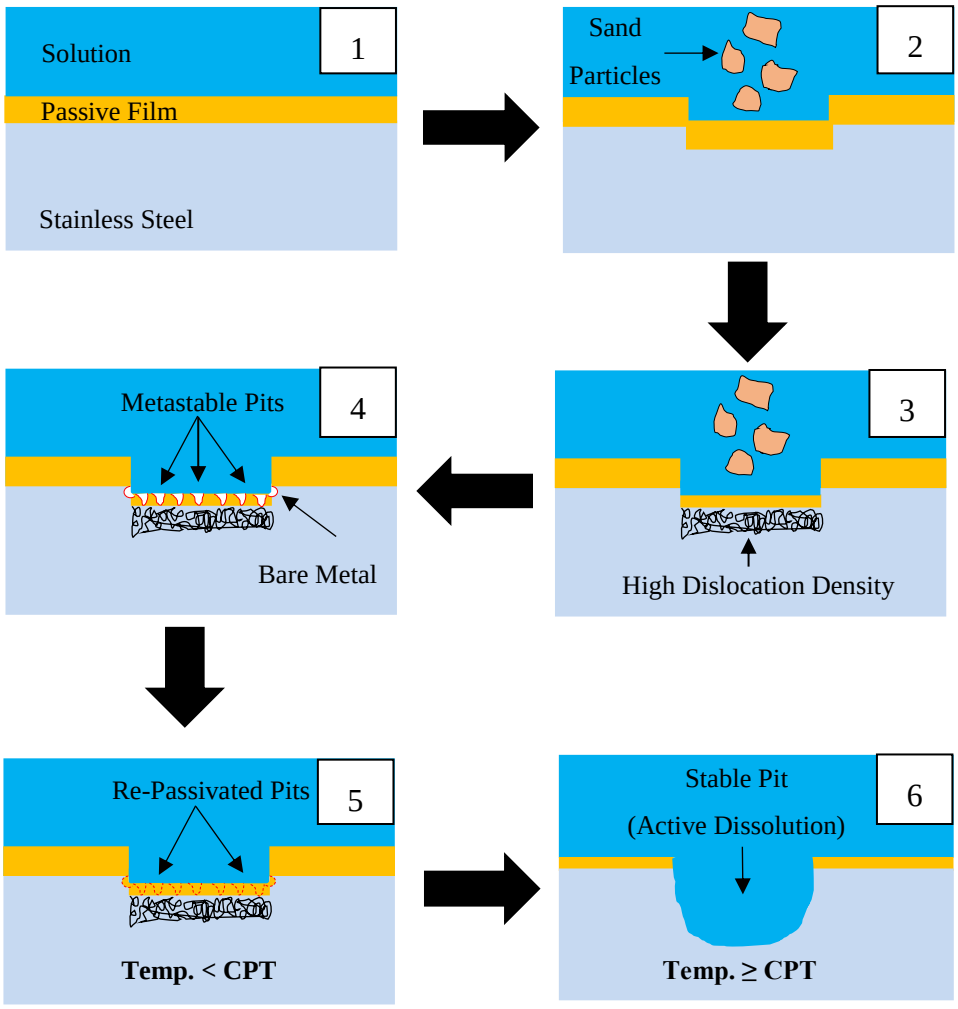

Figure 7-8: Explain how static corrosion may affect erosion-corrosion of stainless steels

7.3 Linking the static corrosion behaviour to erosion-corrosion of stainless steels

It was shown earlier that the repassivation ability of material under static conditions was evaluated using the cyclic potentiodynamic polarization techniques while the same factor was evaluated using the *in-situ* potentiostatic polarization techniques and submerged impingement jet under dynamic conditions. In spite of the difference between these two methods in which the passive film was removed or even the repassivation ability of materials was assessed, as the way in which the passive film was removed under static conditions caused by electrochemical effect whereas it was

caused by the mechanical effect of the sand particles impact under dynamic conditions (see Figure 7-9), both methods will lead to a defective passive film. If this occurs under severe conditions, it will result in formation of stable pits especially when the material to be studied approaching to its CPT as will be clarified in the following section.

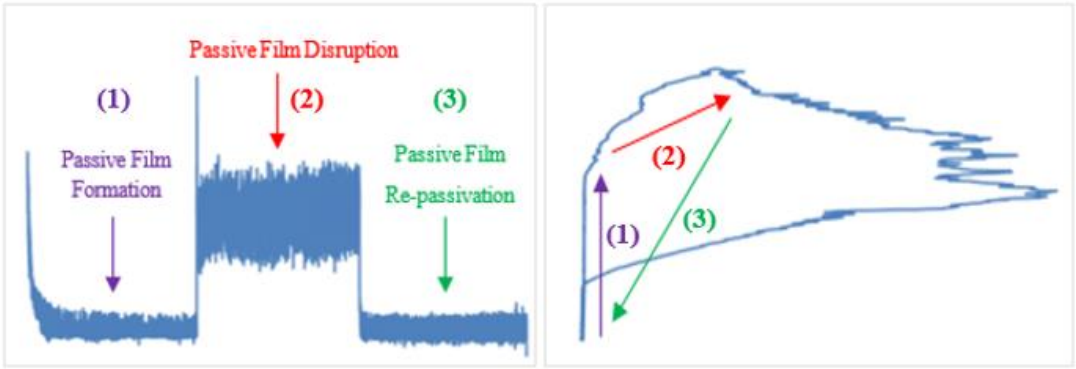

Figure 7-9: Showing the similarity of different stages in both static and dynamic (erosion-corrosion) tests

In order to confirm the above hypothesis, the static test variables, which can give an impression about the material's ability to repassivate its passive film in the static conditions, (i.e. (E_b-E_r) in addition to the maximum current density (i_{max})) were linked with their counterparts under flow conditions (i.e. the repassivation time (t^*)) for both of the studied materials as shown in Figure 7-10 and Figure 7-11. The relationship between the repassivation ability in static condition (E_b-E_r) and the repassivation time resulted from erosion-corrosion condition (t^*) of UNS S32760 and UNS S31803 is shown in Figure 7-10. As can be seen from the figure, both (E_b-E_r) and (t^*) showed a similar behaviour as temperature increased. For example, there was a gradual increase in both parameters in the case of UNS S32760 when the temperature increased from 25^{o}C to 48^{o}C while both of these parameters increased sharply at 61^{o}C. In the case of UNS S31803, there was a sharp increase in both (E_b-E_r) and (t^*) when the temperature increased from 25^{o}C to 48^{o}C and continue to increase at 61^{o}C.

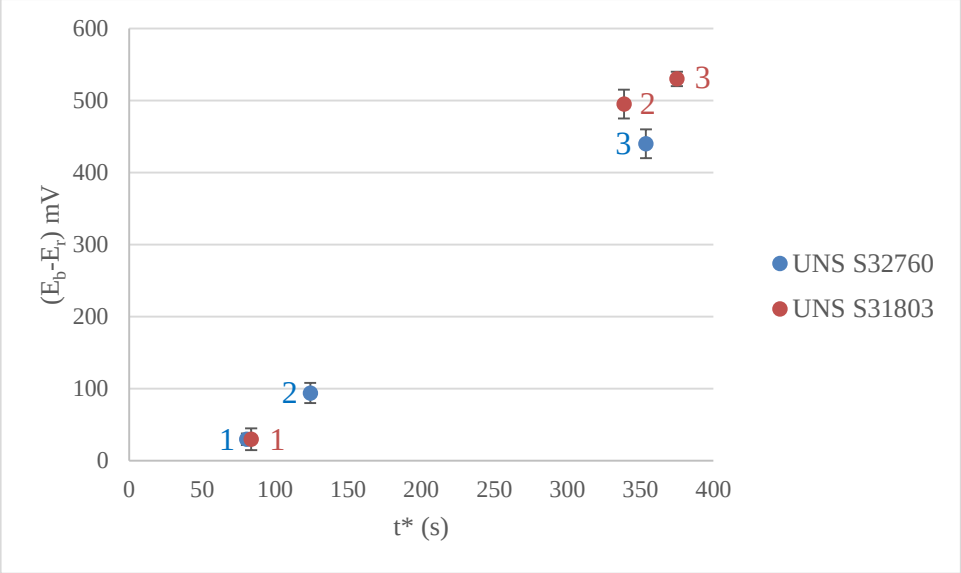

Figure 7-10: The relationship between repassivation ability in static condition (E_b-E_r) with its counterpart under erosion-corrosion condition (t^*) for UNS S32760 and UNS S31803 at different temperatures (1) 25°C, (2) 48°C and (3) 61°C

Figure 7-11, on the other hand, depicts the relationship between the maximum current density (i_{max}) and the repassivation time (t^*) for both materials. It is clear that there is a strong relationship between the repassivation time and the maximum current density of both materials.

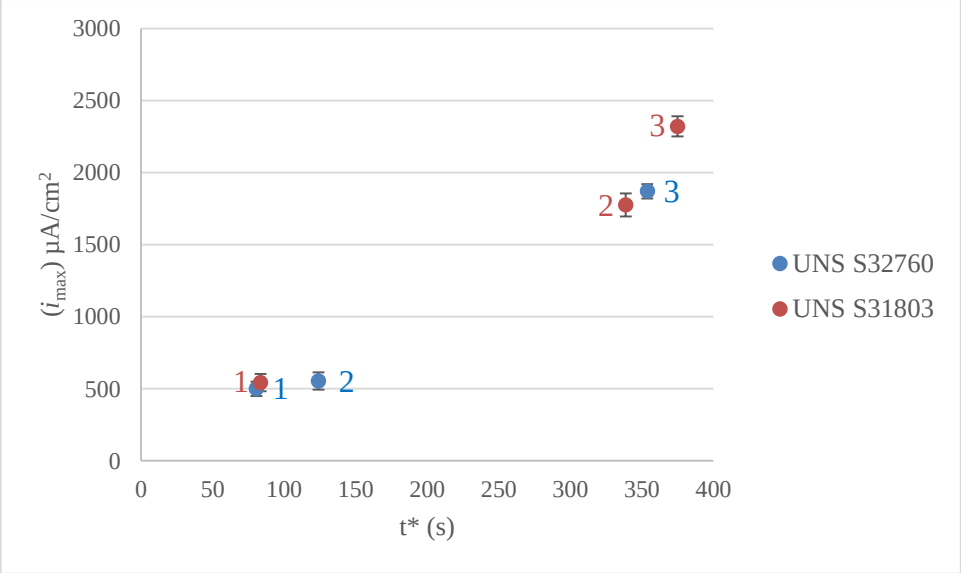

Figure 7-11: The relationship between the maximum current density (i_{max}) and the repassivation time under erosion-corrosion conditions (t^*) for UNS S32760 and UNS S31803 at different temperatures (1) 25°C, (2) 48°C and (3) 61°C

So, it can be implied that there is a good correlation between the static corrosion behaviour and erosion-corrosion of stainless steels. Figure 7-12 summarizes the basic concepts that explain how the static corrosion behavior affects erosion-corrosion of stainless steels.

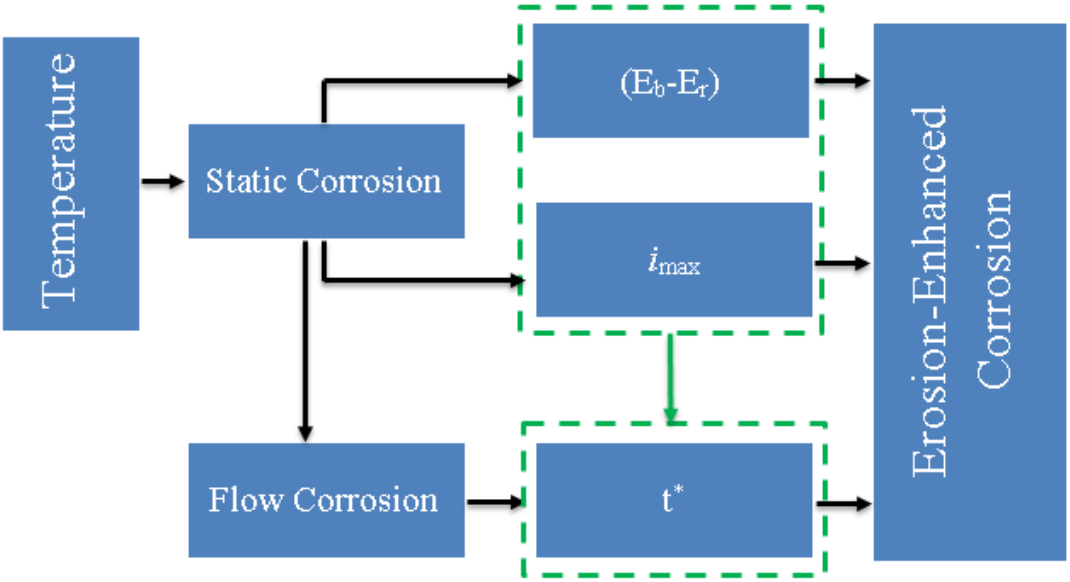

Figure 7-12: Summary of the proposed mechanism showing how static corrosion affect erosion-corrosion of stainless steels

7.4 Change in hardness as an erosion resistance prediction parameter of stainless steels

One of the interesting observations is that the pure erosion of the studied materials was almost the same for the period of time between 5 and 30 minutes. At 60 minutes and afterwards, however, the distinct difference in their erosion resistance was existed. Sand particle impact can cause significant sub-surface microstructural changes for austenite-containing materials. It is known that solid particle erosion involved sand particles entrained by the moving fluid. Each sand particle has a specific kinetic energy depending on the moving fluid flow velocity according to the following equation:

$$KE = 0.5\, mV^2$$

Where:

KE: kinetic energy (J).

m: mass of 1 particle (g).

V: flow velocity (m/s).

When sand particles hit the material surface, the energy will dissipitate and will transfer to the material surface. Due to the absorbed energy, the material surface will experience changes within its subsurface structure. First, there will be a phase transformation from austenite (FCC) to martensite (BCT) at room or low temperature. Also, the grains size will be reduced as shown in Figure 5-45. It can be seen from the figure that both materials experienced a significant grain size reduction with time progression. This is in agreement with Aribo *et al.* [129, 134] who found that an adequate kinetic energy to cause microstructural changes in both lean duplex (UNS S32101) and austenitic (UNS S30403) stainless steels including grain size refinement can be obtained by erosion at 15 m/s and at 500 mg/l sand concentration. This can be seen in Figure 7-13. Similarly, eroding of UNS S31603 at 7m/s and 1wt.% silica sand using slurry pot erosion tester was enough to cause grain size refinenment [131].

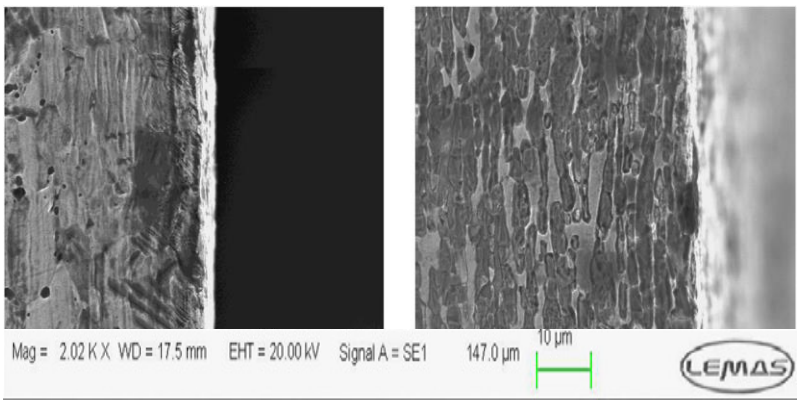

Figure 7-13: Grain size refinement near the deformed surface of the studied materials at 15 m/s and 500mg/l sand concentration obtained by SEM (cross-section)[129, 134]

It is also in agreement with Rajahram *et al.* [132], who noticed presence of nanocrystalline layer (2 µm) thickness from the top surface

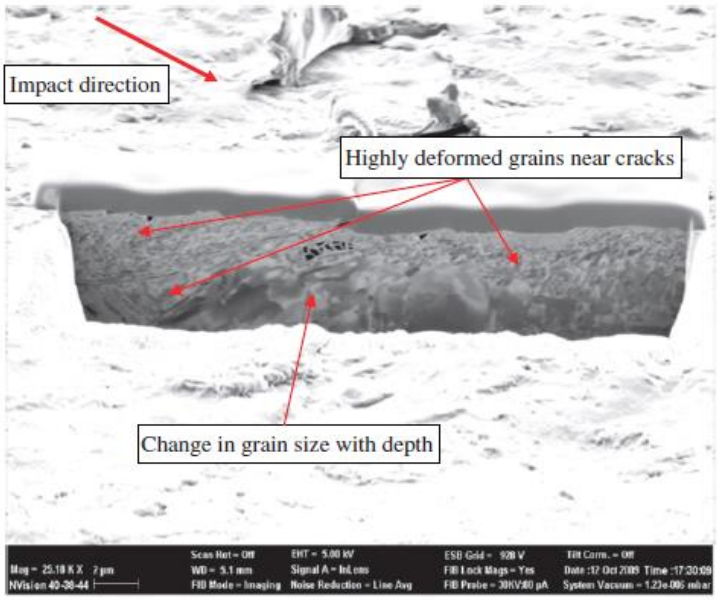

Figure 7-14: Showing the grain size distribution with depth [132]

The grain size refinement will lead to an increase in the hardness of materials. As sand particles impact the material surfce, the latter will be heavily plastically deformed and hence a high dislocation density will be presented. As a result, the dislocation movement will be blocked and hardness will be increased [158] as can be seen in Figure 5-23 and Figure 5-24. This is supported by Bragmann *et al.* [7], who studied the erosion-corrosion of super austenitic (UNS S31254) stainless steel in a CO_2-saturated artificial seawater and they found that low flow velocity (7m/s) and low sand loading (50 mg/l) was not enough to work harden the material surface and there was no change in the obtained hardness value with its counterpart of pre-eroded. At 20 m/s, however, the studied material showed a high increase in hardness after erosion at both (50 and 500) mg/l sand loadings as shown in Figure 7-15.

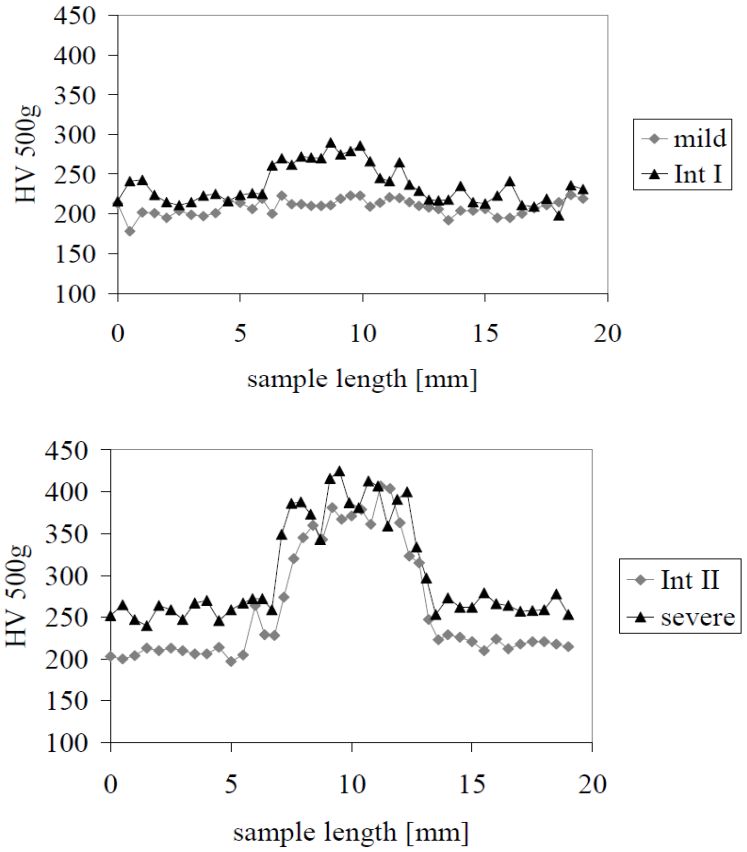

Figure 7-15: Microhardness of UNS S31254 after erosion at 7 m/s and 50 mg/l (mild), 20 m/s and 50 mg/l (Int I), 7 m/s and 500 mg/l (Int II) and 20 m/s and 500 mg/l (severe) [7]

An increase in hardness after erosion in a de-aerated tap water at 15 m/s and 500 mg/l for 4 hours was also noticed on the materials surfaces of UNS S30403, UNS S32101 and UNS S32205 as shown in Figure 7-16 [90].

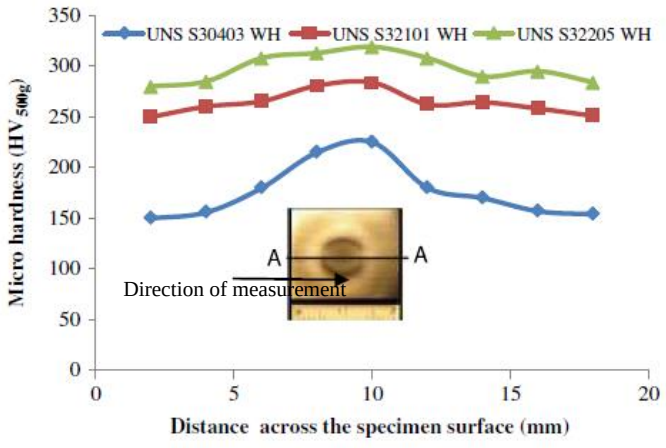

Figure 7-16: Showing an increase in hardness of the studied materials after erosion at 15m/s and 500 mg/l in de-aerated tap water [90]

Also, by comparing the average grain size with the materials hardness, it can be clearly seen as shown in Figure 7-17 and Figure 7-18 for UNS S32760 and UNS S31603 respectively that an inverse proportional relationship between materials hardness and grain size was existed.

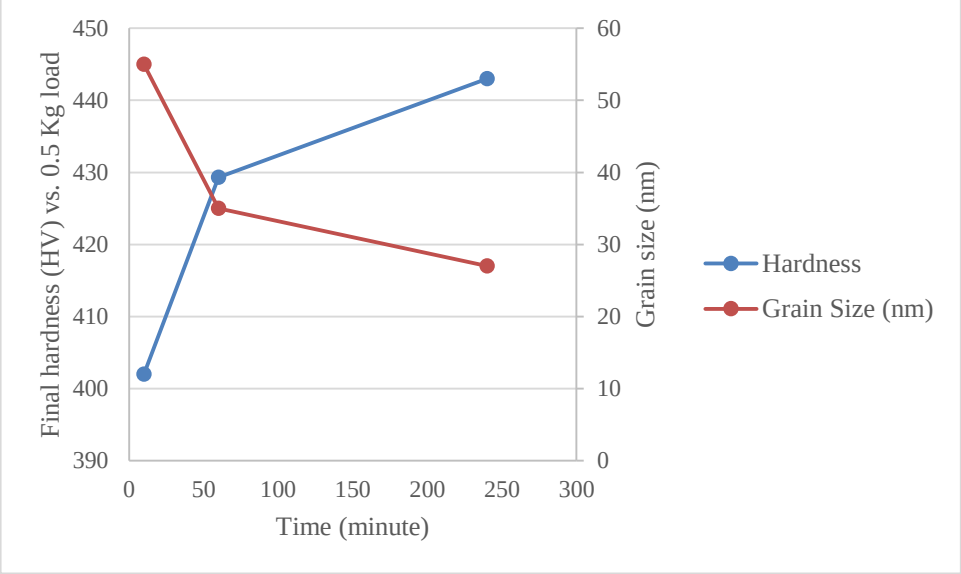

Figure 7-17: The relationship between the final hardness and the grain size of UNS S32760 as a function of time

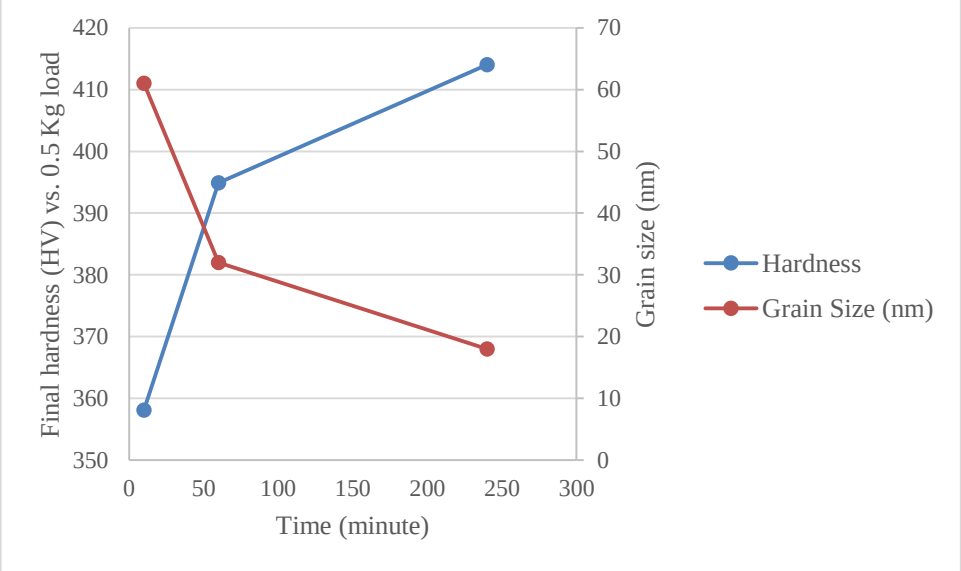

Figure 7-18: The relationship between the final hardness and the grain size of UNS S31603 as a function of time

It is known that the higher hardness of material, a higher the erosion resistance. However, as can be noticed from Figure 7-19 that there was a slight difference in the

final hardness between UNS S32760 and UNS S31603 after deformation. Also, the final hardnesss of both materials began to be closer with time especially at 240 minutes. However, the erosion resistance of both materials decreased and it is more pronounced in the case of UNS S31603 than for UNS S32760 as shown in Figure 7-20 and Figure 7-21.

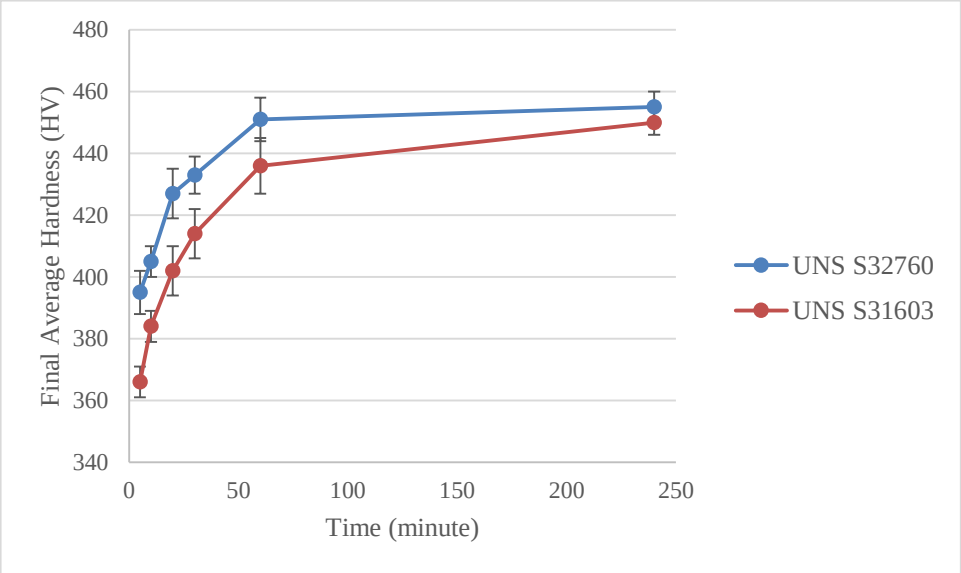

Figure 7-19: The average microhardness of UNS S32760 and UNS S31603 as a function of time

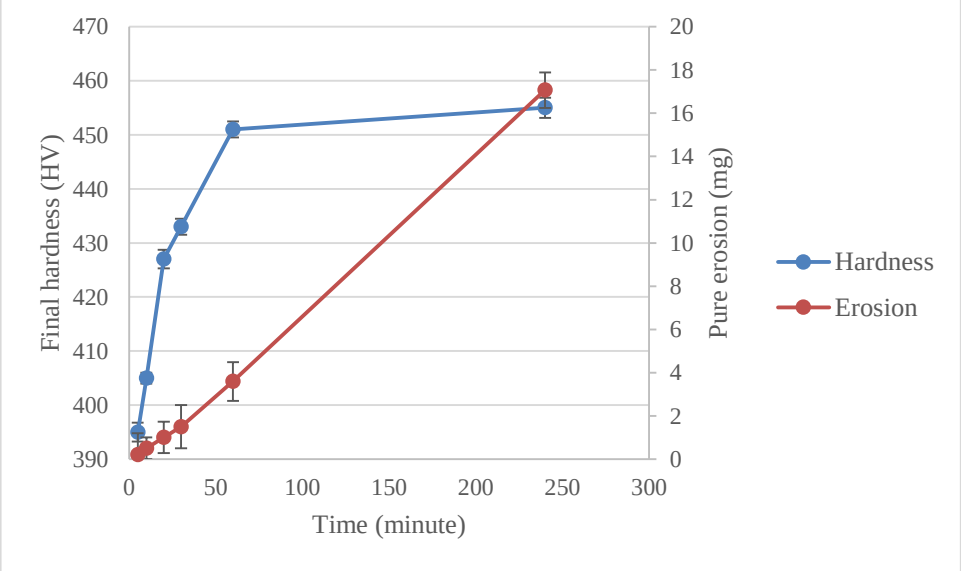

Figure 7-20: The relationship between the final hardness and pure erosion of UNS S32760 as a function of time

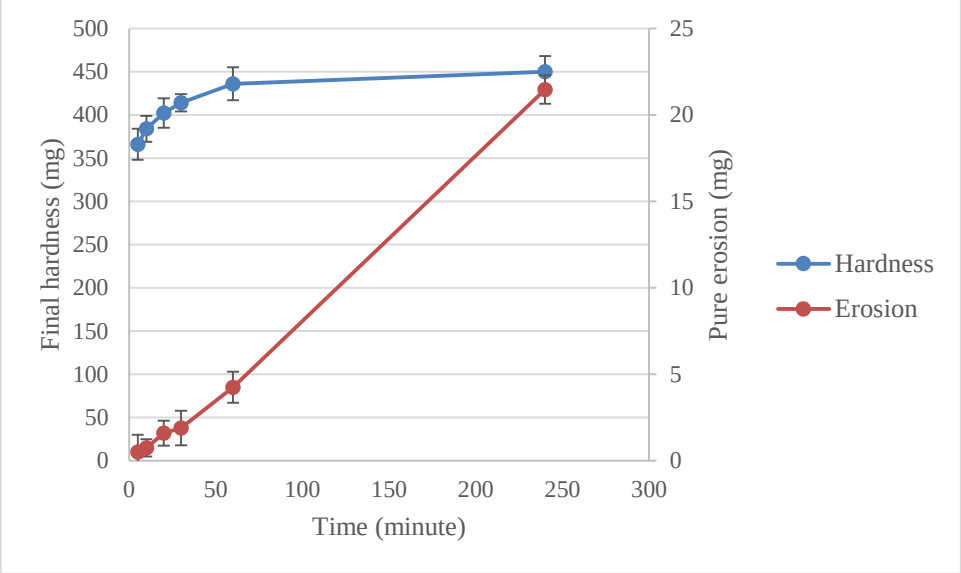

Figure 7-21: The relationship between the final hardness and pure erosion of UNS S31603 as a function of time

Now, the question will be raised is what makes this big difference in terms of erosion resistance although they showed a comparable hardness after deformation? Before answering this question, let us first take a look on Figure 7-22.

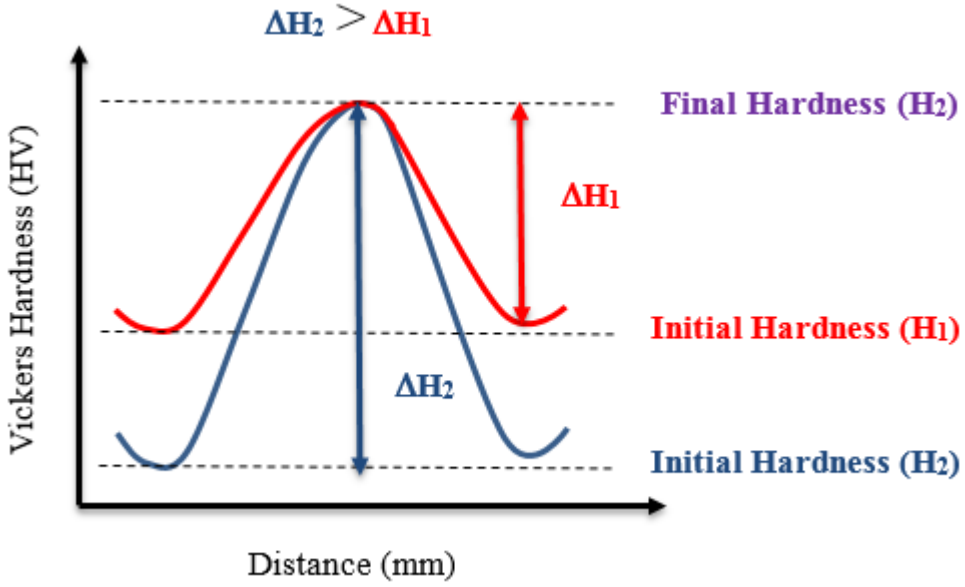

Figure 7-22: Explaining the concept of change in hardness

By analysing the change in hardness, which can be defined as the difference between the final and initial hardness (as – received), it can be noticed that the change in hardness of UNS S31603 was higher than that of UNS S32760 as shown in Figure 7-23. This is in agreement with Aribo *et al.* [90, 129] who found that increase in hardness in the case of UNS S30403 was higher than the one for UNS S32101 and UNS S32205 after erosion at 15 m/s and 500 mg/l sand concentration.

This can probably attributed to differences in their ability to work-hardening. The latter can be implied from what is known as "work-hardening exponent". The higher the work-hardening exponent, the more ability of materials to work-hardening. Work-hardening exponent of UNS S31603 (0.45) [30] is higher than for UNS S32760 (0.1) [159]. Therefore, UNS S31603 showed higher change in hardness than UNS S32760. By comparing the change in hardness of the studied materials with their pure erosion as shown in Figure 7-24 and Figure 7-25, it is clear that this parameter gives more reasonable and accurate trends than the final hardness.

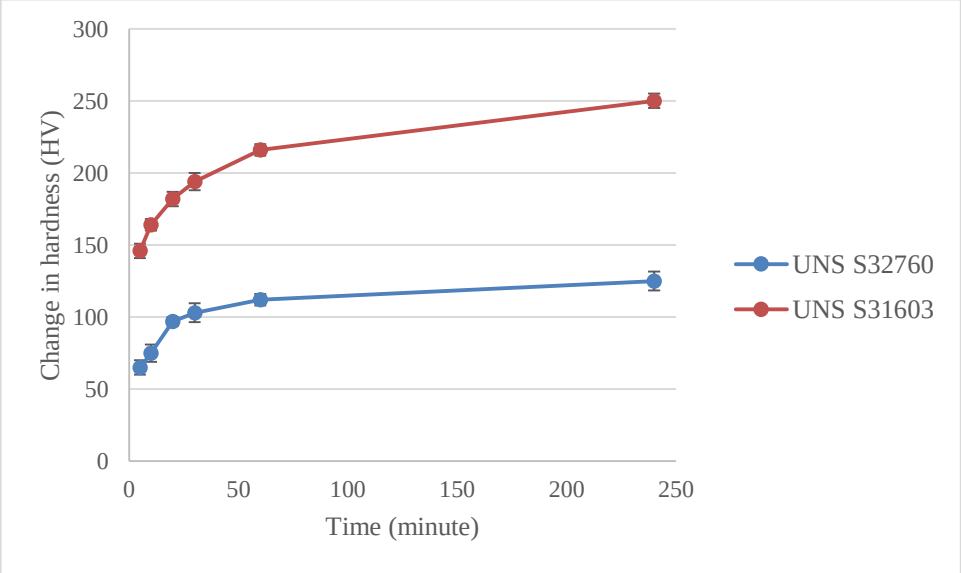

Figure 7-23: The change in hardness of UNS S32760 and UNS S31603 as a function of time

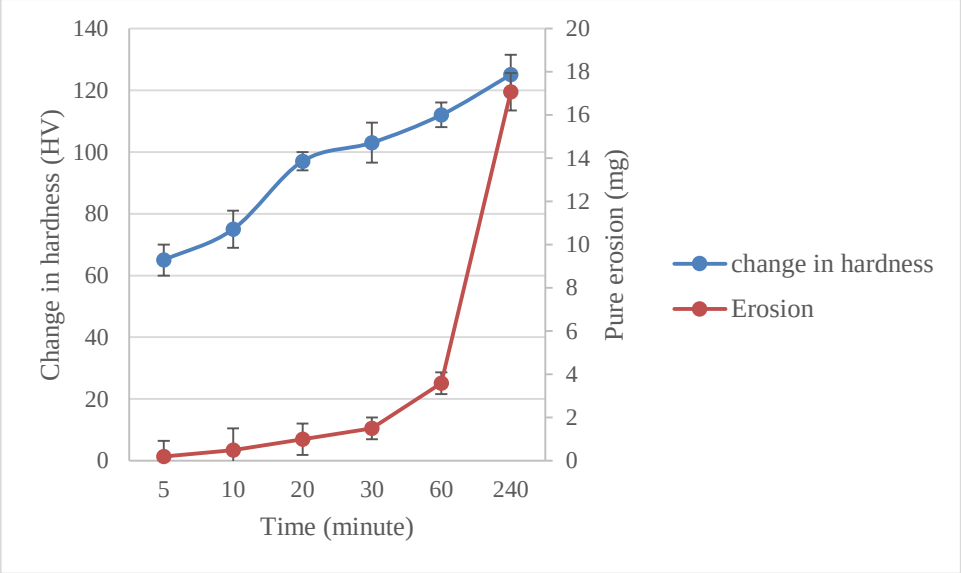

Figure 7-24: The relationship between the change in hardness and pure erosion of UNS S32760 as a function of time

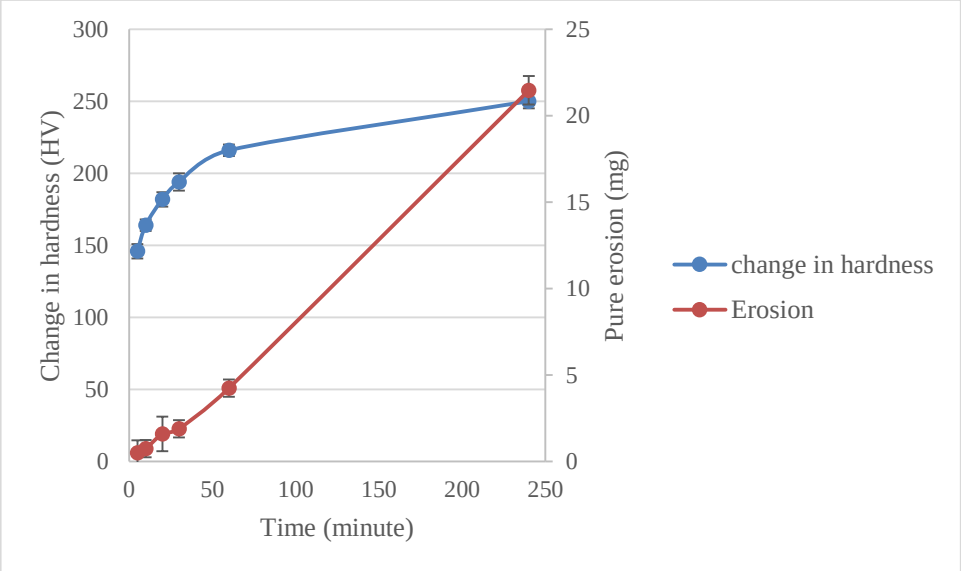

Figure 7-25: The relationship between the change in hardness and pure erosion of UNS S31603 as a function of time

Work-hardening has a significant effect on the mechanical properties of materials. It will lead to an increase in both yield and tensile strength. On the other contrary, the materials ductility will be reduced. So, it is expected that there will be a transition in the materials behaviour from ductile to brittle [160]. As mentioned earlier, UNS S31603 experienced a high change in hardness compared with UNS S32760. This in turn will make the UNS S31603 more brittle than UNS S32760. For this reason, it can

be predicted that sand particles can be embedded within the stagnation area of UNS S31603 [161] (see Figure 5-30) compared with UNS S32760 which showed no or tiny embedded sand particles which is thought to be the sharp edge of particle as can be shown in Figure 5-29. Also, cracks which are resulted from sand particle impact and/or sand embedment were presented within the deformed layer of UNS S31603 at 60 minutes (Figure 5-46) and after wards (Figure 5-47 and Figure 5-48). This was also observed by [160, 161]. However, there were no cracks within the deformed layer of UNS S32760 (Figure 5-50 and Figure 5-51). In terms of brittle materials, higher erosion rates are expected at normal impact angle [21]. So, it is expected that the penetration depth for UNS S31603 which showed brittle behaviour most of the testing time in particular at 60 minutes and afterwards is higher than for UNS S32760. This was confirmed in Figure 5-34. The penetration depth of the studied materials was almost the same until 60 minutes where a distinct difference between the penetration depths of the studied materials was existed.

In order to confirm what has been mentioned in the previous section, a number of tests were done to prove it. It has been mentioned earlier that kinetic energy is a function of particle mass, which is in turn a function of particle diameter, and flow velocity. So, it can be said that changing any of these parameters will affect the kinetic energy of particle and hence the change in hardness and pure erosion degradation rates of the studied materials. For all of the above reasons, both sand particle size and flow velocity (at 500 mg/l sand concentration) were used as candidate factors.

From Figure 7-26 and Figure 7-27, it is obvious that the final hardness of both materials increased, as sand size and flow velocity were increased. Moreover, at mild conditions (for example, at 100 μm particle size or 15 m/s flow velocity), the hardness of material can give an impression about the resistance of material to erosion, as

material with higher hardness shows higher resistance to erosion (green dotted circle). However, the situation will soon change once severe conditions are encountered as material with higher hardness will be less resistant to erosion (red dotted circle). This limits the adoption of the material hardness as an indication to material resistance to erosion particularly in severe environmental conditions

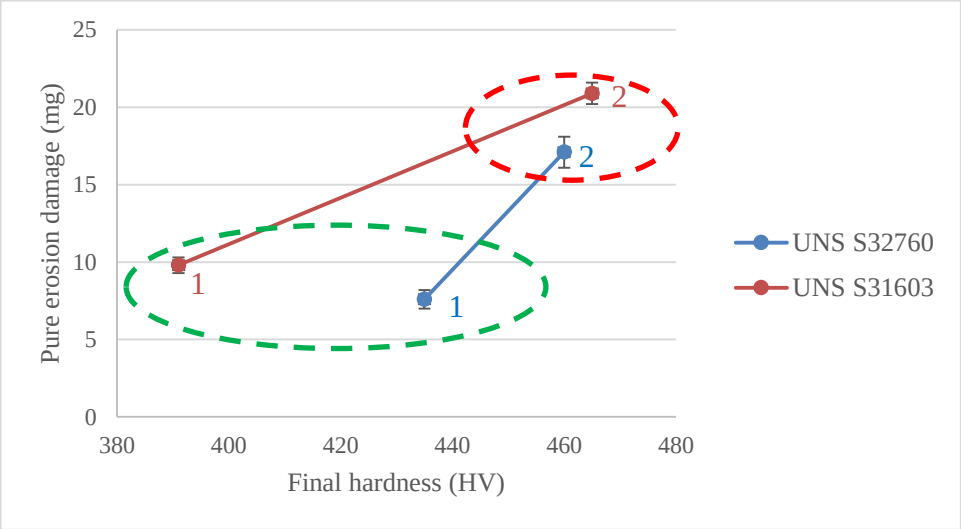

Figure 7-26: The relationship between final hardness and pure erosion of UNS S32760 and UNS S31603 at 20 m/s and 1500 mg/l and at different sand sizes (1) 100 µm and (2) 250 µm

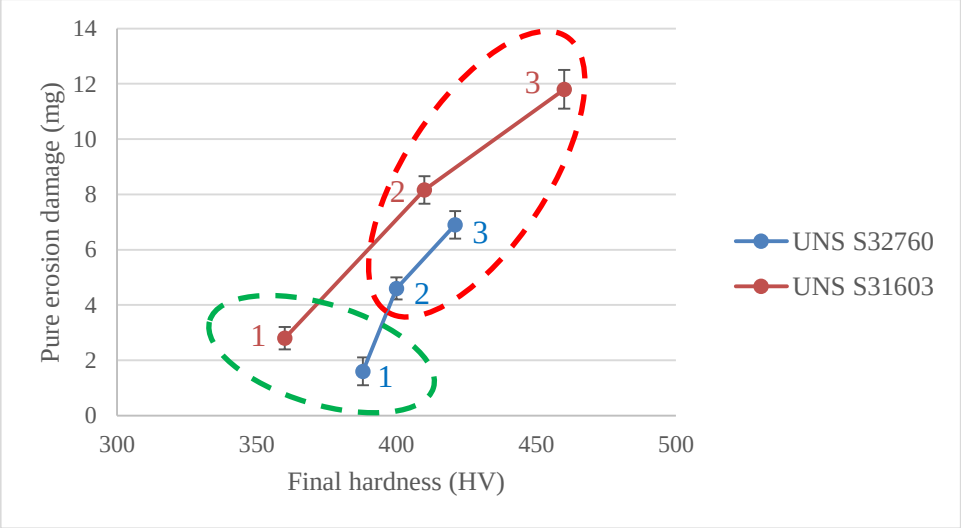

Figure 7-27: The relationship between final hardness and pure erosion of UNS S32760 and UNS S31603 at 250 µm sand size and 500 mg/l sand concentration at different flow velocities (1) 15m/s, (2) 20m/s and (3) 24m/s

By analysing the change in hardness of both materials with their pure erosion degradation rates as shown in Figure 7-28 and Figure 7-29 for UNS S32760 and UNS S31603 respectively, it can be noticed that the change in hardness increased as sand size and flow velocity were increased. Also, weight loss due to pure erosion of both materials increased as the change in hardness increased. Moreover, UNS S31603 showed higher change in hardness compared with UNS S32760 and this in turn led to higher pure erosion.

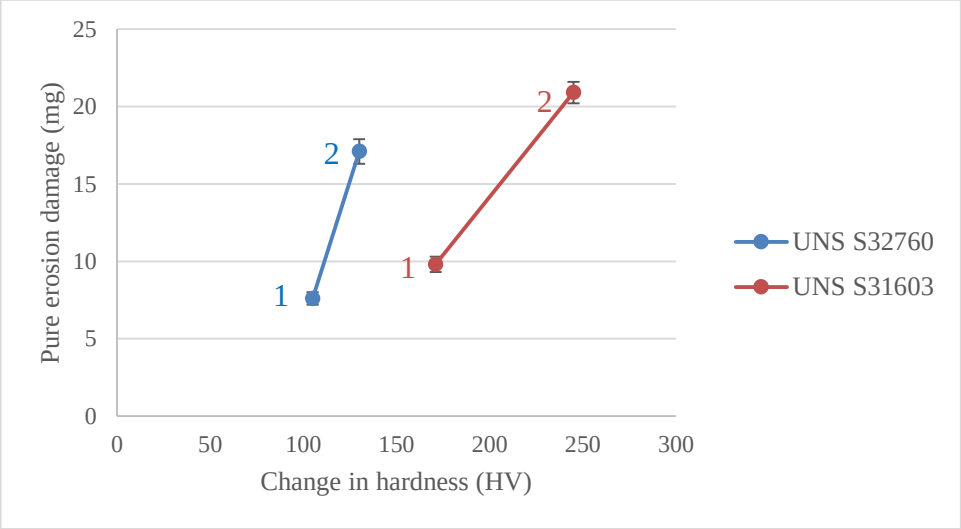

Figure 7-28: The relationship between change in hardness and pure erosion of UNS S32760 and UNS S31603 at 20 m/s flow velocity, 1500 mg/l sand concentration and at different sand sizes (1) 100 µm and (2) 250 µm

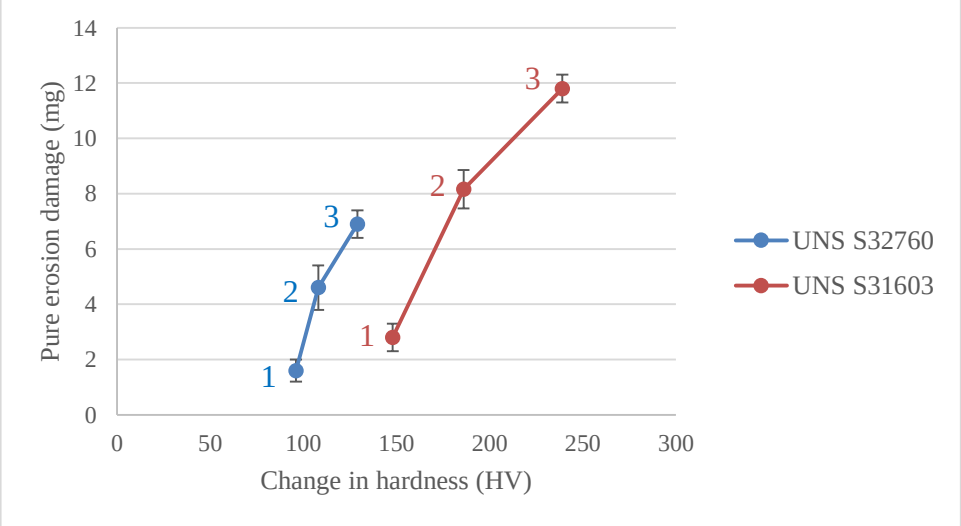

Figure 7-29: The relationship between change in hardness and pure erosion of UNS S32760 and UNS S31603 at 500 mg/l sand concentration (250 µm sand size) and at different flow velocities (1) 15 m/s, (2) 20 m/s and (3) 24 m/s

7.5 Effect of surface deformation on synergy of stainless steels

The most intriguing observation emerged from the obtained results in section 5.4 was the reduction in the corrosion current density and hence erosion-enhanced corrosion of the studied materials as time progresses.

Material hardness is thought to play an important role in erosion-enhanced corrosion. It is confirmed that as the material surface hardened due to sand particles impact with time, the particle energy after a period of time cannot overcome the increase in hardness of the material surface and hence a little area will be depassivated. The surface of material cannot be ripped off and will not be exposed to the corrosive environment and hence erosion-enhanced corrosion will be reduced. Also, this is probably because of ease of chromium diffusion to the surface, which is resulted from high density grain boundaries, and then it will be enriched in the passive film and improves its corrosion resistance [162]. Moreover, it can also probably due to the formation of a more protective passive film on the nanocrystalline surface [163].

Many studies confirmed that corrosion-enhanced erosion is the main component between the TWL components responsible for the distinct difference in the erosion-corrosion resistance of stainless steels. None of these, however, gave a specific concept or even the real reasons behind this behavior. In this study, a number of the obtained findings identified the main causes that may be responsible in some way for this behavior. One of the interesting observation obtained in section 5.5 is that a distinct difference in the corrosion-enhanced erosion of the studied materials at 60 minutes and beyond existed. When sand particles impact the material surface, a part of this surface will be affected by this impact. Consequently, the affected area of material will experience a phase transformation from austenite (FCC) to martensite

(BCT) as can be seen in Figure 5-53 and Figure 5-54. This was also observed by others [129, 134, 161, 164].

It is known that the corrosion resistance of martensite (affected area) is lower than the one of austenite (unaffected area). This can be clearly seen in Figure 5-15 to Figure 5-18. The corrosion rate of the affected and non-affected areas of both materials was significantly different. Also, UNS S31603 showed a higher corrosion rate compared with its counterpart of UNS S32760 as can be seen in Figure 5-19. This difference will encourage a galvanic corrosion between the non-affected and affected areas as can be seen in Figure 5-20. This in turn will be responsible for high anodic dissolution of the affected area in particular for UNS S31603. Presence of cracks within the deformed sub-layer of UNS S31603 (Figure 5-46 and Figure 5-48) underneath the affected area which is highly corroded will ease the material removal. Therefore, the corrosion-enhanced erosion of UNS S31603 was higher than the one of UNS S32760.

7.6 Percentage of contribution of TWL components as a function of impact angle

It should be noted that most of the previous studies have focused largely on evaluating the performance of materials as a function of impact angle through evaluating their TWL and its components. In fact, there have been few studies that have sought to understand the mechanisms of materials removal at different impact angles and to specify the real factors contributed to these mechanisms. Also, the effect of the impact angle on the percentage of contribution of each component of the TWL of stainless steels has not been studied well.

In this section, the percentage of contribution of each component of the total weight loss is determined. This in turn will help to understand how each of these components can affect the general behaviour of the studied materials and will highlight the most influential component that is responsible for a distinct difference in the erosion-corrosion resistance of the studied material at different impact angles and the factors influencing it.

First of all, the percentage of contribution of pure erosion (E%) of the studied materials can be seen in Figure 7-30. The percentage of pure erosion was the highest for all studied materials at different impact angles compared with other components. Also, there was no significant difference in E% of the studied materials as impact angle increases. However, at 75°, there was a remarkable reduction in E%. This probably due to the fact that at high impact angle, the materials may experience an increase in their hardness because of the action of work-hardening [145].

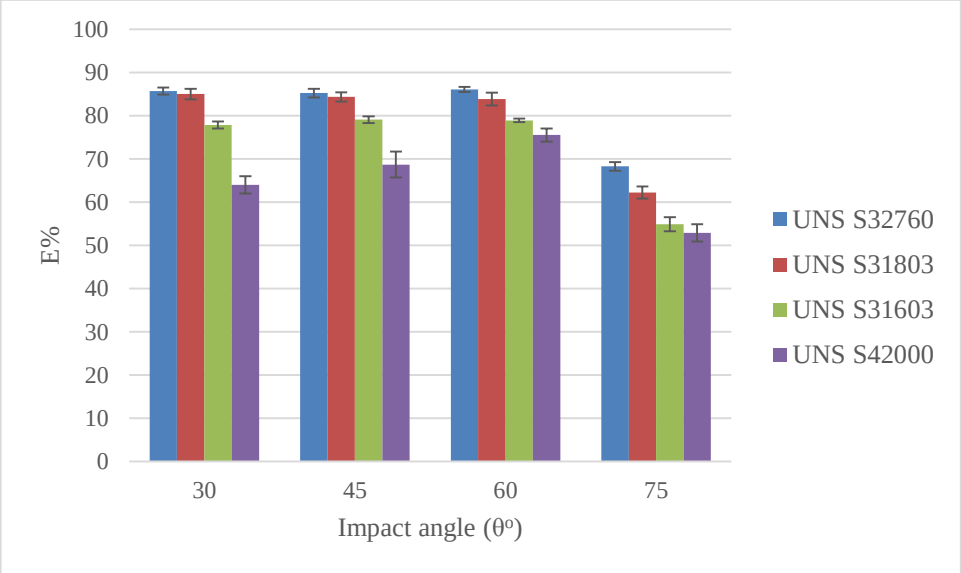

Figure 7-30: The percentage of pure erosion contribution (E%) of the studied materials as a function of impact angle

In terms of the percentage of erosion-enhanced corrosion contribution (dC_E%), UNS S32760, UNS S31803 and UNS S31603 showed a reduction in the dC_E% as the impact

angle was increased as shown in Figure 7-31. The best corrosion resistance of UNS S32760, UNS S31803 and UNS S31603 was found at 60°. This is in accordance with Zhao *et al.* [144] who studied the erosion-corrosion behavior of UNS S31600 at 20.5 m/s, 0.5wt% sand particle concentration and at 45°C at different impact angles and found with the aid of potentiodynamic anodic polarization that the best corrosion resistance of the studied materials was at 60°. This was attributed to the small size holes formed at 60° impact angle resulting from impact of sand particles with the surface of the studied material compared with those formed at 20° and thus the difficulty of the emergence and initiation of pitting corrosion.

UNS S42000 showed an increase in the synergism% with increasing impact angle. This was also observed by Ranjbar *et al.* [142] who studied erosion-corrosion of AISI420 in 3.5wt.% NaCl at 6.5 m/s, 90 g/l sand concentration and at different impact angles (20-90)° as shown in Figure 7-32.

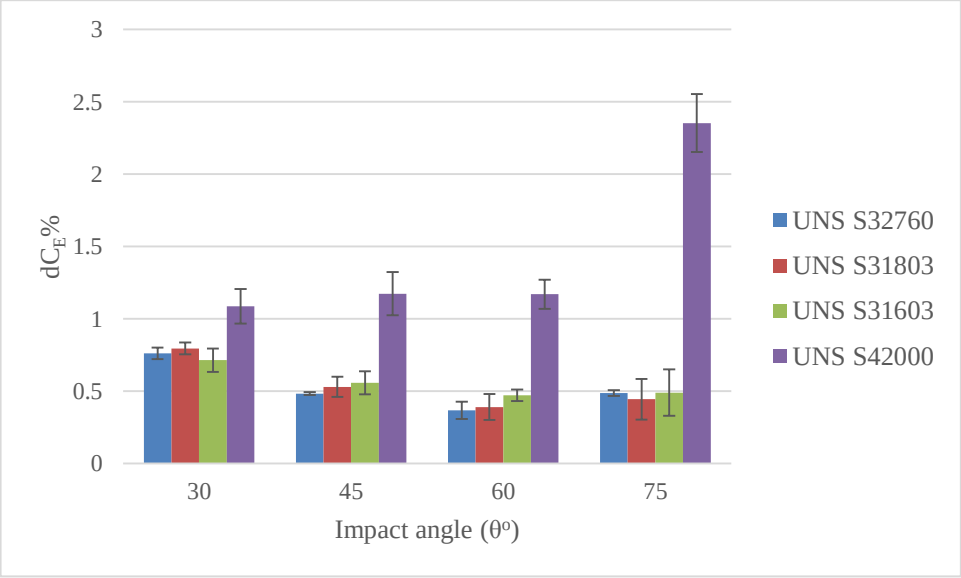

Figure 7-31: The percentage of erosion-enhanced corrosion contribution (dC_E %) of the studied materials as a function of impact angle

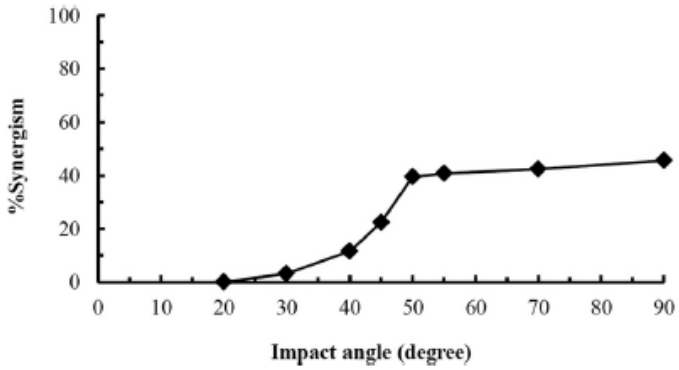

Figure 7-32: Erosion-corrosion synergism of AISI420 as a function of impact angle [142]

Finally, the percentage of corrosion-enhanced erosion contribution (dE_C%) can be shown in Figure 7-33. Clearly, UNS S32760 and UNS S31803 showed lower percentage at all impact angles while dE_C% of UNS S31603 and UNS S42000 was the highest. dE_C% reduced as impact angle was increased. However, there was a sharp increase in dE_C% of all of the studied materials at 75°. This is in agreement with Ghasemi *et al.* [143], who studied the erosion-corrosion behaviour of 316 stainless steel in 3.5wt.% NaCl at 6 m/s and 10wt.% sand loading and found that the synergistic effect was 57%, 37% and 57% at 25°, 55° and 90° impact angle respectively.

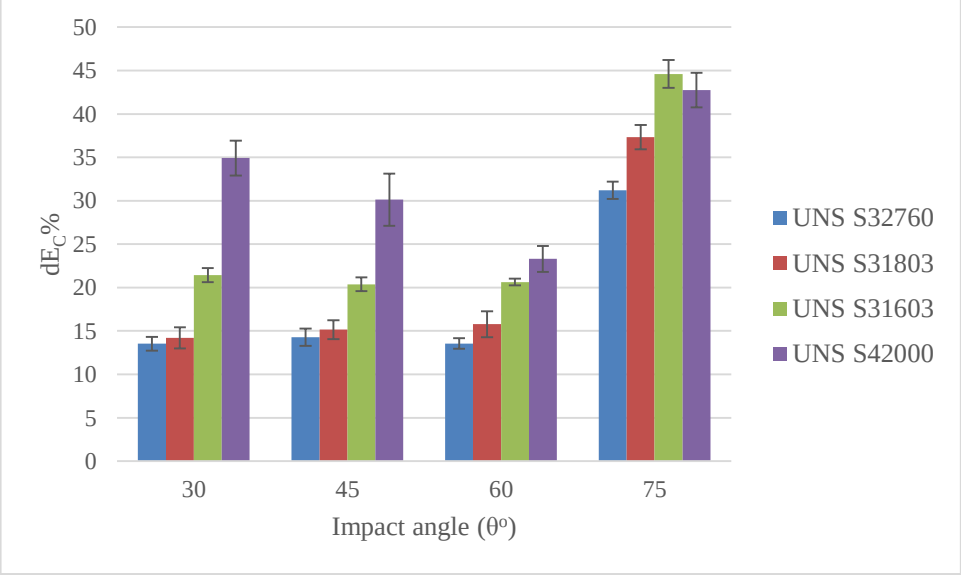

Figure 7-33: The percentage of corrosion-enhanced erosion contribution (dE_C %) of the studied materials as a function of impact angle

It is clear that dE_C% was the influential component which is responsible for the high difference in the material resistance to erosion-corrosion at different impact angles. In the following sections, the main causes for high percentage of corrosion-enhanced erosion contribution of the studied materials at different impact angles will be discussed.

7.6.1 Effect of Pitting Resistance Equivalent Number (PRE_N) on corrosion-enhanced erosion of stainless steels at different impact angle

One of the interesting observations is that UNS S42000 showed lower erosion-corrosion resistance at impact angles 30^o and 45^o compared with UNS S32760 and UNS S31803, although the convergence in their mechanical properties. Interestingly, their pure erosion resistance was almost the same at all impact angles. However, there was a remarkable variation in their corrosion resistance in terms of erosion-enhanced corrosion. It is thought that the significant variance in their PRE_N may has an effective influence on their erosion-corrosion resistance. The corrosion resistance of stainless steels is measured by PRE_N which can be calculated using the following formula:

$$PRE_N = 1 \times \% Cr + 3.3 \times \% Mo + 16 \times \% N$$

PRE_N values are 40, 33 and 13 for UNS S32760, UNS S31803 and UNS S42000 respectively. The effect of PRE_N is evident by its significant effect on several factors which can give an impression about material's resistance to erosion-corrosion. One of these factors is the surface roughness. It is clear from Figure 7-34 that as the impact angle was increased, the surface roughness of all materials decreased. Also, as the PRE_N of the studied materials decreased, their surface roughness increased.

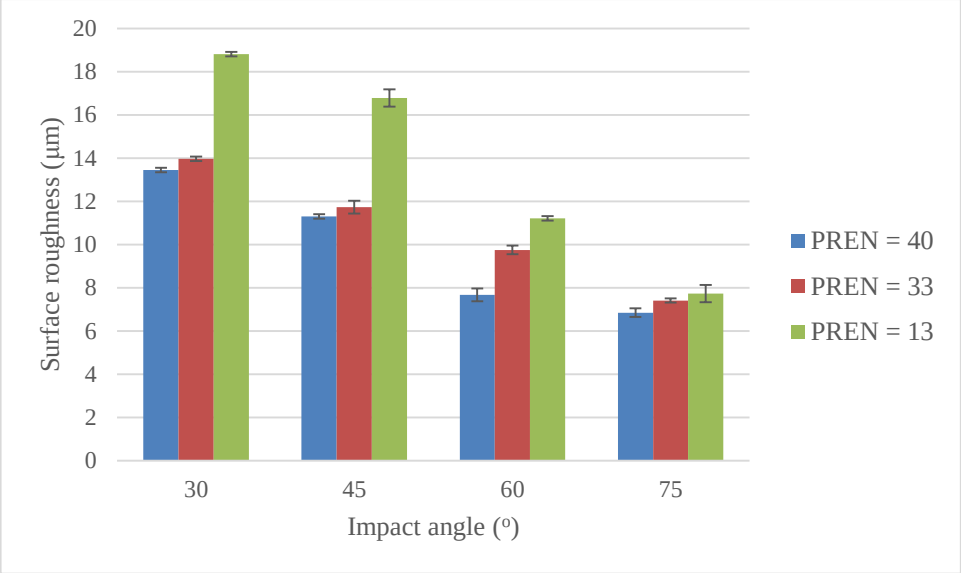

Figure 7-34: The relationship between the surface roughness and PRE_N of the studied materials at different impact angles

Another important factor effectively affected by PRE_N is the wear diameter. Figure 7-35 depicts the relationship between the wear diameter and PRE_N at different impact angles. Clearly, as the impact angle was increased, the wear scar diameter of all materials decreased. Also, as the PRE_N of the studied materials decreased, their wear diameter increased.

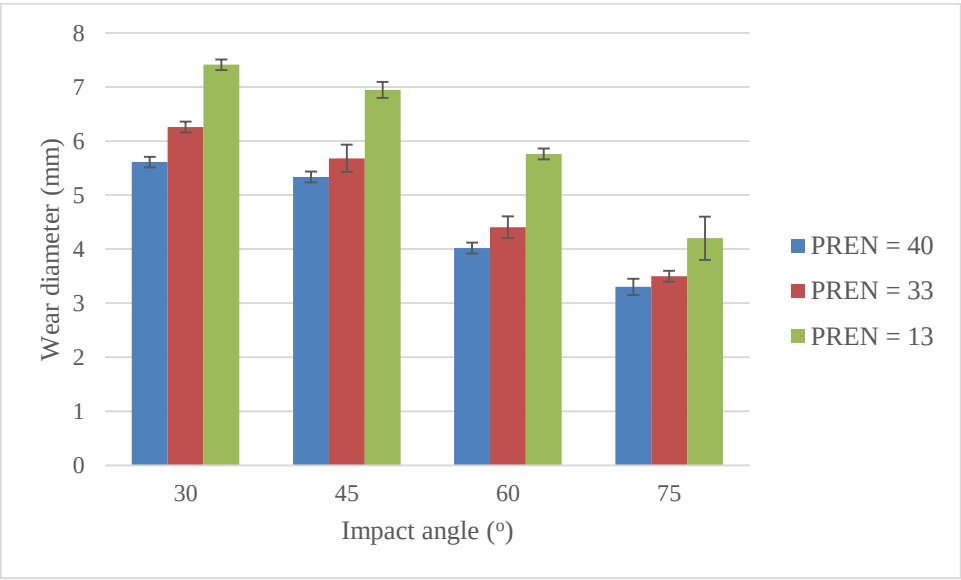

Figure 7-35: The relationship between the wear diameter and PRE_N of the studied materials at different impact angles

One more important observation is that PRE_N affects the penetration depth of the studied materials significantly. Figure 7-36 depicts the relationship between the penetration depth and PRE_N at different impact angles. It is clear from the figure that as the impact angle was increased, the penetration depth of all materials decreased. Also, as the PRE_N of the studied materials decreased, their penetration depth increased.

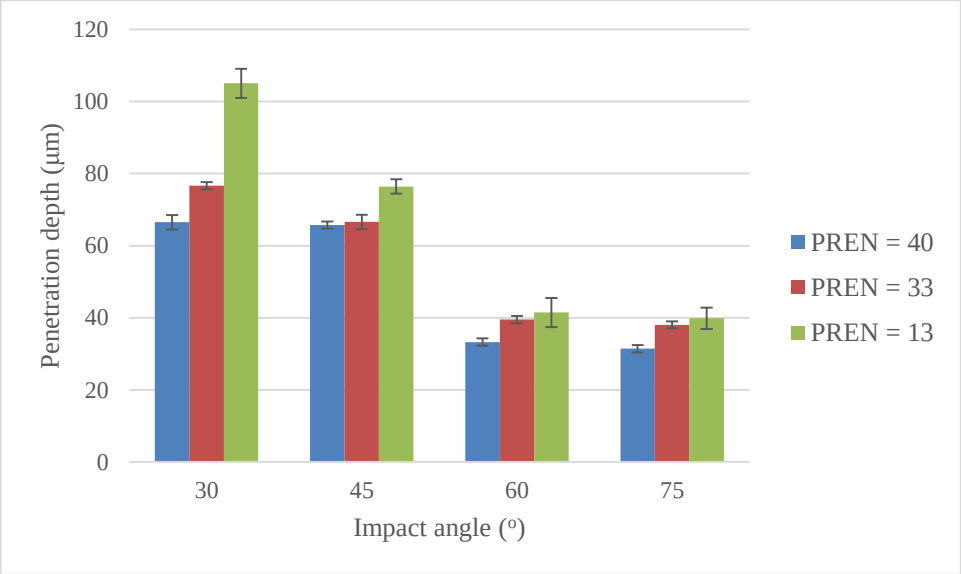

Figure 7-36: The relationship between the penetration depth and PRE_N of the studied materials at different impact angles

Since the mechanical properties of materials are significantly affected by their corrosion resistance, it is expected (especially under high flow conditions) embedment of sand particles in the material surface particularly UNS S42000 due to its low corrosion resistance as can be seen in Figure 6-10. On the other hand, UNS S42000 surface was free from the embedded sand particles after pure erosion as shown in the Figure 6-6. It is clear from above that despite the convergence of the studied materials in the most of their mechanical properties, the variation in their corrosion resistance, which is expressed in terms of PRE_N, plays an influential role in the

susceptibility of materials to resist erosion-corrosion at different impact angles particularly at oblique ones.

7.6.2 The role of sand embedment in corrosion-enhanced erosion of stainless steels

One of the most important observations obtained from section 6.3.1.2 is the presence of sand particles on the material surface of UNS S31603 and UNS S42000. This is in agreement with Ranjbar *et al.* [142] who found that the size of the embedded sand particle (1µm) is much less than the size of the original sand particles used in the test (250-500 µm). This was explained by the fact that the embedded sand particle was just a broken edge of the original sand particle (Figure 7-37).

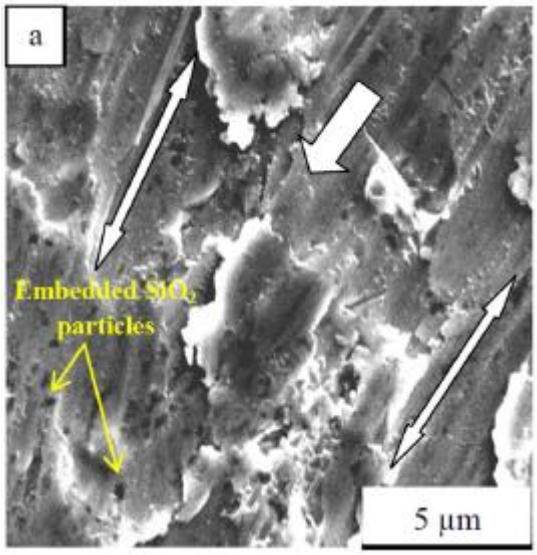

Figure 7-37: SEM images on AISI420 stainless steels surface eroded at 6.5 m/s and at 50^{o} for 45 minutes [142]

When sand particles impact the material surface at an oblique impact angle, materials with low corrosion resistance behaved as a ductile materials due to reduction in their mechanical properties which were affected by the electrochemical corrosion [142]. This in turn will lead to sand embedment within the material surface and longer lips formation than the material with high corrosion resistance (As can be inferred from

the surface roughness data of the studied materials shown in Figure 6-16) and thus removal of the longer lip due to repeated impact of sand particles. This in turn will lead to higher penetration depth (Figure 7-36) and hence higher material degradation [22].

Another scenario may be responsible for the high degradation rates resulting from the sand particle embedment that the impact of a high speed sand particle with another one embedded in the material surface. The repeated impacts result in cracks formation in the embedded sand and then its removal. This in turn will lead to formation of a big hole and a large lips formation that is liable to be removed. This may be exacerbated by supersede of another sand particles and thus repeat the same process and thus increase the penetration depth and hence the erosion rates of material. This effect is illustrated schematically in Figure 7-38.

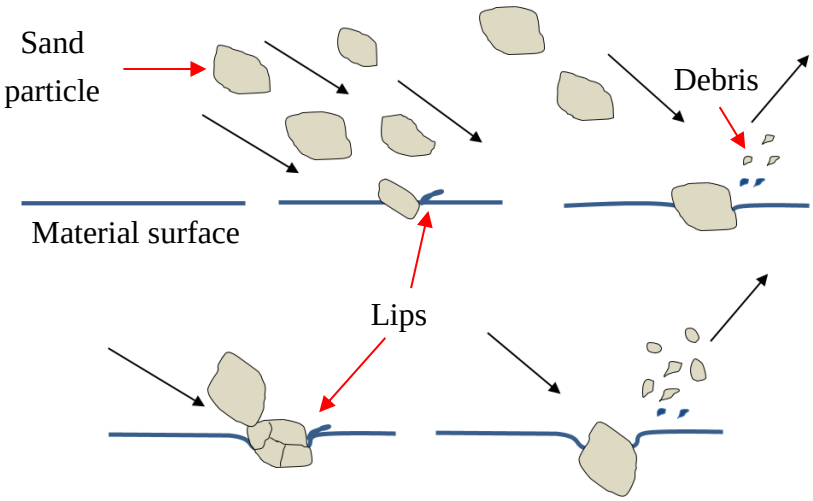

Figure 7-38: The role of embedded sand in corrosion-enhanced erosion of materials at oblique impact angles

7.6.3 Effect of work-hardening on corrosion-enhanced erosion of stainless steels at high impact angle

It has been mentioned in the literature that the surface of the eroded materials at high impact angles will experience less cutting but more work-hardening [142, 143]. However, none of the previous studies have addressed whether the sub-surface of the eroded material will suffer any changes in terms of the microstructure. If so, these changes may have an impact on the erosion-corrosion resistance of materials at the specified impact angle.

One interesting observation obtained with the aid of TEM (Figure 6-18) is the presence of cracks within the sub-surface layer of UNS S31603 and UNS S42000, both of which showed higher corrosion-enhanced erosion compared to the other materials.

It should also be noted that at high impact angles (particularly at high flow velocity), there will be a phase transformation of the austenite to martensite in UNS S32760, UNS S31803 and UNS S31603 (Figure 6-19) and the evolved high corrosion current density was probably due to such transformation as martensite is known for its low corrosion resistance. The presence of these cracks in addition to the effect of corrosion resulting from phase transformation for the austenite containing materials will increase the likelihood of materials removal.

Chapter eight: Conclusions and recommendations for future work

8.1 Conclusions

8.1.1 Conclusions from chapter 4

1- Static corrosion behaviour represented by (E_b-E_r) and (i_{max}) affects erosion-enhanced corrosion of stainless steels as temperature increases in particular at their CPT.

2- Static corrosion behaviour affects the repassivation ability of stainless steels under erosion-corrosion conditions as temperature increases in particular at their CPT.

3- There is a strong link between the repassivation ability of the studied materials under static conditions (i.e. (E_b-E_r) and (i_{max})) and the repassivation time (t^*) under erosion-corrosion conditions.

8.1.2 Conclusions from chapter 5

1- There is no distinct difference in the erosion resistance of UNS S32760 and UNS S31603 at 20 m/s and 1500 mg/l sand concentration for the period of time between 5-30 minutes. However, a difference was suddenly appeared at 60 minutes and afterwards.

2- The hardness of both materials was almost the same at 60 minutes and afterwards.

3- Sand particles were presented on UNS S31603 at most of the test times in particular at 60 minutes and afterwards.

4- Cracks were present either within the sub-deformed layer or even around the embedded sand particles in the case of UNS S31603 while there were no cracks in the case of UNS S32760.

5- The penetration depth difference between the studied materials was significant at 60 minutes and afterwards.

6- The ability of materials to work hardening which is represented by change in hardness seems play a vital role in their erosion resistance particularly in severe conditions.

7- The erosion-enhanced corrosion of the studied materials was slightly different for the period of time between (5-30) minutes and it was equal at 240 minutes.

8- The corrosion-enhanced erosion of both materials was almost the same until 60 minutes and afterwards as it showed a sudden and high increase particularly the one of UNS S31603. It is thought that this because of the surface deformation which enhances the corrosion rates of the studied materials with time especially in the case of UNS S31603 as the latter showed higher corrosion rates. This will lead to a galvanic coupling between the affected (deformed) and non-deformed regions.

8.1.3 Conclusions from chapter 6

1- The percentage of pure erosion contribution for all of the studied materials was the highest compared with the other components. It was almost the same for all of the studied materials at 30, 45 and 60^{o} impact angles. However, lowest values of E% for all materials was obtained at 75^{o}.

2- The percentage of erosion-enhanced corrosion contribution for all of the studied materials was almost the same but UNS S42000 as it showed higher dC_E% in particular at 75^{o} impact angle.

3- The percentage of corrosion-enhanced erosion contribution for all of the studied materials was variant. UNS S31603 and UNS S42000 showed the highest values at all impact angles. At 75°, all of the studied materials showed a sudden increase in dE_C%.

4- In terms of surface analysis, SEM images confirmed presence of embedded sand particles on the material surface of UNS S42000 and UNS S31603 at all impact angles under erosion-corrosion conditions while there was no or very little embedded sand particles on the surfaces of UNS S32760 and UNS S31803. Also, embedded sand particles were not present on the UNS S42000 surface after pure erosion at 30° and 45° impact angles.

5- The highest penetration depth, surface roughness and wear diameter for all of the studied materials were at 30° and 45° impact angles. However, the penetration depth, surface roughness and wear diameter of UNS S32760 and UNS S31803 were lower compared to the other materials. Also, there was no significant difference in the already mentioned parameters for all of the studied materials at 60° and 75° impact angles.

6- PRE_N and sand embedment seem to be responsible for the high corrosion-enhanced erosion percentage of UNS S31603 and UNS S42000 at low impact angles.

7- Work hardening, phase transformation and cracks formation seem to be responsible for the high corrosion-enhanced erosion percentage of all materials especially UNS S31603 and UNS S42000 at high impact angles.

8.1.4 Research Implications

- There is a good link between the static corrosion behaviour and the erosion-corrosion resistance of stainless steels. This link will help to evaluate the erosion-corrosion resistance of commonly used or newly developed materials of similar mechanical properties when it is crucial to take a decision regarding material selection to resist erosion-corrosion under specific operation conditions.
- The change in hardness can be used as an erosion resistance prediction parameter of stainless steels in severe conditions. This will ease the understanding of stainless steels under erosion conditions which is crucial in terms of erosion-corrosion mitigation and modelling.
- The percentage of TWLC contribution is important because it explains the mechanisms by which material is lost under erosion-corrosion conditions. It is something that must be understood if mitigation of erosion-corrosion is to be achieved.

8.2 Recommendations for future work

More works are needed to focus on the stainless steels degradation under erosion-corrosion circumstances following the current study so as to achieve a comprehensive understanding of any remaining ambiguous aspects of this topic. Also, ensuring the smooth flow of production operations without challenges that ultimately lead to the waste a huge amounts of money.

8.2.1 Influence of temperature and erosion time on the chemistry of passive film

Examining the chemical composition of the passive film formed on different types of stainless steels at different temperature before and after erosion-corrosion tests time in both aerated and CO_2-saturated environments using X-Ray Photoelectron Spectroscopy (XPS) technique. This will extend the current knowledge about the influence of the static corrosion behaviour on erosion-corrosion resistance of stainless steels. A range of chloride concentration can also be used to gain a comprehensive understanding.

8.2.2 Linking of the change in hardness with the kinetic energy of sand particles

Evaluating the kinetic energy of the sand particles hit the material surface at different impact angle by Computational Fluid Dynamic (CFD) and then compare it with the change in hardness and the penetration depths of materials. flow velocity in addition to particle size and shape can be changed for better understanding. All of these will effectively contribute to the topic of erosion-corrosion prediction.

8.2.3 Influence of flow velocity on the percentage of the TWL components contribution at different impact angles

The interesting behaviour this study showed was that the percentage of contribution of the TWL components are highly affected by impact angle. It is known that at high flow velocity, such as the one used by this study, the effect of pure erosion will be dominant. The dominancy of any of the TWL components is highly dependent on flow velocity. So, further tests should be carried out using (5, 10, 15) m/s flow velocities. This will allow the investigation of the percentage of the TWL components

contribution at different impact angles. Different types of materials can be used to understand their degradation mechanisms.

Future work should focus also on the evaluating the critical impact angle at which cutting I, cutting II and plastic deformation will take place. This will allow specifying the range of impact angles that any of erosion mechanisms will occur. So, this will help to select the appropriate materials at any of these regions which can withstand at any operation conditions.

References

1. Ahmad, Z., *Principles of corrosion engineering and corrosion control*. 2006: Butterworth-Heinemann.
2. Kutz, M., *Handbook of environmental degradation of materials*. 2005: William Andrew.
3. Kermani, M. and D. Harrop, *The impact of corrosion on oil and gas industry.* SPE Production & Facilities, 1996. 11(03): p. 186-190.
4. Schweitzer, P.A., *Fundamentals of corrosion: mechanisms, causes, and preventative methods*. 2009: CRC Press.
5. Cron, C. and G. Marsh, *Overview of economic and engineering aspects of corrosion in oil and gas production.* Journal of Petroleum Technology, 1983. 35(06): p. 1,033-1,041.
6. Swales, G. and B. Todd. *Nickel-containing alloy piping for offshore oil and gas production*. in *28th Annual Conference of Metallurgists of the Canadian Institute of Mining and Metallurgy. Meeting of Sea and Science, Halifax, Nova Scotia*. 1909.
7. Bargmann, I., Neville, A., Hu, X., Hertzman, S., *Erosion-Corrosion in Oil and Gas- Stainless Steel Under De-Aerated Slurry Impingement Attack*. 2009, National Association of Corrosion Engineers, P. O. Box 218340 Houston TX 77084 USA.
8. Halliburton, *http://halliburtonblog.com/sand-control-mechanism-and-its-impact-on-mature-fields/.* Access Date: 2017.
9. Davis, J.R., *Surface engineering for corrosion and wear resistance*. 2001: ASM international.
10. Hutchings, I.M., *Tribology: friction and wear of engineering materials. Edward Arnold,* 1992.
11. Budinski, K.G., *Guide to friction, wear and erosion testing*. 2007: ASTM International West Conshohocken, PA.
12. Salama, M.M. *Influence of sand production on design and operations of piping systems*. in CORROSION, 2000. NACE International.
13. Landolt, D. and S. Mischler, *Tribocorrosion of passive metals and coatings*. 2011: Elsevier.
14. Finnie, I., *Erosion of surfaces by solid particles.* wear, 1960. 3(2): p. 87-103.

15. Finnie, I. *The mechanism of erosion of ductile metals*. in *3rd US national congress of applied mechanics*. 1958.
16. Bitter, J., *A study of erosion phenomena part I.* wear, 1963. 6(1): p. 5-21.
17. Bitter, J., *A study of erosion phenomena: Part II.* Wear, 1963. 6(3): p. 169-190.
18. Hutchings, I. and P. Shipway, *Tribology: friction and wear of engineering materials*. 2017: Butterworth-Heinemann.
19. Hutchings, I., *Some comments on the theoretical treatment of erosive particle impacts.* 1979.
20. Levy, A.V., *The platelet mechanism of erosion of ductile metals.* Wear, 1986. 108(1): p. 1-21.
21. Baboian, R., *Corrosion tests and standards: application and interpretation*. Vol. 20. 2005: ASTM international.
22. Burstein, G. and K. Sasaki, *Effect of impact angle on the slurry erosion–corrosion of 304L stainless steel.* Wear, 2000. 240(1): p. 80-94.
23. Sun, Y., Babaian-Kibala, E., Hernandez, S., Martin, JW., *Design and Operations Guidelines to Avoid Erosion Problems in Oil and Gas Production Systems-One Operator's Approach*. in *CORROSION*, 2006. NACE International.
24. Chen, Q. and D. Li, *Computer simulation of solid particle erosion.* Wear, 2003. 254(3): p. 203-210.
25. Shewmon, P.G., *Particle size threshold in the erosion of metals.* Wear, 1981. 68(2): p. 253-258.
26. Rajahram, S.S., *Erosion-corrosion mechanisms of stainless steel UNS S31603*. 2010, University of Southampton.
27. Neville, A., Reza, F., Chiovelli, S., Revega, T. , *Erosion–corrosion behaviour of WC-based MMCs in liquid–solid slurries.* Wear, 2005. 259(1): p. 181-195.
28. Dasgupta, R., P. BK, and S. Das, *Effects of sand concentration on slurry erosion of steels.* Materials transactions, JIM, 1998. 39(12): p. 1185-1190.
29. Wood, R.J., *Erosion–corrosion interactions and their effect on marine and offshore materials.* Wear, 2006. 261(9): p. 1012-1023.
30. Sundararajan, G., *The depth of plastic deformation beneath eroded surfaces: The influence of impact angle and velocity, particle shape and material properties.* Wear, 1991. 149(1): p. 129-153.

31. Yang, L., *Techniques for corrosion monitoring*. 2008: Elsevier.
32. Olsson, C.O.A. and D. Landolt, *Passive films on stainless steels—chemistry, structure and growth.* Electrochimica Acta, 2003. 48(9): p. 1093-1104.
33. Bargmann, I.B.M., *MATERIAL SELECTION FOR EROSION-CORROSION IN OIL AND GAS*, in *School of Mechanical Engineering*. 2009, The University of Leeds.
34. Jargelius-Pettersson, R., *Application of the pitting resistance equivalent concept to some highly alloyed austenitic stainless steels.* Corrosion, 1998. 54(2): p. 162-168.
35. El Meguid, E.A. and A.A. El Latif, *Critical pitting temperature for Type 254 SMO stainless steel in chloride solutions.* Corrosion science, 2007. 49(2): p. 263-275.
36. Deng, B., Jiang, Y., Liao, J., Hao, Y., Zhong, C., Li, J., *Dependence of critical pitting temperature on the concentration of sulphate ion in chloride-containing solutions.* Applied surface science, 2007. 253(18): p. 7369-7375.
37. Moayed, M.H., N. Laycock, and R. Newman, *Dependence of the critical pitting temperature on surface roughness.* Corrosion Science, 2003. 45(6): p. 1203-1216.
38. Ebrahimi, N., M.H. Moayed, and A. Davoodi, *Critical pitting temperature dependence of 2205 duplex stainless steel on dichromate ion concentration in chloride medium.* Corrosion Science, 2011. 53(4): p. 1278-1287.
39. Moayed, M.H. and R. Newman, *Deterioration in critical pitting temperature of 904L stainless steel by addition of sulfate ions.* Corrosion Science, 2006. 48(11): p. 3513-3530.
40. Eghbali, F., Moayed, MH., Davoodi, A., Ebrahimi, N., *Critical pitting temperature (CPT) assessment of 2205 duplex stainless steel in 0.1 M NaCl at various molybdate concentrations.* Corrosion Science, 2011. 53(1): p. 513-522.
41. Ernst, P. and R. Newman, *Explanation of the effect of high chloride concentration on the critical pitting temperature of stainless steel.* Corrosion Science, 2007. 49(9): p. 3705-3715.
42. Zakeri, M. and M.H. Moayed, *Investigation on the effect of nitrate ion on the critical pitting temperature of 2205 duplex stainless steel along a mechanistic approach using pencil electrode.* Corrosion Science, 2014. 85: p. 222-231.

43. Ebrahimi, N., Momeni, M., Kosari, A., Zakeri, M., Moayed, M.H., *A comparative study of critical pitting temperature (CPT) of stainless steels by electrochemical impedance spectroscopy (EIS), potentiodynamic and potentiostatic techniques.* Corrosion Science, 2012. 59: p. 96-102.

44. Hoseinpoor, M., Hoseinpoor, M., Momeni, M., Moayed, MH., Davoodi, A., *EIS assessment of critical pitting temperature of 2205 duplex stainless steel in acidified ferric chloride solution.* Corrosion Science, 2014. 80: p. 197-204.

45. Rincon, H.E., R.P. Case, and X. Tang. *Determination Of The Critical Pitting Temperature Of Stainless Steel Using Electrochemical Testing Techniques*. in *CORROSION*, 2012. NACE International.

46. Zhang, T., Wang, D., Shao, Y., Meng, G ., Wang, F., *A new criterion to determine the critical pitting temperature (CPT) based on electrochemical noise measurement.* Corrosion Science, 2012. 58: p. 202-210.

47. Heyn, A., J. Goellner, and A. Burkert. *Determination of critical pitting temperatures using electrochemical noise*. in *CORROSION*, 2004. NACE International.

48. Standard, A., *G150-99,".* Standard Test Method for Electrochemical Critical Pitting Temperature Testing of Stainless Steels, Annual Book of ASTM Standards, Corrosion of Metals; Wear and Erosion, 2010. 03.02.

49. Lee, J.-B., *Effects of alloying elements, Cr, Mo and N on repassivation characteristics of stainless steels using the abrading electrode technique.* Materials Chemistry and Physics, 2006. 99(2): p. 224-234.

50. Park, K.J. and H. Kwon, *Manganese effects on repassivation kinetics and SCC susceptibility of high Mn–N austenitic stainless steel alloys.* Journal of the Electrochemical Society, 2007. 154(9): p. C494-C499.

51. Lu, B., Luo, JL., Mohammadi, F., Wang, K., Wan, XM., *Correlation between repassivation kinetics and corrosion rate over a passive surface in flowing slurry.* Electrochimica Acta, 2008. 53(23): p. 7022-7031.

52. Fernández-Domene, R., Fernández-Domene, RM., Blasco-Tamarit, E., Garcia-Garcia, DM., Garcia-Anton, J., *Repassivation of the damage generated by cavitation on UNS N08031 in a LiBr solution by means of electrochemical techniques and Confocal Laser Scanning Microscopy.* Corrosion Science, 2010. 52(10): p. 3453-3464.

53. Yamamoto, T., Fushimi, K., Seo, M., Tsuri, S., Adachi, T., Habazaki, H., *Depassivation–repassivation behavior of type-312L stainless steel in NaCl solution investigated by the micro-indentation.* Corrosion Science, 2009. 51(7): p. 1545-1553.

54. Fushimi, K., Takase, K., Azumi, K., Seo, M., *Current transients of passive iron observed during micro-indentation in pH 8.4 borate buffer solution.* Electrochimica acta, 2006. 51(7): p. 1255-1263.

55. Sun, D., J. Wharton, and R. Wood, *Micro-and nano-scale tribo-corrosion of cast CoCrMo.* Tribology letters, 2011. 41(3): p. 525-533.

56. Fushimi, K., Shimada, T., Habazaki, H., Konno, H., Seo, M., *Mechano-electrochemistry of a passive surface using an in situ micro-indentation test.* Electrochimica Acta, 2011. 56(4): p. 1773-1780.

57. Seo, M., M. Chiba, and K. Suzuki, *Nano-mechano-electrochemistry of the iron (100) surface in solution.* Journal of Electroanalytical Chemistry, 1999. 473(1): p. 49-53.

58. Smith, A.J., M. Stratmann, and A.W. Hassel, *Investigation of the effect of impingement angle on tribocorrosion using single impacts.* Electrochimica acta, 2006. 51(28): p. 6521-6526.

59. McMahon, A. and J. Martin, *Simulation tests on the effects of mechanical damage or acid cleaning on corrosion resistant alloys used for oil/gas production well tubulars.* Corrosion/2004, paper, 2004(4127).

60. Rincon, H., J.R. Shadley, and E.F. Rybicki, *Erosion Corrosion Phenomena of 13Cr at Low Sand Rate Levels.* CORROSION, 2005. NACE International.

61. Rincon, H., Shadley, JR., Roberts, KP., Rybicki, EF., *Erosion-Corrosion of Corrosion Resistant Alloys Used in the Oil and Gas Industry.* CORROSION, 2008. NACE International.

62. Aribo, S., *Corrosion and Erosion-Corrosion Behaviour of Lean Duplex Stainless Steels in Marine and Oilfield Environments*, in *School of Mechanical Engineering*. The University of Leeds.

63. *ASM Handbook*, B.S.C. S.D.Cramer, Jr., Editor. 2005.

64. Popoola, L.T., Grema, AS., Latinwo, GK., Gutti, B., *Corrosion problems during oil and gas production and its mitigation.* International Journal of Industrial Chemistry, 2013. 4(1): p. 35.

65. Brondel, D., Edwards, R., Hayman, A., Hill, D., Mehta, S., Semerad, T., *Corrosion in the Oil Industry.* Journal of Petroleum Technology, 1987. 39: p. 756-762.

66. Kelland, M.A., *Production chemicals for the oil and gas industry*. 2014: CRC press.

67. Barker, R.J., *Erosion-Corrosion of Carbon Steel Pipework on an Offshore Oil and Gas Facility*, in *Mechanical Engineering*. 2012, The University of Leeds.

68. Dugstad, A., *Fundamental aspects of CO_2 metal loss corrosion-part 1: mechanism.* CORROSION, 2006. NACE International.

69. Kermani, M. and A. Morshed, *Carbon dioxide corrosion in oil and gas production-A compendium.* Corrosion, 2003. 59(8): p. 659-683.

70. Schmitt, G. and M. Horstemeier, *Fundamental aspects of CO_2 metal loss corrosion-Part II: Influence of different parameters on CO_2 corrosion mechanisms.* CORROSION, 2006. NACE International.

71. Ezuber, H.M., *Influence of temperature on the pitting corrosion behavior of AISI 316L in chloride–CO 2 (sat.) solutions.* Materials & Design, 2014. 59: p. 339-343.

72. Costa, E.V.d., Mesquita, TJ., Ferreira, A., Nogueira, RP., *Effect of carbon dioxide and temperature on passive film parametersof superduplex stainless steel.* Materials Research, 2013. 16(4): p. 929-936.

73. Zhang, H., Y. Zhao, and Z. Jiang, *Effects of temperature on the corrosion behavior of 13Cr martensitic stainless steel during exposure to CO_2 and Cl^- environment.* Materials Letters, 2005. 59(27): p. 3370-3374.

74. Kimura, M., K. Sakata, and K. Shimamoto. *Corrosion resistance of martensitic stainless steel OCTG in severe corrosion environments*. in CORROSION, 2007. NACE International.

75. Aribo, S., A. Neville, and X. Hu, *Pitting Behaviour of Lean Duplex Stainless Steels in Marine and Oilfield Environments*. Society of Petroleum Engineers.

76. Payer, N.G.T.a.J.H., *DC Electrochemical Test Methods*. 1998: Natl Assn of Corrosion.

77. Hu, X. and A. Neville, *The electrochemical response of stainless steels in liquid–solid impingement.* Wear, 2005. 258(1): p. 641-648.

78. Zheng, Y.G., Z.M. Yao, and W. Ke, *Erosion–corrosion resistant alloy development for aggressive slurry flows.* Materials Letters, 2000. 46(6): p. 362-368.
79. Giourntas, L., T. Hodgkiess, and A. Galloway, *Comparative study of erosion–corrosion performance on a range of stainless steels.* Wear, 2015. 332: p. 1051-1058.
80. Meng, H., X. Hu, and A. Neville, *A systematic erosion–corrosion study of two stainless steels in marine conditions via experimental design.* Wear, 2007. 263(1): p. 355-362.
81. Revie, R.W., *Oil and Gas Pipelines: Integrity and Safety Handbook*. 2015: John Wiley & Sons.
82. Uhlig, H.H. and R.W. Revie, *Uhlig's corrosion handbook*. Vol. 51. 2011: John Wiley & Sons.
83. Barton, N., *Erosion in elbows in hydrocarbon production systems: Review document.* Health & Safety Executive, TUV NEL Limited, Glasgow, 2003.
84. Rincon, H., J.R. Shadley, and J.F. Chen, *Erosion Corrosion Phenomena of 13Cr Alloy in Flows Containing Sand Particles.* CORROSION, 2002.
85. Davis, J.R., *Corrosion: Understanding the basics*. 2000: ASM International.
86. Efird, K.D., *Jet impingement testing for flow accelerated corrosion.* CORROSION, 2000. NACE International.
87. Efird, K.D., *Jet Impingement Testing for Flow Accelerated Corrosion*. NACE International.
88. Roberge, P.R., *Erosion corrosion*. Vol. 8. 2004: Natl Assn of Corrosion.
89. Hu, X. and A. Neville, *An examination of the electrochemical characteristics of two stainless steels (UNS S32654 and UNS S31603) under liquid–solid impingement.* Wear, 2004. 256(5): p. 537-544.
90. Aribo, S., Barker, R., Hu, X., Neville, A., *Erosion–corrosion behaviour of lean duplex stainless steels in 3.5% NaCl solution.* Wear, 2013. 302(1–2): p. 1602-1608.
91. Madsen, B.W., *Measurement of erosion-corrosion synergism with a slurry wear test apparatus.* Wear, 1988. 123(2): p. 127-142.
92. Wood, R. and S. Hutton, *The synergistic effect of erosion and corrosion: trends in published results.* Wear, 1990. 140(2): p. 387-394.

93. Stack, M., S. Zhou, and R. Newman, *Identification of transitions in erosion-corrosion regimes in aqueous environments.* Wear, 1995. 186: p. 523-532.

94. Neville, A. and X. Hu, *Assessing the Role of Corrosion in Erosion-Corrosion of High Grade Alloys in Aggressive Marine Environments.* CORROSION, 2002.

95. Zheng, Z. and Y. Zheng, *Erosion-enhanced corrosion of stainless steel and carbon steel measured electrochemically under liquid and slurry impingement.* Corrosion Science, 2016. 102: p. 259-268.

96. Zheng, Z., Zheng, YG., Zhou, X., He, SY., Sun, WH., *Determination of the critical flow velocities for erosion–corrosion of passive materials under impingement by NaCl solution containing sand.* Corrosion Science, 2014. 88: p. 187-196.

97. Neville, A., M. Reyes, and H. Xu, *Examining corrosion effects and corrosion/erosion interactions on metallic materials in aqueous slurries.* Tribology International, 2002. 35(10): p. 643-650.

98. Bermúdez, M.-D., Carrión, FJ., Martínez-Nicolás, G., Lopez, R., *Erosion–corrosion of stainless steels, titanium, tantalum and zirconium.* Wear, 2005. 258(1): p. 693-700.

99. Hussain, E.A.M. and M.J. Robinson, *Erosion–corrosion of 2205 duplex stainless steel in flowing seawater containing sand particles.* Corrosion Science, 2007. 49(4): p. 1737-1754.

100. Neville, A., T. Hodgkiess, and J. Dallas, *A study of the erosion-corrosion behaviour of engineering steels for marine pumping applications.* Wear, 1995. 186: p. 497-507.

101. He, D., Jiang, XX., Li, SZ., Guan, HR., *Erosion-corrosion of stainless steels in aqueous slurries—a quantitative estimation of synergistic effects.* Corrosion, 2005. 61(1): p. 30-36.

102. Malka, R., S. Nešić, and D.A. Gulino, *Erosion–corrosion and synergistic effects in disturbed liquid-particle flow.* Wear, 2007. 262(7): p. 791-799.

103. Zheng, Y., Yao, Z., Wei, X., Ke, W., *The synergistic effect between erosion and corrosion in acidic slurry medium.* Wear, 1995. 186: p. 555-561.

104. Zhou, S., M. Stack, and R. Newman, *Electrochemical studies of anodic dissolution of mild steel in a carbonate-bicarbonate buffer under erosion-corrosion conditions.* Corrosion Science, 1996. 38(7): p. 1071-1084.

105. Burstein, G. and K. Sasaki, *The birth of corrosion pits as stimulated by slurry erosion.* Corrosion Science, 2000. 42(5): p. 841-860.

106. Neville, A. and T. Hodgkiess, *Characterisation of high-grade alloy behaviour in severe erosion–corrosion conditions.* Wear, 1999. 233: p. 596-607.

107. Dong, C.F., Xiao, K., Li, XG., Cheng, YF., *Erosion accelerated corrosion of a carbon steel–stainless steel galvanic couple in a chloride solution.* Wear, 2010. 270(1–2): p. 39-45.

108. Guo, H., B. Lu, and J. Luo, *Interaction of mechanical and electrochemical factors in erosion–corrosion of carbon steel.* Electrochimica Acta, 2005. 51(2): p. 315-323.

109. Islam, M.A. and Z.N. Farhat, *The synergistic effect between erosion and corrosion of API pipeline in CO_2 and saline medium.* Tribology International, 2013. 68: p. 26-34.

110. Neville, A., Reyes, M., Hodgkiess, T., Gledhill, A., *Mechanisms of wear on a Co-base alloy in liquid–solid slurries.* Wear, 2000. 238(2): p. 138-150.

111. Li, Y., G. Burstein, and I. Hutchings, *The influence of corrosion on the erosion of aluminium by aqueous silica slurries.* Wear, 1995. 186: p. 515-522.

112. Lu, B. and J. Luo, *Correlation between surface-hardness degradation and erosion resistance of carbon steel—Effects of slurry chemistry.* Tribology International, 2015. 83: p. 146-155.

113. Bidiville, A., Favero, M., Stadelmann, P., Mischler , S., *Effect of surface chemistry on the mechanical response of metals in sliding tribocorrosion systems.* Wear, 2007. 263(1): p. 207-217.

114. Garverick, L., *Corrosion in the petrochemical industry*. 1994: ASM international.

115. Cragnolino, G., *Application of accelerated corrosion tests to service life prediction of materials*. Vol. 4. 1994: ASTM International.

116. Heidersbach, R., *Metallurgy and corrosion control in oil and gas production*. Vol. 14. 2010: John Wiley & Sons.

117. Baboian, R.R.B., *Corrosion tests and standards: application and interpretation*. 2005.

118. Lula, R.A., *Stainless steel.United States:N.P.,*1985.Web.

119. Bhadeshia, H. and R. Honeycombe, *Steels: microstructure and properties*. 2017: Butterworth-Heinemann.

120. Leffler, B., *Stainless steels and their properties.* AvestaPolarit AB, 1996: p. 1-45.
121. Davis, J.R., *Stainless steels*. 1994: ASM international.
122. Sedriks, A.J., *Corrosion of stainless steel, 2.* 1996.
123. McCafferty, E., *Introduction to corrosion science*. 2010: Springer Science & Business Media.
124. Neville, A. and X. Hu, *Mechanical and electrochemical interactions during liquid–solid impingement on high-alloy stainless steels.* Wear, 2001. 251(1–12): p. 1284-1294.
125. Neville, A. and X. Hu, *Assessment of electrochemical response from high alloy stainless steels during slurry impingement and single impacts to improve understanding of erosion–corrosion.* British Corrosion Journal, 2002. 37(1): p. 43-47.
126. Hu, X. and A. Neville, *The effect of an impinging liquid-solid jet on the electrochemical corrosion of stainless steels.* Materials and Corrosion, 2001. 52(8): p. 598-606.
127. Neville, A. and X. Hu, *Assessing the Role of Corrosion in Erosion-Corrosion of High Grade Alloys in Aggressive Marine Environments*. NACE International.
128. Chen, J., J.R. Shadley, and E.F. Rybicki. *Effect of Temperature on the Erosion-Corrosion of 13Cr*. in CORROSION, 2003. NACE International.
129. Aribo, S., Bryant, M., Neville, A., Hu, X., *Erosion-Corrosion of Lean Duplex Stainless Steel (UNS S32101) in a CO_2-Saturated Oilfield Brine.* Proceedings of CORROSION/2013, NACE International, Houston, TX, Paper, 2013(2382).
130. Büscher, R. and A. Fischer, *The pathways of dynamic recrystallization in all-metal hip joints.* Wear, 2005. 259(7): p. 887-897.
131. Rajahram, S., Harvey, TJ., Walker, JC., Wang, SC., Wood, RJK., Lalev, G., *A study on the evolution of surface and subsurface wear of UNS S31603 during erosion–corrosion.* Wear, 2011. 271(9): p. 1302-1313.
132. Rajahram, S., Harvey, TJ., Walker, JC., Wang, SC., Wood, RJK., *Investigation of erosion–corrosion mechanisms of UNS S31603 using FIB and TEM.* Tribology international, 2012. 46(1): p. 161-173.

133. Wood, R., Walker, JC., Harvey, TJ., Wang, S., Rajahram, SS., *Influence of microstructure on the erosion and erosion–corrosion characteristics of 316 stainless steel.* Wear, 2013. 306(1): p. 254-262.

134. Aribo, S., Barker, R., Hu, X., Neville, A., *Erosion–corrosion behaviour of lean duplex stainless steels in 3.5% NaCl solution.* Wear, 2013. 302(1): p. 1602-1608.

135. Islam, M.A. and Z.N. Farhat, *Effect of impact angle and velocity on erosion of API X42 pipeline steel under high abrasive feed rate.* Wear, 2014. 311(1): p. 180-190.

136. Elsamani, M., A. Neville, and J. Ukpai. *Experimental Approach to Evaluate the Effect of Impact Angle on Erosion and Erosion-Corrosion Using Acoustic Emission*. in CORROSION, 2016. NACE International.

137. Hemmati, A., M. Soltanieh, and S. Masoudpanah, *Effect of Flow Velocity and Impact Angle on Erosion–Corrosion Behavior of Chromium Carbide Coating.* Journal of Tribology, 2017. 139(3): p. 031303.

138. Pasha, A., H. Ghasemi, and J. Neshati, *Synergistic Erosion–Corrosion Behavior of X-65 Carbon Steel at Various Impingement Angles.* Journal of Tribology, 2017. 139(1): p. 011105.

139. Abedini, M. and H. Ghasemi, *Synergistic erosion–corrosion behavior of Al–brass alloy at various impingement angles.* Wear, 2014. 319(1): p. 49-55.

140. Azarian, N.S., H.M. Ghasemi, and M.R. Monshi, *Synergistic Erosion and Corrosion Behavior of AA5052 Aluminum Alloy in 3.5 wt% NaCl Solution Under Various Impingement Angles.* Journal of Bio- and Tribo-Corrosion, 2015. 1(2): p. 10.

141. Lopez, D., Congote, JP., Cano, JR., Toro, A., Tschiptschin, AP., *Effect of particle velocity and impact angle on the corrosion–erosion of AISI 304 and AISI 420 stainless steels.* Wear, 2005. 259(1): p. 118-124.

142. Ranjbar, M., H. Ghasemi, and M. Abedini, *Effect of Impact Angle on the Erosion–Corrosion Behavior of AISI 420 Stainless Steel in 3.5 wt.% NaCl Solution.* Journal of Tribology, 2015. 137(3): p. 031604.

143. Ghasemi, H., Karimi, M., Pasha, A., Abedini, M., *Erosion-corrosion behavior of 316-SS in seawater simulated environment at various impingement angles*. in *Proceedings of Regional Tribology Conference 2011: RTC2011*. 2011. Malaysian Tribology Society.

144. Zhao, Y., Zhou, F., Yao, J., Dong, S., Li, N., *Erosion–corrosion behavior and corrosion resistance of AISI 316 stainless steel in flow jet impingement.* Wear, 2015. 328: p. 464-474.

145. Andrews, N., Giourntas, L., Galloway, AM., Pearson, A., *Effect of impact angle on the slurry erosion-corrosion of Stellite 6 and SS316.* Wear, 2014. 320: p. 143-151.

146. Pardo, A., Merino, MC., Coy, AE., Viejo, F., Arrabal, R., Matykina, E., *Pitting corrosion behaviour of austenitic stainless steels – combining effects of Mn and Mo additions.* Corrosion Science, 2008. 50(6): p. 1796-1806.

147. Martin, J.W. and A.J. McMahon. *Simulation Tests On The Effects Of Mechanical Damage O Acid Cleaning On Corrosion Resistant Alloys Used For Oil/Gas Production Well Tubulars*. in CORROSION, 2004. NACE International.

148. Rincon, H., J.R. Shadley, and E.F. Rybicki. *Erosion Corrosion Phenomena of 13Cr at Low Sand Rate Levels*. in CORROSION, 2005. NACE International.

149. Neville, A. and T. Hodgkiess, *An assessment of the corrosion behaviour of high-grade alloys in seawater at elevated temperature and under a high velocity impinging flow*. Corrosion Science, 1996. 38(6): p. 927-956.

150. Dong, C., Luo, H., Xiao, K., Sun, T., Liu, Q., Li , X., *Effect of temperature and Cl− concentration on pitting of 2205 duplex stainless steel.* Journal of Wuhan University of Technology-Mater. Sci. Ed., 2011. 26(4): p. 641-647.

151. Anselmo, N., May, JE., Mariano, NA., Nascente, PAP., Kuri, SE., *Corrosion behavior of supermartensitic stainless steel in aerated and CO_2-saturated synthetic seawater.* Materials Science and Engineering: A, 2006. 428(1): p. 73-79.

152. Park, J., S. Matsch, and H. Böhni, *Effects of temperature and chloride concentration on pit initiation and early pit growth of stainless steel.* Journal of the Electrochemical Society, 2002. 149(2): p. B34-B39.

153. Wang, J., C. Su, and Z. Szklarska-Smialowska, *Effects of Cl− concentration and temperature on pitting of AISI 304 stainless steel.* Corrosion, 1988. 44(10): p. 732-737.

154. Rincon, H., Shadley, JR., Roberts, KP., Rybicki EF., *Erosion-corrosion of corrosion resistant alloys used in the oil and gas industry*. in CORROSION, 2008. NACE International.

155. Luo, H., Wang, X., Dong, C., Xiao, K., Li, X., *Effect of cold deformation on the corrosion behaviour of UNS S31803 duplex stainless steel in simulated concrete pore solution.* Corrosion Science, 2017.

156. Peguet, L., B. Malki, and B. Baroux, *Influence of cold working on the pitting corrosion resistance of stainless steels.* Corrosion Science, 2007. 49(4): p. 1933-1948.

157. Staehle, R.W., *Transient stability of passive films in aqueous solutions.* Corrosion Science, 2007. 49(1): p. 7-19.

158. Wang, X.Y. and D.Y. Li, *Mechanical and electrochemical behavior of nanocrystalline surface of 304 stainless steel.* Electrochimica Acta, 2002. 47(24): p. 3939-3947.

159. Tavares, S.S.M., Pardal, JM., Abreu, HFG., Nunes, CS., Ribeiro da Silva, M., *Tensile properties of duplex UNS S32205 and lean duplex UNS S32304 steels and the influence of short duration 475 ºC aging.* Materials Research, 2012. 15(6): p. 859-864.

160. Aribo, S., *Corrosion and erosion-corrosion behaviour of lean duplex stainless steels in marine and oilfield environments*. 2014, University of Leeds.

161. Rajahram, S.S., Harvey, TJ., Walker, JC., Wang, SC., Wood, RJK., *Investigation of erosion–corrosion mechanisms of UNS S31603 using FIB and TEM.* Tribology International, 2012. 46(1): p. 161-173.

162. Wang, X.Y. and D.Y. Li, *Mechanical, electrochemical and tribological properties of nano-crystalline surface of 304 stainless steel.* Wear, 2003. 255(7): p. 836-845.

163. Wang, L. and D. Li, *Mechanical, electrochemical and tribological properties of nanocrystalline surface of brass produced by sandblasting and annealing.* Surface and Coatings Technology, 2003. 167(2): p. 188-196.

164. Wood, R.J.K., Walker, JC., Harvey, TJ., Wang, S., *Influence of microstructure on the erosion and erosion–corrosion characteristics of 316 stainless steel.* Wear, 2013. 306(1): p. 254-262.